APPLIED COMPUTATIONAL ELECTROMAGNETICS SOCIETY JOURNAL

January 2021
Vol. 36 No. 1
ISSN 1054-4887

The ACES Journal is abstracted in INSPEC, in Engineering Index, DTIC, Science Citation Index Expanded, the Research Alert, and to Current Contents/Engineering, Computing & Technology.

The illustrations on the front cover have been obtained from the research groups at the Department of Electrical Engineering, The University of Mississippi.

JANUARY 2021 REVIEWERS

Ali Al-Azza
Reza K. Amineh
Marco Arjona
Ravi Kumar Arya
Sawyer Campbell
Nunzia Fontana
Stavroula Foteinopoulou
Mohammad Haerinia
Muhammad Hamza
Ahmed Hassan
Mithilesh Kumar
Yuchen Ma
Peyman Mahouti
Wending Mai
Ghanshyam Mishra
Antonino Musolino
Ayodele Oluwole
Antonio Orlandi
Yashwanth Reddy Padooru
James Quinlan
C.J. Reddy
Jimmy Roden
Daniele Romano
Pavel Roy Paladhi
Leonardo Sandrolini
Stefano Selleri
Kamel Sultan
Hossein Torkaman
Bojan Trkulja
Chao Wang
Lu Wang
Jin Wei
Wei-Chung Weng
Yuancheng Xu
Feng Xuejian
Erdem Yazgan
Shihyuan Yeh
Xiaohua Yi
John Young
Wei-Hua Zong

THE APPLIED COMPUTATIONAL ELECTROMAGNETICS SOCIETY JOURNAL

Vol. 36 No. 1 January 2021

TABLE OF CONTENTS

A New Method for Crosstalk Prediction Between Triple-twisted Strand (Uniform and Non-uniform) and Signal Wire based on CDBAS-BPNN Algorithm

Yanxing Ji [1], Wei Yan [1*], Yang Zhao [1], Chao Huang [1], Shiji Li [1], Jianming Zhou [1], and Xingfa Liu [2]

[1] School of Electrical & Automation Engineering
Nanjing Normal University, Nanjing 210046, China
397832514@qq.com, *61197@njnu.edu.cn, zhaoyang2@njnu.edu.cn, 1547796467@qq.com, lishijin@njnu.edu.cn, zhoujianmingz@163.com, liuxingfa@epri.sgcc.com.cn

[2] China State Key Laboratory of Power Grid Environmental Protection
Wuhan Branch of China Electric Power Research Institute, Wuhan 430000, China

Abstract ─ This paper proposes a novel crosstalk prediction method between the triple-twisted strand (uniform and non-uniform) and the signal wire, that is, using back-propagation neural network optimized by the beetle antennae search algorithm based on chaotic disturbance mechanism (CDBAS-BPNN) to extract the per unit length (p.u.l) parameter matrix, and combined with the chain parameter method to obtain crosstalk. Firstly, the geometric model and cross-sectional model between the uniform triple-twisted strand and the signal wire are established, and the corresponding model between the non-uniform triple-twisted strand and the signal wire is obtained by the Monte Carlo (MC) method. Then, the beetle antennae search algorithm based on chaotic disturbance mechanism (CDBAS) and back-propagation neural network (BPNN) are combined to construct a new extraction network of the p.u.l parameter matrix, and the chain parameter method is combined to predict crosstalk. Finally, in the verification and analysis part of the numerical experiments, comparing the crosstalk results of CDBAS-BPNN, BAS-BPNN and Transmission Line Matrix (TLM) algorithms, it is verified that the proposed method has better accuracy for the prediction of the model.

Index Terms ─ Beetle Antenna Search (BAS), Back-Propagation Neural Network (BPNN), chaotic disturbance mechanism, crosstalk, triple-twisted strand.

I. INTRODUCTION

Multi-core stranded wire has the characteristics of low loss, low cost and small coupling [1]. Thus, they are widely used in modern electronic equipment and systems (such as communication systems, aircraft and ships). Although it has good performance in reducing radiated interference, further research is needed to analyze the crosstalk between lines [2-4]. At the same time, with the complexity and miniaturization of equipment, unnecessary electromagnetic interaction or crosstalk between wires will be greatly enhanced, thereby reducing the performance of the equipment.

For the study of cable crosstalk, the traditional method is to directly solve its transmission lines equation through the transmission lines model to obtain crosstalk [5]. However, the cross-sectional position in the twisted-wire pair (TWP) is random and unknown. The randomness of the cross-sectional position brings different p.u.l parameter matrices, so it is difficult to predict its crosstalk directly by traditional methods [6, 7].

Recently, many researchers have studied the prediction of TWP crosstalk. They focused their research on TWP, but relatively little research has been done on the crosstalk of triple-twisted strand. In [8], Taylor extended the results of uniform parallel lines to TWP, which is suitable for non-uniform transmission lines model. However, this method relies on the assumption of torsion and the accuracy is not high. In [9], Cannas proposed to treat non-uniform stranded wires as a cascade of uniform cross-sections and used BPNN to make predictions. In [10], the random displacement spline interpolation (RDSI) was proposed by Dai to generate a set of non-uniform wire harnesses to provide training samples, and then used the trained BPNN to predict the crosstalk, but ordinary BPNN may have high error, and its prediction range is narrow.

According to the theory of cascading transmission lines proposed by Paul and McKnight, cascaded multi-section transmission lines are used to replace the overall wiring harness [11-13]. Therefore, as long as the p.u.l

Submitted On: June 6, 2020
Accepted On: August 9, 2020

https://doi.org/10.47037/2020.ACES.J.360101

parameter matrices at different positions are obtained, the crosstalk of the cable can be obtained by the chain parameter method.

In this paper, the coupling model between the uniform triple-twisted strand and the signal wire is established through the production principle of triple-twisted strand. Based on this, the Monte Carlo (MC) method was used to obtain the coupling model between the non-uniform triple-twisted strand and the signal wire, and the randomness of the non-uniform triple-twisted strand was simulated. In our previous research [14-16], neural networks have been shown to express the relationship between the transmission lines position and the p.u.l parameter matrix. The BPNN algorithm relies heavily on its initial weight and threshold parameters, but its initial weight and threshold is randomly generated, which results in a large difference in the results of each simulation and poor robustness [17-19]. This paper combines the CDBAS algorithm and the BPNN algorithm to obtain a new p.u.l parameter matrix prediction network [20, 21]. Compared with the traditional BPNN algorithm, the convergence speed is faster and the solution accuracy is higher. Then, using the chain parameter model, the near-end crosstalk (NEXT) and far-end crosstalk (FEXT) between the triple-twisted strand and the signal wire are given. The results of numerical experiments verify the effectiveness of the method.

The rest of the paper is organized as follows: In Section II, the model of the triple-twisted strand (uniform and non-uniform) and the signal wire is established. In Section III, the p.u.l parameter matrix at any position of the transmission line is obtained through CDBAS-BPNN, and the voltage and current at both ends of the line are derived. In Section IV, the numerical experiments are used to verify the proposed method, which proves the accuracy of this method. On this basis, the crosstalk results are analyzed, and the terminal voltage characteristics under line-to-line coupling are obtained. Finally, the results are given in Section V.

II. THE MODEL OF TRIPLE-TWISTED STRAND AND SINGLE WIRE

In this paper, based on the production principle of triple-twisted strand, a coupling model of the uniform triple twisted-strand and the signal wire is established, as shown in Fig. 1. The diameter of the core is D, the height from the ground is h, and the distance of the center of the triple-twisted strand from the separate single wire is d. According to the idea of the cascading method, the triple-twisted strand is divided into uniform small pieces along the axial direction. And the following characteristics are assumed: Each transmission line can be considered as a parallel transmission line, there is only one mode of transverse electric and magnetic wave propagation on the transmission line; the geometric shape of the cross-section can be considered as a circular outline; the structure and material of each cable are the same.

Figure 2 shows the coupling model between the non-uniform triple-twisted strand and the signal wire. Except for the uneven twisting of the stranded wire, the other parameters are the same as those in Fig. 1. This paper uses the MC method to randomly simulate a non-uniform model. The coordinate positions of the triple-twisted strand (uniform and non-uniform) and the signal wire can be expressed as formula (1):

$$\begin{cases} m_r(x,y,z) = (\frac{\sqrt{3}}{3}D\cos\theta_z, h+\frac{\sqrt{3}}{3}D\sin\theta_z, z) \\ m_g(x,y,z) = (\frac{\sqrt{3}}{3}D\cos(\theta_z+120°), h+\frac{\sqrt{3}}{3}D\sin(\theta_z+120°), z) \\ m_b(x,y,z) = (\frac{\sqrt{3}}{3}D\cos(\theta_z-120°), h+\frac{\sqrt{3}}{3}D\sin(\theta_z-120°), z) \\ m_s(x,y,z) = (d,0,z) \end{cases}, \quad (1)$$

where m_r, m_g and m_b represent the position coordinates of each point on the triple-twisted strand. m_s indicates the position coordinates of each point on the signal wire. θ_z represents the rotation angle at the axial position z corresponding to the initial position z=0.

Figure 3 is the change of the cross-section of the wire within one revolution of the uniform triple-twisted strand. Different sections correspond to different p.u.l parameter matrices.

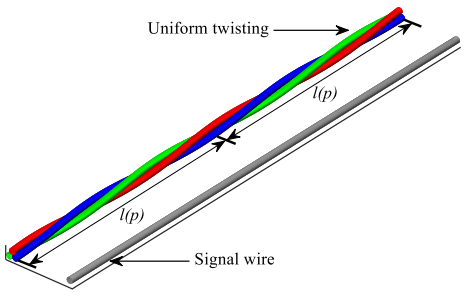

Fig. 1. Geometric model of uniform stranded wire and signal wire.

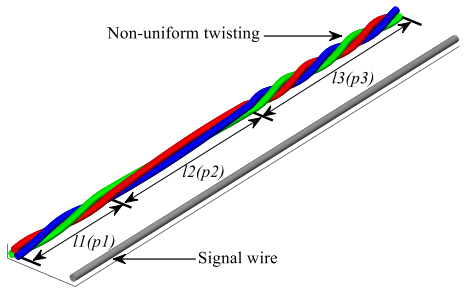

Fig. 2. Geometric model of non-uniform stranded wire and signal wire.

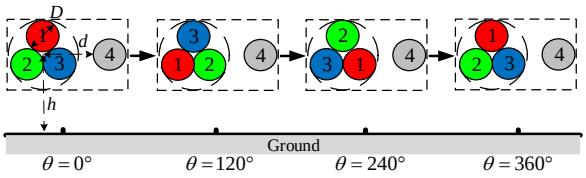

Fig. 3. Changes in the cross-section of the wire harness during a uniform rotation.

In the model of single wire and uniform triple-twisted strand, the rotation angle corresponding to different positions is:

$$\theta_z = \frac{360°z}{p}, \tag{2}$$

where p is the axial length of the triple-twisted strand rotating evenly, that is, the pitch of the transmission line.

In the non-uniform model, only the twisting degree of the triple-twisted strand is non-uniform. Therefore, all its cross-sectional models can be obtained in the uniform model, but the twisting angles corresponding to different positions are different. The MC method can simulate the model of non-uniform triple-twisted strand and the angle of rotation corresponding to the cross-section.

III. ACQUISITION OF PARAMETER MATRIX AND PREDICTION OF CROSSTALK

A. Unit length parameter matrix

In order to facilitate the study, only the uniformly divided model is considered first, and each segment is regarded as a parallel transmission line. The micro-element conduction model of a multi-conductor transmission line per unit length is shown in Fig. 4. r_{ij}, l_{ij}, c_{ij}, and g_{ij}, respectively represent the elements in the resistance **R**, inductance **L**, capacitance **C**, and conductance **G** parameter matrices, where $i, j = 1, 2, 3 \cdots n$.

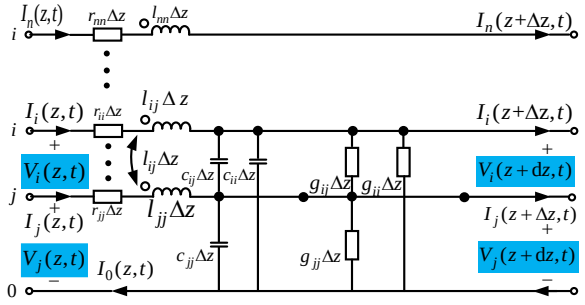

Fig. 4. Unit length equivalent circuit model of multi-conductor transmission line.

The voltage and current of the transmission line satisfy the following equation [10]:

$$\begin{aligned} \frac{\partial \mathbf{V}(z,t)}{\partial z} + \mathbf{R}(z)\mathbf{I}(z,t) + \mathbf{L}(z)\frac{\partial \mathbf{I}(z,t)}{\partial t} = 0 \\ \frac{\partial \mathbf{I}(z,t)}{\partial z} + \mathbf{G}(z)\mathbf{V}(z,t) + \mathbf{C}(z)\frac{\partial \mathbf{V}(z,t)}{\partial t} = 0 \end{aligned}, \tag{3}$$

where $\mathbf{V}(z,t)$ and $\mathbf{I}(z,t)$ are the voltage and current vectors at position z and time t. $\mathbf{R}(z)$, $\mathbf{L}(z)$, $\mathbf{C}(z)$ and $\mathbf{G}(z)$ represent the unit length parameter matrix at position z, which are all symmetric matrices of order $n \times n$.

In the uniform model, since the rotation of the triple-twisted strand is uniform, the parameters in the parameter matrix **X** of 0°~120°, 120°~240°, 240°~360° are all the same, but the positions are different, as long as the corresponding transformation is performed:

$$\mathbf{X}(z(\theta')) = \begin{cases} \mathbf{T}\mathbf{X}(z(\theta))\mathbf{T}^T & ,\theta' \in [120°, 240°) \\ \mathbf{T}^2\mathbf{X}(z(\theta))(\mathbf{T}^T)^2 & ,\theta' \in [240°, 360°) \end{cases}, \tag{4}$$

where **T** is the transformation matrix, which is:

$$\mathbf{T} = \begin{bmatrix} 0 & 0 & 1 & 0 \\ 1 & 0 & 0 & 0 \\ 0 & 1 & 0 & 0 \\ 0 & 0 & 0 & 1 \end{bmatrix}. \tag{5}$$

In the non-uniform model, since the cross-section can be obtained from the uniform model, the parameter matrix **X** can be obtained from the uniform model.

B. Predicting p.u.l parameter by CDBSA-BPNN algorithm

Due to the geometric characteristics of the stranded wire, the **RLCG** parameter matrix at different positions is different. Formula (6) can be obtained from formula (4):

$$\mathbf{X}(z) = f(\theta). \tag{6}$$

It can be seen from formula (6) that different rotation angles correspond to different parameter matrices. There is a nonlinear mapping relationship between the rotation angle and the parameter matrix. Therefore, this paper introduces a BPNN algorithm with strong nonlinear mapping ability. Because there are many elements in the parameter matrix of the triple-twisted strand, as the output of the BPNN, the output of the network may be trapped in the local minimum. Therefore, the CDBAS algorithm is employed to optimize the weight of the BPNN. BAS algorithm is sensitive to the dimensionality of the optimization target. The dimensionality of the weight w composed of w_i and w_{ij} is large in the model of this paper. Thus, the CDBAS algorithm is used for optimization. The topology of CDBAS-BPNN is shown in Fig. 5.

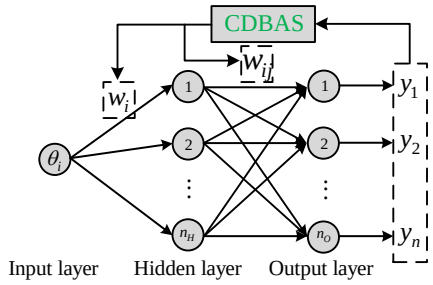

Fig. 5. Topological structure of CDBAS-BPNN.

The input of the network is the rotation angle θ_i ($0 \le \theta_i \le 120^\circ$) of the cross-section *i*. The output is the **RLCG** parameter matrix value of cross-section *i*. Since the parameter matrix is a symmetric matrix, its upper triangle is taken as a row of vectors as the output, the number of vector dimension is:

$$1+2+3+\cdots+\mathrm{n}=\sum n. \tag{7}$$

The number of hidden layers n_h is an empirical value determined by the number of output layers n_o, which can be as follows:

$$n_h = 0.5(n_o+1)+a, \quad a=1,2,\cdots 10. \tag{8}$$

The input layer to the hidden layer uses the sigmoid function *h*(x), and the hidden layer to the output layer uses the linear function *o*(x). The input can get a nonlinear output through forward propagation, and then the CDBAS algorithm is used to back-propagate the error *f*(x) to obtain the global minimum:

$$\begin{cases} h(x) = \dfrac{1}{1+e^{-x}} \\ o(x) = x \end{cases}. \tag{9}$$

The weights w_i and w_{ij} are determined by the CDBAS algorithm. The specific steps are as follows:

Step 1: Determine optimization goals and build search model.

For *N* sets of data, the mean square deviation of the network output and the actual value is:

$$f(x) = \frac{1}{2N}\sum_{i=1}^{N}\sum_{j=1}^{n_2}(y_j - y_j')^2, \tag{10}$$

where y_i' is the actual value of the parameter matrix, and $f(x)$ is the optimized objective function.

List the ownership value as a single row vector *x*, which represents the position of the beetle in the high-dimensional data space. At a certain time *t* the position of the beetle is:

$$x^t = \mathrm{rand}(k,1), \tag{11}$$

where *k* is the dimension of the weight vector, and rand is a *k*-dimensional column vector that generates a uniform distribution.

The search directions of beetle are:

$$\vec{b} = \frac{rand(k,1)}{\left\| rand(k,1) \right\|_2}. \tag{12}$$

By searching to the left or right, the activity of the antennae of the beetle's whiskers can be simulated:

$$x_r^t = x^t + d^t\vec{b}, \quad x_l^t = x^t - d^t\vec{b}, \tag{13}$$

where x_r^t is the position of the search area on the right whisker side, x_l^t is the position of the search area on the left whisker side, d^t is the antenna length of the beetle at time *t*. It should be long enough to cover the appropriate search range so that it can jump out from the local minimum point from the beginning, and then the sensor length gradually decreases with the passage of time *t*.

Step 2: Generate an iterative model of the position of the beetle:

$$x^{t+1} = x^t + \delta^{t+1}\vec{b}\,sign\left(f(x_r^t) - f(x_l^t)\right), \tag{14}$$

where δ is the step size of the search, which illustrates the convergence rate of the decreasing function of *t*. The initialization of δ should be equivalent to the search area. $sign(\cdot)$ represents the symbolic function.

The update rules for search parameters *d* and δ are:

$$\begin{cases} d^t = 0.95d^{t-1} + 0.01 \\ \delta^t = 0.95\delta^{t-1} \end{cases}. \tag{15}$$

Step 3: Generate chaotic sequence.

In the BAS algorithm, since the beetle is a single individual search, its global search effect is poor, and it cannot find the ideal result in a large range. Tent mapping is added to form CDBAS, so that it can search for the best fitness value in a large range.

The formula for Tent mapping is [22]:

$$X_n = \begin{cases} 2x_n & 0 \le x_n \le 1/2 \\ 2(1-x_n) & 1/2 \le x_n \le 1 \end{cases}, \tag{16}$$

where X_n is the n-th dimension variable of the chaotic sequence x^{t+1}, $n=1,2,\cdots k$. x_n is a random number obeying uniform distribution, $x_n \in [0,1]$.

Step 4: Perform chaos disturbance in the position of the beetle whiskers.

Map the chaotic variable back to the position *x* about the beetle:

$$newX_n = \min_n + (\max_n - \min_n)X_n, \tag{17}$$

where max_n and min_n are respectively the maximum and minimum values of the *n*-th dimension variable $newX_n$.

Chaotic disturbance to the position of the beetle:

$$newx^{t+1} = x^{t+1} + step \times (newX_n - x^{t+1})/2, \tag{18}$$

where x^{t+1} is the position of the beetle that needs chaos disturbance, $newX_n$ is the amount of chaos disturbance generated, $newx^{t+1}$ is the new position of the beetle after chaos disturbance, and *step* is the step length of the beetle.

Step 5: Update the optimal position and optimal objective function of beetle.

$$\begin{cases} x_{best} = x^{t+1} \\ f_{best} = f(x^t) \end{cases}. \tag{19}$$

The resulting x_{best} is the weight of the BPNN, and f_{best} is the global optimal error obtained by iteration. The specific process is shown in Fig. 6.

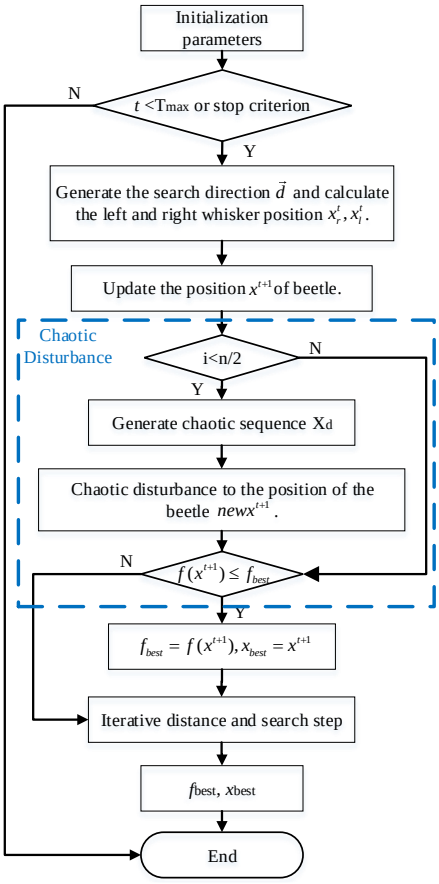

Fig. 6. CDBAS optimization neural network process.

C. Calculation of crosstalk

Turn formula (3) into a frequency domain equation:

$$\begin{cases} \dfrac{d}{dz}\mathbf{V}(z) = -\mathbf{Z}(z)\mathbf{I}(z) \\ \dfrac{d}{dz}\mathbf{I}(z) = -\mathbf{Y}(z)\mathbf{U}(z) \end{cases}, \tag{20}$$

where,

$$\begin{cases} \mathbf{V}(z) = [V_1(z); V_2(z); V_3(z); V_4(z)] \\ \mathbf{I}(z) = [I_1(z); I_2(z); I_3(z); I_4(z)] \\ \mathbf{Z}(z) = \mathbf{R}(z) + jw\mathbf{L}(z) \\ \mathbf{Y}(z) = \mathbf{G}(z) + jw\mathbf{C}(z) \end{cases}. \tag{21}$$

Perform the following modulus transformation,

$$\begin{cases} \mathbf{V}(z) = \mathbf{T}_V(z)\mathbf{V}_m(z) \\ \mathbf{I}(z) = \mathbf{T}_I(z)\mathbf{I}_m(z) \end{cases}. \tag{22}$$

The original equation can be reduced to:

$$\begin{cases} \dfrac{d^2}{dz^2}\mathbf{V}_m(z) = \mathbf{T}_V^{-1}(z)\mathbf{Z}(z)\mathbf{Y}(z)\mathbf{T}_V(z)\mathbf{V}_m(z) \\ \qquad\qquad = r^2\mathbf{V}_m(z) \\ \dfrac{d^2}{dz^2}\mathbf{I}_m(z) = \mathbf{T}_I^{-1}(z)\mathbf{Y}(z)\mathbf{Z}(z)\mathbf{T}_I(z)\mathbf{I}_m(z) \\ \qquad\qquad = r^2\mathbf{I}_m(z) \end{cases}, \tag{23}$$

where r^2 is a diagonal matrix of $n \times n$, and $T_V^+ = T_I^{-1}$, so the characteristic impedance $\boldsymbol{Z}_C$ and $\boldsymbol{Y}_C$ admittance matrix at different positions z are:

$$\begin{aligned} \mathbf{Z}_C(z) &= \mathbf{T}_V(z)r^{-1}(z)\mathbf{T}_V^{-1}(z)\mathbf{Z}(z) \\ \mathbf{Y}_C(z) &= \mathbf{T}_I(z)r^{-1}(z)\mathbf{T}_I^{-1}(z)\mathbf{Y}(z) \end{aligned}. \tag{24}$$

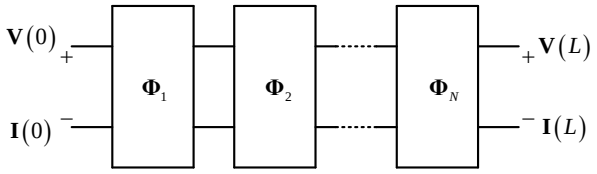

Fig. 7. Transmission line chain parameter model.

As shown in Fig. 7, get different chain parameter matrix:

$$\boldsymbol{\Phi}(z) = \begin{bmatrix} \phi_{11}(z) & \phi_{12}(z) \\ \phi_{21}(z) & \phi_{22}(z) \end{bmatrix}, \tag{25}$$

where $\phi_{11}(z)$, $\phi_{12}(z)$, $\phi_{21}(z)$, $\phi_{22}(z)$ are the chain parameter subarrays, they are:

$$\begin{cases} \phi_{11}(z) = \dfrac{1}{2}\mathbf{Y}^{-1}\mathbf{T}_I\left(e^{r\Delta z} + e^{-r\Delta z}\right)\mathbf{T}_I^{-1}\mathbf{Y} \\ \phi_{12}(z) = -\dfrac{1}{2}\mathbf{Y}^{-1}\mathbf{T}_I\left(e^{r\Delta z} - e^{-r\Delta z}\right)\mathbf{T}_I^{-1} \\ \phi_{21}(z) = -\dfrac{1}{2}\mathbf{T}_I\left(e^{r\Delta z} - e^{-r\Delta z}\right)r^{-1}\mathbf{T}_I^{-1}\mathbf{Y} \\ \phi_{22}(z) = \dfrac{1}{2}\mathbf{T}_I\left(e^{r\Delta z} + e^{-r\Delta z}\right)\mathbf{T}_I^{-1} \end{cases}. \tag{26}$$

Combining the CDBAS-BPNN algorithm to obtain the p.u.l at any position z, all the chain parameters $\boldsymbol{\Phi}(z)$ can be obtained by using formula (26).

The chain parameters of the transmission line are:

$$\boldsymbol{\Phi}(L) = \prod_{k=1}^{N}\boldsymbol{\Phi}_{N-k+1}(\Delta z_{N-k+1}). \tag{27}$$

$$\begin{bmatrix} \mathbf{V}(L) \\ \mathbf{I}(L) \end{bmatrix} = \boldsymbol{\Phi}(L)\begin{bmatrix} \mathbf{V}(0) \\ \mathbf{I}(0) \end{bmatrix}. \tag{28}$$

The terminal constraints are:

$$\begin{cases}\mathbf{V}(0)=\mathbf{V}_S-\mathbf{Z}_S\mathbf{I}(0)\\ \mathbf{V}(L)=\mathbf{V}_L+\mathbf{Z}_L\mathbf{I}(L)\end{cases}, \tag{29}$$

where $\mathbf{V}_S$=[0;0;0;V_S] is the near-end termination voltage source, and $\mathbf{Z}_S$ is the near-end termination impedance. $\mathbf{V}_L$=[0;0;0;0] is the far-end termination voltage source, and $\mathbf{Z}_L$ is the far-end termination impedance.

The resulting crosstalk is:

$$\begin{cases}\text{NEXT}=20\log_{10}(\mathbf{V}(0)/V_s)\\ \text{FEXT}=20\log_{10}(\mathbf{V}(L)/V_s)\end{cases}. \tag{30}$$

IV. VERIFICATION AND ANALYSIS

A. Verification of CDBAS-BPNN algorithm

In order to verify the effectiveness of the proposed method, this paper uses the model shown in Fig. 1. The distance between the triple-twisted strand and the signal wire is d=10mm, and the height of center wire from ground is h=8mm. The relevant parameters of the wire are shown in Table 1.

Table 1: Basic parameters

Name	Value
Wire diameter	0.8mm
Insulation layer thickness	0.6mm
Wire material	Copper
Insulation material	PVC
Wire length	1m

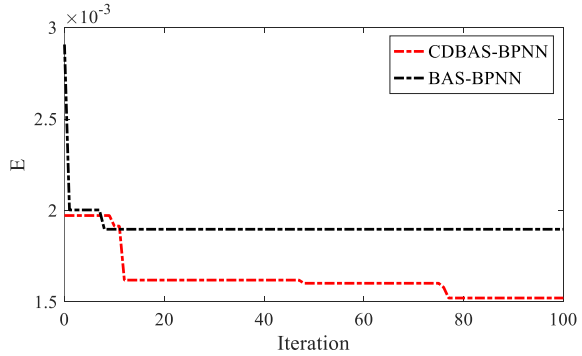

Fig. 8. CDBAS-BPNN iteration diagram.

The initial reference cross-sectional model is the cross section of 0° in Fig. 3. Using ANSYS simulation software to extract the parameter matrix, only need to consider the parameter matrix extraction of 0 ~ 120°, the parameter matrix of other angles can be obtained by formula (4). The **RLCG** matrix values are sampled every 4° between 0 ~ 120°, and there are 30 groups in total, which are used as training data for the CDBAS-BPNN algorithm. The number of hidden layers of BPNN is set to 8 and the number of CDBAS iterations is set to 100. The units of **R**, **L**, **C**, and **G** are Ω/m, nH/m, pF/m, and mS/m, respectively. Figure 8 is the iterative process of the average error of the parameter matrix of the BAS-BPNN and CDBAS-BPNN algorithms. The average errors E of BAS-BPNN and CDBAS-BPNN are 1.85x10^{-3} and 1.51x10^{-3}, respectively. It can be seen that the prediction accuracy of CDBAS-BPNN is better.

B. Analysis of crosstalk results

TLM method is used in the CST Cable Studio software to perform numerical simulation on the model of the triple-twisted strand and the signal wire [22]. Its layout in CST is shown in Fig. 9. Both ends of the triple-twisted strand are connected with 50Ω resistors, and the signal wire is connected to a signal source with an amplitude of 1V and a frequency varying from 0.1MHz to 1GHz.

The crosstalk results of #1, #2, and #3 of the uniform model are shown in Figs. 10, 11, and 12, respectively. The red solid line is the result obtained by the proposed method in this paper. The black dotted line is the result of CST simulation and is used as a reference value. The blue dotted line is the method of BAS-BPNN mentioned in reference [15], which is called the old method. The transmission line is divided into 1200 segments, and the CPU time spent by each group is 75.41s (the old method calculates the payment time is very close), while the CST calculation takes 2.41 minutes, which can reduce a lot of calculation time.

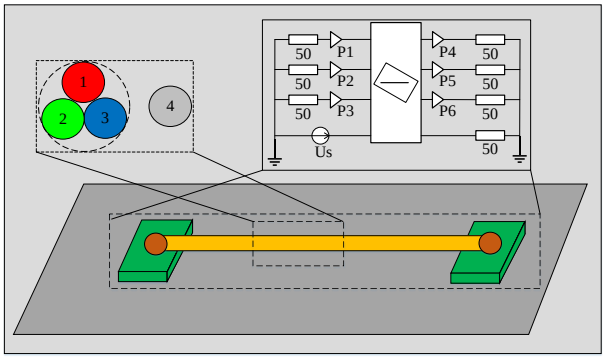

Fig. 9. CST simulation layout of the triple-twisted strand and the signal wire.

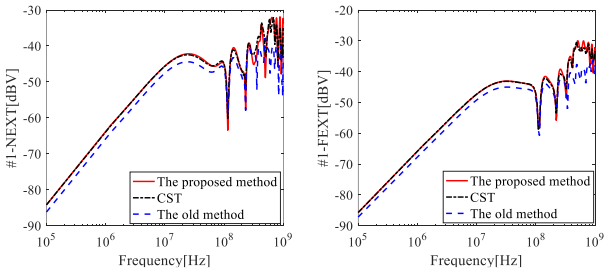

Fig. 10. Uniform #1 crosstalk.

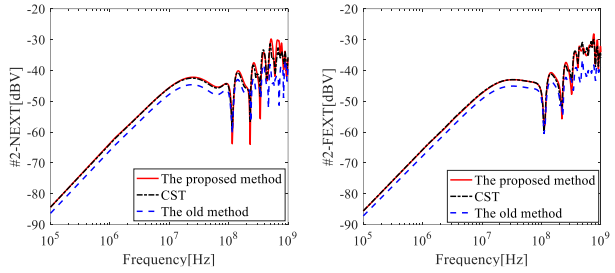

Fig. 11. Uniform #2 crosstalk.

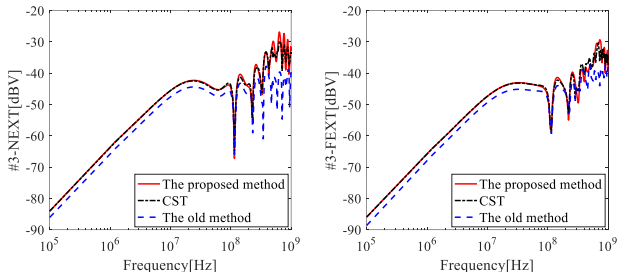

Fig. 12. Uniform #3 crosstalk.

In the low frequency range (0.1MHz < f <100MHz), the results of the two methods are basically the same as the reference value, but the old method still has a certain difference, which is about 1 to 2dB worse than the reference value. In the middle and high frequency range (100MHz < f < 1GHz), the old method starts to deviate from the reference value, especially in the high frequency range, the old method and the reference value began to have serious deviations, but the proposed method and the reference value can still maintain a good agreement.

It can be seen from Table 2 that the results are very consistent with the CST simulation results, the smallest average error is 0.06%, and the largest average error is 3.77%. However, the curve in the high frequency range (500MHz < f <1GHz) is less consistent than the curve in the low frequency range (0.1MHz < f <100MHz).

Table 2: Average error (%) of the uniform model

f/MHz		CDBAS-BPNN			BAS-BPNN		
	Wire	#1	#2	#3	#1	#2	#3
0.1~100	NEXT	0.07	0.59	0.10	3.92	4.69	4.69
	FEXT	0.06	0.08	0.28	4.02	4.60	4.28
100~500	NEXT	3.77	2.01	2.79	7.96	10.2	13.6
	FEXT	0.25	1.44	2.47	10.7	12.6	5.70
500~1000	NEXT	1.17	2.69	3.01	17.5	15.9	27.3
	FEXT	0.75	1.51	2.23	17.3	18.8	16.1

The crosstalk results of the non-uniform model are shown in Figs. 13, 14, 15 respectively. The red solid line is the result obtained by the method in this paper, and the CPU time spent by each group is 82.35s, and the CST calculation takes 3.36 minutes. The black dotted line is the result of CST simulation and is used as a reference value. The blue dotted line is the result of the old method. In the low frequency range (0.1MHz< f <100MHz), the results are basically similar to the uniform model. In the intermediate frequency range (100MHz< f <500MHz), the method proposed in this paper is more consistent with the reference value than the old method. In the high-frequency range (500MHz< f <1GHz), the near-end crosstalk obtained by the method in this paper is basically consistent, but the far-end crosstalk is slightly larger than the reference value.

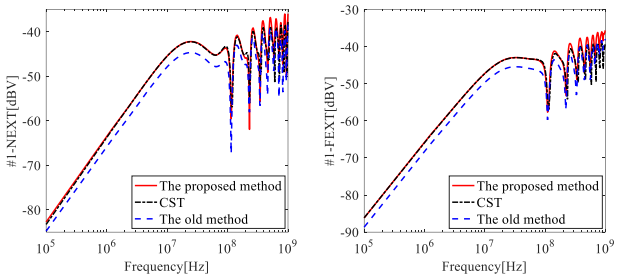

Fig. 13. Non-uniform # 1 crosstalk.

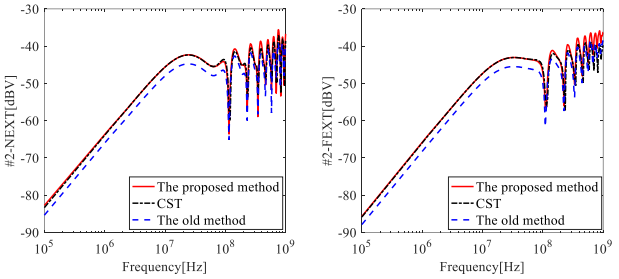

Fig. 14. Non-uniform # 2 crosstalk.

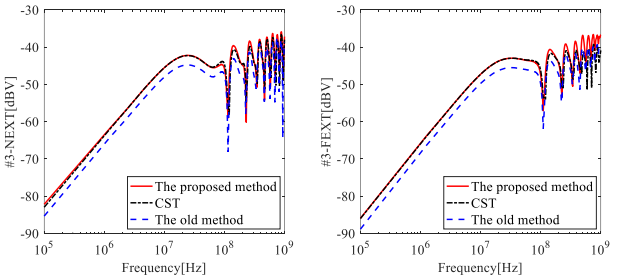

Fig. 15. Non-uniform # 3 crosstalk.

It can be seen from Table 3 that the smallest average error is 0.05% and the largest average error is 9.30%. However, in the high frequency range (500MHz <f <1GHz), the NEXT curve of the triple-twisted strand is more consistent than the FEXT curve result. The possible reason is that the non-uniform model is repeatedly iterated, which makes the far-end crosstalk result fluctuate greatly.

Table 3: Average error (%) of the non-uniform model

f/MHz		CDBAS-BPNN			BAS-BPNN		
	Wire	#1	#2	#3	#1	#2	#3
0.1~100	NEXT	0.06	0.22	0.43	6.01	5.58	5.74
	FEXT	0.22	0.32	0.43	6.07	5.91	6.06
100~500	NEXT	0.77	1.27	0.89	4.94	3.78	4.29
	FEXT	2.90	2.57	3.04	2.80	2.53	3.31
500~1000	NEXT	4.07	2.67	2.23	3.61	2.66	4.34
	FEXT	8.14	8.22	9.30	2.36	1.99	2.44

Comparing the uniform model and the non-uniform model, it can be seen that the non-uniform results fluctuate more in the high-frequency range, while the uniform results fluctuate less in its range. This is the performance of the randomness of the non-uniform model in the results. The result corresponding to each frequency point in the non-uniform model will cause a large error in the actual measurement. It is difficult to make a small change in the corresponding frequency range like the result in a uniform model, and the measurement accuracy is high.

V. CONCLUSION

For the coupling model of triple-twisted strand and signal wire, this paper proposes a p.u.l parameter matrix prediction process based on CDBSA-BPNN algorithm. Combined with the chain parameter method of the transmission line, a new method to predict the crosstalk between the triple-twisted strand and the signal wire is proposed. Numerical experimental results show that the method has good applicability and effectiveness, especially in the low-frequency and intermediate-frequency bands with high consistency. The results also show that the use of a non-uniform model can reduce the difference in crosstalk between strands, but will cause the crosstalk results to suffer greater fluctuations in the high-frequency range. The estimation results of the crosstalk between the triple-twisted strand and the signal wire can provide important guiding significance and reference value for the electromagnetic compatibility design in engineering practice. However, this paper does not consider the effect of frequency on the p.u.l parameter matrix and the triple-twisted strand. Therefore, there is still a lot of research space after this paper.

ACKNOWLEDGMENT

The paper is supported by National Natural Science Foundation of China (51475246), National Natural Science Foundation of Jiangsu Province (BK20161019), Aviation Science Foundation (20172552017), Key Project of Social Development in Jiangsu Province (BE2019716), Nanjing International Industrial Technology Research and Development Cooperation Project (201911021).

REFERENCES

[1] Y. Yan, L. Meng, X. Liu, T. Jiang, J. Chen, and G. Zhang, "An FDTD method for the transient terminal response of twisted-wire pairs illuminated by an external electromagnetic field," *IEEE Transactions on Electromagnetic Compatibility*, vol. 60, no. 2, pp. 435-443, Apr. 2018.

[2] C. Paul and J. McKnight, "Prediction of crosstalk involving twisted pairs of wires-Part I: A transmission-line model for twisted-wire pairs," *IEEE Trans. Electromagn. Compat.*, vol. EMC-21, no. 2, pp. 92-105, May 1979.

[3] R. Stolle, "Electromagnetic coupling of twisted pair cables," *IEEE J. Sel. Areas Comm.*, vol. 20, no. 5, pp. 883-892, June 2002.

[4] F. Grassi and S. A. Pignari, "Immunity to conducted noise of data trans-mission along DC power lines involving twisted-wire pairs above ground," *IEEE Trans. Electromagn. Compat.*, vol. 55, no. 1, pp. 195-207, Feb. 2013.

[5] C. R. Paul, *Analysis of Multiconductor Transmission Lines*. Hoboken, NJ, USA: Wiley, 1994.

[6] Y. Yan, L. Meng, X. Liu, T. Jiang, J. Chen, and G. Zhang, "An FDTD method for the transient terminal response of twisted-wire pairs illuminated by an external electromagnetic field," *IEEE Trans. Electromagn. Compat.*, vol. 60, no. 2, pp. 435-443, Apr. 2018.

[7] S. Chabane, P. Besnier, and M. Klingler, "A modified enhanced transmission line theory applied to multiconductor transmission lines," *IEEE Trans. Electromagn. Compat.*, vol. 59, no. 2, pp. 518-528, Apr. 2017.

[8] C. D. Taylor and J. P. Castillo, "On the response of a terminated twisted-wire cable excited by a plane-wave electromagnetic field," *IEEE Trans. Electromagn. Compat.*, vol. EMC-22, no. 1, pp. 16-19, Feb. 1980.

[9] B. Cannas, A. Fanni, and F. Maradei, "A neural network approach to predict the crosstalk in non-uniform multiconductor transmission lines," *In Proc. IEEE Int. Symp. Circuits Syst.*, Phoenix-Scottsdale, AZ, USA, pp. 573-576, June 2002.

[10] F. Dai, G. Bao, and D. Su, "Crosstalk prediction in non-uniform cable bundles based on neural network," *Proceedings of the 9th in Symp. on Antennas*, Propagation and EM Theory, Guangzhou, China, pp. 1043-1046, Nov. 2010.

[11] C. Jullien, P. Besnier, M. Dunand, and I. Junqua, "Advanced modeling of crosstalk between an unshielded twisted pair cable and an unshielded wire above a ground plane," *IEEE Trans. Electromagn. Compat.*, vol. 55, no. 1, pp. 183-194, Feb. 2013.

[12] A. Shoory, M. Rubinstein, A. Rubinstein, and F. Rachidi, "Simulated NEXT and FEXT in twisted wire pair bundles," *Proc. EMC Eur. Symp.*, York, U.K., pp. 266-271, Sept. 2011.

[13] M. Tang and J. Mao, "A precise time-step integration method for transient analysis of lossy nonuniform transmission lines," *IEEE Trans. Electromagn Compat.*, vol. 50, no. 1, pp. 166-174, Feb. 2018.
[14] C. P. Yang, W. Yan, Y. Zhao, Y. Chen, C. M. Zhu, and Z. B. Zhu, "Analysis on RLCG parameter matrix extraction for multi-core twisted cable based on back propagation neural network algorithm," *IEEE Access*, vol. 7, pp. 126315-126322, Aug. 2019.
[15] C. Huang, Y. Zhao, W. Yan, Q. Liu, and J. Zhou, "A new method for predicting crosstalk of random cable bundle based on BAS-BP neural network algorithm," *IEEE Access*, vol. 8, pp. 20224-20232, Jan. 2020.
[16] Q. Liu, Y. Zhao, W. Yan, C. Huang, A. Mueed, and Z. Meng, "A novel crosstalk estimation method for twist non-uniformity in twisted-wire pairs," *IEEE Access*, vol. 8, pp. 38318-38326, Feb. 2020.
[17] X. Yi, "Selection of initial weights and thresholds based on the genetic algorithm with the optimized back-propagation neural network," *In Proc. 12th Int. Conf. Fuzzy Syst. Knowl. Discovery (FSKD)*, Zhangjiajie, China, pp. 173-177, Aug. 2015.
[18] T. Rashid, *Make Your Own Neural Network*. 1st ed., Charleston, SC, USA: CreateSpace Independent Publishing Platform, 2016.
[19] M. Hassoun, *Fundamentals of Artifificial Neural Networks. Cambridge*, MA, USA: Bradford Book, 2003.
[20] H. Khan, X. Cao, S. Li, V. N. Katsikis, and L. Liao, "BAS-ADAM: an ADAM based approach to improve the performance of beetle antennae search optimizer," *IEEE/CAA Journal of Automatica Sinica*, vol. 7, no. 2, pp. 461-471, Mar. 2020.
[21] W. Bo, W. Jindong, Z. Hengwei, and Y. Dingkun, "Dynamic service selection based on chaotic mutation multi-objective particle swarm algorithm," *Proceedings of 2013 3rd International Conference on Computer Science and Network Technology*, Dalian, pp. 113-117, Oct. 2013.
[22] CST Microwave Studio, ver. 2008, Computer Simulation Technology, Framingham, MA, 2008.

Yanxing Ji was born in Jiangsu Province, China. He received the B.S degree in school of Yancheng Institute of Technology, Yancheng, China, in 2018. He is currently working toward the Master's degree in Electrical Engineering at Nanjing Normal University, Nanjing, China. His main research interests include multi-conductor transmission lines and EMC.

Wei Yan Doctor & Assoc. Professor from Nanjing Normal University. He obtained the Physics and Electronics Ph.D. and Electrical Engineering M.S. from Nanjing Normal University in 2014 and 2011. He is the Senior Member of China Electrical Technology Association and the evaluation expert of the Electromagnetic Compatibility Calibration Specification of China.

Yang Zhao received his B.E., M.E., and Ph.D. degree all in Power Electronic Technology from Nanjing University of Aeronautics and Astronautics, Nanjing, China, in 1989 and 1992, and 1995, respectively. He is currently the Professor with Nanjing Normal University. His research interests are in the areas of Electromagnetic Compatibility, Power Electronics and Automotive Electronics.

Chao Huang was born in Anhui Province, China. He received the B.S degree in school of Electrical Engineering and Automation from Anhui University of Technology, Maanshan, China, in 2018. He is currently working toward the Master's degree in Electrical Engineering at Nanjing Normal University, Nanjing, China. His main research interests include multi-conductor transmission lines and EMC.

Shiji Li received his Electrical Engineering M.S. from Nanjing Normal University in 2013. He is currently the Lecturer with Nanjing Normal University. His research interests are in the areas of Electromagnetic Compatibility and Industrial electric Automation.

Jianming Zhou was born in Jiangsu Province, China. He received the B.S degree in school of Electrical Engineering and Automation from Tianping College of Suzhou University of Science and Technology, Suzhou, China, in 2019. He is currently working toward the Master's degree in Electrical Engineering at Nanjing Normal University, Nanjing, China. His major research interests include new technology of electrical engineering.

Crosstalk Reduction on Delay Line with Rectangular-Patches (RPs) Design

Ding-Bing Lin [1], Ariana Tulus Purnomo [1], and Chung-Pin Huang [2]

[1] Department of Electronic and Computer Engineering
National Taiwan University of Science and Technology, Taipei, Taiwan
dblin@mail.ntust.edu.tw, d10602808@mail.ntust.edu.tw

[2] Advanced Development Department
WIESON Technologies Co., LTD., New Taipei, Taiwan
raber@wieson.com

Abstract ─ In this paper, a novel helix delay line with RPs structures is proposed to investigate the performance of crosstalk reduction. In the past, conventional delay lines consist of equal-length parallel unit lines which are closely packed to minimize the fabricated cost and routing area. All spacing between the adjacent parallel unit lines of delay lines should be smaller. When the operating signal frequency ups to the GHz level, the electromagnetic noise has become a dominant issue coupling from adjacent lines. It is called as a crosstalk source. The crosstalk may affect system-level timing. Besides, it causes error switching of logic gates that will reduce the signal quality. The feature of proposed helix delay line is that the far-end crosstalk (FEXT) is a dominated noise that accumulates at the receiving end. RPs structures are added and aligned at the center of the two parallel adjacent unit lines of the proposed helix delay line, which are used to reduce the difference between inductive and capacitive coupling coefficient ratios, and to reduce FEXT that maintains the signal integrity (SI) quality on receiving end.

Index Terms ─ Far-End Crosstalk (FEXT), helix delay lines, Rectangular-Patches (RPs), Signal Integrity (SI).

I. INTRODUCTION

Crosstalk is usually represented in terms of near-end crosstalk (NEXT) and FEXT [1]. FEXT is induced by the difference between the inductive coupling ratio and the capacitive coupling ratio. In addition, FEXT is also proportional to the length of parallel trace and exists in an inhomogeneous environment only, e.g., the microstrip geometry [2], [3]. In the past several years, the popular delay lines are with serpentine routing and spiral routings [4], [5]. In conventional serpentine and spiral delay lines, NEXT is a dominant noise that propagates to the receiving end. The noise accumulated at the receiving end will result in time-domain transmission (TDT) waveform degradation and affect the eye-diagram quality. Although there are many strategies for crosstalk noise reduction in early studies, the crosstalk noise such as NEXT always exists.

In order to reduce the NEXT and FEXT between adjacent parallel lines of the delay line, many design rules and techniques have been adopted by designers. A well-known 3W rule is a general method of reducing the crosstalk in which separation between adjacent lines of three times of line width [6]. A guard trace added within two adjacent lines is also a common method for crosstalk reduction. However, a guard trace without a terminator will experience noise and act as a potential source of noise for the victim [7], [8]. In contrast to the guard trace without termination, two terminators matching the line impedance can be placed on both ends of the guard trace to terminate the noise energy and reduce the crosstalk [9]. In the shorting-vias guard trace method [10], guard trace with grounded vias can maintain the stable grounded potential at every via point. In the via fences method [11], it is well known that a guard trace which is shorted at multiple points will lead to the lowest amount of crosstalk. It is because the via fence is designated to reduce the coupling between two adjacent lines. In order to reduce the crosstalk in parallel double microstrip lines, the optimal number and location of grounded vias method will be adapted for preventing the crosstalk as well [8]. In addition, a serpentine guard trace with the grounded vias was proposed to reduce the crosstalk between two adjacent parallel lines [12]. Besides, a new design of FEXT crosstalk reduction is proposed by using the rectangular-shape resonators on two parallel-coupled microstrip lines [13]. Nowadays, there are some studies for FEXT reduction such as using a homogeneous dielectric substrate on PCBs [14], coated graphene on microstrip lines [15], surface mount capacitors on FEXT mitigation [16], and RSR for FEXT mitigation [17]. However, using a homogenous dielectric substrate, graphene, and capacitor increases the PCB cost and probably increase the production loss.

Submitted On: June 16, 2020
Accepted On: November 29, 2020

https://doi.org/10.47037/2020.ACES.J.360102

Based on the last studied in [18], some new investigations and extensions in FEXT reduction are shown in this paper. For example, the derivation on the section of the three-coupled lines is equivalent to the mathematical models of the mutual-capacitance. The design methodologies in determining the dimensions of RPs for increasing the mutual-capacitance between the adjacent parallel lines, and the representations of both three-coupled lines and two-coupled lines sections are concatenated together for FEXT calculation. This equation is presented in this paper.

This paper is organized as follows: a brief characterization of crosstalk is revisited in Section II. The proposed helix delay line and the crosstalk analysis are illustrated in Section III. In Section IV, we focus on the design methodology of determining the dimensions of RPs. In addition, equivalent capacitance circuit model of the three-coupled lines section, and the relationship between capacitance values and inductance values are also presented. The comparisons between the simulated and the measured results are presented in Section V. Some Brief conclusions are presented in Section VI. Finally, one RPs design example for increasing mutual-capacitance in two parallel adjacent unit lines was shown in the appendix section to improve the readability of this paper.

II. INTRODUCTION TO NEXT AND FEXT

Crosstalk occurs due to the coupling effects caused by the mutual-capacitance and the mutual inductance of the victim and aggressor lines, driven by the transient signals in the aggressor. The end of the victim closer to the driver (receiver) of the aggressor is called the near (far) end. When the rise and fall times of the aggressor's transient logic state change continuously, the signal operation of the victim will be destroyed because the energy coupling is transferred from the aggressor [1]. Crosstalk is usually represented in terms of NEXT and FEXT. The formulas for NEXT and FEXT can be represented as:

$$V_{NEXT} = \frac{V_{in}}{4}\left(\frac{L_m}{L_S} + \frac{C_m}{C_T}\right), \quad (1)$$

$$V_{FEXT} = \frac{-V_{in} \cdot TD}{2t_r}\left(\frac{L_m}{L_S} + \frac{C_m}{C_T}\right), \quad (2)$$

where V_{in} is the input voltage, TD is the time delay, t_r is the rising time, L_S is the self-inductance, L_m is the mutual-inductance, C_T is the self-capacitance, and C_m is the mutual-capacitance [19]. As can be seen from equation (2), the amplitude of FEXT is determined by the difference between the inductive coupling ratio (L_m/L_s) and the capacitive coupling ratio (C_m/C_T). For example, in some practice cases, the unit length of two adjacent parallel lines with microstrip geometry, where the dielectric constant of the surrounding air is less than that of the inside PCB dielectric constant, the inductive coupling ratio is always larger than the capacitive coupling ratio. Thus, FEXT is a negative pulse.

III. CROSSTALK IN HELIX DELAY LINE

The novel helix delay line without RPs structures and with RPs structures are shown in Fig. 1 (a) and Fig. 1 (b), respectively. In Fig. 1 (a), all unit lines (e.g., sections of A-C, C-D, etc.) in the helix delay line always keep counter-clockwise routing. Besides, it has the same width and spacing between adjacent unit lines that is used to maintain the impedance under the acceptable level. In addition, both the helix delay line without RPs and the helix delay line with RPs structures are employed with microstrip geometry. The via hole is used to connect the line between the top and the bottom layers at point R under the line impedance that maintains the acceptable level. The cross-sectional view is shown in Fig. 1 (c).

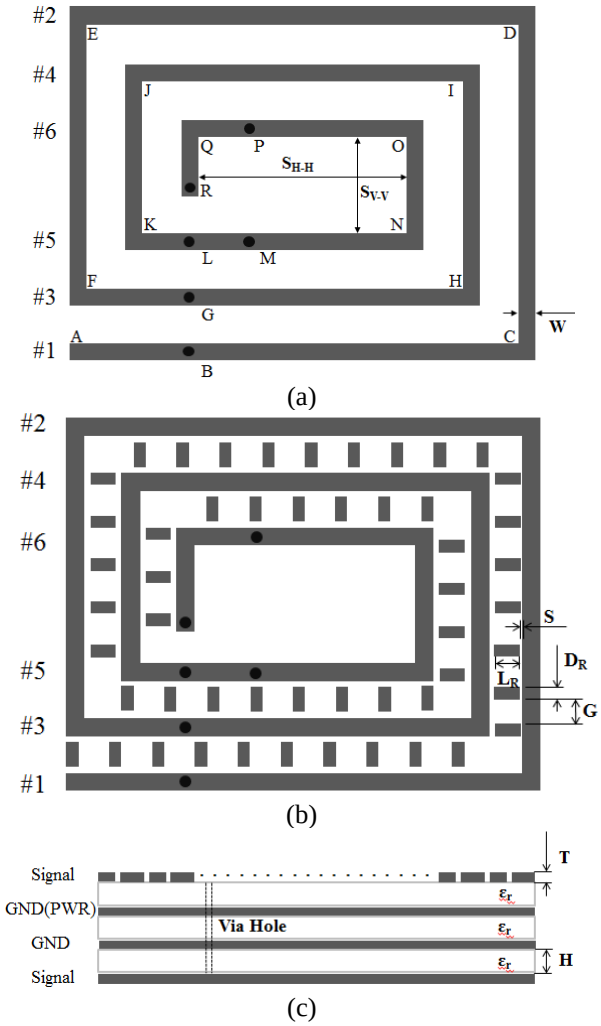

Fig. 1. The schemes of helix delay line. (a) without rectangular-patches (RPs); (b) with rectangular-patches (RPs); (c) the cross-sectional view.

Based on the assumption that the weak coupling condition was considered in the helix delay line, the noise induced on the adjacent victim line rarely affects

the main stimulus signal on the aggressor line [20], [21]. As can be seen in Fig. 1 (a), when a main stimulus step signal travels down all unit lines (i.e., point A to C, C to D, etc.) to the receiving end (i.e., point R) of the helix delay line, the crosstalk will be induced. The best two units are formed when two unit lines are in the nearest neighborhood to the main stimulus signal. E.g., when a main stimulus step signal propagates to point G of #3 unit line, meanwhile, crosstalk was induced on point B of #1 unit line and point L of #5 unit line. In point B of #1 unit line, the crosstalk is the result of the mutual capacitance in conjunction with the mutual inductance between adjacent unit lines. Thus, it can be divided into two directions. Due to the fact that this crosstalk observed on the adjacent unit lines (i.e., #1 unit line) far away from the driver end of point F, one crosstalk propagates to the point C of #1 unit line and it finally propagates to point R of receiving end. It is given by *FEXT* ($V_{far\text{-}end}$). Another one propagates to point A of #1 unit line. Because this crosstalk is close to the driver end of point F, it is given by *NEXT* ($V_{near\text{-}end}$). The same condition happens when a main step stimulus signal is at point G of #3 unit line. The crosstalk was induced on point L of #5 unit line and can divide it into two directions. One propagates to the point N of #5 unit line, given by *FEXT* ($V_{far\text{-}end}$). Another one propagates to point K of #5 unit line, given by *NEXT* ($V_{near\text{-}end}$). The FEXT on point B of #1 propagates to the receiving end of the helix delay line behind the main stimulus signal. On the contrary, the FEXT on point L of #5 propagates to receiving end of helix delay line ahead of the main stimulus signal.

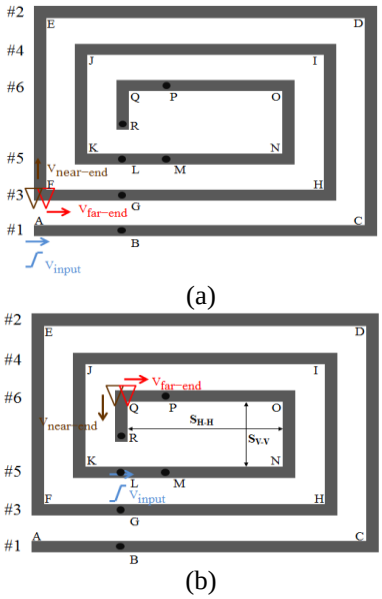

Fig. 2. The crosstalk on the helix delay line. (a) NEXT and FEXT on #3 unit line; (b) NEXT and FEXT on #6 unit line.

For a simple crosstalk analysis, let us consider the crosstalk that can be seen on all unit lines. It propagates to the receiving end ahead of the main stimulus signal when the main stimulus signal travels down all unit lines of the helix delay line. As can be seen in Fig. 2 (a), we consider a helix delay line with twelve unit lines. When a main stimulus step signal with amplitude (V_{input}) and rise time (t_r) was driven at point A of #1 unit line, crosstalk was induced at point F of #3 unit line and can divide into two parts. One is a FEXT at point F of #3 unit line. It propagates toward the point H of #3 unit line. This crosstalk finally propagates to the receiving end of point R. Another one is NEXT at point F of #3 unit line. It propagates toward the point E of #2 unit line. This crosstalk finally propagates to the driver end of point A. As can be seen in Fig. 2 (b), when a main stimulus step signal propagates to point L of #5 unit line, crosstalk current is induced at point Q of #6 unit line. Because the crosstalk is the result of the mutual capacitance in conjunction with the mutual inductance between adjacent unit lines, it can divide into two directions. One propagates to the point O of #6 unit line. Finally, this crosstalk propagates to point A of #1 unit line. Besides, this crosstalk is observed on the adjacent unit lines (i.e., #6 unit line) that is far away from the driver end when the main stimulus signal propagates along #5 unit line, given by *FEXT* ($V_{far\text{-}end}$). Another one is that it propagates to point R of receiving end. This crosstalk can be seen on the adjacent unit lines close to the driver end when the main stimulus signal propagates along #5 unit line, given by *NEXT* ($V_{near\text{-}end}$). The same analysis method can consider the crosstalk which can be seen on all unit lines and propagates to the receiving end behind the main stimulus signal.

All $V_{far\text{-}end}$ induced from adjacent unit lines will propagate to point R of receiving end when a main stimulus step signal travels down all unit lines from point A of #1 unit line to L of #5 unit line. On the other hand, in Fig. 2 (b), the distance of both $S_{V\text{-}V}$ and $S_{H\text{-}H}$ (e.g., the adjacent unit lines distance between point N to O and O to Q) is larger enough as compared with the distance between two parallel adjacent unit lines (i.e., the distance between #1 and #3 unit lines, etc.). The $V_{near\text{-}end}$ can be neglected. Thus, the TDT waveform at the receiving end is mainly affected by $V_{far\text{-}end}$ in the proposed helix delay line.

IV. RPs TO INCREASE THE MUTUAL-CAPACITANCE OF ADJACENT UNIT LINES SECTION OF HELIX DELAY LINE

RPs are regularly added and aligned at the center of the two parallel adjacent unit lines of the helix delay line. As mentioned in Section II, the amplitude of FEXT is determined by the difference between the inductive coupling ratio (L_m/L_s) and the capacitive coupling ratio (C_m/C_T). Therefore, the design topology of FEXT

reduction in the proposed helix delay line with microstrip geometry is to increase the C_m. In order to minimize the difference between inductive coupling ratios and capacitive coupling ratios, in term of adding RPs at the center of the two parallel adjacent unit lines of the helix delay line, the FEXT formula is represented by (2).

In order to develop the design rule of RPs, and the spacing between adjacent RPs in the helix delay line, firstly, the helix delay line with RPs should be divided into several parallel three-coupled lines sections (the cross-sectional view of helix delay line with RPs structures) and several two-coupled lines sections (the cross-section view of the helix delay line without RPs structures), as shown in Fig. 3. Secondly, two equations are presented to achieve the self-capacitance and the mutual-capacitance of a parallel three-coupled lines section of helix delay line, as shown in (3) and (4). Due to the assumption that the surrounding conductors are not ferromagnetic, both parallel three-coupled lines and two-coupled lines sections of helix delay line with the dielectric can be replaced by using the air. Thus, it can achieve their self-inductance and mutual-inductance values. Finally, an industry case is described in detail and presented. This part presents the increasing of mutual-capacitance in the helix delay line with adding RPs in its adjacent parallel lines section to reduce the FEXT. In this paper, the width and the length of each RPs are denoted as L_R and D_R. The distance between two edges of adjacent RPs is denoted as G, as shown in Fig. 1 (b). The RPs design starts from determining the physical dimensions of L_R and D_R. The L_R and D_R of each RPs should be shorter than the one-tenth wavelength of the system rise time. The rise time typically takes a signal to transition between its magnitude within 10 ~ 90% edge rate [19]. In addition, to neglect the mutual coupling from adjacent RPs, the distance between adjacent RPs should be no shorter than three times of the D_R of RPs. Finally, the width and the length of each RPs can be achieved as the design above.

A. Equivalent inductance and capacitance circuit models in the three-coupled lines section

In Fig. 3, we assume that the cross-sectional dimensions of parallel three-coupled lines and two-coupled lines sections of helix delay line are different in the Z direction. The per-unit-length capacitance and inductance will be the functions of position in Z direction. For an example, *C(Z)* and *L(Z)*. This non-uniform transmission line is not easy to be solved because the resulting of per-unit-length parameters will be the functions of the independent variables in the same fashion as a non-constant coefficient ordinary differential equation. In addition, by making the approximation of the gap between consecutive patches in the *Z* direction, it significantly increases the size than in the *X* direction. Thus, per-unit-length parameters will be the functions of positions *X*, these approximations can be reached by neglecting the fringing of the field [22]. Thus, the lumped circuit approximation method in this paper is used to present the circuit model of each parallel uniform three-coupled lines section and each parallel uniform two-coupled lines section. Besides, it also adds the representations of them for FEXT calculation. For example, in the two-coupled lines section, the cross section of helix delay without RPs structures, it is easy to achieve all inductance and capacitance values for evaluating the NEXT and FEXT. An example in the three-coupled lines section, the cross section of helix delay with RPs structures, equation (3) [23], and (4) are presented in this paper to achieve the equivalent values of self-capacitance and mutual-capacitance. The equivalent values of the mutual-capacitance (i.e., C'_m) and the self-capacitance (i.e., C'_{11}) on three-coupled lines section can be directly derived as:

$$C'_m = C_{31} + \frac{C_{21} \cdot C_{32}}{C_{2g} + C_{21} + C_{32}}, \tag{3}$$

$$C'_{11} = C_{11} + \frac{C_{21} \cdot C_{21}}{C_{2g} + C_{21} + C_{32}}, \tag{4}$$

where C_{11} is the self-capacitance of aggressor line, C_{22} is the self-capacitance of patch, C_{31} is the mutual-capacitance between aggressor line and victim line, C_{21} and C_{32} are the mutual-capacitance between patch and unit line, C_{2g} is the self-capacitance of the patch to ground, and $C_{2g} = C_{22} - C_{21} - C_{32}$. Based on the assumption that the cross-section of the three-coupled lines section is a symmetrical geometry, and RPs is aligned at the center of the two-unit lines, the $C_{21} = C_{32}$. From (3), increasing the C_{21} and C_{32} will get higher C'_m which can significantly lower the difference between the inductive and the capacitive coupling ratios. Because the aggressor and victim lines of the three-coupled lines section are symmetrical geometries, the $C'_{11} = C'_{33}$. The capacitance circuit model of the three-coupled lines section and its equivalent circuit model are shown in Fig. 4 and Fig. 5, respectively.

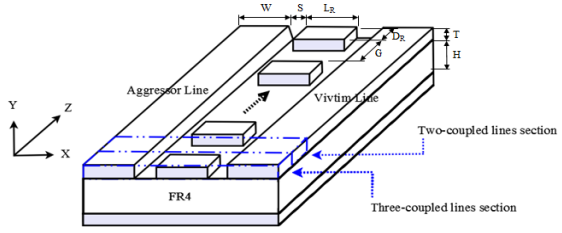

Fig. 3. A cross-sectional view of the two parallel adjacent unit lines with RPs structures.

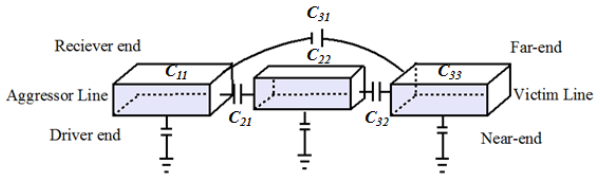

Fig. 4. A capacitance circuit model of helix delay line with RPs.

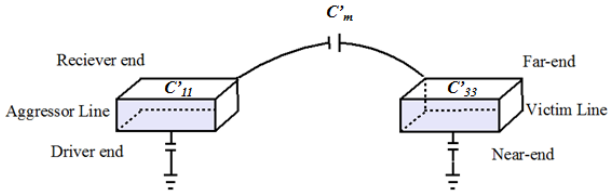

Fig. 5. An equivalent capacitance circuit model of helix delay line with RPs.

Let us assume that any medium surrounding the conductors are not ferromagnetic in the helix delay line and permeability of free space $\mu = \mu_0$. We designate the capacitance matrix with the surrounding medium removed and replaced by free space having permeability ε_0 and permeability μ_0 as C_0. Since inductance depends on the permeability of the surrounding medium and does not depend on the permittivity of the medium, the inductance matrices either self-inductance or mutual-inductance can be obtained from C_0 using the relations for a homogeneous medium, given as [24]:

$$L = \mu_0 \varepsilon_0 C_0^{-1}. \quad (5)$$

B. RPs parameters study

Figure 6 shows the simulation results of FEXT observed in two adjacent parallel lines with varying the S between the RPs and two adjacent parallel lines when dimensions are selected by W = 0.66 mm, H = 0.4 mm, T = 0.035 mm. As can be seen in Table 1, it is evident that the FEXT reduction can reach by 5.2% when the RPs dimensions are selected with L_R = 0.66 mm, D_R = 0.75 mm, and S = 0.1 mm, compared to the two parallel adjacent lines without RPs. Additionally, when the cases of S = 0.075 mm and S = 0.05 mm, the larger value of mutual-capacitance C_m can increase the ratio of C_m to C_T. The FEXT reductions can reach 13.6% and 33.7%. All results are simulated by a 3-D full-wave CST simulator [25] with a single-ended step signal of 50 ps rise time. Figure 7 compares the simulated TDT waveforms of varying L_R of RPs when considering a twenty-unit lines helix delay line with RPs structures. The dimensions are with W = 0.4 mm, H = 0.27 mm, D_R = 0.1 mm, G = 0.3 mm, T = 0.045 mm, $S_{H\text{-}H}$ = 1.2 mm, $S_{V\text{-}V}$ = 1.6 mm, ε_r = 4.3, and loss tangent = 0.035.

All simulation are implemented by a 3-D CST simulator, and the input source is chosen as a single-ended step signal with 50 ps rising time. In Fig. 7, the TDT voltage drops around 0.7-0.8ns on the case of helix delay line without RPs design because the FEXT accumulating at receiving end. A contrast to the helix delay line with RPs design, when the dimensions are selected with L_R = 0.45mm, L_R = 0.4mm, and L_R = 0.35 mm, the voltage drop has a visible reduction to the case of helix delay line without RPs design. Besides, the simulation results indicates that the smaller distance between the unit line and RPs on the case with L_R = 0.45mm (S = 0.075mm), the number of voltage drop has smallest one among four cases. It means that the smallest distance has the largest number of C_m between unit line and RPs. Figure 8 and Fig. 9 compare the simulation results for both transmission and reflection coefficients of the proposed helix delay line with RPs structures and without RPs structures. It shows that the helix delay line with RPs structures can maintain the acceptable level of transmission and reflection coefficients compared to the case of helix delay line without RPs.

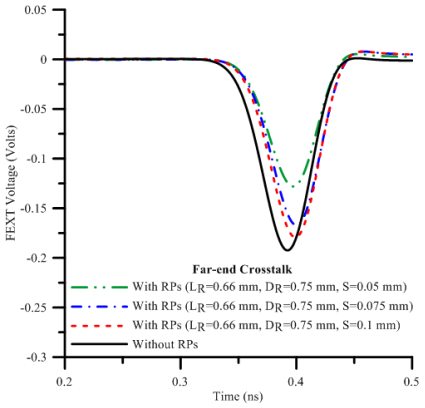

Fig. 6. The simulated waveform of FEXT.

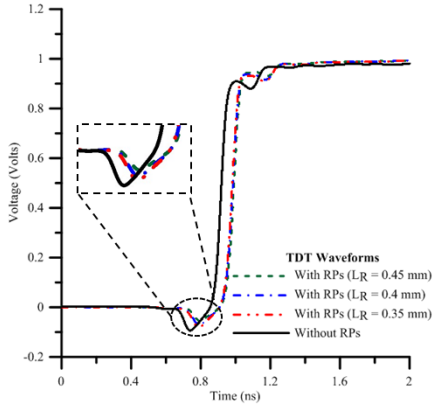

Fig. 7. The simulated TDT waveforms with varying the width of RPs.

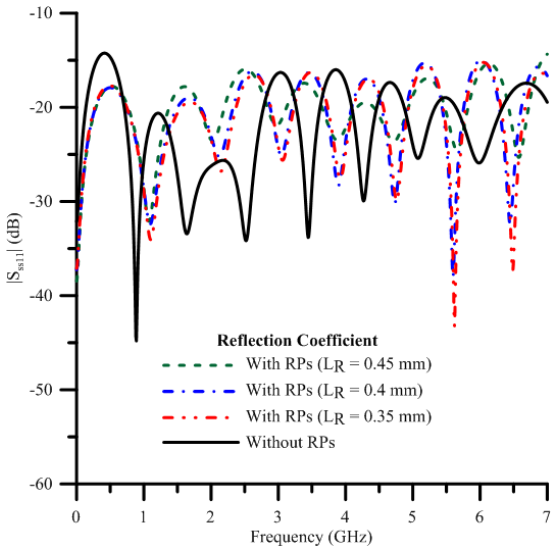

Fig. 8. The simulated reflection coefficient with varying the width of RPs.

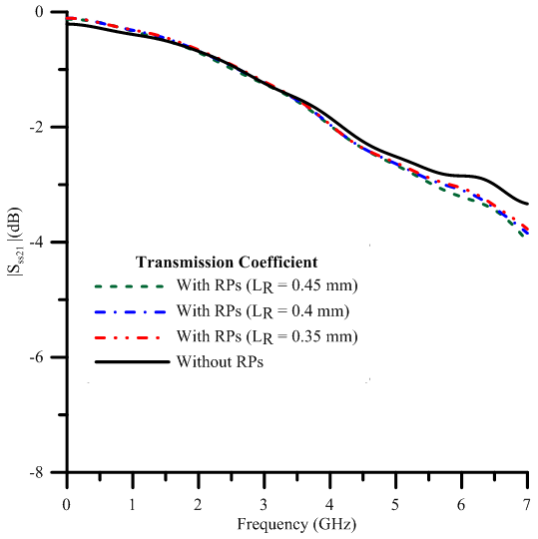

Fig. 9. Simulated transmission coefficient with varying the width of RPs.

Table 1: Simulated results of FEXT

Geometry	**FEXT (Volts)**
Two parallel adjacent unit lines without RPs	-0.193
Two parallel adjacent unit lines with RPs (L_R=0.66mm, D_R=0.75mm, S=0.1mm)	-0.183
Two parallel adjacent unit lines with RPs (L_R=0.66mm, D_R=0.75mm, S=0.075 mm)	-0.167
Two parallel adjacent unit lines with RPs (L_R=0.66mm, D_R=0.75mm, S=0.05mm)	-0.128

V. MEASUREMENT VALIDATION

The time-domain input source is selected as a single-ended step signal with an amplitude VS and the rise time t_r launched by the voltage source. Input source is connected to the driver at the end of the helix delay line in the top layer. The single-ended impedance of each unit line section of the helix delay line is 50 Ω. The source and the load resistances are chosen as R_S = R_L = 50 Ω. The load resistor is connected to the receiving end. The time-domain and the frequency-domain simulations are performed by 3-D CST full-wave simulator. Keysight 86100C TDR and E5071C VNA are used to perform measurement validations of time-domain and frequency-domain. The schematic setup is shown in Fig. 10. There are four schemes to verify the crosstalk reduction on the proposed helix delay line with RPs structures which are based on the common setting, such as the physical length between the source end to the receiving end, a number of unit lines, the spacing between adjacent unit lines, and the circuit size of the PCB.

The following four delay lines are compared. The first is the proposed helix delay line with thirteen-unit lines (1). The dimensions are with W = 0.45 mm, H = 0.305 mm, T=0.045 mm, $S_{H\text{-}H}$=2.25 mm, $S_{V\text{-}V}$=2.25 mm, FR4 with ε_r = 4.3, loss tangent = 0.035 and all spacing between adjacent unit lines are 0.6 mm. The second is the proposed helix delay line with RPs structures (2). The dimensions are with W = 0.45 mm, L_R = 0.45 mm, D_R = 0.1 mm, S = 0.075 mm and G = 0.3 mm. The third is the dimensions in serpentine delay line (3) and the fourth is the spiral delay line (4) with W = 0.45 mm, H = 0.305 mm, T=0.045 mm, FR4 with ε_r = 4.3, loss tangent = 0.035 and all spacing between adjacent unit lines are 0.6 mm, as shown in Fig. 11.

In eye-diagram between two cases of helix delay line with RPs and the case of helix delay line without RPs, it shows that the increment of the mutual-capacitance improves the waveform quality of the eye diagram. Because the RPs are added in the helix delay line, the eye-opening can be increased by 0.05 V. Figure 12 (a) and Fig. 12 (b) presents that the overshooting and undershooting can be reduced by 0.048 V and 0.049 V. As can be seen in Fig. 12 (b) and Fig. 12 (c), the overshooting and undershooting in the eye-diagram of helix delay line with RPs structures can significantly reduce by ((0.165 - 0.035) / 0.165) × 100% = 78.8% and ((0.169 - 0.043) / 0.169) × 100% = 74.6% compared to serpentine delay line. Besides, the crosstalk accumulates the receiving end of the serpentine delay line and appears as the undershooting and overshooting in the eye-diagram, as shown in Fig. 12 (c). Similarly, as can be seen in Fig. 12 (b) and Fig. 12 (d), the overshooting and undershooting in the eye-diagram of helix delay line with RPs structures can significantly reduce by ((0.069 - 0.035) / 0.069) ×

100% = 49.3% and ((0.075 - 0.043) / 0.075) × 100% = 42.7% compared to spiral delay line.

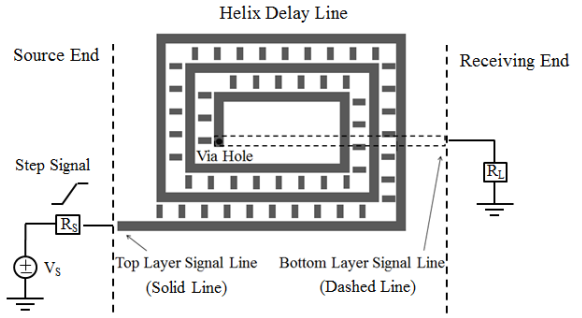

Fig. 10. The graphical schematic for time-domain simulation and measurement.

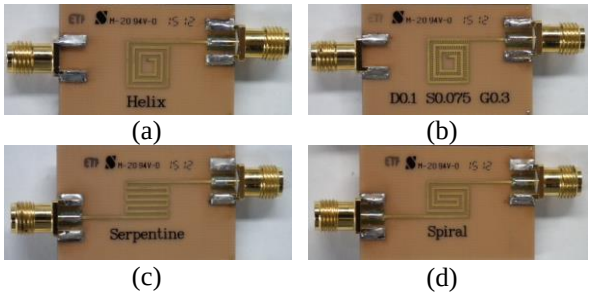

Fig. 11. The photographs of fabricated delay line. (a) The helix delay line; (b) the helix delay line with RPs structures; (c) the serpentine delay line; (d) the spiral delay line.

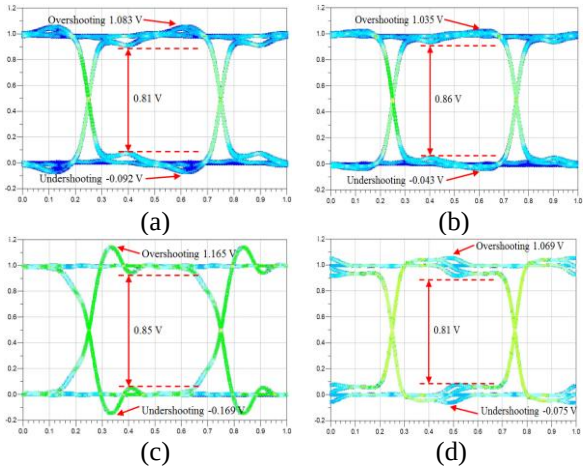

Fig. 12. The measurement results of eye-diagram. (a) The helix delay line; (b) the helix delay line with RPs; (c) the serpentine delay line; (d) the spiral delay line.

In Fig. 13, the helix delay line with RPs structures can significantly increase the mutual-capacitance and minimize the difference between the inductive with the capacitive coupling ratios. Thus, the helix delay line with RPs structures can significantly reduce the TDT waveform penalty around 0.6 ns. Keysight 86100C TDR measures the results with single-ended ramped step signal of 50 ps rise time. Figure 14 and Fig. 15 compare the measurement results of the transmission and reflection coefficients for the helix delay line without RPs, the helix delay line with RPs, the serpentine and the spiral delay lines. The results are measured by Keysight E5071C VNA. In Fig. 14 and Fig. 15, the helix delay line with RPs structures can maintain a significant level of both transmission and reflection coefficients compared to others. Thus, the proposed helix delay line with RPs does not spoil the signal transmission.

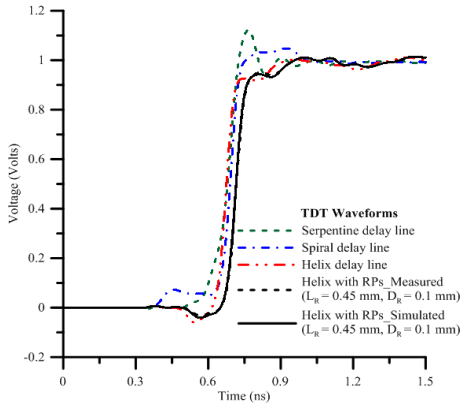

Fig. 13. The comparison between simulation and measurement of TDT waveforms.

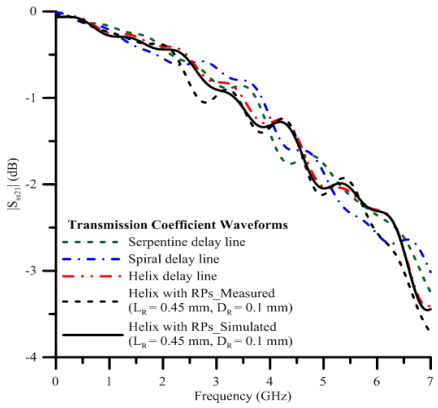

Fig. 14. The comparison between simulation and measurement of transmission coefficient.

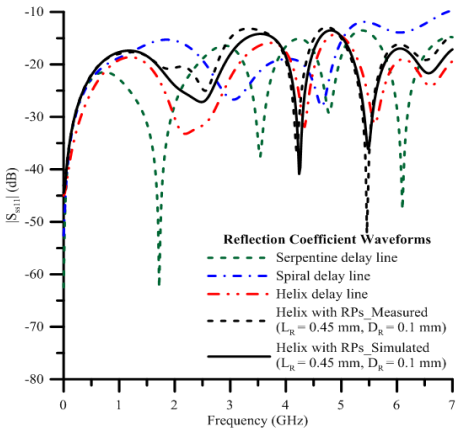

Fig. 15. The comparison between simulation and measurement of reflection coefficient.

VI. CONCLUSION

3W spacing, guard trace with ground-via, guard trace with terminators, a homogeneous dielectric substrate, grapheme coated, adding capacitors on between adjacent lines, and using RSR are common methods applied to the crosstalk reduction in past studies. Although there are with good crosstalk reduction performance, yet many ground-via, homogeneous dielectric substrate, graphene, and capacitors will increase the manufacturing cost and ground-via. Besides, the capacitors will limit the routing flexibility. In contrast to the proposed helix delay line with RPs structures, it does not need many ground-via, terminators, capacitors, and extra covering materials. Thus, it efficiently decreases the manufacturing cost, mitigates the limitation of the routing area, and reduces the routing space for reaching a miniature design. Besides, compared to the conventional packed serpentine and spiral delay lines, the NEXT is a dominant noise that is accumulated at the receiving end. The NEXT always exists and may affect the system-level timing that causes error switching in logic gates. The proposed novel helix delay lines, FEXT is a dominant noise, it can be significantly reduced with RPs. The RPs was used to significantly increase the mutual-capacitance between adjacent parallel lines of the helix delay line.

In simulation and measurement results, the helix delay line with RPs structures can significantly reduce the FEXT compared to the helix delay line without RPs structures. Besides, it improves the quality of the eye-diagram compared to the conventional serpentine and spiral delay lines. Some comparisons with the others conventional delay lines are also made to evaluate the transient TDT waveform. It is also found that the proposed helix delay line with RPs structure design has lower overshooting and undershooting voltage which can maintain eye-diagram quality.

ACKNOWLEDGMENT

This work was supported by the Ministry of Science and Technology, Taiwan, under grant MOST 108-2221-E-011-035.

APPENDIX

RPs design for increasing mutual-capacitance in two parallel adjacent unit lines

In this section, in order to make a clear view about the increasing of mutual-capacitance in two parallel adjacent unit lines by adding the RPs structures, an industrial case of the two parallel adjacent lines with the length of 0.05025 m was adapted. Besides, we also provide the comparison between the proposed circuit model and 3-D full-wave simulation. The two-coupled lines section of this industrial case (i.e., the cross-sectional view of two parallel adjacent unit lines without RPs section) is shown in Fig. 3. The dimensions are with W = 0.66 mm, H = 0.4 mm, T = 0.035 mm. The spacing between adjacent unit lines is 0.86 mm. The length of each two-coupled lines section is 2.25 mm. The values of the mutual-capacitance, the self-capacitance, mutual-inductance, and self-inductance are C_m = 3.29 pF/m, C_T = 110 pF/m, L_m = 28.9 nH/m and L_S = 319 nH/m, extracted from Keysight ADS circuit simulator.

Table 2: Inductive and capacitive values of the three-coupled lines section

Capacitance (pF/m)					
C_{11}	C_{21}	C_{22}	C_{32}	C_{33}	C_{31}
128	36.3	150	36.3	128	0.91
Inductance (nH/m)					
L_{11}	L_{21}	L_{22}	L_{32}	L_{33}	L_{31}
284	*103*	*259*	*103*	*284*	*35.9*

The three-coupled lines section of this industrial case (i.e., the cross-sectional view of two parallel adjacent unit lines with RPs section) is shown in Fig. 3. The RPs are aligned regularly at the center of the two adjacent lines. The dimensions are L_R = 0.66 mm, D_R = 0.75 mm and S = 0.1 mm. The values of the mutual-capacitance, the self-capacitance, the mutual-inductance, and the self-inductance in the three-coupled lines section are listed in Table 2, extracted from Keysight ADS circuit simulator as well. The equivalent values of the mutual-capacitance and the self-capacitance in the three-coupled lines section would be achieved through (3) and (4). Their equivalent values of the self-inductance and the mutual-inductance can be achieved through (5). The equivalent values are with C_m = 9.69 pF/m, C_T = 136.8 pF/m, L_m = 29.7 nH/m and L_S = 218 nH/m. We assume that the noise source on the aggressor line was driven with the step single-ended signal, and the rise time of step signal is 50 ps. The current velocity is 1.66×10^8 m/s (i.e., 1.66×10^8

m/s = 1 / ((136.8 pF/m + 9.69 pF/m) × (218 nH/m + 29.7 nH/m))$^{1/2}$). Therefore, both dimensions of L_R and D_R of each RPs should be shorter than 0.83 mm (i.e., 0.83 mm = ((1.66×10^8 m/s) × (50 ps)) / 10).

Finally, the lumped values of inductance and capacitance of each two-coupled lines section and each three-coupled lines section can be added together to calculate the FEXT. In this industrial case, the length is 0.03825 m of two-coupled lines section (i.e., 0.03825 m = 17 × 2.25 mm, 17 two-coupled lines sections) and 0.012 m of three-coupled lines section (i.e., 0.012 m = 16 × 0.75 mm, 16 three-coupled lines sections) when the total length of the parallel adjacent lines is 0.05025 m. The lumped values are with C_m = 4.82 pF/m (i.e., 4.82 pF/m = (3.29 pF/m × 0.03825 m) / 0.05025 m + (9.69 pF/m × 0.012 m) / 0.05025 m), C_T = 117 pF/m (i.e., 117 pF/m = (110 pF/m × 0.03825 m) / 0.05025 m + (136.8 pF/m × 0.012 m) / 0.05025 m), L_m = 29.1 nH/m (i.e., 29.1 nH/m = (28.9 nH/m × 0.03825 m) / 0.05025 m + (29.7 nH/m × 0.012 m) / 0.05025 m) and L_S = 295 nH/m (i.e., 295 nH/m = (319 nH/m × 0.03825) / 0.05025 m + (218 nH/m × 0.012 m) / 0.05025 m). Therefore, all capacitance and inductance coupling ratios, including two-coupled lines section (i.e., 0.0299 = (3.29 pF/m / 110 pF/m), 0.0906 = (28.9 nH/m / 319 nH/m)), equivalent three-coupled lines section (i.e., 0.0708 = (9.69 pF/m / 136.8 pF/m), 0.1362 = (29.7 nH/m / 218 nH/m)), lumped two-coupled lines section and equivalent three-coupled section (i.e., 0.0412 = (4.82 pF/m / 117 pF/m), 0.0986 = (29.1 nH/m / 295 nH/m)), are listed in Table 3.

Table 3: Inductive and capacitive coupling ratios

Coupling Ratios	Two-Coupled Lines Section	Equivalent Three-coupled Lines Section	Lumped Two-coupled Lines Section and Equivalent Three-coupled Lines Section
$\lvert C_m/C_T \rvert$	0.0299	0.0708	0.0412
$\lvert L_m/L_S \rvert$	0.0906	0.1362	0.0986
$\lvert L_m/L_S \rvert - \lvert C_m/C_T \rvert$	0.0607	0.0654	0.0574
$\lvert L_m/L_S \rvert + \lvert C_m/C_T \rvert$	0.1205	0.2070	0.1398

REFERENCES

[1] M. S. Sharawi, "Practical issues in high speed PCB design," *IEEE Potentials*, vol. 23, no. 2, pp. 24-27, Apr.-May 2004.

[2] Y. S. Cheng, W. D. Guo, G. H. Shiue, H. H. Cheng, C. C. Wang, and R. B. Wu, "Fewest vias design for microstrip guard trace by using overlying dielectric," *2008 IEEE-EPEP Electrical Performance of Electronic Packaging*, pp. 321-324, Oct. 2008.

[3] S. K. Lee, K. Lee, H. J. Park, and J. Y. Sim, "FEXT-eliminated stub-alternated microstrip line for multi-gigabit/second parallel link," *Electronics Letters*, vol. 44, no. 4, pp. 272-273, Feb. 2008.

[4] R. B. Wu and F. L. Chao, "Laddering wave in serpentine delay line," *IEEE Trans. Comp., Pkg., Manuf. Technol., B*, vol. 18, no. 4, pp. 644-650, Nov. 1995.

[5] R. B. Wu and F. L. Chao, "Flat spiral delay line design with minimum crosstalk penalty," *IEEE Trans. Comp., Pkg., Manuf. Technol., B*, vol. 19, no. 2, pp. 397-402, May 1996.

[6] Mark I. Montrose, *EMC and the Printed Circuit Board: Design, Theory, and Layout Made Simple*, John Wiley and Sons, INC, California, 1998.

[7] C. H. Chen, W. T. Huang, C. T. Chou, and C. H. Lu, "Accurate design methodology to prevent crosstalk," *Electron. Lett.*, vol. 43, no. 3, pp. 11-12, Feb. 2007.

[8] W. T. Huang, C. H. Lu, and D. B. Lin, "The optimal number and location of grounded vias to reduce crosstalk," *Progress In Electromagnetics Research*, vol. 95, pp. 241-266, 2009.

[9] R. Y. Sharma, T. Chakravarty, and A. B. Bhattacharyya, "Transient analysis of microstrip-like interconnections guarded by ground tracks," *Progress In Electromagnetics Research*, vol. 82, pp. 189-202, 2008.

[10] D. N. Ladd, and G. I. Costache, "SPICE simulation used to characterize the crosstalk reduction effect of additional tracks grounded with vias on printed circuit boards," *IEEE Transactions on Circuits and Systems II: Analog and Digital Signal Processing*, vol. 39, no. 6, pp. 342-347, June 1992.

[11] A. Suntives, A. Khajooeizadeh, and R. Abhari, "Using via fences for crosstalk reduction in PCB circuits," *IEEE Int. Symp. Electromagn. Compat.*, pp. 34-37, Aug. 2006.

[12] W. T. Huang, C. H. Lu, and D. B. Lin, "Design of suppressing crosstalk by vias of serpentine guard trace," *PIERS Proceedings*, pp. 484-488, Mar. 2010.

[13] D. B. Lin, C. K. Wang, C. H. Lu, and W. T. Huang, "Using rectangular-shape resonators to improve the far-end crosstalk of the coupled microstrip lines," *PIRES Proceedings*, pp. 20-23, Mar. 2011.

[14] Q. M. Cai, L. Zhu, X. B. Yu, L. Zhang, C. Zhang, Y. Y. Zhu, and X. Cao, "Far-end crosstalk mitigation using homogeneous dielectric substrate in DDR5," *2019 12th International Workshop on the Electromagnetic Compatibility of Integrated Circuits (EMC Compo)*, pp. 198-200, Oct. 2019.

[15] M. I. Refaie, W. S. El-Deeb, and M. I. Abdalla, "A study of using graphene coated microstrip lines for crosstalk reduction at radio frequency," *35th National Radio Science Conference*, pp. 86-90, Mar. 2018.

[16] Z. Chen, "PCB microstrip line far-end crosstalk mitigation by surface mount capacitors," *2019 IEEE 69th Electronic Components and Technology Conference (ECTC)*, pp. 1989-1995, May 2019.

[17] L. Zhang, Q. M. Cai, X. B. Yu, L. Zhu, C. Zhang, Y. Ren, and J. Fan, "Far-end crosstalk mitigation for microstrip lines in high-speed PCBs," *2019 Cross Strait Quad-Regional Radio Science and Wireless Technology Conference (CSQRWC)*, pp. 1-3, July 2019.

[18] D. B. Lin, C.-P. Huang, C.-H. Lin, H.-N. Ke, W.-S. Liu, "Using rectangular-patches (RPs) to reduce far-end crosstalk noise and improve eye-diagrams on microstrip helix delay line," *IEEE International Symposium on Electromagnetic Compatibility and EMC Europe*, pp. 612-615, Aug. 2015.

[19] S. H. Hall, G. W. Hall, and J. A. McCall, *High-Speed Digital System Design, A Handbook of Interconnect Theory and Design Practices*, John Wiley and Sons, Inc., New York, 2000.

[20] D. J. Riley and L. D. Bacon, "On the limitation of the weak-coupling assumption for crosstalk analysis based on quasi-TEM propagation," *IEEE Trans. Electromagn. Compat.*, vol. 32, pp. 28-37, Feb. 1990.

[21] W. D. Guo, G. H. Shiue, and R. B. Wu, "Comparison between serpentine and flat spiral delay lines on transient reflection/transmission waveforms and eye diagram," *IEEE Trans. Microw. Theory Tech.*, vol. 54, no. 4, pp. 1379-1387, Apr. 2006.

[22] Clayton R. Paul, *Analysis of Multiconductor Transmission Lines*, 2nd ed., John Wiley and Sons, Canada, 2008.

[23] K. Lee, H. B. Lee, H. K. Jung, J. Y. Sim, and H. J. Park, "A serpentine guard trace to reduce the far-end crosstalk voltage and the crosstalk induced timing jitter of parallel microstrip lines," *IEEE Trans. Adv. Packag.*, vol. 31, no. 4, pp. 809-817, Nov. 2008.

[24] C. Wei, R. F. Harrington, J. R. Mautz, and T. K. Sarkar, "Multiconductor transmission lines in multi-layered dielectric media," *IEEE Transmission on Microwave Theory and Techniques*, vol. 32, no. 4, pp. 439-445, Apr. 1984.

[25] Computer Simulation Technology, ver. 2015, CST Studio Suite, Dassault System, France, 2015.

Ding-Bing Lin received the M.S. and Ph.D. degrees in Electrical Engineering from the National Taiwan University, Taipei, Taiwan, in 1989 and 1993 respectively. From Aug. 1993 to July 2016, he had been on the faculty of the Electronic Engineering Department, National Taipei University of Technology, Taipei, Taiwan, where he was an Associate Professor, a Professor and a Distinguished Professor in 1993, 2005 and 2014 respectively. Since Aug. 2016, he had been with National Taiwan University of Science and Technology, Taipei, Taiwan, where he is currently a Professor of the Electronic and Computer Engineering Department. His current research interests include wireless communication, radio multipath fading channel modeling, mobile antennas, high-speed digital transmission, and microwave engineering. From 2015 to 2018, he served as the Taipei Chapter Chair, IEEE EMC society. Now he serves as Associate Editor of IEEE Transactions of Electromagnetic Compatibility. He also serves on the Editorial Board member of the International Journal of Antennas and Propagation since 2014. So far he has published more than 100 papers in the international journals and conferences.

Ariana Tulus Purnomo received the B.S. and M.S. degrees in Electrical Engineering from the Institute Technology Bandung (ITB), Bandung, Indonesia, 2015 and 2017 respectively. Besides, she also received her M.E. degree in Interdisciplinary Program of Information System from Pukyong National University (PKNU), Busan, South Korea in 2017. She is currently working toward the Ph.D. degree with the Department of Electronic and Computer Engineering, National Taiwan University of Science and Technology, Taiwan, under the supervision of Dr. Ding-Bing Lin. Her current research interests include wireless communication, radio multipath fading channel modeling, high-speed digital transmission, and microwave engineering.

Chung-Pin Huang received the M.S. and Ph.D. degrees in Graduate Institute of Computer and Communication Engineering, from the National Taipei University of Technology, Taipei, Taiwan, in 2011 and 2016 respectively. He joined the Cable Assembly Research Department, WIESON Technologies Company, Ltd., Taipei, as an SI Engineer, in 2001, where he was a Manager of the CAE Laboratory from 2004 to 2015 and where he is currently a Chief Technology Officer. His current research interests include signal integrity for high-speed connector, high-speed digital system design, and electromagnetic compatibility for high-speed components.

Parameter Identification of the Planar Integrated EMI Filter Based on the Improved Immune Algorithm

Jinjun Bai, Hong Zhao*, Yulei Liu, and Kaibin Guo

College of Marine Electrical Engineering
Dalian Maritime University, Dalian, 116026, China
baijinjun@dlmu.edu.cn, zhaohong@dlmu.edu.cn, lyl15056811702abc@163.com, guokaibin112233@163.com

Abstract ─ The planar integrated EMI filter has been widely used because of its small size and good high-frequency characteristics. During the production process, if the electrical parameters of the integrated LC structure can be accurately identified, it will help improve the high-frequency characteristics of the filter. However, this identification problem is a multi-peak problem, which can easily fall into a local optimal solution. Based on the Feature Selective Validation method, this paper proposes an improved Immune Algorithm. The proposed method keeps changing the fitness function in the iterative process to avoid the algorithm falling into the local optimal solution. Finally, comparing with the measured impedance characteristic curve, it is verified that the proposed method is more accurate than the common Immune Algorithm.

Index Terms ─ Feature selective validation, immune algorithm, parameter identification, planar integrated EMI filter.

I. INTRODUCTION

In 2003, Chen from Virginia University of Technology proposed the Planar Electromagnetic Integration technology and applied it to Electromagnetic Interference (EMI) filter design [1,2]. The Planar Integrated EMI filter uses thin film technology to connect cores with different permeability to the printed circuit board, and the integrated LC (means inductance and capacitance) structure is formed to realize the filtering function. Its advantages are small size, easy modularization, and high frequency performance.

In 2013, Huang from South China University of Technology proposed common mode windings overlapped and interleaved layout technology, in order to improve the high frequency performance of the planar integrated EMI filter [3]. In 2014, Wang from Nanjing University of Aeronautics and Astronautics devised ring EMI filter structure. Using axisymmetric electrostatic field model and harmonic magnetic field model, the theoretical analysis of its electromagnetic characteristics has been realized [4]. In recent years, integrated EMI filters have been widely used in engineering practice, especially the design of DC–DC Power Electronic Converter [5, 6].

Reference [4] points out that the integrated LC structure determines the main performance of the Planar Integrated EMI Filter. In the production process, if the integrated LC structure parameters are identified accurately, the integrated LC structure can be improved according to the target performance, then the development cycle can be shortened and the development cost can be reduced.

The parameter identification of the integrated LC structure is a typical multi-peak problem [3], and the identification result is easy to fall into the local optimal solution, so it is difficult to obtain real parameter results. Many modern intelligent optimization algorithms try to solve the multi-peak problem [7-9], the most successful of which is the Immune Algorithm evolved from the Genetic Algorithm [10,11]. However, when using these algorithms, the calculation method of the fitness function has not changed, so it cannot completely solve the problem of falling into the local optimal solution.

This paper proposes an improved Immune Algorithm based on the Feature Selective Validation (FSV) method, which can make the fitness function change continuously during the iteration process, in order to completely solve the problem of falling into the local optimal solution.

The paper is organized as follows: Section II introduces the problem of LC structural parameter identification of the planar integrated EMI filter briefly. Parameter identification based on common Immune Algorithm is presented in Section III. Section IV proposes parameter identification based on improved Immune Algorithm, and its verification is shown in Section V. The conclusions are given in Section VI.

II. PARAMETER IDENTIFICATION PROBLEM OF INTEGRATED LC STRUCTURE

The planar integrated EMI filter is composed of the EI type magnetic core, the integrated Differential Mode (DM) capacitor, the integrated LC module and the

Submitted On: July 27, 2020
Accepted On: November 30, 2020
https://doi.org/10.47037/2020.ACES.J.360103

leakage layer, as shown in Fig. 1. It is the integrated LC structure that plays a decisive role in its performance, as shown in Fig. 2. The integrated LC structure uses printed circuit board manufacturing technology to form winding conductors on both sides of the substrate with a higher dielectric constant, and distributed capacitance will be generated between the upper and lower conductors. At the same time, the magnetic core with higher magnetic permeability will cause inductance in the winding conductor. The dielectric constant of the dielectric layer and the geometric properties of the wire will affect the integrated capacitance parameter, and the magnetic core permeability and the number of coil turns will affect the integrated inductance parameter.

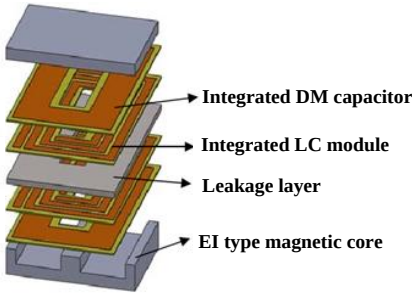

Fig. 1. Composition of the planar EMI filter.

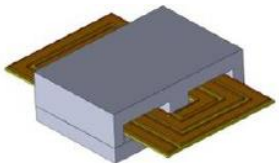

Fig. 2. Integrated LC module with magnetic core.

The lumped parameter model shown in Fig. 3 is used to describe the electrical properties of the integrated LC structure, and then the analysis of high-frequency filtering characteristics can be realized [4]. R represents the loss resistance of the connecting wire, and L is the inductance of the connecting wire. M represents the coupling inductance between the upper and lower conductors, C is the concentrated capacitance to approximate the distributed capacitance between the equivalent layers, and C_p is the parasitic capacitance between turns.

In order to identify the parameter values in the model, four impedance characteristic test experiments are designed under four working conditions. The schematic diagram is shown in Fig. 4.

Case 1: Between terminals B and C is in an open circuit, measure the impedance between terminals A and D:

$$Z_{AD}=\frac{1}{2}\left[R+\frac{(L+M)/C_p}{j\omega(L+M)+2/j\omega C_p}+\frac{2}{j\omega C}\right]. \quad (1)$$

Case 2: Between terminals C and D is in an open circuit, measure the impedance between terminals A and B:

$$Z_{AB}=\frac{2Z_2/j\omega C}{Z_2+2/j\omega C}, \quad (2)$$

$$Z_2=2\left[R+\frac{(L-M)/C_p}{j\omega(L-M)+1/j\omega C_p}+\frac{2}{j\omega C}\right]. \quad (3)$$

Case 3: Terminals C and D are short-circuited together, and the impedance between terminals A and B is measured:

$$Z_{AB}=\frac{2Z_3/j\omega C}{Z_3+2/j\omega C}, \quad (4)$$

$$Z_3=2\left[R+\frac{(L-M)/C_p}{j\omega(L-M)+1/j\omega C_p}\right]. \quad (5)$$

Case 4: Terminals B and C are short-circuited together, and the impedance between terminals A and D is measured:

$$Z_{AD}=\frac{4Z_4/j\omega C}{Z_4+2/j\omega C}, \quad (6)$$

$$Z_4=2\left[R+\frac{(L+M)/C_p}{j\omega(L+M)+1/j\omega C_p}\right]. \quad (7)$$

Using the impedance characteristic curve to determine the equivalent lumped parameter model is a parameter identification problem, and the parameters to be identified are the electrical parameters in the model in Fig. 3. Intelligent optimization algorithms can solve this problem. Taking genetic algorithm as an example, the chromosome is the parameters to be identified. The value range of the parameters can be estimated by the length of the PCB board wire, the distance between the boards and the dielectric constant of the medium. The fitness function is the difference between the model calculated impedance curve and the actual measured impedance curve.

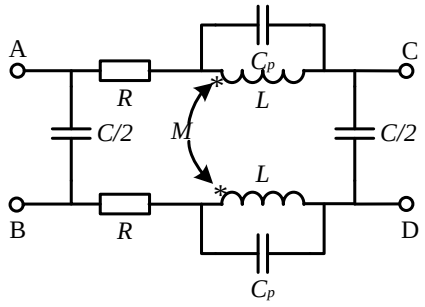

Fig. 3. Lumped parameter model of the integrated LC module [4].

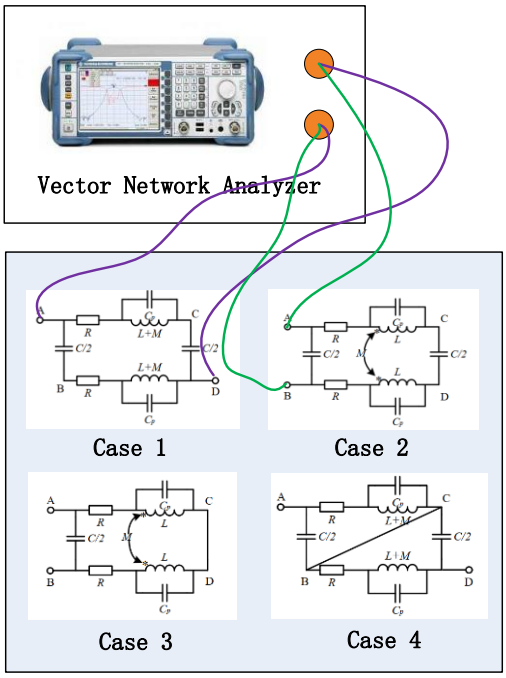

Fig. 4. Schematic diagram of impedance characteristic test experiment.

It is worth noting that different combinations of inductance and capacitance can resonate at the same frequency, so it is easy to fall into a local optimal solution. In other words, parameter identification of integrated LC structure is a multi-peak problem.

III. PARAMETER IDENTIFICATION BASED ON IMMUNE ALGORITHM

In the iterative process of traditional intelligent optimization algorithms, random and unguided searches are performed in the solution space. Although it provides opportunities for evolution, there is inevitably the possibility of degradation. The essential reason for the degradation is that the calculation rule of the fitness function does not change, which will seriously affect the diversity of the solution results. As a result, the identification result converges to the local optimal solution and cannot reach the true global optimal solution.

In the Immune Algorithm, the antibody concentration evaluation operator is introduced according to the concepts of antibodies and antigens in biology. This will avoid the rapid reduction of the diversity of solutions, so as to reduce the possibility of the algorithm falling into the local optimum [11]. The calculation formula of the antibody concentration evaluation operator is arranged as:

$$den(\mathrm{A}_i)=\frac{1}{N}\sum_{j=1}^{N}S(\mathrm{A}_i,\mathrm{A}_j), \tag{8}$$

where A_i represents an antibody consisting of a vector of parameters to be identified, $den(\mathrm{A}_i)$ is the antibody concentration evaluation operator of the antibody A_i. N is the total number of antibodies, and function $S(\mathrm{A}_i,\mathrm{A}_j)$ is represented as:

$$S(\mathrm{A}_i,\mathrm{A}_j)=\begin{cases}1, res(\mathrm{A}_i,\mathrm{A}_j)<\delta\\ 0, res(\mathrm{A}_i,\mathrm{A}_j)\geq\delta\end{cases}. \tag{9}$$

$res(\mathrm{A}_i,\mathrm{A}_j)$ indicates the similarity between two antibodies, usually described by Euclidean distance. δ is the similarity threshold.

Combining the original fitness function value (referred to as the antibody affinity operator in the Immune Algorithm), the incentive calculation operator is obtained according to the following formulas as the final fitness evaluation result of the antibody:

$$sim(\mathrm{A}_i)=a\times aff(\mathrm{A}_i)-b\times den(\mathrm{A}_i), \tag{10}$$

or

$$sim(\mathrm{A}_i)=aff(\mathrm{A}_i)\mathrm{e}^{-a\times den(\mathrm{A}_i)}. \tag{11}$$

Where $aff(\mathrm{A}_i)$ is the antibody affinity operator, a and b are constants determined based on actual calculation.

In this paper, the antibody affinity operator $aff(\mathrm{A}_i)$ is given by FSV method [12,13]. The FSV method is an automated validation method recommended by IEEE Standard 1597.1/2, in order to quantitatively evaluate the difference between Computational Electromagnetics (CEM) simulation results and the reference data. The reference data are the actual measurement results provided according to the Fig. 4.

The main idea of the FSV is shown in Fig. 5. Fourier transform decomposes simulation results and the reference data into three kinds of data with different frequency components. The Amplitude Difference Measure (ADM) is reconstructed from the difference of low frequency data, and the Feature Difference Measure (FDM) is reconstructed from the difference of high frequency data. The Global Difference Measure (GDM) is the final quantitative evaluation value, which combines the results of the ADM and the FDM. The smaller the difference, the smaller the value of GDM, which indicates that the CEM simulation results are better. In this case, the $aff(\mathrm{A}_i)$ is provided as:

$$aff(\mathrm{A}_i)=\sum_{k=1}^{3}FSV_{GDM}\left[Test_{Z_k},Cal_{Z_k}(\mathrm{A}_i)\right], \tag{12}$$

where $Cal_{Z_k}(\mathrm{A}_i)$ means the impedance calculation of the antibody A_i according to the equations from (1) to (5). $Test_{Z_k}$ is the measured result provided by the Impedance Analyzer, and FSV_{GDM} means the GDM value given by the FSV method.

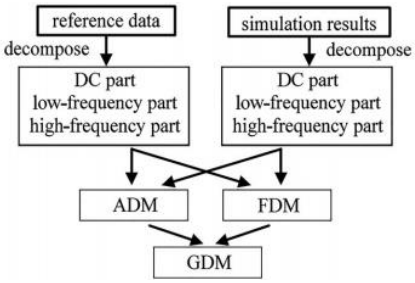

Fig. 5. Main idea of the FSV method [12].

There are four working conditions in Fig. 4. In this paper, the first three working conditions are used to perform the parameter identification as the training set. Then the Case 4 will be treated as the testing set in order to verify the accuracy of the identification results. Thus, the $aff(\mathrm{A}_i)$ result in equation (12) is the sum of the three GDM values.

Noteworthy, only the amplitude results of impedance are applied for the parameter identification in the equation (12), and the phase results are not used.

In the Immune Algorithm, the antibody concentration evaluation operator increases the possibility of antibody mutation, and improves the probability of the algorithm jumping out of the local optimal solution. However, the calculation rule of the antibody affinity operator has not changed, so it has not completely solved the problem of falling into the local optimal solution.

IV. PARAMETER IDENTIFICATION BASED ON IMPROVED IMMUNE ALGORITHM

This section proposes an improved Immune Algorithm, which makes the value of the antibody affinity operator continuously change with the increase of genetic algebra, in order to completely solve the problem of falling into a local optimal solution.

In the FSV method, the GDM is calculated by the ADM and the FDM. The formula is presented as:

$$GDM = \sqrt{\left(k_{ADM} \cdot ADM\right)^2 + \left(k_{FDM} \cdot FDM\right)^2}, \quad (13)$$

where k_{ADM} and k_{FDM} are the weights of ADM and FDM respectively, they are between 0 and 1. Reference [12] gives the weight assignment rules in the standard FSV method.

According to the above properties, the values of k_{ADM} and k_{FDM} can be changed in the iterative process, so that the calculation result of the antibody affinity operator $aff(\mathrm{A}_i)$ is constantly changing during the algorithm implementation process. In this paper, the following weight assignment rule is proposed as:

$$k_{ADM} = 0.2 + 0.8 \times (1 - \frac{gen}{M_{gen}}), \quad (14)$$

and

$$k_{FDM} = 0.2 + 0.8 \times \frac{gen}{M_{gen}}. \quad (15)$$

Where *gen* represents the ongoing genetic algebra, and M_{gen} is total genetic algebra.

Noteworthy, according to the principle of immune algorithm, the larger the gap between parameter 0.2 and 1, the more drastic the fitness function changes, and the easier it is to jump out of the local optimal solution. After testing, the minimum gap required to identify the problem in this article is 0.6, in other words, the parameters can be 0.4 and 1.0. Meanwhile, the algorithm needs to ensure a certain stability in the later stage of the iteration, so the weight parameters are set to 0.2 and 1.0.

In the early stage of the algorithm for parameter identification, ADM plays a decisive role in calculating the result of the antibody affinity operator, while FDM plays a major role in the later stage. This means that the difference in amplitude can be continuously adjusted in the early stage of identification, and the difference in details can be continuously adjusted in the later stage, which fully meets the expectations of evolutionary algorithms.

Most importantly, this method keeps the calculation rule of the antibody affinity operator changing during the iteration. In this way, the diversity of antibodies in the Immune Algorithm can be maintained to the greatest extent, and it is easier to jump out of the local optimal solution to achieve the global optimal solution.

V. ALGORITHM VALIDITY VERIFICATION

In order to verify the accuracy of the proposed method, the real object is produced for providing the standard data, shown as Fig. 6.

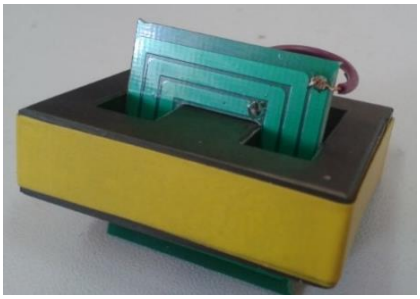

Fig. 6. Physical image of integrated LC module.

The shape of the magnetic core is EE type. The material of the dielectric layer is FR-4, and its thickness is 0.8mm. For the wire related parameters, the number of turns is 3 with the width 2mm. The spacing between the wires is 0.5mm, and the thickness of the wires is $35\mu m$.

A. Parameter identification results based on the experimental data of Case 1, Case 2 and Case 3

As shown in the lumped parameter model in Fig. 3, there are five parameters to be identified, namely C, C_p, L, M and R. Therefore, the dimension of the antibody in the Immune Algorithm is 5. The total number of antibodies is 200, and the maximum immune generation is 150.

The search range of some parameters to be evaluated can be estimated based on the actual LC structure, such as C is from 1×10^{-11}F to 10×10^{-11}F, C_p is from 1×10^{-13}F to 10×10^{-13}F, and L is from 1×10^{-8}H to 10×10^{-8}H. Other parameters can only be estimated based on engineering experience, such as M is from 0H to 10×10^{-9}H, and R is from 0Ω to 10×10^{-3}Ω.

The incentive calculation operator is finally selected as formula (10), in which both a and b are assigned 1. According to the first three working conditions, the parameter identification based on the improved Immune Algorithm is completed, in which the impedance characteristic frequency range is from 10MHz to 1GHz. The antibody affinity operator is the sum of three GDM values from the comparison of the difference between model calculation results and actual measurement results. In the improved Immune Algorithm, it is worth noting that the GDM values are calculated by formula (13) and formula (14).

The identification results of the improved Immune Algorithm are C=4.4×10^{-11}F, C_p=5.8×10^{-13}F, L=6.6×10^{-8}H, M=1.4×10^{-10}H and R=8.7×10^{-6}Ω. For comparison, the identification results of the common Immune Algorithm are C=4.0×10^{-11}F, C_p=5.2×10^{-13}F, L=7.2×10^{-8}H, M=5.3×10^{-10}H and R=3.2×10^{-6}Ω.

The comparison of the results under the three working conditions is given in Fig. 7, Fig. 8 and Fig. 9. The red line represents the actual impedance characteristic curve from the measurement, the black line represents the impedance characteristic curve formed by the Immune Algorithm identification results, and the blue line represents the impedance characteristic curve formed by the identification results of the improved Immune Algorithm.

Using the FSV method, the accuracy of the identification results of the Immune Algorithm and the improved Immune Algorithm can be compared, as shown in Table 1. It shows that the improved Immune Algorithm is more accurate. It also means that the identification result of Immune Algorithm is the local optimal solution, while the improved Immune Algorithm is the global optimal solution. Meanwhile, Table 2 shows the comparison of average relative errors, and it can also give the same conclusion obviously.

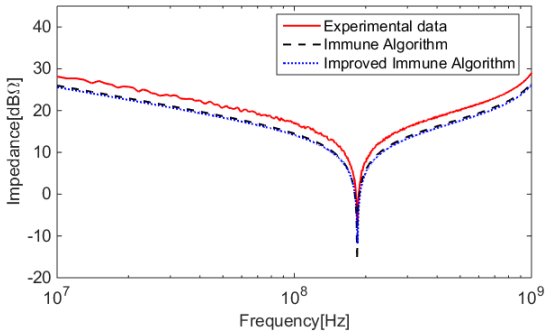

Fig. 7. Comparison of impedance simulation results in Case 1.

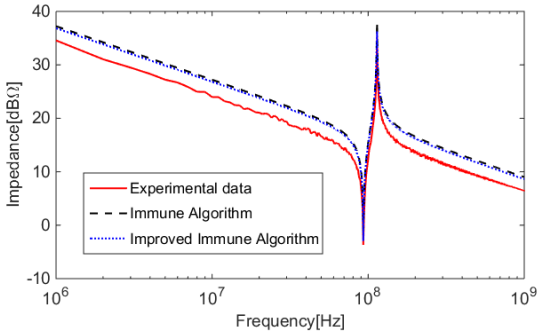

Fig. 8. Comparison of impedance simulation results in Case 2.

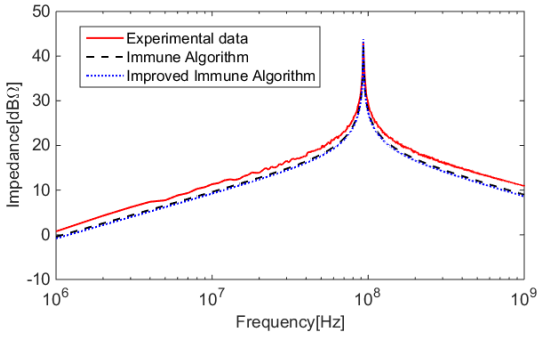

Fig. 9. Comparison of impedance simulation results in Case 3.

Table 1: FSV values for verifying algorithm accuracy

	Immune Algorithm	**Improved Immune Algorithm**
Case 1	0.24	0.23
Case 2	0.20	0.19
Case 3	0.22	0.22
Total	0.66	0.64

Table 2: The comparison of average relative errors

	Immune Algorithm	Improved Immune Algorithm
Case 1	12.27%	12.98%
Case 2	22.83%	19.94%
Case 3	13.36%	15.02%
Mean	16.15%	15.98%

Figure 10 shows the change of the fitness function of the improved Immune Algorithm in the iterative process. This property determines that the proposed method is easier to jump out of the local optimal solution than the common Immune Algorithm. Furthermore, the red line shows that the common Immune Algorithm has converged around the 90th generation, indicating that the selection of the number of chromosomes and genetic algebra is appropriate.

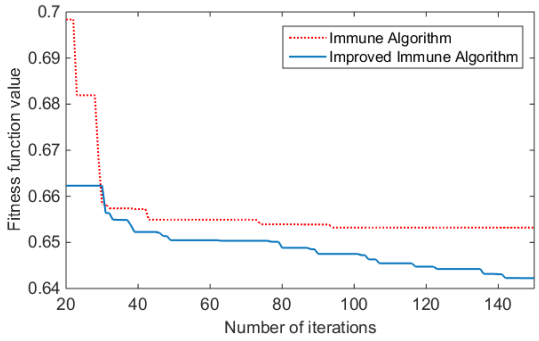

Fig. 10. Change of fitness function in iterative process.

B. Algorithm validity verification according to the experimental data of Case 4

The comparison of the results under the fourth working condition is given in Fig. 11. Meanwhile, Fig. 12 provides the local zoom results of Fig. 11. It is shown that the improved Immune Algorithm is more accurate than the Immune Algorithm.

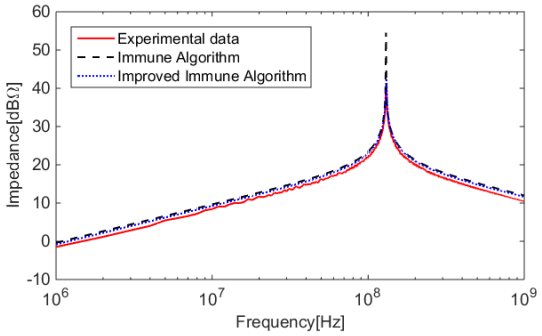

Fig. 11. Comparison of impedance simulation results in Case 4.

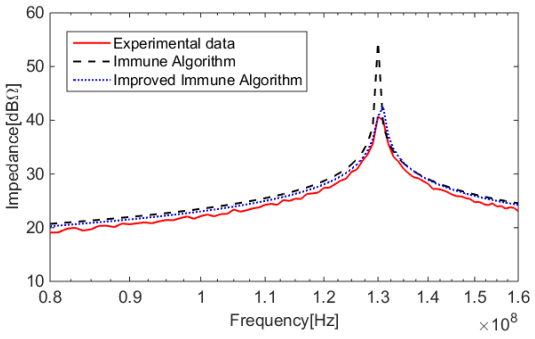

Fig. 12. Local zoom results of Fig. 11.

Using the FSV method, the GDM of the common Immune Algorithm is 0.22, and that of the improved Immune Algorithm is 0.18. Meanwhile, the average relative error of the common Immune Algorithm is 10.43%, and that of the improved Immune Algorithm is 7.06%. It means that the identification results provided by the improved Immune Algorithm are more accurate.

VI. CONCLUSION

Base on the FSV method, this paper proposes an improved Immune Algorithm, in order to solve multi-peak parameter identification problem. Take the parameter identification problem of the integrated LC structure in the Planar Integrated EMI Filter as an example, it is proved that the proposed method is more accurate, because it is easier to jump out of the local optimal solution than the common Immune Algorithm. This achievement not only helps to improve the high-frequency characteristics of the Planar Integrated EMI Filter, but also reduces its manufacturing cost.

ACKNOWLEDGMENT

This work was supported by the Fundamental Research Funds for the Central Universities under Grant 3132020105.

REFERENCES

[1] R. Chen R, J. D. Van Wyk, S. Wang, and W. G. Odendaal, “Planar electromagnetic integration technologies for integrated EMI filters,” *Industry Applications Conference*, pp. 1582-1588, 2003.

[2] R. Chen, J. D. Van Wyk, S. Wang, and W. G. Odendaal, “Improving the characteristics of integrated EMI filters by embedded conductive layers,” *IEEE Transactions on Power Electronics*, vol. 20, no. 3, pp. 611-619, 2005.

[3] H. Huang, L. Deng, B. Hu, and G. Wei, “Techniques for improving the high-frequency performance of the planar CM EMI filter,” *IEEE Transactions on Electromagnetic Compatibility*,

vol. 55, no. 5, pp. 901-908, 2013.

[4] S. Wang and C. Xu, "Extraction of magnetic parameters for elements of a planar EMI filter," *IEEE Transactions on Electromagnetic Compatibility*, vol. 56, no. 2, pp. 360-366, 2014.

[5] J. S. N. T. Magambo, R. Bakri, X. Margueron, P. L. Moigne, A. Mahe, S. Guguen, and T. Bensalah, "Planar magnetic components in more electric aircraft: Review of technology and key parameters for DC–DC power electronic converter," *IEEE Transactions on Transportation Electrification*, vol. 3, no. 4, pp. 831-842, 2017.

[6] J. L. Kotny, T. Duquesne, and N. Idir, "Modeling and design of the EMI filter for DC-DC SiC-converter," *2014 International Symposium on Power Electronics, Electrical Drives, Automation and Motion*, Ischia, pp. 1195-1200, 2014.

[7] S. Wang, M. Roger, J. Sarrazin, and C. Lelandais-Perrault, "Hyperparameter optimization of two-hidden-layer neural networks for power amplifiers behavioral modeling using genetic algorithms," *IEEE Microwave and Wireless Components Letters*, vol. 29, no. 12, pp. 802-805, 2019.

[8] M. Sato, Y. Fukuyama, T. Iizaka, and T. Matsui, "Total optimization of energy networks in a smart city by multi-swarm differential evolutionary particle swarm optimization," *IEEE Transactions on Sustainable Energy*, vol. 10, no. 4, pp. 2186-2200, 2019.

[9] D. Zhang, X. You, S. Liu, and K. Yang, "Multi-colony ant colony optimization based on generalized Jaccard similarity recommendation strategy," *IEEE Access*, vol. 7, pp. 157303-157317, 2019.

[10] Y. Wang, X. Geng, F. Zhang, and J. Ruan, "An immune genetic algorithm for multi-echelon inventory cost control of IOT based supply chains," *IEEE Access*, vol. 6, pp. 8547-8555, 2018.

[11] B. Mohammadi-Ivatloo, A. Rabiee, and A. Soroudi, "Nonconvex dynamic economic power dispatch problems solution using hybrid immune-genetic algorithm," *IEEE Systems Journal*, vol. 7, no. 4, pp. 777-785, 2013.

[12] A. P. Duffy, A. Orlandi, and G. Zhang, "Notice of retraction: Review of the feature selective validation method (FSV). Part I—Theory," *IEEE Transactions on Electromagnetic Compatibility*, vol. 60, no. 4, pp. 814-821, 2018.

[13] A. Orlandi, A. P. Duffy, and G. Zhang, "Notice of retraction: Review of the feature selective validation method (FSV). Part II - Performance analysis and research fronts," *IEEE Transactions on Electromagnetic Compatibility*, vol. 60, no. 4, pp. 1029-1035, 2018.

Discontinuous Galerkin Time Domain Method with Dispersive Modified Debye Model and its Application to the Analysis of Optical Frequency Selective Surfaces

Wending Mai, Benjamin Zerbe, and Douglas H. Werner

The Pennsylvania State University, University Park, PA 16802 USA
wdmai@psu.edu, baz5128@psu.edu, dhw@psu.edu

Abstract ─ We develop a discontinuous Galerkin time domain (DGTD) algorithm with an experimentally validated modified Debye model (MDM) to take metal dispersion into consideration. The MDM equation is coupled with Maxwell's equations and solved together through the auxiliary differential equation (ADE) method. A Runge-Kutta time-stepping scheme is proposed to update the semi-discrete transformed Maxwell's equations and ADEs with high order accuracy. Then we employ the proposed algorithm to analyze an infinite doubly periodic frequency selective surface (FSS) operating in the optical regime that exhibits transmission enhancement due to the surface plasmatic effect. The accuracy and the efficiency enhancements are validated through a comparison with commercial simulation software. This work represents the first integration of MDM with DGTD, which enables the DGTD algorithm to efficiently analyze metallic structures in the optical regime.

Index Terms ─ Auxiliary Differential Equation (ADE) method, Discontinuous Galerkin Time Domain (DGTD), Frequency Selective Surface (FSS), Modified Debye Model (MDM), prism elements.

I. INTRODUCTION

The necessity of handling dispersive media is important to several applications. For example, applications in optical electromagnetic wave therapy, imaging, and bio-electromagnetic hazards require the simulation of waves in biological tissues that are inherently dispersive. Similarly, undersea and underground penetrating radar applications assume geological media that are also inherently dispersive. Optical or terahertz frequency selective surfaces (FSS) [1]–[3], electromagnetic band gap (EBG) structures [4], and engineered materials (*e.g.*, metamaterials) [5]–[9] are also inherently dispersive. These structures, which are comprised of a repeating metallic pattern, have a wide range of applications in electromagnetic and optical engineering. Several closed form mathematical models have been proposed to represent material dispersion properties. For example, researchers have used the Debye model to simulate the relaxation property, the Lorentz model to represent the resonance process, and the Drude model to take into consideration cold-plasma features. Moreover, the auxiliary differential equation method (ADE) was proposed to circumvent the time-consuming convolution operation. It was originally introduced in conjunction with the finite difference time domain (FDTD) technique [10], [11], and then also implemented in FETD [12] and DGTD [13] methods. The DGTD technique has become the subject of much attention due to its high degree of accuracy, which stems from flexible meshing and high order basis functions. Moreover, it is efficient because of its suitability for element-wise parallelization. More recently, a combination of different models, namely the generalized dispersion model (GDM), was incorporated into DGTD to facilitate full wave simulation of dispersive materials [14]-[22].

The conventional Debye model is widely used to model dispersive dielectric materials in the microwave regime. However, it cannot accurately represent metals that are dispersive in the optical regime. By adding an extra conductivity term, the modified Debye model (MDM) has been used in the FDTD method to model dispersive metals in the optical regime [10], [11]. With the additional conductive term, the degree of freedom of MDM is the same as the Drude model. Therefore, research shows that these two models can be viewed as mathematically equivalent. The MDM model is capable of representing Drude-like metals in the optical regime, while keeping the simplicity of the Debye model. Therefore, it can be easily adapted by researchers familiar with microwave Debye materials to explore the dispersive properties in the optical regime. Many studies have been performed to determine the optimal parameter settings for MDM that accurately fit experimental data over a broad frequency band [23]–[25]. However, there has apparently been no prior work done to incorporate MDM with DGTD to facilitate the efficient modeling of

Submitted On: August 4, 2020
Accepted On: December 10, 2020
https://doi.org/10.47037/2020.ACES.J.360104

dispersive metals.

This paper presents the first integration of the MDM and DGTD methods. It enables a prism-based DGTD algorithm to efficiently analyze dispersive planar metallic structures in the optical regime. A frequency selective surface (FSS) composed of a gold film with a periodic array of air holes was analyzed to validate the accuracy and efficiency of the proposed algorithm. In Section II, the prism-based DGTD method with the MDM is presented. A numerical example is shown in Section III to validate the accuracy and efficiency improvement of the proposed method.

II. FORMULATION

In order to take into account the material dispersion of metal in the optical spectrum, researchers have collected experimental data. In order to fit the measured data, and to conduct associated time-domain simulations, various methods have been proposed. Krug *et al.* have attempted to extract gold parameters in the near-infrared range. But their results deviate significantly from accepted experimental values [23]. Jin *et al.* have recently determined gold parameters applicable in the wavelength range 550–950 nm [24]. More recently, Gai et al proposed a series of modified Debye model parameters for metals that are applicable for broadband calculations [25]. The conventional Debye model was modified by adding an extra conductivity term to better represent metal's dispersive performance at optical frequencies:

$$\varepsilon_{\mathrm{r}} = \varepsilon_{\infty} + \frac{\varepsilon_s - \varepsilon_{\infty}}{1+i\omega\tau} + \frac{\sigma}{i\omega\varepsilon_0}, \tag{1}$$

where ε_{r} is the complex relative permittivity, ε_s and ε_{∞} are the zero-frequency (static) and infinite-frequency relative permittivity values, respectively. ω is the angular frequency, while the component $i\omega$ in the frequency domain represents the engineering convention corresponding to time-varying fields as $e^{i\omega t}$. Here ε_0 is the permittivity of free space, τ is the relaxation time, and σ is the introduced conductivity. We should also note that Eq. (1) represents a purely mathematical model and, therefore, is not based on any physical description of separating bound charges and free charges or the associate currents [26].

Figure 1 demonstrates the material dispersion of gold as determined from experimental measurements and from the modified Debye fitting model. The parameters of the model are set as: $\varepsilon_s = -15789$, $\varepsilon_{\infty} = 11.575$, $\sigma = 1.6062 \times 10^7\ S/m$, and $\tau = 8.71 \times 10^{-15} s$ [25]. As shown in Fig. 1, both the real and the imaginary parts of the modified Debye model permittivity agree well with those obtained from the measurements [27]. Hence, it can be concluded that the modified Debye model with the indicated parameters is accurate over a broad frequency band: 250 THz to 428 THz. The bandwidth of the model spectrum is limited physically by the existence of inter-band transitions, which are not accounted for in the MDM.

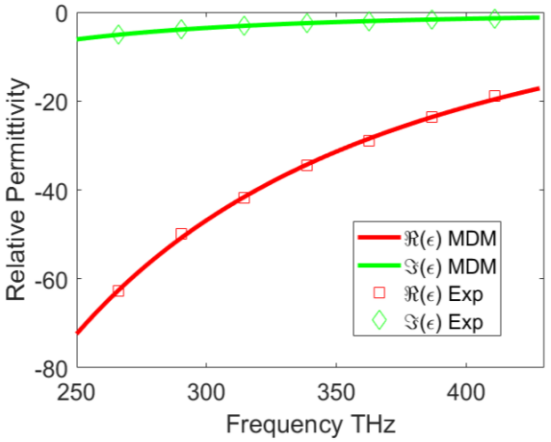

Fig. 1. Comparison between the relative permittivity of gold from the modified Debye model (MDM) and from experimentally determined results (Exp) [27].

Previously, the modified Debye model has been incorporated into the FDTD method [10]–[11], [25]. In this work, and for the first time, we integrated the modified Debye model with DGTD for accurate and efficient computation of dispersive material systems.

By considering the displacement current $\overrightarrow{J_D} = i\omega\vec{D}$, the conductivity in (1) can be incorporated into Ampere's equation with the MDM term:

$$\nabla \times \vec{\boldsymbol{H}} = \sigma\vec{\boldsymbol{E}} + i\omega\varepsilon_0\varepsilon_{\infty}\vec{E} + \overrightarrow{\boldsymbol{J_p}}, \tag{2}$$

where $\vec{\boldsymbol{E}}$ and $\vec{\boldsymbol{H}}$ represent the frequency domain (bold) electric and magnetic field vectors, respectively, while the introduced polarization current vector $\overrightarrow{\boldsymbol{J_p}}$ is defined as:

$$\overrightarrow{\boldsymbol{J_p}} = i\omega\varepsilon_0\left(\frac{\varepsilon_s - \varepsilon_{\infty}}{1+i\omega\tau}\right)\vec{E}. \tag{3}$$

Through application of an inverse Fourier transformation, (3) can be recast in the form of an auxiliary differential equation (ADE):

$$\frac{d\overrightarrow{J_p}}{dt} = \frac{\varepsilon_0(\varepsilon_s - \varepsilon_{\infty})}{\tau}\frac{d\vec{E}}{dt} - \frac{\overrightarrow{J_p}}{\tau} \tag{4}$$

Here, the ADE in (4) only contains a first-order time derivative term. Solving this is more efficient than for models with higher order time derivative terms.

Accordingly, the dispersive form of Maxwell's curl equations can be transformed into the time domain as:

$$\mu_r\mu_0\frac{d\vec{H}}{dt} = -\nabla \times \vec{E}, \tag{5}$$

$$\sigma\vec{E} + \varepsilon_r\varepsilon_0\frac{d\vec{E}}{dt} + \overrightarrow{J_p} = \nabla \times \vec{H}, \tag{6}$$

where $\vec{E}$, $\vec{H}$, and $\overrightarrow{J_p}$ are the electric, magnetic and polarization vectors in the time domain (unbold).

Suppose that the computational domain is split into N non-overlapping prismatic elements Ω_m, where the electric and magnetic fields, as well as the electric

polarization vector are expanded by the basis functions $\vec{\Phi}_k^i(r)$:

$$\overrightarrow{E^m}(r,t) = \sum_{l=1}^{N_e^m} e_l^m(t)\vec{\Phi}_l^m(r), \quad (7)$$

$$\overrightarrow{H^m}(r,t) = \sum_{l=1}^{N_h^m} h_l^m(t)\vec{\Phi}_l^m(r), \quad (8)$$

$$\overrightarrow{J_p^m}(r,t) = \sum_{l=1}^{N_j^i} j_l^m(t)\vec{\Phi}_l^m(r), \quad (9)$$

where N_e^m, N_h^m, and N_j^m represent the number of basis functions for $\vec{E}$, $\vec{H}$ and $\overrightarrow{J_p}$ in element *m*, respectively.

The integration of the DGTD method and the MDM outlined in the previous section is independent of the element type. But for planar structures such as FSS and metasurfaces, it is more optimal to discretize them into triangular prisms instead of conventional tetrahedrons. The prismatic discretization of space will not only reduce the element number, but also improve the mesh quality, which is often problematic for a tetrahedral-based mesh when dealing with very thin layer structures.

To model the curl operator in Maxwell's equations, we introduce a numerical upwind flux that is based on the Rankine Hugoniot jump relations. Then, by performing Galerkin testing over Maxwell equations, and taking into account the numerical flux and MDM term, we obtain the following DGTD semi-discretized matrix equations:

$$\frac{de^m}{dt} = \frac{1}{\varepsilon_0\varepsilon_\infty}\{\bar{M}_e^{m^{-1}} \cdot \Big[\bar{S}_e^m h^m + \sum_{f=1}^{N_m^f}\big(\bar{F}_{ee}^{mm,f} e_f^m + \bar{F}_{ee}^{mn,f} e_f^n + \bar{F}_{eh}^{mm,f} h_f^m + \bar{F}_{eh}^{mn,f} h_f^n\big) + \beta \cdot \bar{F}_e^{m,M_s}\Big] - \sigma e^m - \varepsilon_0 j^m\}, \quad (10)$$

$$\frac{dh^m}{dt} = \bar{M}_h^{m^{-1}}/\mu_0\mu_r \cdot \Big[-\bar{S}_h^m e^m + \sum_{f=1}^{N_m^f}\big(\bar{F}_{hh}^{mm,f} h_f^m + \bar{F}_{hh}^{mn,f} h_f^n + \bar{F}_{he}^{mm,f} e_f^m + \bar{F}_{he}^{mn,f} e_f^n\big) + \beta \cdot \bar{F}_h^{m,M_s}\Big], \quad (11)$$

$$\frac{dp^m}{dt} = \frac{(\varepsilon_s - \varepsilon_\infty)}{\tau}\frac{de^m}{dt} - \frac{j^m}{\tau}, \quad (12)$$

where $\bar{M}, \bar{S}$, and $\bar{F}$ denote the mass matrix, the stiffness matrix and the flux matrix, respectively, whose detailed definitions can be found in [22]. The quantities e^m and h^m are the electronic and magnetic column vectors containing the unknown coefficients in element *m*. The coefficients with a subscript *f* correspond to those on face *f* between element *m* and *n*. If the face *f* is on the excitation port, $\beta = 1$; or else, $\beta = 0$. Note here that the σ and $\overrightarrow{J_p}$ terms introduced in (4) are incorporated into (12).

Next, the fourth-order four-stage explicit Runge-Kutta method (ERK) is adopted by setting the operator $\mathcal{L}_i(u_n^i, t_n)$ equal to the right-hand side of (10), (11), and (12):

$$\begin{cases} k^{(1)} = \mathcal{L}_i(u_n^m, t_n) \\ k^{(2)} = \mathcal{L}_i\left(u_n^m + \frac{1}{2}\delta t \cdot k^{(1)}, t_n + \frac{1}{2}\delta t\right) \\ k^{(3)} = \mathcal{L}_i\left(u_n^m + \frac{1}{2}\delta t \cdot k^{(2)}, t_n + \frac{1}{2}\delta t\right) \\ k^{(4)} = \mathcal{L}_i\left(u_n^m + \delta t \cdot k^{(3)}, t_n + \delta t\right) \\ u_{t_{n+1}}^m = u_{t_n}^m + \frac{1}{6}\delta t \cdot \left(k^{(1)} + 2k^{(2)} + 2k^{(3)} + k^{(4)}\right) \end{cases}, \quad (13)$$

where $k^{(1-4)}$ are the partial terms associated with the ERK method, while $u_{t_n}^m$ represents the unknowns $e_{t_n}^m$, $h_{t_n}^m$, or $j_{t_n}^m$when solving for the electric field, magnetic field, or the polarization current vector at time step t_n, respectively. Also, δt is the maximum time-step size for the DGTD mesh, which is determined by the Courant-Freidrichs-Lewy (CFL) condition [16]. The physical time is equal to $t_n\delta t$.

It should be noted that (12) contains the term $\frac{de^m}{dt}$, which can be substituted with the right-hand side of (10). Therefore, it is efficient to arrange the iteration order to avoid redundant computation in the following way:

Step 1: Calculate $k_e^{(1)}$ and $k_h^{(1)}$ using (10) and (11).

Step 2: Calculate $k_j^{(1)}$ from (12) by setting $\frac{de^m}{dt} = k_e^{(1)}$ in Step 1.

Similarly, always calculate $k_e^{(m)}$ before $k_j^{(m)}$, and then calculate $k_j^{(m)}$ by setting $\frac{d\vec{E}}{dt} = k_e^{(m)}$, where m=1, 2, 3, 4.

III. NUMERICAL EXAMPLES

A. Reflection and transmission of a thin gold film

To validate the accuracy and convergence of the proposed DGTD + MDM method, we first studied a simple example in which a planewave propagates through a thin gold film upon normal incidence. The analytical results of the transmission and reflection can be derived from closed-formed Fresnel equations.

The gold film has a thickness of 5 nm. It is illuminated by a sinusoidally modulated Gaussian pulse. The transient response of the reflection and transmission coefficients is shown in Fig. 2 (a) with a mesh configuration consisting of prismatic elements. Through Fourier transformation, both the reflection and transmission coefficients can be recovered as shown in Fig. 2 (b). The results of the proposed DGTD + GDM algorithm match very well with the analytical data. As can be seen, a thin gold film becomes more transparent as the frequency increases, within the targeted spectral range.

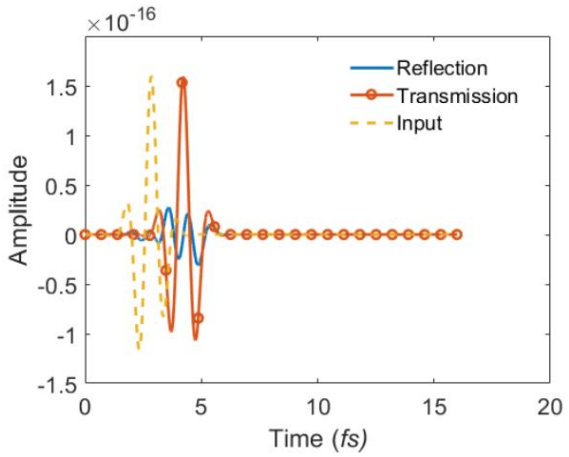

(a)

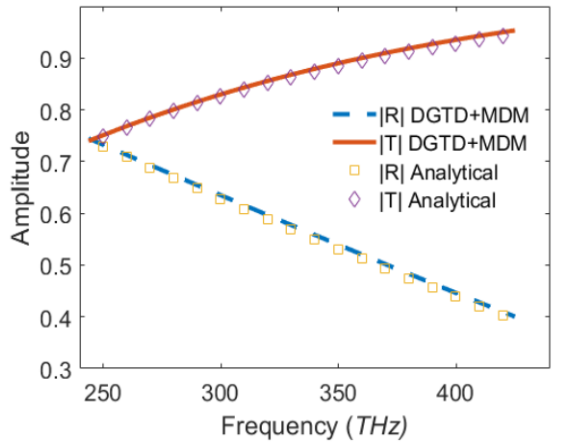

(b)

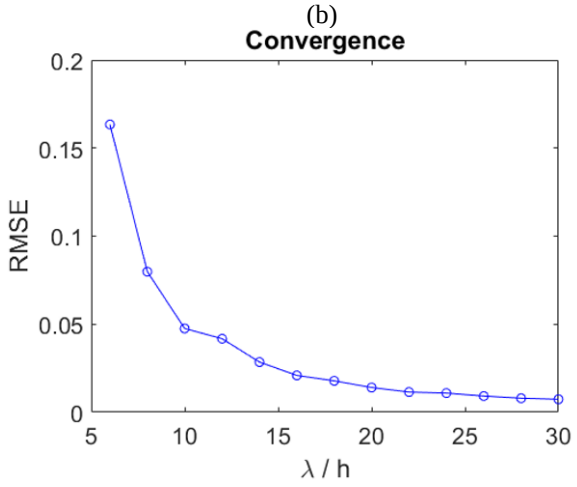

(c)

Fig. 2. Simulated results of the plane wave passing through a thin gold film. (a) The amplitude of the transient S-parameters. (b) Comparison of the frequency domain S-parameters from the prism-based DGTD with the modified Debye model and from the Fresnel equations. (c) Convergence plot showing accuracy improvement along with the refined mesh size.

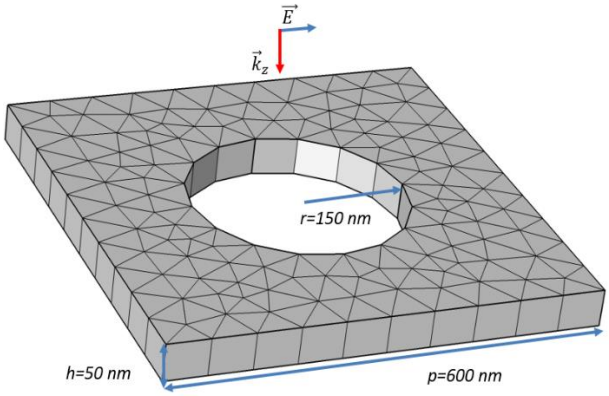

Fig. 3. Geometry of the unit cell of a gold nano-hole array frequency selective surface and its prismatic spatial discretization.

In order to investigate the accuracy of the proposed DGTD + GDM method, the relative errors of the numerical and analytical results are depicted as a function of the mesh size. Fig. 2 (c) shows the convergence plot which provides a means for quantifying the degree of accuracy improvement against refinements in the mesh. The algorithm was tested for different mesh sizes, where a measure of the accuracy was determined from the root mean square error (RMSE), which here is defined as:

$$RMSE = \sqrt{\frac{\sum_1^{N_f} (R/T^{DGTD+GDM} - R/T^{Analytical})^2}{N_f}}, \quad (14)$$

such that the performance was compared at N_f sampling frequencies. The convergence test was done with center frequency of 360 *THz*.

B. Illumination on a thin gold hole array

At this point we apply the prism-based DGTD method with the MDM to compute the S-parameters of a representative FSS structure for validation. Fig. 3 illustrates a single unit cell of the doubly periodic infinite FSS. The unit cell of the FSS under consideration contains a thin layer of a nano-hole array, where the gold film has a thickness of 50 nm. The 150 nm radius holes are spaced with a 600 nm lattice period [15]. Prismatic mesh cells represent the optimal discretization for such thin planar structures. The excitation of the normally incident field is modeled by a magnetic current with an amplitude corresponding to a sinusoidally modulated Gaussian pulse in order to generate a wideband response.

Figure 3 also depicts the prismatic spatial discretization utilized by the proposed algorithm. The minimum element length is about 34 nm, while the time step δt is set to 9.5 atto seconds. As can be seen, compared with a conventional tetrahedral mesh, the prismatic mesh represents the optimal choice for

discretizing such planar structures.

S-parameters are a typically used metric to demonstrate the frequency dependent performance of an FSS. To extract the S-parameters, we expand the electric coefficient corresponding to the mode distribution at the input and output wave port j. The transient results generated by the prism-based DGTD with the modified Debye model are shown in Fig. 4 (a). A total of 6,000 time steps were computed, corresponding to nearly 58 femto-seconds. In order to demonstrate the frequency selective property, the transient S-parameters shown in Fig. 4 (a) are Fourier transformed to the frequency domain and plotted in Fig. 4 (b). For comparison, Fig. 4 (b) also contains the simulated result obtained from the commercial CST software package [28]. Since most commercial software packages, including CST, are not able to simulate MDM materials, the comparison was made with simulation results from CST's frequency domain solver (FEM) using imported experimental dispersion data [27]. Figure 4 (b) shows that the result of the proposed algorithm yields good agreement with CST. Some minor disagreement exists because of the difference between the frequency- and time-domain methods, as well as the discrepancy between the experimental material dispersion and the modified Debye fitting model. Moreover, the prism-based DGTD with the MDM algorithm requires only 45 seconds to perform the computations, while the CST software with default settings consumes 93 seconds, as shown in Table 1. This computational efficiency enhancement comes from the optimal spatial discretization enabled by prismatic elements, the first-order derivative modified Debye model, and the ease by which parallel computing can be utilized within the DGTD framework.

The gold nano-hole array demonstrates band-pass performance, with a remarkable transmission enhancement observed at 390 THz. As presented in [29], this type of extraordinary transmission behavior can be primarily attributed to the excitation of a surface plasmon at the metallic hole array structure interface. Concisely, the incident light couples into electromagnetic surface waves (i.e., surface plasmon polaritons (SPPs) at the metal-dielectric interface), which then radiate through reciprocal interactions with the structure. This, in turn, produces unique features in the transmission and reflection spectra. The numerical simulations were performed on a laptop with a 2.6 GHz Intel i6700HQ CPU, 4 cores, 8 threads, and 16 GB of memory. The algorithm has been fully parallelized with all 8 threads using OpenMP.

Table 1: Comparison of the number of elements, number of unknowns, CPU time, and memory consumption for different methods

Method	Tetra CST FEM + Exp	Prism DGTD + MDM
Number of Elements*	12,105	7,168
Number of Unknowns	79,344	193,536
CPU Times (s)	93	45
Memory (MB)	923	1,978

* For better comparison, the tetrahedral and prism meshes in this table have the same upper bound of mesh size (element length).

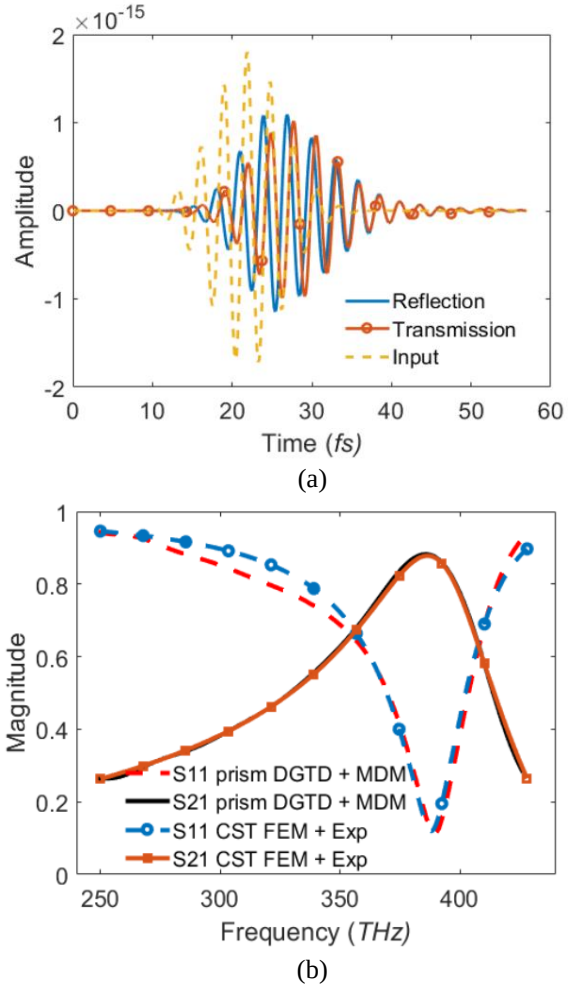

Fig. 4. Simulated results of the gold nano-hole array frequency selective surface. (a) The amplitude of the transient S-parameters. (b) Comparison of the frequency domain S-parameters from the prism-based DGTD with the modified Debye model (MDM) and from the *CST* FEM solver with imported experimental dispersive permittivity (Exp) [27].

IV. CONCLUSION

A prism-based DGTD algorithm together with a modified Debye model was proposed for simulating electromagnetic fields of planar metal structures (*e.g.*, FSS and metasurfaces) that are dispersive in the optical spectrum. The ADE method and a high-order Runge-Kutta scheme were introduced as effective methodologies for integrating the modified Debye model into DGTD. The proposed algorithm was then used to simulate an FSS consisting of a gold film with a patterned nano-hole array, which was shown to exhibit enhanced transmission at a specific frequency in the optical regime due to the surface plasmatic effect. The extracted S-parameters agree well with the results produced by commercial software packages. Moreover, the DGTG formulation was found to be more efficient than the commercial solvers due to the prismatic elements, the first-order derivative modified Debye model, and the ability to readily exploit parallel computing architectures.

ACKNOWLEDGMENT

This work was supported in part by the Penn State MRSEC, Center for Nanoscale Science (NSF DMR-1420620), DARPA/DSO Extreme Optics and Imaging (EXTREME) Program (HR00111720032), National Science Foundation of China (61901132).

REFERENCES

[1] B. A. Munk, *Frequency Selective Surfaces: Theory and Design*. John Wiley & Sons, 2005.

[2] S. Mahashabde, A. S. Sobolev, M. A. Tarasov, G. E. Tsydynzhapov, and L. S. Kuzmin, "Planar frequency selective bolometric array at 350 GHz," *IEEE Transactions on Terahertz Science and Technology*, vol. 5, no. 1, pp. 37-43, Jan. 2015.

[3] T. Hong, W. Xing, Q. Zhao, Y. Gu, and S. Gong, "Single-layer frequency selective surface with angular stability property," *IEEE Antennas and Wireless Propagation Letters*, vol. 17, no. 4, pp. 547-550, Apr. 2018.

[4] F. Yang and Y. Rahmat-Samii, *Electromagnetic Band Gap Structures in Antenna Engineering*. Cambridge University Press, Cambridge, UK, 2009.

[5] B. A. Munk, *Metamaterials: Critique and Alternatives*. John Wiley & Sons, 2009.

[6] F. Capolino, *Theory and Phenomena of Metamaterials*. CRC Press, 2009.

[7] M. L. N. Chen, L. J. Jiang, and W. E. I. Sha, "Artificial perfect electric conductor-perfect magnetic conductor anisotropic metasurface for generating orbital angular momentum of microwave with nearly perfect conversion efficiency," *Journal of Applied Physics*, vol. 119, no. 6, p. 064506, Feb. 2016.

[8] X. Zheng, W. Smith, J. Jackson, B. Moran, H. Cui, D. Chen, J. Ye, N. Fang, N. Rodriguez, T. Weisgraber, and C. M. Spadaccini, "Multiscale metallic metamaterials," *Nat. Mater.*, vol. 15, no. 10, pp. 1100-1106, Oct. 2016.

[9] W. Mai, D. Zhu, Z. Gong, X. Lin, Y. Chen, J. Hu, and D. H. Werner, "Broadband transparent chiral mirrors: Design methodology and bandwidth analysis," *AIP Advances*, vol. 9, no. 4, p. 045305, Apr. 2019.

[10] K. S. Kunz, *The Finite Difference Time Domain Method for Electromagnetics*. CRC Press, 1993.

[11] A. Taflove, A. Oskooi, and S. G. Johnson, Eds., *Advances in FDTD Computational Electrodynamics: Photonics and Nanotechnology*. Boston: Artech House, 2013.

[12] J.-M. Jin, *The Finite Element Method in Electromagnetics*. Third edition, Hoboken, New Jersey: John Wiley & Sons Inc., 2014.

[13] S. D. Gedney, J. C. Young, T. C. Kramer, and J. A. Roden, "A discontinuous Galerkin finite element time-domain method modeling of dispersive media," *IEEE Transactions on Antennas and Propagation*, vol. 60, no. 4, pp. 1969-1977, Apr. 2012.

[14] Q. Ren, H. Bao, S. D. Campbell, L. J. Prokopeva, A. V. Kildishev, and D. H. Werner, "Continuous-discontinuous Galerkin time domain (CDGTD) method with generalized dispersive material (GDM) model for computational photonics," *Opt. Express*, vol. 26, no. 22, p. 29005, Oct. 2018.

[15] H. Bao, L. Kang, S. D. Campbell, and D. H. Werner, "Discontinuous Galerkin time domain analysis of electromagnetic scattering from dispersive periodic nanostructures at oblique incidence," *Opt. Express*, vol. 27, no. 9, p. 13116, Apr. 2019.

[16] W. Mai, J. Hu, P. Li, and H. Zhao, "An efficient and stable 2-D/3-D hybrid discontinuous Galerkin time-domain analysis with adaptive criterion for arbitrarily shaped antipads in dispersive parallel-plate pair," *IEEE Transactions on Microwave Theory and Techniques*, vol. 65, no. 10, pp. 3671-3681, Oct. 2017.

[17] W. Mai, P. Li, C. G. Li, M. Jiang, W. Hao, L. Jiang, and J. Hu, "A straightforward updating criterion for 2-D/3-D hybrid discontinuous Galerkin time-domain method controlling comparative error," *IEEE Transactions on Microwave Theory and Techniques*, vol. 66, no. 4, pp. 1713-1722, Apr. 2018.

[18] W. Mai, P. Li, H. Bao, X. Li, L. Jiang, J. Hu, and D. H. Werner, "Prism-based DGTD with a simplified periodic boundary condition to analyze FSS with D2n symmetry in a rectangular array under normal incidence," *IEEE Antennas and Wireless Propagation Letters*, vol. 18, no. 4, pp. 771-775, Apr. 2019.

[19] Q. Hong and J Kraus, "Uniformly stable discontinuous Galerkin discretization and robust iterative solution methods for the Brinkman problem," *SIAM J. Numer. Anal*., vol. 54, no. 5, pp. 2750-2274, Sep. 2006.
[20] S. P. Gao, Y. L. Lu, and Q. S. Cao, "Hybrid method combining DGTD and TDIE for wire antenna-dielectric interaction," *Applied Computational Electromagnetics Society Journal*, vol. 30, no. 6, 2015.
[21] L. Zhao, G. Chen, and W. Yu, "An efficient algorithm for SAR evaluation from anatomically realistic human head model using DGTD with hybrid meshes", *Applied Computational Electromagnetics Society Journal*, vol. 31, no. 6, 2016.
[22] W. Mai, S. D. Campbell, E. B. Whiting, L. Kang, P. L. Werner, Y. Chen, and D. H. Werner, "Prismatic discontinuous Galerkin time domain method with an integrated generalized dispersion model for efficient optical metasurface analysis," *Opt. Mater. Express*, vol. 10, pp. 2542-2559, 2020.
[23] J. T. Krug, E. J. Sánchez, and X. S. Xie, "Design of near-field optical probes with optimal field enhancement by finite difference time domain electromagnetic simulation," *J. Chem. Phys.*, vol. 116, no. 24, pp. 10895-10901, June 2002.
[24] E. X. Jin and X. Xu, "Plasmonic effects in near-field optical transmission enhancement through a single bowtie-shaped aperture," *Appl. Phys. B*, vol. 84, no. 1, pp. 3-9, July 2006.
[25] H. Gai, J. Wang, and Q. Tian, "Modified Debye model parameters of metals applicable for broad-band calculations," *Appl. Opt.*, vol. 46, no. 12, p. 2229, Apr. 2007.
[26] S. A. Maier, *Plasmonics: Fundamentals and Applications*. New York: Springer, 2007.
[27] E. D. Palik, *Handbook of Optical Constants of Solids*. Academic, p. 294, 1985.
[28] CST Microwave Studio, ver. 2008, Computer Simulation Technology, Framingham, MA, 2008.
[29] J. W. Yoon and R. Magnusson, "Fano resonance formula for lossy two-port systems," *Opt. Express*, vol. 21, no. 15, pp. 17751-17759, July 2013.

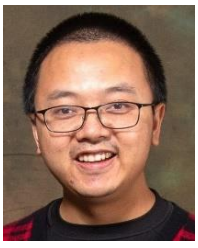

Wending Mai received the B.S. degree in Electronic Information Science and Technology, M.S. degree in Radio Physics, and Ph.D. degree in Electromagnetic and Microwave Technology from the University of Electronic Science and Technology of China, Chengdu, China, in 2007, 2010, and 2019 respectively.

In 2007, he was a Student Researcher in the Lenovo Research Institute, Chengdu. From 2010 to 2012, he was a Marketing Engineer in Texas Instruments Incorporated, Dallas, TX, USA. From 2013 to 2015, he was an Assistant Professor in Xichang College. From 2017 and 2019, he has been a Visiting Scholar and a Postdoc in the Computational Electromagnetics and Antennas Research Laboratory, The Pennsylvania State University, University Park, PA, USA. His current research interests include knot electromagnetics, computational electromagnetics, metamaterials and microwave imaging.

Mai is a Senior Member of the Institute of Electrical and Electronics Engineers (IEEE), a Member of the Applied Computational Electromagnetics Society (ACES), and a Member of the Institute of Physics (IOP). He is the recipient of the Excellent Student Paper Award presented by the IEEE Chengdu Section in 2017, and the Best Paper Award (ranked first) from the Chinese Journal of Radio Science in 2018.

Benjamin Zerbe graduated from Grove City College in 2017 with a bachelor's degree in Applied Physics and Computer Engineering and a minor in Computer Science. While there, he engaged in nano-fabrication and Casimir-Polder effect research under Dr. Jeffrey Wolinski. After graduation, he joined E x H, Inc. and worked on the GEMSIF electromagnetics design suite and its various solvers and optimization algorithms. He joined CEARL in 2020 and is currently working towards his Ph.D. in Electrical Engineering under the guidance of Prof. Douglas H. Werner.

His research interests include computational electromagnetics, computational physics, machine learning, metamaterials, optimization algorithms, and antenna design.

Douglas H. Werner received the B.S., M.S., and Ph.D. degrees in Electrical Engineering and the M.A. degree in Mathematics from The Pennsylvania State University (Penn State), University Park, PA, USA, in 1983, 1985, 1989, and 1986, respectively. He holds the John L. and Genevieve H. McCain Chair Professorship in the Department of Electrical Engineering, Penn State. He is the Director of the Computational Electromagnetics and Antennas Research Laboratory (CEARL: http://cearl.ee.psu.edu/) and a faculty member of the Materials Research Institute (MRI), Penn State. He holds 20 patents, has published over 900 technical articles and proceedings articles, and has authored 30 book chapters

with several additional chapters currently in preparation. He has published several books, including Frontiers in Electromagnetics (Piscataway, NJ, USA: IEEE Press, 2000), Genetic Algorithms in Electromagnetics (Hoboken, NJ, USA: Wiley/IEEE, 2007), Transformation Electromagnetics and Metamaterials: Fundamental Principles and Applications (London, U.K.: Springer, 2014), Electromagnetics of Body Area Networks: Antennas, Propagation, and RF Systems (Hoboken: Wiley/IEEE, 2016), and Broadband Metamaterials in Electromagnetics: Technology and Applications (Pan Stanford Publishing, 2017). He has also contributed chapters for several books, including Electromagnetic Optimization by Genetic Algorithms (New York: Wiley Interscience, 1999), Soft Computing in Communications (New York: Springer, 2004), Antenna Engineering Handbook (New York: McGraw-Hill, 2007), Frontiers in Antennas: Next Generation Design and Engineering (New York: McGraw-Hill, 2011), Numerical Methods for Metamaterial Design (New York: Springer, 2013), Computational Electromagnetics (New York: Springer, 2014), Graphene Science Handbook: Nanostructure and Atomic Arrangement (Abingdon, Oxfordshire, U.K.: CRC Press, 2016), Handbook of Antenna Technologies (New York: Springer, 2016), and Transformation Wave Physics: Electromagnetics, Elastodynamics and Thermodynamics (Boca Raton, FL, USA: CRC Press, 2016). His research interests include computational electromagnetics (MoM, FEM, FEBI, FDTD, DGTD, CBFM, RCWA, GO, GTD/UTD), antenna theory and design, phased arrays (including ultrawideband arrays), microwave devices, wireless and personal communication systems (including body-area networks), wearable and e-textile antennas, RFID tag antennas, conformal antennas, reconfigurable antennas, frequency-selective surfaces, electromagnetic wave interactions with complex media, metamaterials, electromagnetic bandgap materials, zero and negative index materials, transformation optics, nanoscale electromagnetics (including nanoantennas), fractal and knot electrodynamics, and nature-inspired optimization techniques (genetic algorithms, clonal selection algorithms, particle swarm, wind-driven optimization, and various other evolutionary programming schemes). Werner is a fellow of the IEEE, IET, OSA, ACES, and the PIERS Electromagnetics Academy. He is also a Senior Member of the National Academy of Inventors (NAI) and SPIE. He was a recipient of the 1993 Applied Computational Electromagnetics Society (ACES) Best Paper Award, the 1993 International Union of Radio Science (URSI) Young Scientist Award, and the Pennsylvania State University Applied Research Laboratory Outstanding Publication Award in 1994. He has coauthored (with one of his graduate students) an article published in the IEEE Transactions on Antennas and Propagation which received the 2006 R. W. P. King Award. He also received the inaugural IEEE Antennas and Propagation Society Edward E. Altshuler Prize Paper Award, the Harold A. Wheeler Applications Prize Paper Award in 2011 and 2014, respectively, the DoD Ordnance Technology Consortium (DOTC) Outstanding Technical Achievement Award in 2018, the 2015 ACES Technical Achievement Award, the 2019 ACES Computational Electromagnetics Award, the IEEE Antennas and Propagation Society 2019 Chen-To Tai Distinguished Educator Award, the College of Engineering PSES Outstanding Research Award, the Outstanding Teaching Award in March 2000 and March 2002, respectively, and the PSES Premier Research Award in 2009. He was also presented with the IEEE Central Pennsylvania Section Millennium Medal. He is a former Associate Editor of Radio Science, a former Editor of the IEEE Antennas and Propagation Magazine, an Editorial Board Member of Scientific Reports (a Nature subjournal), an Editorial Board Member of EPJ Applied Metamaterials, an Editor of the IEEE Press Series on Electromagnetic Wave Theory and Applications, and a member of URSI Commissions B and G, Eta Kappa Nu, Tau Beta Pi, and Sigma Xi.

Optimization of Loneys Solenoid Design Using a Dynamic Search Based Technique

Shanshan Tu [1], Obaid U. Rehman [2*], Sadaqat U. Rehman[3], Shafi U. Khan[4], Muhammad Waqas [5], and Ajmal Farooq [6]

[1] Department of Computer Science, Beijing University of Technology, Beijing, 10024, China
sstu@bjut.edu.cn

[2] Department of Electrical Engineering, Sarhad University of Science and IT, Peshawar, 25000, Pakistan
*obaid.ee@suit.edu.pk

[3] Department of Computer Science, Namal Institute, Mianwali, 42250, Pakistan
engr.sidkhan@gmail.com

[4] Department of Electronics, Islamia College University, Peshawar, 25000, Pakistan
shafielectronics@icp.edu.pk

[5] Department of Computer Science & Engineering
Ghulam Ishaq Khan Institute of Engineering Sciences & Technology, Topi, 23460, Pakistan
engr.waqas2079@gmail.com

[6] Department of Electrical Engineering, UET Mardan, Mardan, 25000, Pakistan
farooqaj@yahoo.com

Abstract ─ Particle swarm optimizer is one of the searched based stochastic technique that has a weakness of being trapped into local optima. Thus, to tradeoff between the local and global searches and to avoid premature convergence in PSO, a new dynamic quantum-based particle swarm optimization (DQPSO) method is proposed in this work. In the proposed method a beta probability distribution technique is used to mutate the particle with the global best position of the swarm. The proposed method can ensure the particles to escape from local optima and will achieve the global optimum solution more easily. Also, to enhance the global searching capability of the proposed method, a dynamic updated formula is proposed that will keep a good balance between the local and global searches. To evaluate the merit and efficiency of the proposed DQPSO method, it has been tested on some well-known mathematical test functions and a standard benchmark problem known as Loney's solenoid design.

Index Terms ─ Design optimization, probability distribution, quantum mechanics, searched based technique.

I. INTRODUCTION

Over the last few decades, random optimization methods, including evolutionary technique and swarm intelligence, such as genetic algorithm (GA), evolutionary strategies (ES), genetic programming and evolutionary programming (EP) have been used to solve different global optimization problems. These techniques are inspired by different natural evolutionary phenomena.

Many efforts have been made to develop a global stochastic technique for hard optimization problems. Some of the latest updated literature is recorded in the following paragraph.

An adaptive null-steering beamformer based on Bat Algorithm for the uniform linear array was presented in [1]. The optimization of radome-enclosed antenna arrays was proposed to compensate the distortion error of radome-enclosed antenna arrays [2]. A radiation pattern synthesis of non-uniformly excited planar arrays was presented [3]. An updated version of artificial immune system algorithm was proposed for electromagnetic applications [4]. A new quantum-based approach was proposed for the electromagnetic applications in [5]. An improved particle swarm optimization was applied to electromagnetic devices [6]. A hybrid harmony search method and ring theory based evolutionary algorithm was presented for feature selection [7]. A newly emerging nature inspired optimization algorithms were reviewed

Submitted On: July 29, 2020
Accepted On: December 6, 2020
https://doi.org/10.47037/2020.ACES.J.360105

in [8]. A pareto optimal characterization of a microwave transistor was presented [9]. A multiple black hole inspired meta heuristic searching method was proposed to optimize the combinatorial testing [10]. In [11], a whale optimization technique based on lamarckian learning was proposed to solve global optimization problems. A quantum inspired particle swarm method with enhanced strategy was applied to optimizing the electromagnetic devices [12]. An improved quantum particle swarm method was applied to solve the electromagnetic design problem [13].

Thus, a continued research and development is needed to search a global optimizer to optimize hard engineering design problems. However, according to the no free lunch theorem, all these optimizers are problem oriented, so, an effort is required to seek a global optimizer. In this context, some modification has been proposed in this work for the optimization of Loney solenoid design.

Moreover, particle swarm optimization is an essential member of a broader class of swarm intelligence. This method originated in 1995 by John Kennedy and Robert Hart as an imitation of insect's social behavior [14].

Since 1995, many efforts have been made to make PSO a global optimizer. Consequently, introducing the quantum mechanics into PSO, called quantum behaved particle swarm optimizer (QPSO) [15]. The numerical results on some widely used benchmark problems have demonstrated the superiority of QPSO over basic PSO. However, there are still many issues in QPSO that needs to be addressed. In this context, a new mutation phenomenon is applied to the particle with the global best position of the swarm that will avoid the premature convergence and significantly improves its global searching capability. Also, a parameter updated formula is proposed that will bring a good balance between the local and global searches. Thus, a dynamic quantum-inspired particle swarm method (DQPSO) is applied to Loney's solenoid design as reported in this work.

II. QPSO APPROACH

The trajectory analysis [16] illustrates that the PSO convergence behavior can be guaranteed if each particle converges to its local attractor $pi = (p_{i,1}, p_{i,2}, ..., p_{i,d})$, of which the coordinates are:

$$p_i(t) = (c_1 p_i(t) + c_2 p_g(t)) / (c_1 + c_2), \quad \text{or} \quad p_i(t) = \varphi \cdot p_i(t) + (1-\varphi) \cdot p_g(t), \tag{1}$$

where $\varphi = c_1 r_1 / (c_1 r_1 + c_2 r_2)$. It has been shown that the local attractor is stochastic of particle *i* and lies in a hyper rectangle with p_i and p_g are the two ends of its diagonal.

In quantum potential delta model [15], the position of a particle is given by:

$$x_i(t) = p_i(t) \pm \frac{L(t)}{2} \ln(1/u). \tag{2}$$

In [14], a parameter *L(t)* is defined as:

$$L(t) = 2 \cdot \beta \cdot \left| p_i(t) - x_i(t) \right|. \tag{3}$$

Then the position is updated as follows:

$$x_i(t+1) = p_i(t) \pm \beta \cdot \left| p_i(t) - x_i(t) \right| \cdot \ln(1/u), \tag{4}$$

where *u* is a random number within the interval [0,1], β is the contraction expansion coefficient (CE) parameter and is used to control the convergence behavior of the QPSO and is represented by:

$$\beta = 0.5 + (1.0 - 0.5)(Maxiter - t) / Maxiter. \tag{5}$$

This parameter is initially set to 1 and then linearly decreased to 0.5.

To evaluate *L(t)*, the mean best position is defined as the average of the personal best position of the swarm, i.e.,

$$m(t) = (m_1(t), m_2(t), ..., m_d(t)) = \left(\frac{1}{N}\sum_{i=1}^{N} p_{i,1}(t), \frac{1}{N}\sum_{i=1}^{N} p_{i,2}(t), ..., \frac{1}{N}\sum_{i=1}^{N} p_{i,d}(t) \right), \tag{6}$$

where *N* represents the swarm size. The parameter *L* will become,

$$L(t) = 2 \cdot \beta \cdot \left| m(t) - x_i(t) \right|. \tag{7}$$

Thus, the position of particles will be updated as:

$$x_i(t+1) = p_i(t) \pm \beta \cdot \left| m(t) - x_i(t) \right| \cdot \ln(1/u). \tag{8}$$

The equation (8) is called the position updated equation of the quantum particle swarm algorithm.

III. PROPOSED METHOD

The quantum inspired particle swarm method has many issues, especially when dealing with complex optimization problems. Because at the start of the search process, the diversity of the algorithm is high, however, it reduces quickly at the later stage of the evolution process. Thus, to improve the QPSO performance in terms of the final solution searched and convergence speed much effort has been made and different variants of QPSO have been developed. However, most of these methods are problem oriented. Thus, a continued research and development is needed to develop a global optimizer to optimize complex design problems.

The mutation phenomena were brought from the evolutionary algorithm to maintain the diversity of the population. Thus, it plays a vital role in exploring the searching capability of the algorithm. Different approaches such as Gaussian, exponential, Cauchy etc., and other probability distributions methods are used to produce random numbers and improve the position updated equation of QPSO. Thus, a new outcome has been presented for the mutation operator in QPSO by using the beta probability distribution method. The proposed DQPSO method will be ensured to keep the high diversity and avoid trapping into local optima. The flow chart of a proposed DQPSO is given in Fig. 1.

A. Introduction of a mutation operation

A beta mutation mechanism is applied to the global best (G_{best}) position of the particle to intensifying the diversity of the swarm and avoid the particles from being trapped into local optima. Hence, it will also improve the QPSO performance in terms of the solution quality and global searching capability.

In this method, the beta mutation is combined with the G_{best} particle as follows:

$$G_{mutated} = G_{best} + beta(rand), \quad (9)$$

where *beta(rand)* is the random number generated with the beta probability distribution method.

The proposed mutation strategy will enhance the searching capability of the proposed DQPSO method. Hence, the mutated particle will explore more searched area to achieve the best optimal outcomes and avoid the algorithm to trap into local minima.

B. Parameter updating mechanism

The contraction expansion coefficient (CE) β is the control parameter used for tuning the proposed DQPSO. It plays a vital role in controlling the convergence speed of the proposed DQPSO method. Therefore, different researchers have proposed different mechanisms to tune this parameter [16]. The general mechanism for this parameter is to set to 1 and reduced linearly to 0.5 initially. It also plays a vital role in maintaining a right balance between the local and global searches. However, if the parameter is not adjusted correctly then it may disturb the local and global searches and the algorithm will be trapped into local minima. Thus, to address this issue, it is significantly essential to adjust the value of β parameter properly.

Therefore, a new dynamic updated strategy for β parameter is proposed to maintain a good cooperation between the exploration and exploitation searches and avoid the proposed DQPSO method to stuck into local minima:

$$\beta = 1 + \frac{0.5}{\log(G_{mutated} + 0.2)}. \quad (10)$$

The relationship between the β and $G_{mutated}$ parameters is shown in Fig. 2. It should be noticed from Fig. 2, that if the individual (particle) is far away from the mean best position, then one expects a small value of β to help it come back; In contrast if the particle is just near to the mean best position, then one prefers a high β to force it to bounce away. This will bring a good balance between the local and global searches and avoid the algorithm to trap into local minima.

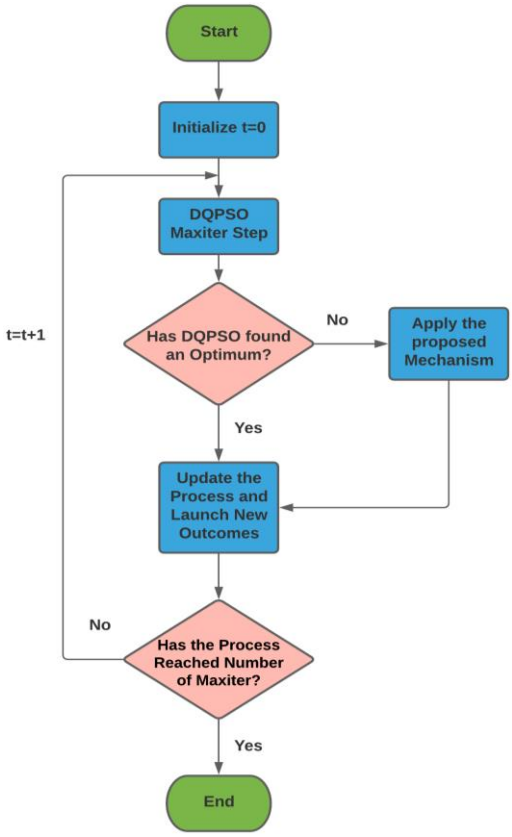

Fig. 1. Flow chart of the proposed DQPSO method.

IV. NUMERICAL RESULTS

To evaluate the performance and global searching capability of the proposed DQPSO algorithm, first three benchmarks shifted versions of mathematical test functions [17] are used as reported:

$$f_1(x) = \sum_{i=1}^{D} \left(\prod_{j=1}^{i} z_j\right)^2 + f\_bias_1, z = x - 0, x = [x_1, x_2, ..., x_D],$$

$$x \in [-100, 100]^D.$$

Global optimum: $x^* = 0, f_1(x^*) = f\_bias_1 = -450$, (11)

$$f_2(x) = \sum_{i=1}^{D} (100.(z_{i+1} - {z_i}^2)^2 + (z_i - 1)^2) + f\_bias_2,$$

$$z = x - 0 + 1, x = [x_1, x_2, ..., x_D], x \in [-100, 100]^D.$$

Global optimum: $x^* = 0, f_2(x^*) = f\_bias_2 = 390$, (12)

$$f_3(x) = \frac{1}{4000} \sum_{i=1}^{D} {z_i}^2 - \prod_{i=1}^{D} \cos\left(\frac{z_i}{\sqrt{i}}\right) + 1 + f\_bias_3,$$

$$z = x - 0, x = [x_1, x_2, ..., x_D], x \in [-600, 600]^D.$$

Global optimum: $x^* = 0, f_3(x^*) = f\_bias_3 = 390$. (13)

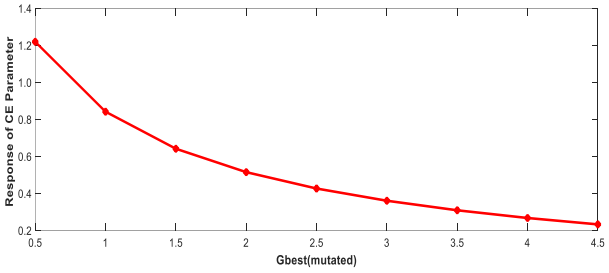

Fig. 2. Relationship between β and Gbest (mutated).

The proposed DQPSO is then compared with the basic QPSO [15], LTQPSO [18] and MQPSO [19] methods.

All these functions are minimization problems and the minimum value for each objective function is zero. Table 1 presents the average performance comparison of different optimizers. Moreover, Figs. 3~5 gives the convergence comparison of the proposed DQPSO with other optimal methods in a logarithmic scale of the best objective function on three well-known test problems using the swarm size of 80 with the number of iterations is 2000 for the 30-dimension problem.

It can be illustrated in Table 1 that the proposed DQPSO and MQPSO have a good performance on most of the shifted version problems. However, the QPSO and LTQPSO could not produce better outcomes and falls into local minima. Thus, it is concluded that the proposed DQPSO improved significantly as compared to other tested optimizers.

Table 1: Mean (first row) and variance (second row) of different optimizer for 30-dimension problems

Algorithms	$f_1(x)$	$f_2(x)$	$f_3(x)$
QPSO	5.9342×10^{-6} 2.8627×10^{-10}	0.1376 3.8629×10^{-2}	3.0716×10^{-2} 4.8620×10^{-3}
LIQPSO	1.23924 0.38211	5.09190 0.52149	2.9314×10^{-2} 7.6824×10^{-4}
MQPSO	1.1339×10^{-7} 2.7820×10^{-13}	7.8273×10^{-2} 5.7432×10^{-5}	5.8461×10^{-3} 1.6560×10^{-7}
DQPSO	3.4182×10^{-9} 1.5086×10^{-17}	8.2016×10^{-4} 5.2791×10^{-8}	6.2041×10^{-5} 5.3942×10^{-10}

V. LONEY'S SOLENOID BENCHMARK PROBLEM

To validate the proposed DQPSO performance for electromagnetic design. It is used to solve the Loney's solenoid problem. The literature has several references to optimization techniques that have been applied to Loney's solenoid design [20]-[22].

Loney's solenoid is a standard nonlinear benchmark problem in magnetostatics inverse problems [20]. Figure 6 show the upper half plane of the axial cross section of the system. Loney's solenoid problem's key point is to find the position and size of two correcting coils to produce an approximate constant magnetic field in the interval of the axis.

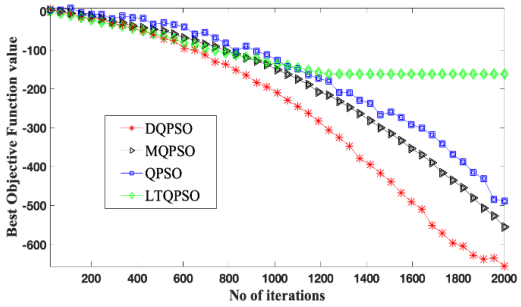

Fig. 3. Convergence plots of different optimization methods solving function f_1.

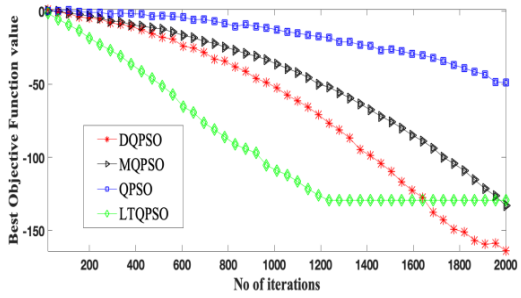

Fig. 4. Convergence plot of different optimization methods solving function f_2.

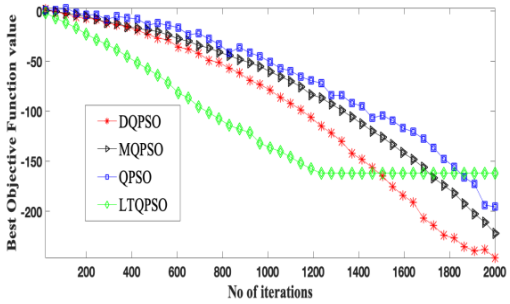

Fig. 5. Convergence plot of different optimization methods solving function f_3.

The Loney's solenoid problem has two variables, which are *s* and *l*, and the optimization problem is aiming to find the global minima of $f(s, l)$, i.e.,

$$\min f(s,l). \tag{14}$$

The objective function *f* can be formulated as:

$$f(s,l) = \frac{B_{\max} - B_{\min}}{B_0}, \tag{15}$$

where *B*max and *B*min represent the maximum and minimum value of the magnetic flux density within the

interval $(-z_0, z_0)$, respectively; and B_0 is the magnetic flux density at $z_0 = 0$.

In particular, three different "areas" can be recognized in the domain of f with values of $f > 4\cdot10^{-8}$ (high level region), $3\cdot10^{-8} < f < 4\cdot10^{-8}$ (low level region), and $f < 3\cdot10^{-8}$ (very low-level region—global minimum region). The very low-level region is a small ellipsoidal shaped area within the thin low-level valley. In both very low- and low-level small changes in one of the parameters can give rise to changes in objective function values of several orders of magnitude.

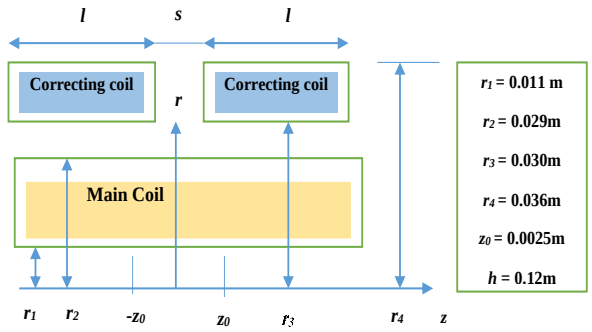

Fig. 6. Upper half plane of the axial cross section of Loney's solenoid problem.

Table 2: Comparison of different optimizer for Loney solenoid problem

Optimizer	$f(s,l)\times10^{-8}$			
	Minimum (Best)	Mean	SD	Maximum
LTQPSO	3.7416	8.5294	3.8926	14.7682
QPSO	3.6792	5.2867	2.2496	8.7293
MQPSO	3.5728	6.5934	1.7454	8.6719
QBSO	3.3990	3.5749	0.7295	4.7614
DQPSO	3.3876	3.4982	0.9837	4.7428

Table 3: Best solution for Loney solenoid problem

Optimizer	Parameters			Computation Time
	$s(cm)$	$l(cm)$	$f(s,l)\times10^{-8}$	
LTQPSO	14.60984	15.8997	3.7416	1729
QPSO	13.9675	5.4006	3.6792	1688
MQPSO	13.2813	3.3107	3.5728	1667
DQPSO	11.8301	1.6496	3.3876	1598

For a fair comparison, this case study is solved using the proposed DQPSO method, original QPSO [15], LTQPSO [18], MQPSO [19] and the results obtained by the QBSO method [22] is taken from literature for comparison.

Moreover, each optimizer is run independently 30 times with the corresponding number of maximum generations is 200. The optimal outcomes of different algorithms are tabulated in Table 2.

It can be concluded from the outcomes of Table 2 that the proposed DQPSO outperforms LTQPSO, QPSO, MQPSO and QBSO methods on minimum (best) objective functions values.

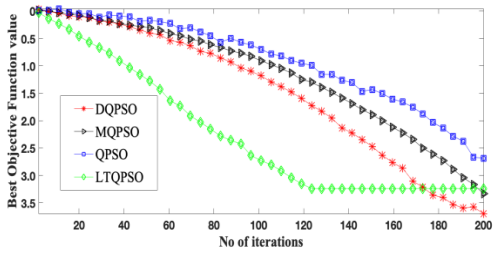

Fig. 7. Comparison of different optimal methods solving Loney Solenoid design.

Since the iterative number is an appropriate parameter to measure the computational time, and one can evaluate the computational efficiency using this parameter as shown in Table 3.

One can also analyze from the statistics of Fig. 7, that QPSO has the weakness of slow convergence behavior and is pertinent to trap into local optima. Though DQPSO has a fast convergence behavior, it is easy to avoid the local optimum. Thus, it can be illustrated that the proposed DQPSO avoids a possible local stuck and tradeoff between local and global searches. The new mechanism of mutation methodology and dynamic parameter can enhance the diversity of population and solution quality. As a result, the proposed DQPSO performance is much better than other tested optimizers.

VI. CONCLUSION

An improved version of quantum inspired particle swarm method has been presented in this work for the optimization of loneys solenoid design. The proposed dynamic QPSO was tested on some shifted version benchmark functions and loneys solenoid problem. The numerical outcomes and statistical analysis illustrate the merit and efficiency of the proposed DQPSO method as compared to other tested optimizers. Thus, the proposed method has significantly improved its solution quality and achieved an optimal solution for the tested problems. However, for future work, the proposed DQPSO method will be applied to other engineering design problems.

REFERENCES

[1] T. V. Luyen and T. V. B. Giang, "Null steering beam-former using bat algorithm," *Applied Computational Electromagnetics Society (ACES) Journal*, vol. 33,

no. 1, pp. 23-29, 2018.

[2] C. Zhai, X. Zhao, Y. Wang, Y. Zhang, and M. Tian, "PSO algorithm combined with parallel higher order MoM to compensate the influence of radome on antennas," *Applied Computational Electromagnetics Society (ACES) Journal*, vol. 32, no. 3, pp. 215-220, 2017.

[3] R. Bera, D. Mandal, R. Kar, and S. P. Ghoshal, "Optimal design of elliptical array antenna using opposition based differential evolution technique," *Applied Computational Electromagnetics Society (ACES) Journal*, vol. 32, no. 9, pp. 833-841, 2017.

[4] O. Kilic and Q. M. Nguyen, "Enhanced artificial immune system algorithm and its comparison to bio-inspired optimization techniques for electromagnetic applications," *Applied Computational Electromagnetic Society (ACES) Journal*, vol. 33, no. 2, pp. 132-135, 2018.

[5] S. Tu, O. U. Rehman, S. U Rehman, S. U. Khan, M. Waqas, and R Zhu, "A novel quantum particle swarm optimization algorithm for electromagnetic application," *IEEE Access*, vol. 8, iss. 1, pp. 21909-21916, 2020.

[6] S. Khan, S. Yang, and O. U. Rehman, "A global particle swarm optimization algorithm applied to electromagnetic design problem," *International Journal of Applied Electromagnetics and Mechanics*, vol. 53, pp. 451-467, 2017.

[7] S. Ahmed, K. K. Ghosh, P. K. Singh, Z. W. Geem, and R. Sarkar, "Hybrid of harmony search algorithm and ring theory-based evolutionary algorithm for feature selection," *IEEE Access*, vol. 8, pp. 102629-102645, 2020. doi: 10.1109/ACCESS.2020.2999093.

[8] H. Li, X. Liu, Z. Huang, C. Zeng, P. Zou, Z. Chu, and J. Yi, "Newly emerging nature-inspired optimization - Algorithm review, unified framework, evaluation, and behavioural parameter optimization," *IEEE Access*, vol. 8, pp. 72620-72649, 2020. doi: 10.1109/ACCESS.2020.2987689.

[9] F. Güneş, A. Uluslu, and P. Mahouti, "Pareto optimal characterization of a microwave transistor," *IEEE Access*, vol. 8, pp. 47900-47913, 2020. doi: 10.1109/ACCESS.2020.2978415.

[10] H. N. Nsaif Al-Sammarraie and D. N. A. Jawawi, "Multiple black hole inspired meta-heuristic searching optimization for combinatorial testing," *IEEE Access*, vol. 8, pp. 33406-33418, 2020. doi: 10.1109/ACCESS.2020.2973696.

[11] Q. Zhang and L. Liu, "Whale optimization algorithm based on lamarckian learning for global optimization problems," *IEEE Access*, vol. 7, pp. 36642-36666, 2019. doi:10.1109/ACCESS.2019.2905009.

[12] O. U. Rehman, S. Yang, S. U. Khan, and S. U. Rehman, "A quantum particle swarm optimizer with enhanced strategy for global optimization of electromagnetic devices," *IEEE Transactions on Magnetics*, vol. 55, no. 8, pp. 7000804, 2019.

[13] O. U. Rehman, S. Tu, S. U. Rehman, S. U. Khan, and S. Yang, "Design optimization of electromagnetic devices using an improved quantum inspired particle swam optimizer," *Applied Computational Electromagnetics Society (ACES) Journal*, vol. 33, no. 9, pp. 951-956, 2018.

[14] J. Kennedy and R. Eberhart, "Particle swarm optimization," *In Proceedings of IEEE International Conference on Neural Network*, Perth, WA, vol. 4, pp. 1942-1948, 1995.

[15] J. Sun, B. Feng, and W. B. Xu, "Particle swarm optimization with particles having quantum behavior," in *IEEE Proceeding of Congr. Evol. Comput*., pp. 325-331, 2004.

[16] J. Sun, W. Fang, X. Wu, V. Palade, and W. Xu, "Quantum behaved particle swarm optimization: analysis of the individual particle's behavior and parameter selection," *Evolutionary Computation.*, vol. 20, no. 3, pp. 349-393, 2012.

[17] P. N. Suganthan, N. Hansen, J. J. Liang, K. Deb, Y. P. Chen, A. Auger, and S. Tiwari, "Problem definitions and evaluation criteria for the CEC 2005 special session on real parameter optimization," *Technical Report*, Nanyang Technological University, Singapore and Kangal, Report Number 2005005 (Kanpur Genetic Algorithms Laboratory, IIT Kanpur) 2005.

[18] Q. M. Qian, C. Tokgo, C. Kim, J. Han, and K. Song, "A hybrid improved quantum behaved particle swarm optimization algorithm using adaptive coefficient and natural selection method," *7th International Conference on Advanced Computational Intelligence*, Mount Wuyi, Fujian, China, pp. 312-317, Mar. 2015.

[19] O. U. Rehman, S. Tu, S. Khan, H. Khan, and S. Yang, "A modified quantum particle swarm optimizer applied to optimization design of electromagnetic devices," *International Journal of Applied Electromagnetics and Mechanics*, vol. 58, pp. 347-357, 2018.

[20] P. Di Barba, A. Gottvald, and A. Savini, "Global optimization of Loney's solenoid: A benchmark problem," *International Journal of Applied Electromagnetics and Mechanics*, vol. 6, pp. 273-276, 1995.

[21] H. B. Duan and J. N. Li, "A new method for Loney's solenoid problem: Gaussian harmony search algorithm," *IEEE Transactions on Magnetics*, vol. 50, Art. ID 7026405, 2014.

[22] H. Duan and C. Li, "Quantum behaved brain storm optimization approach to solving Loney's solenoid problem," *IEEE Transactions on Magnetics*, vol. 51, no. 1, pp. Art ID. 7000307, 2015.

Separation of Radiated EMI Noise based on Joint Approximate Diagonalization Algorithm

Zhibo Zhu [1], Wei Yan [1], Yang Zhao [1,*], Xingfa Liu [2], and Tao Zhang [1]

[1] School of Electrical and Automation Engineering
Nanjing Normal University, Nanjing, 210046, China
1822628862@qq.com, 61197@njnu.edu.cn, zhaoyang2@njnu.edu.cn*, 2901286136@qq.com

[2] State Key Laboratory of Power Grid Environmental Protection
Wuhan Branch of China Electric Power Research Institute Co., Ltd, Wuhan, 430074, China
1826579591@qq.com

Abstract ─ Power electronic devices and electrical equipment produce a large quantity of radiated electromagnetic interference (EMI) in the working process. Electromagnetic field analysis method of the near-field and far-field of the antenna can be employed to separate the radiated interference noises. However, the method has low separation accuracy and requires a lot of time. A novel method based on joint approximate diagonalization algorithm (JADA) to separate the radiated EMI noise is proposed in this paper. Compared with the traditional independent component algorithm method, the accuracy is improved by 14% and the efficiency is increased by 30%. The common-differential mode mixed noise source is taken as the experimental object to demonstrate the effectiveness and simplicity of the proposed method.

Index Terms ─ Common-differential mode mixed source, JADA algorithm, noise separation, radiated EMI.

I. INTRODUCTION

With the increasing integration and complexity, power electronic device radiates a large number of electromagnetic interference (EMI) noises, which leads to the abnormal operation of other devices and electrical equipment around [1-5]. In order to control the radiated EMI within a safe range, the prediction and separation of radiated EMI noise sources have become a burning issue to be solved [6-8].

Electromagnetic field analysis methods are widely used in the research of radiated EMI noises at the moment. A novel method has been proposed to predict the far-field radiation using the magnetic near-field component on a Huygens's box in [9-10], the effect of inaccuracy of magnetic field and the incompleteness of the Huygens's box on far-field results has been investigated. The radiated EMI has been designed as a time harmonic electromagnetic wave in [11], 3D finite elements (3DFE) model has been used to evaluate the different distributing effects that the switching frequencies may have on the radiated EMI. The far-field radiated EMI emission of a power converter caused by common-mode current on attached cables has been demonstrated in [12-13], and an antenna model has been developed to estimate the far-field radiation of a power converter. A Green's function approach for the computation of broadband stochastic radiated EMI field energy densities has been presented in [14], which predicted and separated the far-field radiated EMI. Symmetrical component theory has been applied to analyze the characteristics of EMI noises in power electronic system in [15-16], and a multiphase noise separator has been built. A method for the measurement of the field generated by multiple uncorrelated sources has been proposed in [17-18], the contribution of each source has been determined with the assistance of the blind signal separation technique. Therefore, it is meaningful to separate the radiated EMI noise effectively.

The above methods can separate the radiated EMI noise to a certain extent, but there are still some defects that need further improvement, for example, it is necessary to use electromagnetic field analysis software, which has a large amount of calculation and low precision. The motivation of this paper is to propose a JADA-based method, which can be used to separate the radiated EMI noise. Compared with the Electromagnetic field analysis method, the JADA algorithm separates the radiated EMI noise from the perspective of signal analysis, the amount of calculation of JADA algorithm is smaller, which can separate the radiated EMI noise more accurately and more efficiently. To verify the validity of the proposed method, both simulation and experiment are presented.

Submitted On: August 25, 2020
Accepted On: November 30, 2020

https://doi.org/10.47037/2020.ACES.J.360106

II. SEPARATION OF THE RADIATED EMI NOISE BASED ON JADA ALGORITHM

A. Radiated EMI source

In this section, a radiated EMI noise source model is established, as shown in Fig. 1. There are *n* noise sources in the model, the total radiated noises are formed by E_1, E_2, E_3, …, E_N, which are produced by each radiated source.

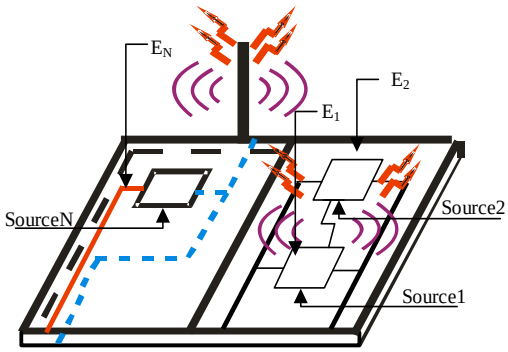

Fig. 1. Radiated EMI noise source model.

B. Separation of radiated EMI based on JADA

On the basis of independent component algorithm (ICA), JADA algorithm is used to separate the radiated EMI noise, which introduces the fourth order cumulative quantity matrix of multivariate data, and performs eigen-decomposition to separate the mixed signals.

Since the components of the radiated EMI noise are independent of each other, JADA algorithm makes full use of algebraic method, combines with matrix theory, simplifies the algorithm, improves the robustness of the algorithm. JADA algorithm has strong radiated EMI noise separation capability, which can also separate the small sensor noise in the original signal. In order to ensure the feasibility of algorithm separation, the signal to noise ratio (SNR) of the original noise signals is higher than 6dB.

The signals of the radiated EMI noise source model can be expressed as:

$$\begin{aligned} &x(t) = A * s(t) = \sum_{p=-\infty}^{+\infty} A_p s(t-p), t = 1, 2, \ldots, \\ &s(t) = [s_1(t), \ldots, s_n(t)]^T, n = 1, 2, ..., \\ &x(t) = [x_1(t), \ldots, x_n(t)]^T, \end{aligned} \tag{1}$$

where $x(t)$ are *m* mixed signals; $s(t)$ are *n* radiated EMI noise signals; A_p is the hybrid filter, *p* is time delay:

$$y(t) = B_p * x(t) = \sum_{p=-\infty}^{+\infty} B_p A_p s(t-p), \tag{2}$$

where $y(t)$ is a *n*-dimensional column vector and B_p is an n*n matrix. The purpose is to find a separation filter B_p such that $y(t)$ is an estimate of the signals $s(t)$.

The principle of the JADA algorithm to separate the radiated EMI noise signals includes mainly the following three sections.

B.1. Zero mean processing

Zero mean is mainly to eliminate the constant in the signal. The theory of blind signal separation is generally based on the assumption that the original signal component is zero mean, but the radiated EMI noise signals cannot meet this condition, so it is necessary to carry out zero mean processing on the actual data to meet the theoretical premise, and build a reasonable mathematical model. In fact, the zero mean processing of data is the translation transformation of data, which does not affect the overall distribution of data, but change the range of data values. This processing method is reasonable.

For the sampling data whose mean value is not zero, formula (3) is used to make the data zero mean:

$$X' = X - E(X), \tag{3}$$

where X is the collected radiated EMI data, $E(X)$ is mathematical expectation, and X' is the data after the zero mean. The actual sampling data is often discrete, so the calculation is generally replaced by the arithmetic average.

When $x(t)$ is a fourier transform data with a mean value not zero, the values in the vector $x_i(t)$ are all complex numbers, and the zero mean processing can be expressed as:

$$x_i(t)' = x_i(t) - \frac{1}{n}\sum_{i=1}^{n} x_i(t), i = 1, 2, ..., n. \tag{4}$$

B.2. Whitening processing

Whitening can remove the correlation between the signals and make the second-order statistics as independent as possible. In addition, whitening can effectively simplify the algorithm and speed up the calculation.

Whitening processing is a linear transformation of the data, which can be expressed as formula (5):

$$\tilde{x} = Tx, \tag{5}$$

where matrix T is a whitened matrix; the correlation matrix $R_{\tilde{x}}$ of transformed random data $\tilde{x}$ has the following property:

$$R_{\tilde{x}} = E\left[\tilde{x}\tilde{x}^H\right] = I, \tag{6}$$

where I is a unit matrix.

So the purpose of whitening is to find the whitening matrix T, which makes the data correlation matrix after whitening become a unit matrix. This section uses the eigenvalue decomposition method of correlation matrix to realize whitening.

Suppose the covariance matrix of X is C_X, has:

$$C_X = XX^T = U\Lambda U^T, \tag{7}$$

where

$$\Lambda=Diag\left[\lambda_1,\lambda_2,\cdots,\lambda_m\right], \tag{8}$$

where X^{T} is the transpose matrix of X, U^{T} is the transpose matrix of U, λ_{m} is the eigenvalue of C_{X}; each column of U is a eigenvector of C_{X}.

So the whitening matrix W_{p} is:

$$W_p=\Lambda^{-\frac{1}{2}}U^T. \tag{9}$$

B.3. Eigen-decomposition transformation

Let Z be the signal after whitening:

$$Z=W_pA_pS=W_pA_p*s(t). \tag{10}$$

Suppose M is an n*n matrix, and the four-dimensional cumulant matrix $Q_{\mathrm{Z}}(M)$ of Z is defined as:

$$[Q_Z(M)]_{ij}=\sum_{k=1}^{n}\sum_{l=1}^{n}K_{ijkl}(z)m_{kl},\ i,j=1,2,...,n, \tag{11}$$

where $K_{ijkl}(z)$ is the fourth-order tensor of the four components i, j, k, l in vector Z.

Let $V=W_p A_p$, according to formula (10), has:

$$Z=VS. \tag{12}$$

Because the variance of the source signal S and the whitened data Z is 1, each element in S is independent of each other, and each element in Z is orthogonal to each other, thus V must be orthogonal and unified. Make $M=v_iv_i^T$, the fourth-order tensor matrix with M as the weight matrix can be transformed into:

$$Q_Z(M)=\lambda M, \tag{13}$$

where $\lambda=k_4(s_i)$ is the kurtosis of source s_i, so M is called the eigen-matrix of $Q_Z(M)$, while $\lambda=k_4(s_i)$ is the eigen-value of $Q_Z(M)$.

So as long as the eigen-decomposition of $Q_Z(M)$ is completed, the eigen-matrix M and eigen-value λ can be obtained. If the kurtosis of each source are different, the v_i and λ_i are also different. We can get the column vectors of V, and then we can get the independent components of A_{p}.

When the eigen-values have multiple roots, the results of formula (9) and formula (11) are unstable, so the algorithm needs to be improved. The basic idea is: according to formula (13), find a matrix V that can diagonalize $Q_Z(M)$ through $V^TQ_Z(M)V$:

$$\begin{aligned}\Lambda(M)&=V^TQ_z(M)V\\&=Diag[k_4(s_1)v_1Mv_1^T,...,k_4(s_n)v_nMv_n^T].\end{aligned} \tag{14}$$

In fact, the result of taking only one matrix M is not very accurate. We can use a group of matrix M = [M_1, M_2, …, M_{p}] to find $Q_Z(M_i)$ for each M_i, and find matrix V to satisfy the maximum possible diagonalization of each $Q_Z(M_i)$ at the same time. The square sum of the non-diagonal elements in $V^TQ_Z(M)V$ can be used as a measure degree of diagonalization:

$$D_M(V)=\sum_{M_1\in M}Off[V^TQ_Z(M_i)V]. \tag{15}$$

According to formula (11), if V is found to make the criterion of $D_M(V)$ minimum, the estimation $\bar{A}$ of the mixed matrix and the estimation $y(t)$ of the original signal $s(t)$ can be obtained:

$$\bar{A}=T^{-1}V=T^TV, \tag{16}$$

$$y(t)=V^TTX(t). \tag{17}$$

C. Implementation steps of separating the radiated EMI noise sources based on JADA algorithm

The radiated EMI noises are separated based on the JADA algorithm in this paper, and the specific steps are as follows.

Step 1: The mutually independence and identically distributed radiated EMI noise signals $s(t)$ are collected by testing, and the mixed signals $x(t)$ are obtained by formula (1).

Step 2: Make the sampling data zero mean, eliminate the constant in $s(t)$.

Step 3: Design the whitening matrix W_{p} remove the correlation between the signals.

Step 4: $Q_Z(M)$ is decomposed by formula (13), the kurtosis of each source can be gained.

Step 5: Find V to make the criterion of $D_M(V)$ minimum, according to formula (17), the estimated signals $y(t)$ can be obtained.

Step 6: For the purpose of judging the separation performance of the JADA algorithm, the similarity coefficient (SC) is applied to measure the approximation between the source signals and the separated signals. When SC is closer to 1, the separation effect of the algorithm is better:

$$SC_{i,j}=\left|\sum_{t=1}^{n}s_j(t)y_i(t)\right|\Big/\sqrt{\sum_{t=1}^{n}s_j^2(t)\sum_{t=1}^{n}y_i^2(t)}. \tag{18}$$

III. SIMULATION OF THE SIGNALS BASED ON JADA ALGORITHM

To verify the effectiveness of the proposed algorithm, the separation simulation of the signals is studied. As shown in Fig. 2 (a), sine signal (blue line), trapezoidal wave signal (yellow line), sawtooth signal (red line) and random signal (purple line) are created. A four order hybrid filter is used to mix the signals, and the waveforms are shown in Fig. 2 (b). According to the JADA algorithm theory, the mixed signals are separated into four mutually independent signals, the waveforms of separated signals are shown in Fig. 2 (c). In addition, the ICA algorithm is employed to separate signals, the waveforms are shown in Fig. 2 (d).

Comparing the source signals in Fig. 2 (a) with the separated signals in Fig. 2 (c), it can be concluded that the mixed signals in Fig. 2 (b) can be successfully separated into the four signals by the JADA algorithm, and the separated results are similar to the source signals. The similarity coefficient *SC* of the sine signal is 0.97, and other three signals are 0.96, 0.95 and 0.96, respectively. In addition, by comparing the results in Fig. 2 (c) and Fig. 2 (d), it can be seen that the accuracy of JADA algorithm is better than that of ICA algorithm. Therefore, the JADA algorithm is employed to the signal separation.

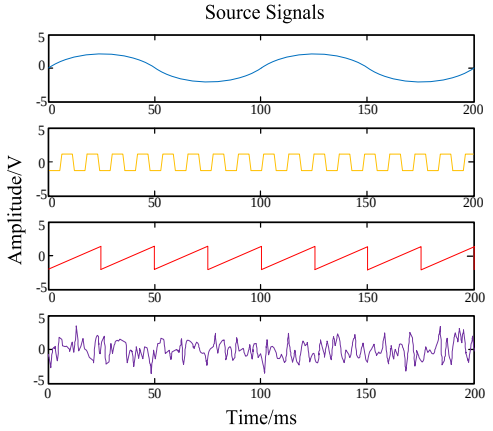

(a) Source signals

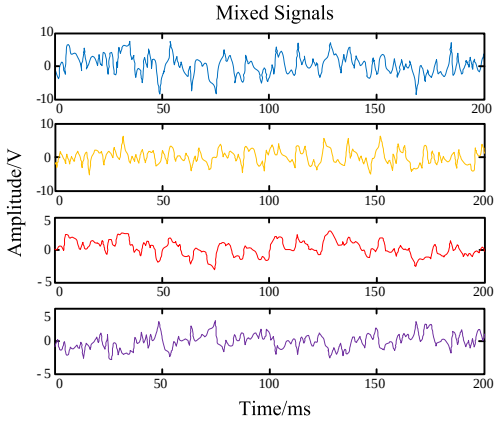

(b) Mixed signals

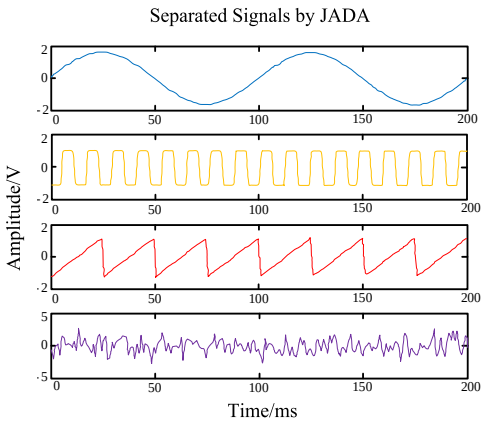

(c) Separated signals by JADA algorithm

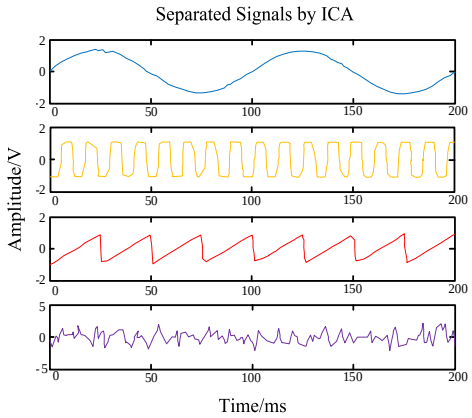

(d) Separated signals by ICA algorithm

Fig. 2. JADA algorithm characteristic simulation.

IV. EXPERIMENT OF THE RADIATED EMI NOISE BASED ON JADA ALGORITHM

In this paper, the experiment of the common-differential mode radiated EMI noises is made to verify the effectiveness of the JADA algorithm. The experiment layout is shown in Fig. 3. One end of the magnetic field probe (R&S HZ-11) is connected to the channel of the oscilloscope (R&S Tektronix DPO5204), and the other end measures the radiated EMI noise.

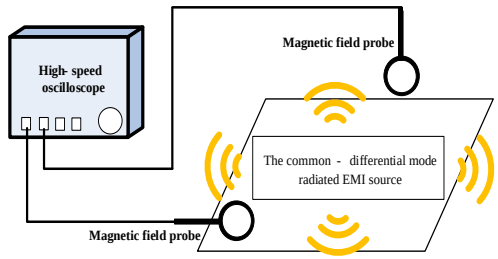

Fig. 3. Experiment layout of radiated EMI noise.

As shown in Fig. 4, in this experiment, the 20M crystal oscillator is used as common mode interference source, and the 30M crystal oscillator is used as differential mode interference source. The white noises and the radiated EMI noises are obtained through the two magnetic field probes and the high-speed oscilloscope. The two probes are fixed, and distance between the probes and the crystal oscillators is within 1cm. The experiment white noises and the radiated EMI noises generated by crystal oscillators are shown in Fig. 4 (a) and Fig. 4 (b), respectively.

The JADA algorithm is applied to separate the mixed signals obtained by the experiment, the separated results of the common mode radiated EMI noise and the differential mode radiated EMI noise are shown in Fig. 5 (a). Compared with the source noises, the *SC* of the common noise and the differential noise are 0.97 and 0.96, respectively, which suggests that the JADA

algorithm is feasible to separate the radiated EMI noises.

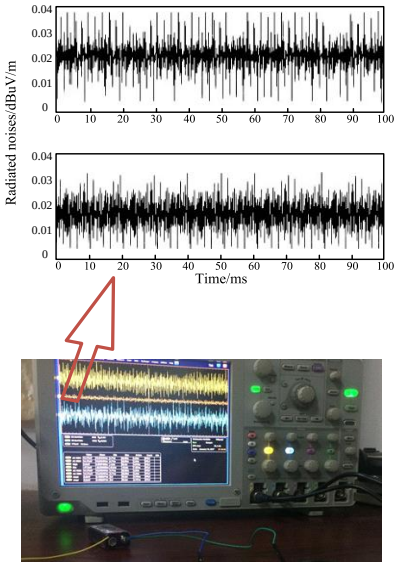

(a) The common-differential mode white noises

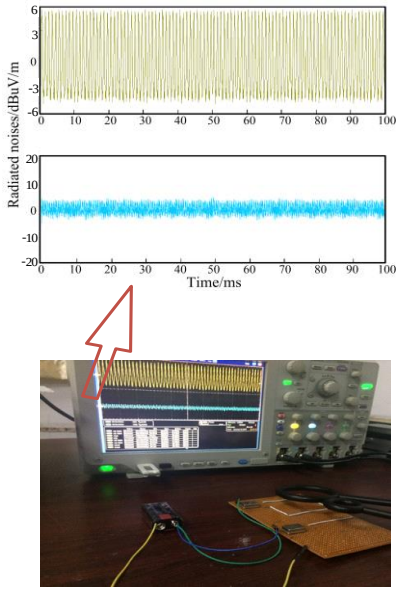

(b) The common-differential mode radiated EMI noises

Fig. 4. The common-differential mode radiated EMI experiment.

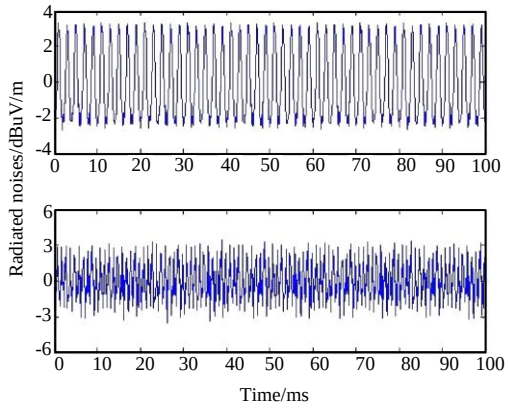

(a) Separated radiated EMI noises by JADA algorithm

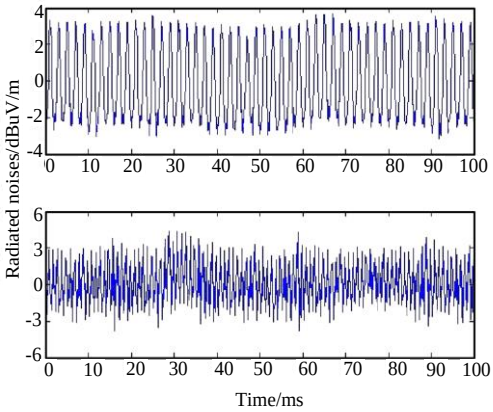

(b) Separated radiated EMI noises by ICA algorithm

Fig. 5. Common-differential mode separated radiated EMI noises.

As shown in Fig. 5, compared the separated results by JADA algorithm in Fig. 5 (a) with the ICA algorithm in Fig. 5 (b), JADA algorithm can separate the radiated EMI noises more accurately and more efficiently. The *SC* of the two noises are shown in Table 1. It can be clear seen that the JADA algorithm accuracy is 14% higher than the ICA algorithm. In addition, from the number of iterations in Table 1, it can be found that the JADA algorithm is more efficient, with an increase of more than 30%. In addition, JADA algorithm introduces the the fourth-order cumulant matrix based on ICA, which has better generality.

Table 1: Comparison of separation characteristics of two algorithms

Radiated Source Model	JADA Algorithm			ICA Algorithm		
	Similarity Coefficient		Number of Iterations	Similarity Coefficient		Number of Iterations
	Common Noise	Differential Noise		Common Noise	Differential Noise	
Common-differential mode	0.97	0.96	24	0.81	0.82	36

V. CONCLUSION

A new radiated EMI noises separation method based on the JADA algorithm is proposed in this paper. Simulation and experiment results demonstrate that the JADA algorithm can successfully separate radiated EMI noise, which verify the validity of the separation method.

Compared with the ICA algorithm, the accuracy and the efficiency have been greatly improved. The work provides the reference for separating the sources which produce the radiated noise, and contributes to conduct the targeted suppression research in the near future.

ACKNOWLEDGMENT

This paper is sponsored by National Natural Science Foundation of China (51475246), Key Projects of Social Sevelopment in Jiangsu Province (BE2019716), Nanjing International Industrial Technology R & D Cooperation Project (201911021), Open Fund Project of State Key Laboratory of Power Grid Environmental Protection (GYW51202001558).

REFERENCES

[1] D. M. Diego and R. Adroaldo, "Electromagnetic modeling of electronic device by electrical circuit parameters," *Applied Computational Electromagnetics Society Journal*, vol. 31, no. 1, pp. 58-65, Jan. 2016.

[2] J. Yao, S. Wang, and H. Zhao, "Measurement techniques of common mode currents, voltages, and impedances in a flyback converter for radiated EMI diagnosis," *IEEE Transactions on Electromagnetic Compatibility*, vol. 61, no. 6, pp. 1997-2005, Dec. 2019.

[3] A. Mueed, Y. Zhao, Y. Wei, Z. B. Zhu, and Q. L. Liu, "Analysis of lossy multiconductor transmission lines (MTL) using adaptive cross approximation (ACA)," *Applied Computational Electromagnetics Society Journal*, vol. 34, no. 11, pp. 1769-1776, Nov. 2019.

[4] W. Yan, Q. Liu, C. Zhu, Y. Zhao, and Y. Shi, "Semi-inverse method to the Klein-Gordon equation with quadratic nonlinearity," *Applied Computational Electromagnetics Society Journal*, vol. 33, no. 8, pp. 842-846, Aug. 2018.

[5] C. Zhu, W. Yan, S. Liu, and L. Geng, "Analysis on crosstalk for coplanar irregular-placed cables based on cascading method and cubic spline interpolation algorithm," *Applied Computational Electromagnetics Society Journal*, vol. 35, no. 5, pp. 572-579, May 2020.

[6] C. Xiao and T. Zhao, "Identification method of EMI sources based on measured single-channel signal and its application in aviation secondary power source design," *IEEE Transactions on Electromagnetic Compatibility*, vol. 59, no. 2, pp. 439-446, Apr. 2017.

[7] K. Takahashi, Y. Murata, Y. Tsubaki, T. Fujiwara, H. Maniwa, and N. Uehara, "Mechanism of near-field coupling between noise source and EMI filter in power electronic converter and its required shielding," *IEEE Transactions on Electromagnetic Compatibility*, vol. 61, no. 5, pp. 1663-1672, Oct. 2019.

[8] W. Song, W. Zheng, Z. Han, and X. Sheng, "RCS reduction and radiation improvement of a circularly polarized patch antenna using AMC structures," *Applied Computational Electromagnetics Society Journal*, vol. 34, no. 10, pp. 1500-1507, Oct. 2019.

[9] X. Gao, J. Fan, Y. Zhang, H. Kajbaf, and D. Pommerenke, "Far-Field prediction using only magnetic near-field scanning for EMI test," *IEEE Transactions on Electromagnetic Compatibility*, vol. 56, no. 6, pp. 1335-1343, Dec. 2014.

[10] I. B. Trad, H. Rmili, M. Sheikh, B. Hakim, and J. Floch, "Design of a printed metamaterial-inspired electrically small Huygens source antenna for cognitive radio applications," *Applied Computational Electromagnetics Society Journal*, vol. 35, no. 7, pp. 837-842, July 2020.

[11] A. Rosales, A. Sarikhani, and O. A. Mohammed, "Evaluation of radiated electromagnetic field interference due to frequency swithcing in PWM motor drives by 3D finite elements," *IEEE Transactions on Magnetics*, vol. 47, no. 5, pp. 1474-1477, May 2011.

[12] H. Chen, T. Wang, L. Feng, and G. Chen, "Determining far-field EMI from near-field coupling of a power converter," *IEEE Transactions on Power Electronics*, vol. 29, no. 10, pp. 5257-5264, Oct. 2014.

[13] Y. Li, W. Cao, P. Zuo, Y. Li, Z. Gao, M. Wang, H. Zheng, and E. Li, "Analysis of multilayer structure near- and far-field radiation by the coupled PP-PEEC and field-equivalence principle method," *IEEE Transactions on Electromagnetic Compatibility*, vol. 61, no. 2, pp. 495-503, Apr. 2019.

[14] J. A. Russer, M. Haider, and P. Russer, "Time-Domain modeling of noisy electromagnetic field propagation," *IEEE Transactions on Microwave Theory and Techniques*, vol. 66, no. 12, pp. 5415-5428, Dec. 2018.

[15] S. Wang, "Modeling and Design of EMI noise separators for multiphase power electronics systems," *IEEE Transactions on Power Electronics*, vol. 26, no. 11, pp. 3163-3173, Nov. 2011.

[16] S. Wang, F. Luo, and F. C. Lee, "Characterization and design of three-phase EMI noise separators for three-phase power electronics systems," *IEEE Transactions on Power Electronics*, vol. 26, no. 9, pp. 2426-2438, Sep. 2011.

[17] Y. Liu, J. Li, C. Hwang, and V. Khilkevich, "Near-Field scan of multiple noncorrelated sources using blind source separation," *IEEE Transactions on Electromagnetic Compatibility*, vol. 62, no. 4, pp. 1376-1385, Aug. 2020.

[18] C. Wang and R. Jia, "A source signal recovery method for underdetermined blind source separation based on shortest path," *Applied Computational Electromagnetics Society Journal*, vol. 35, no. 4, pp. 406-414, Apr. 2020.

Zhibo Zhu received his B.S. degree in Automation from Nanjing University of Information Science and Technology, Nanjing, China, in 2017. He is currently working in Electromagnetic Compatibility and Power Electronics Devices with Nanjing Normal University. His interest is the design of Electromagnetic Compatibility of chips.

Wei Yan received his Electrical Engineering M.Sc. and Physics and Electronics Ph.D. degrees from Nanjing Normal University, Nanjing, China, in 2011, and 2014, respectively. Since 2014, he has been with Nanjing Normal University, where he is currently an Associate Professor. His research interests include integrated circuit electromagnetic compatibility testing, and electromagnetic compatibility design, etc.

Yang Zhao received his B.S., M.Sc., and Ph.D. degrees all in Power Electronic Technology from Nanjing University of Aeronautics and Astronautics, Nanjing, China, in 1989 and 1992, and 1995, respectively. Since 2002, he has been with Nanjing Normal University, where he is currently the Professor. His research interests are in the areas of Electromagnetic Compatibility, Power Electronics and Automotive Electronics.

A Dual-band Monopole Antenna with EBG for Wearable Wireless Body Area Networks

Chao Wang [1], Liang Zhang [2*], Shenbing Wu [1], Shijie Huang [1], Changqing Liu [1], and Xianliang Wu [1]

[1] Key Lab of Ministry of Education of Intelligent
Computing & Signal Processing, Anhui University, Hefei City, China
P18201026@stu.ahu.edu.cn, P18201031@stu.ahu.edu.cn, P18201028@stu.ahu.edu.cn,
P18201024@stu.ahu.edu.cn, xlwu@ahu.edu.cn

[2] AnHui Province Key Laboratory of Simulation and Design
Electronic Information System, Hefei Normal University, Hefei City, China
liangzh@hfnu.edu.cn

Abstract ─ This paper proposes a dual-band wearable monopole antenna adopting an electromagnetic band-gap (EBG) structure, which operates at 2.45 and 5.8 GHz ISM bands and is suitable for wearable applications. Both the monopole antenna and the EBG structure are fabricated on an F4B semi-flexible substrate having a dielectric constant of 2.2. The EBG structure effectively isolates the human body from the radiation of the antenna and reduces the specific absorption rate (SAR) of it by more than 97.5%. This improves the antenna gain and the peak gain reaches 9.1 dBi at 5.8 GHz. The wearable performance of the antenna showed that it can sustain good performance even under realistic human body loading. Besides, the antenna has a small size, which makes it ideal for wearable applications.

Index Terms ─ Dual-band, EBG structure, low SAR value, wearable antenna.

I. INTRODUCTION

In the last decade, wireless body area networks (WBAN) received significant attention from the researchers, and several applications, such as elderly/ child health monitoring, battlefield search and rescue, and wearable watches, aroused [1-2]. As one of the communication bands of the WBAN system, publicly available 2.40-2.48 and 5.725-5.875 GHz scientific, industrial, and medical (ISM) bands are assigned.

Wearable antennas for WBAN applications require placement on the human body, which necessitates body-related factors, such as bending deformation and high loss to be taken into account during the design process [3]. Furthermore, to avoid the potential impact of radiation on human health, the SAR value of antennas has to be minimized [4]. The literature has several designs of wearable antennas, where planar inverted F antennas [5], monopole antennas [6-8], and microstrip antennas [9-10] have been proposed for wearable applications to achieve reasonable bending robustness. However, due to their nearly omnidirectional radiation characteristics, a large amount of electromagnetic energy radiation penetrates the human body. Currently, isolating the radiation of the antenna to the human body and reducing the SAR value are challenging issues [11]. A common method is to introduce an EBG structure [12-19] into the wearable antenna design, thereby achieving the purpose of separating the antenna radiation from the human body, and greatly reducing the SAR value of the antenna. However, the use of EBG also brings other drawbacks, such as increment in the antenna size and narrower impedance bandwidth.

This paper proposes a dual-band monopole wearable antenna with an EBG structure. The wearable antenna has small size and high gain characteristics compared to the configurations in Table 4 reporting wearable applications, which are applied to WBAN covering two ISM bands: 2.40-2.48 GHz and 5.725-5.875 GHz. Among them, the 2.45 GHz impedance bandwidth is 3.70% (2.40-2.49 GHz), where the 5.8 GHz impedance bandwidth reaches 28.9% (4.85-6.49 GHz). The EBG structure can significantly reduce the SAR value of the monopole antenna by more than 97.5%. Besides, the monopole antenna combined with EBG can still maintain good performance during human loading. These characteristics make the antenna suitable for wearable applications.

II. ANTENNA AND EBG DESIGN

A. Antenna design

This paper proposes a dual-band wearable monopole

Submitted On: September 16, 2020
Accepted On: November 30, 2020

https://doi.org/10.47037/2020.ACES.J.360107

antenna with an EBG structure. The design dielectric constant of 2.2 and a loss tangent of 0.007. It is fed by a coplanar waveguide (CPW). Figure 1 (a) shows the structure parameters of the antenna. The antenna was simulated using the electromagnetic simulation software HFSS 2019. The final design values of the proposed antenna are as follows: W = 26, W_1 = 22.4, Ws = 10.85, L = 26, L_1 = 13.7, L_2 = 12.5, R = 5.5, Wf = 3.3, g = 0.5, Le = 22.57, L_m = 21.57, L_n = 13.07, d_1 = d_2 = 1.5, h = 7, Ls = 12, s = 2.25, ss = 0.5 (unit: mm).

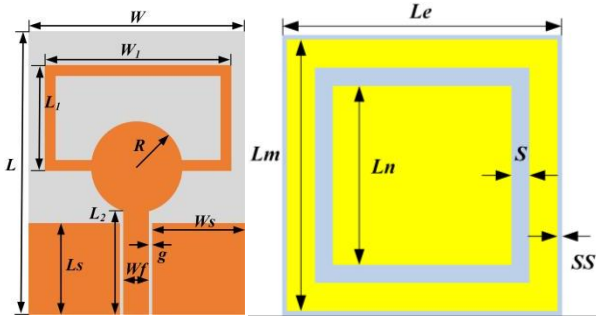

(a) (b)

Fig. 1. Configuration of (a) monopole antenna and (b) EBG unit.

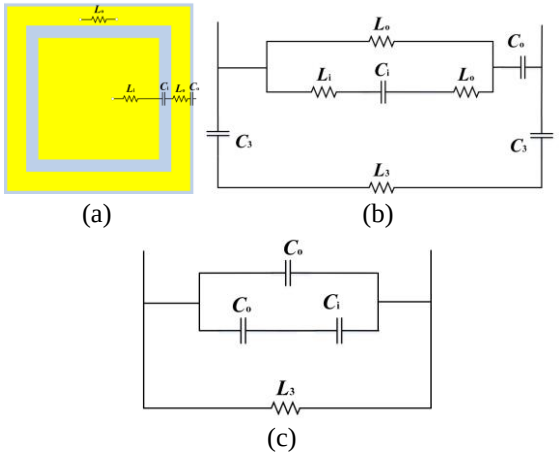

(a) (b) (c)

Fig. 2. Equivalent circuit of EBG: (a) equivalent capacitance and inductance, (b) equivalent circuit diagram, and (c) simplified equivalent circuit diagram.

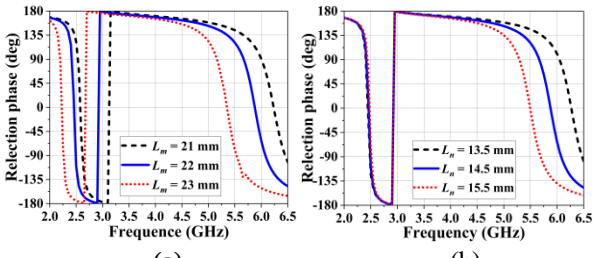

(a) (b)

Fig. 3. Influence of the EBG structure parameters on the reflection phase: (a) *Lo*; (b) *Li*.

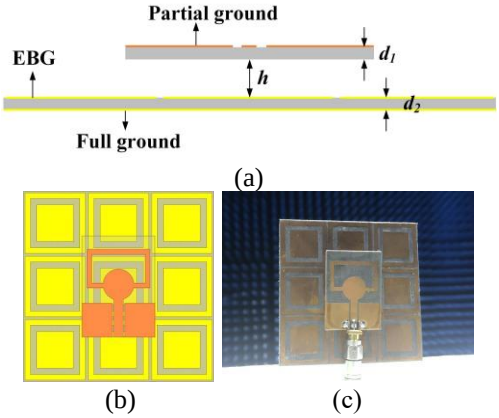

(a)

(b) (c)

Fig. 4. Configuration of the antenna with the EBG structure: (a) cross-sectional view, (b) top view, and (c) prototype measured.

B. EBG design

The high-impedance EBG structure is obtained by periodically arranging the metal patches on a dielectric substrate, where the patches can be of various shapes. As the frequency changes, the impedance of the EBG surface shows a $0 \rightarrow \infty \rightarrow 0$ behavior, which is $180° \rightarrow 0° \rightarrow -180°$ for the reflected phase. When the reflected phase θ is $\pm 180°$, the EBG surface impedance gets closer to 0, which is equivalent to the surface of a perfect electrical conductor (PEC). The phase of the reflected electromagnetic field is opposite to the phase of the incident electromagnetic wave. When the reflected phase θ is 0°, the surface impedance goes to infinite, and the phase of the reflected electromagnetic field is in-phase with the phase of the incident electromagnetic wave. At this time, the EBG surface exhibits an in-phase reflection. The frequency range of the $\pm 90°$ near the zero reflection phase belongs to the in-phase reflection area, while the other frequency ranges belong to the out-of-phase reflection area. Figure 1 (b) shows the geometry of the designed EBG unit. The frequency range of the reflected phase of the EBG unit $-90°$ to $+90°$, can be operated at 2.45 and 5.8 GHz ISM bands by adjusting the structural parameters.

Figures 2 (a) and (b) show the equivalent circuit diagram of the above-mentioned EBG structure to further explain its suppression effect on the surface waves. In these, C_o, C_i, and C_3 stand for the equivalent capacitances between the adjacent unit cells, the outer rectangular ring and the inner patch gap, and the top layer and the ground plane, respectively. Also, L_o and L_i respectively represent the equivalent inductance of the upper metal patch and the inner rectangular ring patch, where L_3 is the equivalent inductance of the ground plane

of the lower layer. Since the equivalent inductance of the upper surface of the EBG unit is much smaller than the equivalent capacitance, the series inductance-capacitance element can be equivalent to a single capacitance element. Furthermore, the capacitance C_3 can be ignored, and hence the equivalent circuit can be further simplified as shown in Fig. 2 (c). The surface impedance of the EBG can be expressed as:

$$Z = \frac{1}{j\omega C + \frac{1}{j\omega L_3}} = \frac{j\omega L_3}{1 - \omega^2 L_3 C}. \quad (1)$$

Then, the zero reflection phase point (θ = 0°) of the EBG is:

$$\omega = 2\pi f = \frac{1}{\sqrt{L_3 C}}. \quad (2)$$

Finally, the resonance frequency of the EBG is:

$$f = \frac{1}{2\pi\sqrt{L_3 C}}. \quad (3)$$

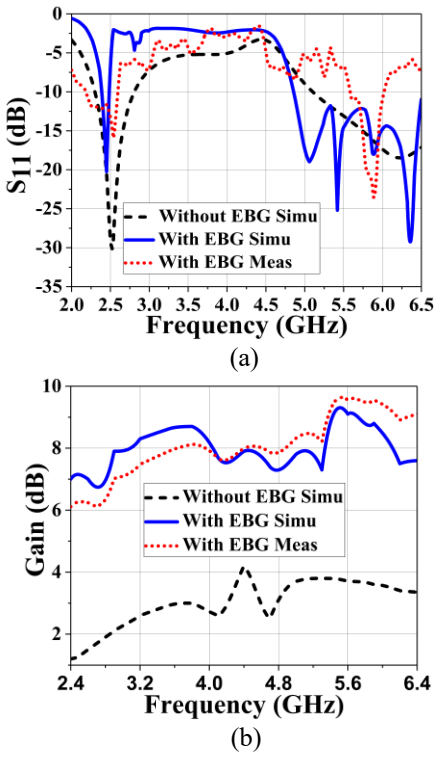

Fig. 5. Simulated performance of the antenna with and without the EBG structure and measured performance of the antenna with the EBG structure: (a) S11; (b) gain.

By incorporating (2) into (1), we can get: $Z \to \infty$, i.e., the surface impedance of the EBG goes to infinite. The EBG structure has two zero-phase reflection points: i) $C_L = C_o + C_i$ at the low frequency of 2.45 GHz, and ii) $C_H = C_o$ at the high frequency of 5.8 GHz. Hence, by designing the zero-phase point of the EBG near the resonant frequency of the antenna, the antenna performance can be improved.

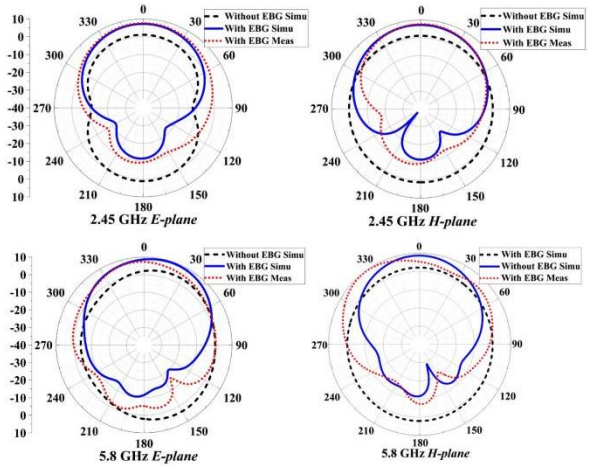

Fig. 6. The radiation pattern of the antenna in different frequency bands.

The outer and inner rectangles of the EBG unit determine the reflected phase resonance of the low and high frequencies, respectively. Here, adjusting the inner and outer rectangular parameters L_n and L_m can change the equivalent capacitances C_i and C_o. In this way, the resonance frequency of the EBG structure can be adjusted to work at 2.45 and 5.8 GHz. The effects of L_m and L_n on the reflection phase of the EBG structure are analyzed, and the results are shown in Fig. 3 (a) and Fig. 3 (b), respectively. The results indicated that L_m can control the resonance frequency of the low and high-frequency bands, and the EBG unit can be obtained to operate the isotropic reflection phase at 2.45 GHz by adjusting L_m. When L_n changes, only a large change occurs at high frequencies, where the 2.45 GHz band is almost unchanged, indicating that they have little influence on each other. Hence, by adjusting L_n, the EBG unit can obtain an isotropic reflection phase working at 5.8 GHz, thereby realizing the 2.45 and 5.8 GHz dual-band. The size of the final EBG structure is optimized to be 23 × 23 × 1.5 mm. Finally, the −90° to +90° reflection phase bandwidth of the EBG structure is 2.41-2.49 GHz and 5.66-6.07 GHz.

C. Antenna and EBG combination

Within the -90° to +90° reflection phase bandwidth of the EBG structure range, the reflected wave from the EBG will constructively interfere with the radiating wave in the free space. However, the practical array size needs to be determined since it is impossible to realize the simulated infinite array. Small size is generally desirable, however the resonating frequency of the microstrip antenna and EBG reflector changes, and the antenna does not operate adequately when the EBG array is too small. This is because the parasitic capacitance

between the antenna and the EBG array affects the performance of the whole structure [21]. Therefore, when determining the period of the EBG array, it is necessary to adjust the structural parameters of the EBG, the antenna, and the height between them to obtain the desired resonance point and achieve good impedance matching.

Table 1: Human tissue dielectric characteristics at 2.4 GHz [24]

Layer	Thickness	ε_r	Conductivity σ (S/m)
Skin	2	37.95	1.49
Fat	8	5.27	0.11
Muscle	23	52.67	1.77

Table 2: Human tissue dielectric characteristics at 5.8 GHz [24]

Layer	Thickness	ε_r	Conductivity σ (S/m)
Skin	2	35.14	3.717
Fat	8	4.955	0.29313
Muscle	23	48.49	4.9615

Figure 4 (a) illustrates the cross-sectional view of the antenna with the EBG structure, after the height adjustment, where the impedance matching is best when the antenna is placed 7 mm above the EBG. Figure 4 (b) shows the effect diagram after combination, where a 3×3 EBG array is selected considering the size of the EBG structure and the performance of the antenna with the EBG. When measuring the S_{11} and the radiation pattern, the gap between the antenna and the EBG is filled with foam to reduce losses and prevent any electrical contact, where Fig. 4 (c) depicts the measured prototype. Throughout the measures, the height of the foam and the position of the antenna were carefully measured to reduce the error. Subsequently, the S_{11} gathered by simulations and measurements are compared, and the results are given in Fig. 5 (a). It is observed that the antenna equipped with EBG has a bandwidth of 2.40-2.49 GHz in the low-frequency band, and 4.95-6.49 GHz in the high-frequency band, which can completely cover the 2.40-2.48 GHz and 5.725-5.875 GHz ISM bands. Figure 5 (b) compares the gain of the antenna with and without the EBG structure, which reveals that the EBG significantly increases the gain to a peak level of 9.1 dBi at 5.8 GHz. Finally, we observed that the simulations and the measurements are no big difference in antenna gain.

Figure 6 compares the simulated radiation patterns of the antenna with and without the EBG structure. Besides, the measured radiation patterns with the EBG structure is also compared. As shown, the radiation without the EBG is omnidirectional, i.e., a large number of electromagnetic signals will penetrate the human body. The addition of the EBG structure, however, enables the antenna to increase its front-to-back ratio (FBR) by 18.2 dB at 2.45 GHz and by 19.8 dB at 5.8 GHz. This makes the antenna unidirectional, significantly reducing the number of electromagnetic signals entering the human body. This phenomenon is highly desired in the design of wearable antennas. Figure 6 also shows that the simulated and measured radiation patterns are not quite different.

III. WEARABLE PERFORMANCE ANALYSIS

Due to the highly lossy characteristics of human tissue, the antenna performance is adversely affected when placed on the human body. As shown in Fig. 7, the antenna is placed on the arms, chest, and legs, and its reflection coefficient is measured by using a vector network analyzer. The results gathered are compared with the free space measurements. Figure 8 reveals that placing the antenna on the human body can achieve a good impedance matching, which allows 2.40-2.48 and 5.725-5.875 GHz ISM bands to be covered completely without effect on the antenna usage.

(a) (b) (c)

Fig. 7. The antenna with the EBG structure placed at different parts of a real human body: (a) arm; (b) chest; (c) leg.

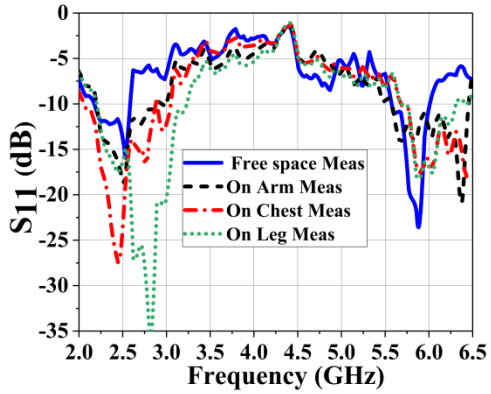

Fig. 8. Measured S_{11} of the antenna with the EBG on a real human body.

Table 3: SAR values of the antenna

With/Without EBG	1g/10g	Frequency (GHz)	Limit SAR (W/Kg)	Max SAR (W/Kg)	Input Power
Without EBG	1g	2.4	1.6	4.96	100mW
		5.8	1.6	10.9	100mW
	10g	2.4	2.0	2.6	100mW
		5.8	2.0	3.19	100mW
With EBG	1g	2.4	1.6	0.123	100mW
		5.8	1.6	0.212	100mW
	10g	2.4	2.0	0.0452	100mW
		5.8	2.0	0.0563	100mW

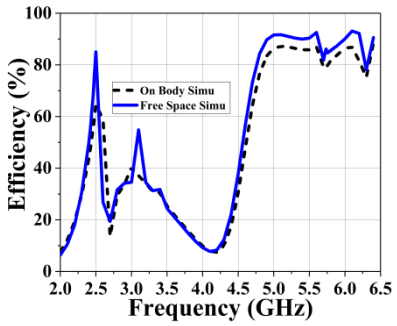

Fig. 9. Antennas simulate radiation efficiency on free space and human models.

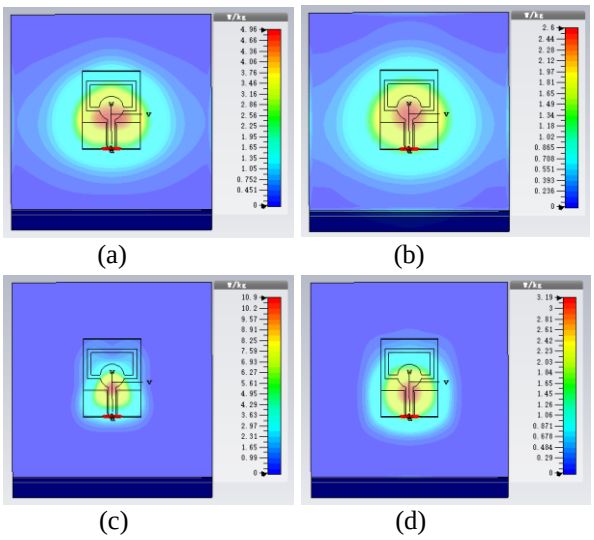

Fig. 10. Simulated SAR values for antennas without EBG. (a) 2.4 GHz, 1 g standard; (b) 2.4 GHz, 10 g standard; (c) 5.8 GHz, 1 g standard; (d) 5.8 GHz, 10 g standard.

In addition to the S_{11} analysis, the effect of the human tissue on radiation efficiency is also studied. Figure 9 shows the radiation efficiency of the antenna that is simulated for the free space and the human tissue model. The results reveal that the antenna achieves an efficiency of 64.6% at 2.45 GHz and 85.6% at 5.8 GHz without the human tissue model. When the human tissue model is added, the efficiency reduces to 53.2% at 2.45 GHz and 81.6% at 5.8 GHz.

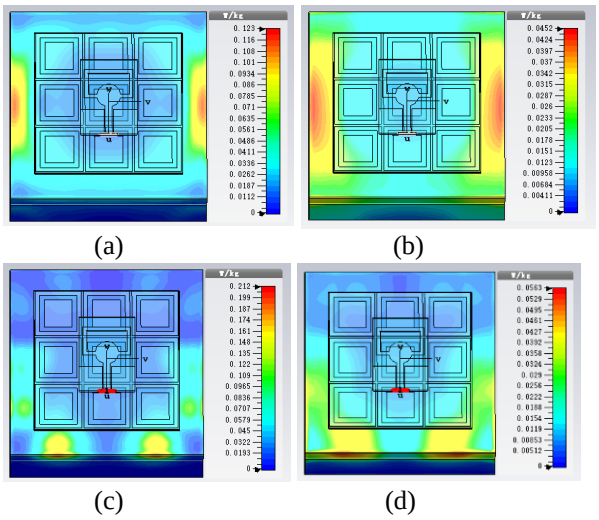

Fig. 11. Simulated SAR values for antennas with EBG. (a) 2.4 GHz, 1 g standard; (b) 2.4 GHz, 10 g standard; (c) 5.8 GHz, 1 g standard; (d) 5.8 GHz, 10 g standard.

The SAR value is crucial in understanding the effect of antenna radiation on the human body. There are two international SAR standards: one is the American standard, the other is the European standard. For the formed, enforced by the Federal Communications Commission (FCC), the threshold is 1.6 W / kg averaged over 1 g of tissue. For the latter, enforced by the International Electrotechnical Commission (IEC), the threshold is 2 W / kg averaged over 10 g of tissue [22-23]. Thus, the antennas for wearable applications must be carefully designed as complying with this regulation. To evaluate the SAR value of the antenna, a three-layer human tissue with a size of 90 × 90 × 33 mm was modeled in the CST Microwave Studio. In specific, skin, muscle, and fat tissues with a thickness of 2 mm, 8 mm, and 23 mm are used [24]. The dielectric characteristics of the

human tissue model at the frequencies of 2.4 GHz and 5.8 GHz are shown in Table 1 and Table 2, respectively. The antenna with and without the EBG structure was placed 2 mm above the human tissue for SAR analysis.

Table 4: Compare with paper on wearable antennas based on EBG or AMC

Ref.	Dimensions (mm^2)	Bandwith (GHz)	Peak Gain (dBi)	Size Comparison
[14]	200 × 200	2.45 (9.85%)	2.42	840.2%
[17]	147 × 147	2.45 (37.00%)	3.58	453.9%
		5.8 (5.04%)	6.08	
[16]	130.8 × 130.8	1.55 (1.84%)	5.1	359.3%
		2.45 (0.736%)	5.03	
[18]	124 × 124	2.45 (2.04%)	6.0	322.9%
[15]	100 × 100	3.65 (6.5%)	8.0	210.0%
		5.4 (6.5%)	8.0	
[12]	81 × 81	2.45 (14.7%)	7.3	137.8%
[19]	60 × 60	2.45 (18.4%)	6.5	75.6%
Work	69 × 69	2.45 (3.7%)	7.0	100%
		5.8 (28%)	9.1	

Figure 10 shows the SAR values of the antenna without the EBG structure. Under the 1 g standard, the SAR value of the antenna is 4.96 W / kg at 2.4 GHz and 10.9 W / kg at 5.8 GHz. For the 10 g standard, the values change to 2.6 W / kg at 2.4 GHz and 3.19 W / kg at 5.8 GHz. It should be noted that these values violate both American and European standards. Figure 11 shows the SAR values of the antenna with the EBG structure. Under the 1g standard, the SAR value reduces to 0.123 W / kg at 2.4 GHz and 0.212 W / kg at 5.8 GHz, which are respectively 97.5% and 98.1% lower than that of the antenna without the EBG structure. Under the 10g standard, the SAR value reduces to 0.0452 W / kg at 2.4 GHz and 0.0563 W / kg at 5.8 GHz, which are respectively 98.3% and 98.2% lower than that of the antenna without the EBG structure. As expected, these results validated that the EBG can reduce the SAR value of the monopole antenna. This is because the EBG changes the monopole antenna's radiation from omnidirectional to unidirectional, surpassing the surface electromagnetic waves to pass through the substrate, not the human body. Table 3, listing the SAR values studied in this paper, reveals that the antenna adopting the EBG has a very low SAR value, which complies with both American and European standards.

VI. CONCLUSION

In this paper, a dual-band wearable monopole antenna with a EBG structure was proposed. The antenna has small size and high gain characteristics compared to the Table 4 measure configurations reported for wearable applications. The proposed antenna has a working bandwidth of 2.40-2.49 GHz (3.70%) at 2.45 GHz a gain of 7.0 dBi. The bandwidth at 5.8 GHz rarely reaches to 4.85-6.50 GHz (28.9%), where the gain is approximately 9.1 dBi at 5.8 GHz. The EBG structure not only isolates the antenna from the human body but also improves the radiation gain compared to the monopole antennas without the EBG structure. More specifically, it increases the monopole antenna front-to-back ratio (FBR) by 18.2 dB (at 2.45 GHz) and 19.8 dB (at 5.8 GHz) and drops the SAR value more than 97.5%. Furthermore, it is shown that realistic human body loading have a small effect on antenna performance. Therefore, it is validated that the proposed antenna has a strong potential for wearable applications.

REFERENCES

[1] T. H. Nguyen, T. L. H. Nguyen, and T. P. Vuong, "A printed wearable dual band antenna for remote healthcare monitoring device," *2019 IEEE-RIVF International Conference on Computing and Communication Technologies (RIVF)*, 1-5, Danang, Vietnam, Mar. 2019.

[2] Y. Liao, M. S. Leeson, and M. D. Higgins, "A communication link analysis based on biological implant wireless body area networks." *Applied Computational Electromagnetics Society Journal*, pp. 619-628, June 2016.

[3] D. Ferreira, P. Pires, R. Rodrigues, and R. F. Caldeirinha, "Wearable textile antennas: Examining the effect of bending on their performance," *IEEE Antennas and Propagation Magazine*, vol. 59, no. 3, pp. 54-59, June 2017.

[4] M. I. Hossain, M. R. I. Faruque, and M. T. Islam, "A new design of cell phone body for the SAR reduction in the human head," *Applied Computational Electromagnetics Society Journal*,

pp. 792-798, July 2015.

[5] W. El Hajj, C. Person, and J. Wiart, "A novel investigation of a broadband integrated inverted-F antenna design application for wearable antenna," *IEEE Transactions on Antennas and Propagation*, vol. 62, no. 7, pp. 3843-3846, Apr. 2014.

[6] P. Saha, D. Mitra, and S. K. Parui, "A frequency and polarization agile disc monopole wearable antenna for medical applications," *Radioengineering*, pp. 74-80, Jan. 2020.

[7] M. R. Haraty, M. Naser-Moghadasi, A. A. Lotfi-Neyestanak, and A. Nikfarjam, "Transparent flexible antenna for uwb applications," *Applied Computational Electromagnetics Society Journal*, pp. 1426-1430, Dec. 2016.

[8] A. Kashkool, S. Yahya, H. Al-Rizzo, A. Al-Wahhamy, and A. A. Issac, "On the design and simulation of antennas on ultra-thin flexible substrates," *Applied Computational Electromagnetics Society Journal*, pp. 798-801, July 2018.

[9] Y. J. Li, Z. Y. Lu, and L. S. Yang, "CPW-fed slot antenna for medical wearable applications," *IEEE Access*, vol. 7, pp. 42107-42112, July 2019.

[10] Z. Hamouda, J. L. Wojkiewicz, A. A. Pud, L. Kone, S. Bergheul, and T. Lasri, "Flexible UWB organic antenna for wearable technologies application," *IET Microwaves, Antennas & Propagation*, vol. 12, no. 2, pp. 160-166, Dec. 2017.

[11] J. Trajkovikjand and A. K. Skrivervik, "Diminishing SAR for wearable UHF antennas," *IEEE Antennas and Wireless Propagation Letters*, vol. 14, pp. 1530-1533, Nov. 2014.

[12] G. P. Gao, B. Hu, S. F. Wang, and C. Yang, "Wearable circular ring slot antenna with EBG structure for wireless body area network," *IEEE Antennas and Wireless Propagation Letters*, vol. 17, no. 3, pp. 434-437, Jan. 2018.

[13] J. Wu and B. N. Li, "Development of a magneto inductive lens for magnetic resonance imaging," *IEEE Instrumentation and Measurement Magazine*, pp. 56-60, June 2017.

[14] H. Lago, P. J. Soh, M. F. Jamlos, N. Shohaimi, S. Yan, and G. A. Vandenbosch, "Textile antenna integrated with compact AMC and parasitic elements for WLAN/WBAN applications," *Applied Physics A*, vol. 122, no. 12, pp. 1059-1065, Nov. 2016.

[15] S. Karamzadeh and V. Rafiei, "Dual-band antenna modification by using dual bad EBG structure for WLAN/WiMAX applications," *Journal of Instrumentation*, 1-8, Apr. 2020.

[16] K. N. Paracha, S. K. A. Rahim, P. J. Soh, M. R. Kamarudin, K. G. Tan, Y. C. Lo, and M. T. Islam, "A low profile, dual-band, dual polarized antenna for indoor/outdoor wearable application," *IEEE Access*, vol. 7, pp. 33277-33288, Feb. 2019.

[17] M. N. Ramli, P. J. Soh, M. F. Jamlos, H. Lago, N. M. Aziz, and A. A. Al-Hadi, "Dual-band wearable fluidic antenna with metasurface embedded in a PDMS substrate," *Applied Physics A*, vol. 123, no. 2, pp. 149-156, Feb. 2017.

[18] A. Alemaryeen and S. Noghanian, "AMC integrated textile monopole antenna for wearable applications," *Applied Computational Electromagnetics Society Journal*, pp. 612-618, June 2016.

[19] G. Gao, S. Wang, R. Zhang, C. Yang, and B. Hu, "Flexible ebg-backed pifa based on conductive textile and pdms for wearable applications," *Microwave and Optical Technology Letters*, pp. 1733-1741, Apr. 2020.

[20] S. S. Bhatia and J. S. Sivia, "A novel design of circular monopole antenna for wireless applications," *Wireless Personal Communications: An International Journal*, pp. 1153-1161, Dec. 2016.

[21] S. Kim, Y. J. Ren, H. Lee, A. Rida, S. Nikolaou, and M. M. Tentzeris, "Monopole antenna with inkjet-printed ebg array on paper substrate for wearable applications," *IEEE Antennas and Wireless Propagation Letters*, pp. 663-666, Nov. 2012.

[22] H. M. Madjar, "Human radio frequency exposure limits: An update of reference levels in Europe, USA, Canada, China, Japan and Korea," *International Symposium on Electromagnetic Compatibility*, pp. 467-473, Nov. 2016.

[23] M. A. B. Mazady, G. Schmid, R. Uberbacher, and M. Ali, "SAR induced by low and high directivity antenna apertures at distances greater than 25 mm from the body," *Applied Computational Electromagnetics Society Journal*, vol. 30, no. 9, pp. 940-951, Sep. 2015.

[24] M. A. Stuchly and S. S. Stuchly, "Dielectric properties of biological substances-tabulated," *Journal of Microwave Power*, vol. 15, no. 1, pp. 19-25, Jan. 1980.

Compact ACS-Fed UWB MIMO Antenna with Dual Band Notches

Qin Li, Yufa Sun, and Hongyu Fang

School of Electronics and Information Engineering
Anhui University, HeFei, 230601, China
2602046423@qq.com, yfsun_ahu@sina.com, hy966969@163.com

Abstract ─ In order to improve the channel capacity of communication equipment and reduce the size of antenna, an asymmetric coplanar strip (ACS) fed four-element UWB MIMO antenna with dual band notches is proposed in this paper. The antenna has a simple structure and a compact size of 37×37 mm². The antenna consists of four modifled staircase-shaped radiation elements and four floor on the same side. The antenna elements are placed vertically without additional decoupling structure, and the isolation less than -15 dB in the working bandwidth of 2.9-10.6 GHz can be obtained by using polarization diversity. In addition, the antenna has the notched characteristic of WiMAX and WLAN band. The antenna has good gain and low envelop correlation coefficient (ECC), and the simulation results agree with the measured results, which indicates that the antenna is suitable for UWB system.

Index Terms ─ ACS, band notches, MIMO antenna, polarization diversity, UWB.

I. INTRODUCTION

Ultra wide band (UWB) technology is widely used in many fields of wireless communication due to its inherent advantages such as high transmission rate, strong confidentiality, low cost and low power consumption. However, the power spectral density of UWB system is very low and the problem of signal fading is more prominent under the influence of multipath effect. Multiple Input Multiple Output (MIMO) technology can greatly improve the efficiency of spectrum and realize large capacity and high rate in the limited spectrum resources. The combination of UWB and MIMO technology can perfectly solve the multipath fading problem to improve the communication quality. Meanwhile, the range of UWB includes narrowband systems such as WiMAX (3.3-3.8 GHz) and WLAN (5.15-5.825 GHz). Therefore, it is particularly important to solve the interference between UWB and some narrowband system.

The combination of UWB and MIMO technology has been paid more and more attention by researchers and achieved considerable development. For UWB MIMO system, how to maintain acceptable isolation between antenna elements on the basis of ensuring that the antenna has simple structure and compact size is a challenging task. References [1, 2] introduce the fence-type decoupling structure at the ground to enhance the isolation in operating band. Referencess [3-5] design the T-shaped decoupling structure by extending the branches on the ground, adding parasitic units and slotting on the ground, respectively. The inherent directional radiation of slot antenna and asymmetrical placement are used to obtain high isolation in [6]. The vertical placement of the antenna elements is used in [7-9] to reduce coupling, which is a common way for MIMO antennas to obtain high isolation. The neutralization line is implemented to minimize the mutual coupling between the radiation patches in [10]. Defected Ground Structures (DGS) and structures inspired from Frequency Selective Surfaces (FSS) are used to enhance the isolation in [11]. Polarization diversity among different kinds of antennas can realize lower coupling between antenna elements, and by using a couple of inverted L-shaped stubs and an inverted Z-shaped stub as decoupling structures can obtain a high isolation in [12]. Reference [13] shows that by cutting the antenna element in half, the mutual coupling can be significantly reduced due to the inherent symmetry of the antenna element. By etching two L-shaped slots in the radiators and attaching a rectangular patch on the back, the isolation is enhanced in [14]. In addition, for the realization of notched characteristic, C-shaped [4, 15-17], L-shaped [9] structures are mostly introduced on ground or radiation patch. However, these proposed antennas rarely take into account compact size, simple structure, high isolation and notched characteristic at the same time.

This paper proposes a compact UWB MIMO antenna with dual band notches. The antenna structure is simple, and the different elements are placed vertically. With the use of polarization diversity, less than -15 dB isolation can be achieved in the whole UWB range without additional decoupling structure. The introduction of L-shaped parasitic elements makes the antenna realize notched characteristic in WiMAX band. In addition, the

Submitted On: August 19, 2020
Accepted On: November 30, 2020
https://doi.org/10.47037/2020.ACES.J.360108

interference of WLAN band is suppressed by the slot on the floor consisting of a C-shaped and two L-shaped structures. (We abbreviate it as LCL-shaped)

II. ANTENNA DESGIN

A. Design of UWB MIMO antenna element

Antenna 1 shown in Fig. 1 (a) is a planar monopole antenna with regular rectangular radiation patch, which is printed on the FR4 substrate with thickness of 1.6 mm and size of 22×22 mm². As shown in Fig. 1 (b), the radiation patch of antenna 1 is improved into a stepped structure to form antenna 2. This progressive form increases the uniform distribution of surface current and improves the stability of input impedance, so it greatly increases the working bandwidth of the antenna element. Impedance matching can be further improved by adjusting the width of the center conductor connecting the radiation patch. Figure 2 shows the simulated S_{11} of antenna 1 and 2. According to the figure, the bandwidth of the antenna 2 can cover the whole UWB range.

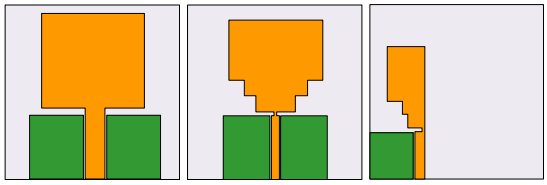

(a) Antenna 1 (b) Antenna 2 (c) Antenna 3

Fig. 1. Design of UWB MIMO antenna element.

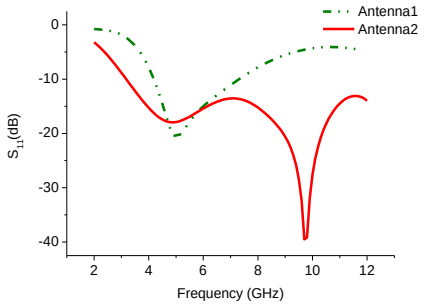

Fig. 2. Simulated S_{11} of antenna 1 and 2.

To further reduce the antenna size, we use the feeding method of an ACS to cut the antenna 2 in half to form antenna 3 and optimize the parameters, as shown in Fig. 1 (c).

B. Design of UWB MIMO antenna

In the previous section, the design of the UWB antenna element was preliminarily completed. In this section, we mainly introduce the integrated design of four-element UWB MIMO antenna. Four elements that are identical to antenna 3 are integrated to form antenna 4 as shown in Fig. 3. In antenna 4, four ports are placed orthogonally to each other to improve the isolation through polarization diversity. Figure 4 shows the simulated S_{11} of antenna 3 and 4. According to the figure, S_{11} does not change much after the antenna is integrated.

Further, we show the isolation between antenna elements. According to the principle of reciprocity, we only demonstrate the isolation between antenna elements in adjacent (S_{12}) and diagonal (S_{13}) positions in Fig. 5. In the integrated antenna, we do not need to use an additional decoupling structure, only using polarization diversity can achieve isolation requirements.

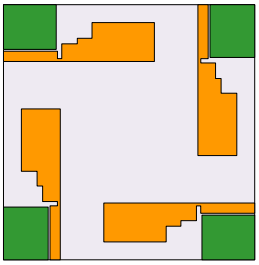

Fig. 3. Antenna 4 integrated by four antenna 3.

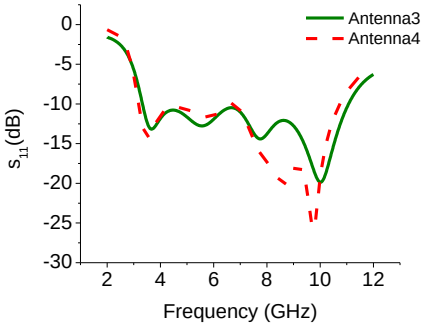

Fig. 4. Simulated S_{11} of antenna 3 and 4.

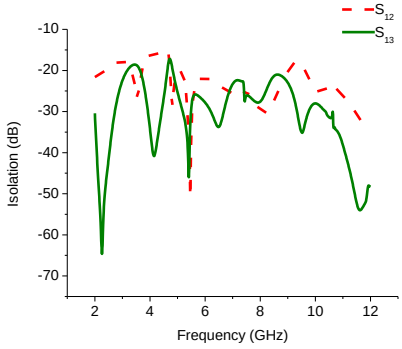

Fig. 5. Simulated isolation of the MIMO antenna.

C. Design of dual-notched UWB MIMO antenna

In order to suppress the interference of WiMAX band, an inverted L-shaped parasitic unit is added on the

top of the four radiation patches respectively. The initial length L of the parasitic unit can be obtained by Eq. (1) [9]. Here f_{notch} is center frequency of the notch-band, c is the speed of light in free space, and ε_r is the relative dielectric constant:

$$L = \frac{c}{2f_{notch}\sqrt{\varepsilon_r}}. \quad (1)$$

The UWB MIMO antenna with WiMAX band-rejection and its simulated S_{11} are shown in Fig. 6. From Fig. 6, we can see that the simulated S_{11} is less than -10 dB from 2.9 to 10.6 GHz except for the rejected band of WiMAX.

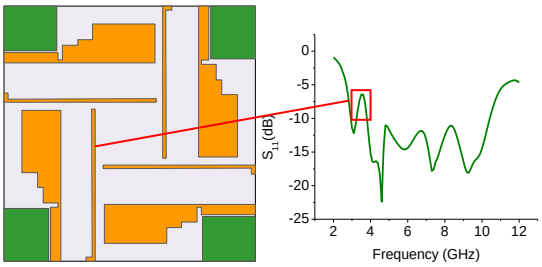

Fig. 6. UWB MIMO antenna with WiMAX band-rejection and its simulated S_{11}.

To further suppress the interference of WLAN band, we designed a LCL-shaped slot on the ground, which is a combination of one C-shaped and two L-shaped structure. The length of the LCL-shaped slot is optimized according to Eq. (1).

The final four-element UWB MIMO antenna with dual-notched is shown in Fig. 7 (a), and the relevant dimensions are shown in Fig. 7 (b). The simulated S_{11} of the proposed antenna is shown in Fig. 8. As can be seen from Fig. 8, the proposed UWB MIMO antenna can achieve a working bandwidth of 2.9-10.6 GHz under the return loss of -10 dB except for the rejected bands of WiMAX and WLAN. The notch frequency band realized by the L-shaped parasitic unit and the LCL-shaped slot is 3.32-3.79 GHz and 5.17-5.77 GHz, respectively.

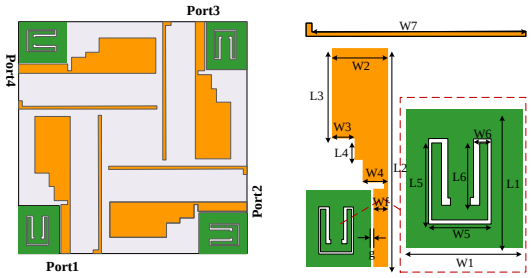

(a) Proposed MIMO antenna (b) Size

Fig. 7. Four-element UWB MIMO antenna with dual-notched.

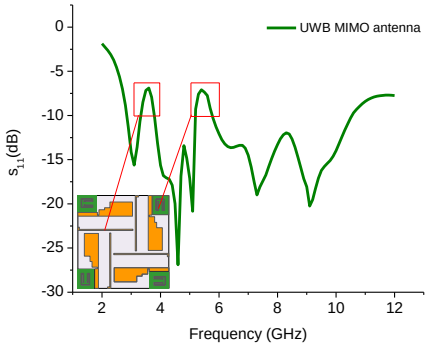

Fig. 8. Simulated S_{11} of proposed MIMO antenna.

The total size of proposed UWB MIMO antenna with dual band notches is 37×37 mm², and the detailed dimensions are shown in Table 1.

Table 1: Dimensions of the proposed antenna

Parameters	L1	L2	L3	L4	L5
Value/mm	6.9	21.8	9.2	2.3	3.7
Parameters	L6	W1	W2	W3	W4
Value/mm	3.1	6.4	5.5	2	2.5
Parameters	W5	W6	W7	Wf	g
Value/mm	3.2	0.8	21.7	1.5	0.2

III. RESULTS AND DISCUSSION

The UWB MIMO antenna proposed in this paper is simulated and optimized by HFSS 15. In order to further verify the practical value and the reliability of the method, the proposed antenna is fabricated based on the size given in Table 1. Figure 9 shows the picture of the fabricated MIMO antenna. By using the vector network analyzer, we measured the S-parameters of the antenna. The radiation pattern and gain of the antenna are also tested in a microwave anechoic chamber.

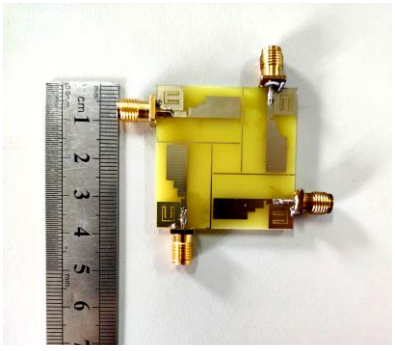

Fig. 9. Photograph of the fabricated MIMO antenna.

A. S parameter

Figure 10 shows the simulated and measured S_{11} of

the proposed antenna, it can be seen from the figure that the working bandwidth of the measured antenna is 2.9-10.6 GHz except for WiMAX and WLAN notched bands, which is basically consistent with the simulation results.

The simulated and measured isolations are shown in Fig. 11. From the figure we can see that the measured isolation between antenna elements is less than -15 dB. The deviation between the test and simulation results is acceptable.

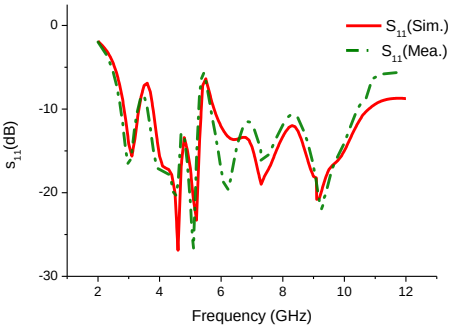

Fig. 10. Simulated and measured S_{11}.

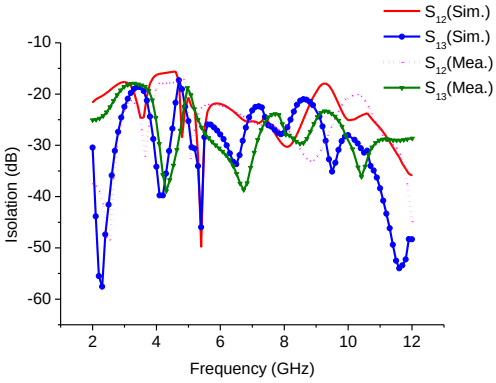

Fig. 11. Simulated and measured isolation.

B. Notch characteristics

To verify the notch characteristics of the UWB MIMO antenna, we analyzed the surface current distributions of the MIMO antenna at 3.5 GHz and 5.5 GHz, as shown in Fig. 12. When the MIMO antenna is working at 3.5 GHz, most of the surface current is concentrated on the L-shaped structure, and the notch band realized at 3.32-3.79 GHz can effectively suppresses interference in the WiMAX band. When the MIMO antenna is working at 5.5 GHz, most of the surface current is concentrated on the LCL-shaped slot, and the notch band realized at 5.17-5.77 GHz can effectively suppresses interference in the WLAN band.

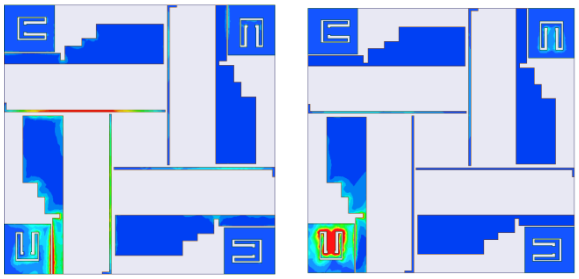

(a) 3.5 GHz (b) 5.5 GHz

Fig. 12. Surface current distributions at (a) 3.5 GHz and (b) 5.5 GHz.

C. Radiation pattern and gain

Figure 13 shows the measured and simulated 2D radiation patterns of proposed MIMO antenna at 4.5, 7.5 and 9.5 GHz. The radiation patterns are measured when the target antenna element is excited and other three antenna elements are terminated with the 50 Ω load. It can be noted from the figure that the simulated and measured results are well matched, and the overall radiation pattern is relatively stable over the entire UWB bandwidth.

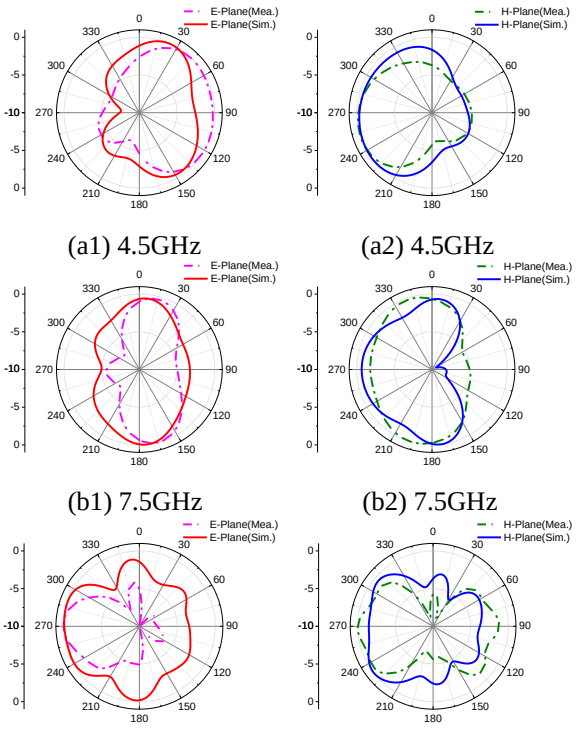

(a1) 4.5GHz (a2) 4.5GHz

(b1) 7.5GHz (b2) 7.5GHz

(c1) 9.5GHz (c2) 9.5GHz

Fig. 13. Simulated and measured radiation patterns at 4.5 GHz, 7.5 GHz and 9.5 GHz.

The isolation mechanism can be better understood by the diversity of radiation pattern when different ports are excited. Figure 14 shows the simulated three-dimensional radiation patterns of the proposed UWB MIMO antenna when port 1 to 4 are separately excited and other ports are terminated with matched loads. The four ports are placed vertically and rotated 90° counterclockwise, so that the radiated field appears rotated 90° in the xy plane, and the pattern diversity is obtained.

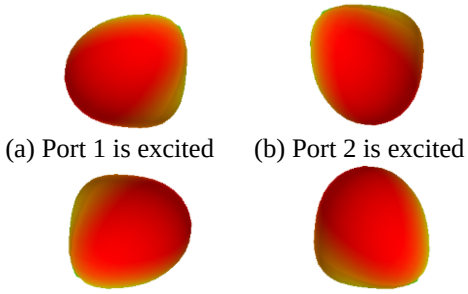

(a) Port 1 is excited (b) Port 2 is excited

(c) Port 3 is excited (d) Port 4 is excited

Fig. 14. Simulated 3D radiation patterns of the proposed antenna.

The simulated and measured gains of the proposed UWB MIMO antenna are shown in Fig. 15. From the figure we can see that the gain of proposed antenna is relatively stable and its measured value varies from 0 to 6 dBi within the UWB band except two notched-bands, which indicates that this antenna has good gain characteristic.

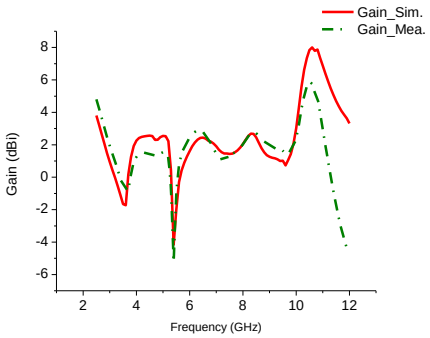

Fig. 15. Simulated and measured gains.

D. Diversity analysis

The diversity characteristic of the proposed antenna can be evaluated by ECC, which represents the correlation of received signals between antenna elements. Generally, low ECC always leads to high diversity gain. For N-element MIMO antenna, the ECC of antenna element *i* and antenna element *j* can be calculated by Eq. (2) [15]:

$$\mathrm{ECC} = \frac{\left|\sum_{n=1}^{N} S_{i,n}{}^{*} S_{n,j}\right|^{2}}{\prod_{k=(i,j)}\left[1-\sum_{n=1}^{N} S_{i,n}{}^{*} S_{n,k}\right]}. \quad (2)$$

The results of ECC are shown in Fig. 16. It can be seen from the figure that the ECC of the proposed antenna is less than 0.02 expect the notch-bands, which indicates the MIMO antenna has a good diversity characteristic.

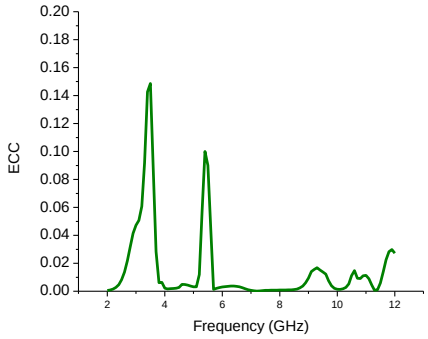

Fig. 16. ECC of the proposed MIMO antenna.

Finally, the comparisons of the recently published four-element UWB MIMO antennas in [8, 9, 11-15, 17, 18] and the proposed antenna in this paper are listed in Table 2. By comparison, it can be concluded that the UWB MIMO antenna proposed in this paper has a simpler structure and a more compact size in addition to satisfying the requirement of UWB. On the premise of compact size, the antenna can satisfy the isolation of -15 dB without decoupling structure. In addition, the antenna also realizes the characteristic of dual-notched.

IV. CONCLUSION

In this paper, a compact UWB MIMO antenna fed by ACS is proposed. The four ports of the antenna are placed vertically, and the isolation less than -15 dB is obtained by using the polarization diversity in the whole UWB range. The L-shaped parasitic unit realizes the notched characteristic in WiMAX band. In addition, the LCL-shaped slot on the ground realizes the suppression of WLAN band. The simulation results show that the antenna has good characteristic, and the measured results agree well with the simulated results, which indicates that the proposed antenna is suitable for UWB applications.

ACKNOWLEDGMENT

This work was supported in part by the National Natural Science Foundation of China under Grant 62071004 and the Project of Anhui Local High-level University Construction Under Grand 2013gx001.

Table 2: Comparisons of published four-element UWB MIMO antennas and the proposed antenna

Designs	Size (mm^2)	Band (GHz)	Isolation (dB)	Notched Band	Gain (dBi)	ECC (Except Notches)	Decoupling Structure
[8]	50×39	2.7-12	-17	1	2.5-6	/	/
[9]	81×81	3.03-10.74	-20	2	0-9	0.025	/
[11]	58×79	3-11	-15	0	/	/	yes
[12]	70×41	3.1-12	-17	0	1-4	0.012	yes
[13]	70×70	2-14	-15	0	2-6	0.007	/
[14]	36×36	3.1-10.6	-15	0	1.5-3.7	0.02	yes
[15]	73×73	3-18	-20	2	/	0.0015	/
[17]	45×45	2-10.6	-17	1	2-5	0.01	yes
[18]	40×40	2.94-14	-17	0	1-5	0.03	/
Proposed	37×37	2.9-10.6	-15	2	0-6	0.02	/

REFERENCES

[1] L. L. Wang, Z. H. Du, H. L. Yang, R. Y. Ma, Y. C. Zhao, X. Q. Cui, and X. L. Xi, "Compact UWB MIMO antenna with high isolation using fence-type decoupling structure," *IEEE Antennas and Wireless Propagation Letters*, vol. 18, no. 8, pp. 1641-1645, 2019.

[2] H. Qin and Y. F. Liu, "Compact UWB MIMO antenna with ACS-fed structure," *Progress in Electromagnetics Research C*, vol. 50, pp. 29-37, May 2014.

[3] R. Chandel, A. K. Gautam, and K. Rambabu, "Design and packaging of an eye-shaped multiple-input-multiple-output antenna with high isolation for wireless UWB applications," *IEEE Transactions on Components, Packaging and Manufacturing Technology*, vol. 8, no. 4, pp. 635-642, Apr. 2018.

[4] A. Bhattacharya, B. Roy, R. F. S. Caldeirinha, and A. K. Bhattacharjee, "Low-profile, extremely wideband, dual-band-notched MIMO antenna for UWB applications," *International Journal of Microwave and Wireless Technologies*, vol. 11, no. 7, pp. 719-728, Feb. 2019.

[5] C. M. Luo, J. S. Hong, and L. L. Zhong, "Isolation enhancement of a very compact UWB-MIMO slot antenna with two defected ground structures," *IEEE Antennas and Wireless Propagation Letters*, vol. 14, pp. 1766-1769, 2015.

[6] G. Srivastava and A. Mohan, "Compact MIMO slot antenna for UWB applications," *IEEE Antennas and Wirel. Propaga. Lett.*, vol. 15, pp. 1057-1060, 2016.

[7] A. A. Ibrahim, J. Machac, and R. M. Shubair, "UWB MIMO antenna for high speed wireless applications," *Applied Computational Electromagnetics Society Journal*, vol. 34, no. 9, pp. 1294-1299, Feb. 2019.

[8] M. S. Khan, A. D. Capobianco, S. Asif, A. Iftikhar, B. Ijaz, and B. D. Braaten, "Compact 4×4 UWB-MIMO antenna with WLAN band rejected operation," *Electronics Letters*, vol. 51, no. 14, pp. 1048-1050, July 2015.

[9] K. Srivastava, A. Kumar, B. K. Kanaujia, S. Dwari, and S. Kumar, "A CPW-fed UWB MIMO antenna with integrated GSM band and dual band notches," *Inter. Journal of RF and Microwave Computer-Aided Engineering*, vol. 29, no. 1, May 2019.

[10] R. N. Tiwari, P. Singh, and B. K. Kanaujia, "A compact UWB MIMO antenna with neutralization line for WLAN/ISM/mobile applications," *International Journal of RF and Microwave Computer-Aided Engineering*, vol. 29, no. 11, July 2019.

[11] T. Shabbir, R. Saleem, A. Akram, and F. Shafique, "UWB-MIMO quadruple with FSS-inspired decoupling structures and defected grounds," *Applied Computational Electromagnetics Society Journal*, vol. 30, no. 2, pp. 184-190, Oct. 2015.

[12] L. S. Yang, M. Xu, and C. Li. "Four-element MIMO antenna system for UWB applications," *Radio-engineering*, vol. 28, no. 1, pp. 60-67, Apr. 2019.

[13] A. A. R. Saad, "Approach for improving inter-element isolation of orthogonally polarised MIMO slot antenna over ultra-wide bandwidth," *Electronics Letters*, vol. 54, no. 18, pp. 1062-1064, May 2018.

[14] Z. Y. Zhang, F. Zhang, and W. P Tian, "Compact 4-port ACS-fed UWB-MIMO antenna with shared radiators," *Progress in Electromagnetics Research Letters*, vol. 55, pp. 81-88, Aug. 2015.

[15] A. S. Eltrass and N. A. Elborae, "New design of UWB-MIMO antenna with enhanced isolation and dual-band rejection for WiMAX and WLAN systems," *IET Microwaves, Antennas & Propagation*, vol. 13, no. 5, pp. 683-691, Feb. 2019.

[16] Z. Y. Li, C. Y. Yin, and X. S. Zhu, "Compact UWB MIMO Vivaldi antenna with dual band-notched characteristics," *IEEE Access*, vol. 7, pp. 38696-38701, Apr. 2019.

[17] S. Tripathi, A. Mohan, and S. Yadav, "A compact Koch fractal UWB MIMO antenna with WLAN band-rejection," *IEEE Antennas and Wireless Propagation Letters*, vol. 14, pp. 1565-1568, 2015.

[18] A. A. R. Saad and H. A. Mohamed, "Conceptual design of a compact four-element UWB MIMO slot antenna array," *IET Microwaves, Antennas & Propagation*, vol. 13, no. 2, pp. 208-215, Jan. 2019.

Isolation Enhancement between Ports of a Compact Ultra-wideband MIMO Antenna

Yantao Yu, Shenshen Mao, Meng Li, and Danting He

School of Microelectronics and Communication Engineering, Chongqing University, Chongqing, 400044, China
yantaoyu@cqu.edu.cn

Abstract ─ In this paper, a novel compact multiple-input multiple-output (MIMO) antenna with enhanced port isolation is proposed for ultra-wideband (UWB) applications. The UWB MIMO antenna contains two coplanar annular monopoles etched on the front side of the FR-4 substrate. The dielectric substrate has a relative permittivity of 4.4 and a size of 80 mm × 40 mm × 1.6 mm. The irregular ground is printed on the back side of the substrate. In order to enhance the port isolation between the two monopoles, the expanded ground is exploited in the proposed design. In addition, the ground is etched with some slots to achieve good impedance matching. Both the simulated and measured results show that the proposed antenna achieves good impedance matching as well as high port isolation over the entire UWB band. Moreover, the proposed antenna has good spatial diversity characteristics. In summary, the proposed UWB MIMO antenna can be well applied to the ultra-wideband wireless communication system.

Index Terms ─ Isolation, monopole antenna, multi-input multi-output, ultra-wideband.

I. INTRODUCTION

Compared to the traditional narrowband communications, the ultra-wideband (UWB) multiple-input multiple-output (MIMO) communication has many advantages such as high speed, large capacity and high spectrum utilization. However, there are many challenges in designing the UWB MIMO antennas, mainly the problems of impedance matching and mutual coupling reduction over the entire UWB band [1]. Some useful methods have been proposed to enhance the isolation between the elements of the MIMO antennas. One method is optimizing the layout of the antenna elements and making use of the polarization characteristics of the antennas to reduce the mutual coupling [2-6]. In [2], the MIMO slot antenna without any decoupling structure achieves a high isolation by placing the four antenna elements asymmetrically. Isolation can be improved by introducing a parasitic resonant structure to between the antenna elements. For example, a metal strip reflector was used to isolate the two array elements in [7-10]. In addition, the defective ground structures (DGS) are also very frequently used in improving the port isolation of the antennas [11-14]. In [11], the isolation between the two antenna elements is improved by adding a slot on the ground. Furthermore, other metheds including loading a ground branch are also effective to suppress the mutual coupling and enhance the port isolation between the array elements [15-22].

In this paper, a novel compact UWB MIMO antenna is proposed. Two coplanar annular monopole UWB antennas are placed side by side. The port isolation is improved by expanding the ground plane. Both the simulated and measured results show that the isolation between the array elements has been effectively increased over the entire UWB band. The details of the proposed design and the results are presented in the following sections.

II. ANTENNA DESIGN AND ANALYSIS

The geometry of the proposed UWB MIMO antenna is illustrated in Fig. 1. The FR4 substrate is used in the design of the antenna, which has a relative permittivity of 4.4 and a thickness of 1.6 mm. Two coplanar annular monopole antennas are printed side by side on the front side of the substrate, while the ground is on its back side. The proposed antenna has a width of W = 80 mm and a length of L = 40 mm. The microstrip line with a width of W_1 = 3 mm is used to feed each element. In order to increase the port isolation between the two antenna elements, the ground plane is expanded outwards at the middle portion, as shown in Fig. 1. The antenna achieves a good impedance matching by slotting the extended ground and the portion of the ground below the microstrip feed line.

The proposed UWB MIMO antenna is simulated and optimized by using ANSYS HFSS, and the optimized dimensions of the antenna are shown in Table 1. The simulated *S*-parameters of the proposed antenna are shown in Fig. 2. Due to the symmetry of the antenna structure, only the curves of the S_{11} and S_{12} are plotted in the figure. From the figure, we can see that the S_{11} is lower than -10 dB in the range of 2.13

Submitted On: July 31, 2020
Accepted On: December 6, 2020
https://doi.org/10.47037/2020.ACES.J.360109

GHz to 11.03 GHz covering the entire UWB band, which indicates that the proposed MIMO antenna has been well matched. In addition, the S_{12} is almost lower than -20 dB, which means that the port isolation between the two elements is kept at a high level.

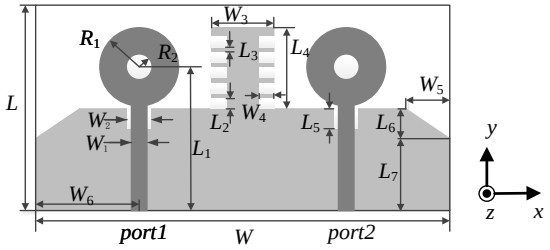

Fig. 1. Geometry of the proposed UWB MIMO antenna.

Table 1: Optimized dimensions of the antenna (unit: mm)

Parameter	Value	Parameter	Value
W_2	4	L_1	28
W_3	12	L_2	2
W_4	3	L_3	1
W_5	8.5	L_4	16.2
W_6	20	L_5	4.3
R_1	7.6	L_6	5.8
R_2	2.5	L_7	14

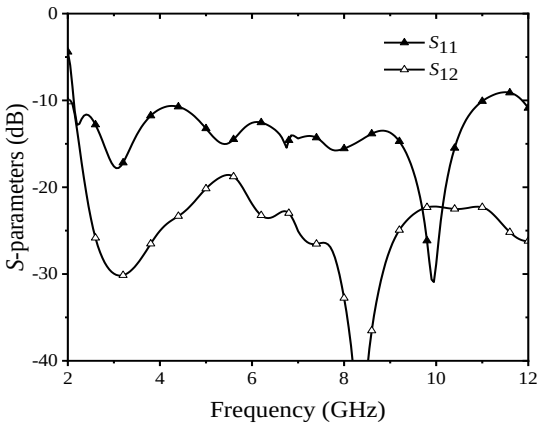

Fig. 2. Simulated *S*-parameters of the proposed UWB MIMO antenna.

Figure 3 shows the design process of the proposed UWB MIMO antenna. The *S*-parameters of the three antennas are compared in Fig. 4. As can be seen from the figure, for the initial design, antenna 1, the value of S_{12} is mainly between -10 dB and -20 dB in the UWB operating band, which indicates that the two elements are not highly isolated. In the antenna 2, the ground is expanded outward with a rectangular shape between the elements, thus making S_{12} below -20 dB. And this result is a solid evidence for effective isolation enhancement. However, as is shown, with the expanded ground, the S_{11} of the antenna 2 is higher than -10 dB from about 4 GHz to 7 GHz, which means that expending the ground plane has a negative impact on the impedance matching and makes it worse. In order to achieve a good impedance matching again, as shown in the antenna 3, we etch slots on certain part of the ground. The slots are etched not only behind the feedlines but also within the rectangular shape expanded. The number of the slots within the expanded ground is the result of optimization. From Fig. 4, we can observe that in the UWB band, the S_{11} of the antenna 3 is lower than -10 dB, and the S_{12} is almost kept lower than -20 dB. It indicates that the antenna 3 achieves both good impedance matching and high port isolation.

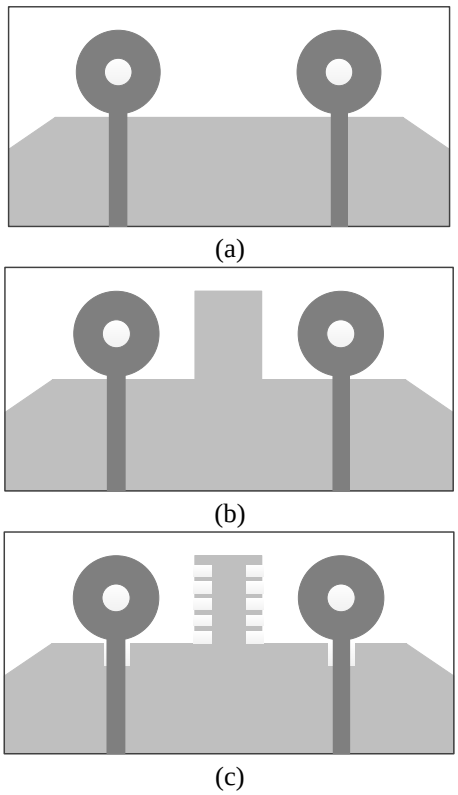

Fig. 3. Design process of the proposed antenna: (a) antenna 1, (b) antenna 2, and (c) antenna 3.

When the antenna elements are placed closely to each other, adding an excitation to one of the antenna ports will generate an induced current at the other port, which is the cause of the strong mutual coupling. Therefore, in order to reduce the coupling and enhance the isolation, it is necessary to suppress the generation of the induced current. This is the purpose of expanding the ground. The surface current distribution of the antenna 1 and the antenna 3 at the different frequencies

are shown in Fig. 5, respectively. From the figure, it can be seen that when the excitation is added to the port 1 without the expanded ground, an obviously large induced current is generated nearby the port 2. Thus, there is a strong coupling between the two antenna elements. Expanding the ground plane, on the contrary, makes the induced current mainly distributed around the extended part of the ground and weak around the port 2. Therefore, the coupling between the antenna elements is effectively reduced and the port isolation is enhanced.

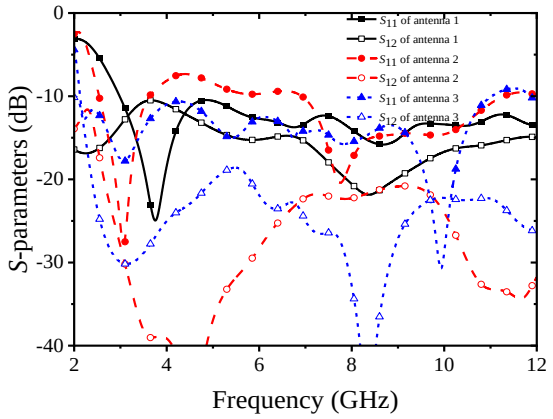

Fig. 4. The simulated *S*-parameters of the two-element monopole array.

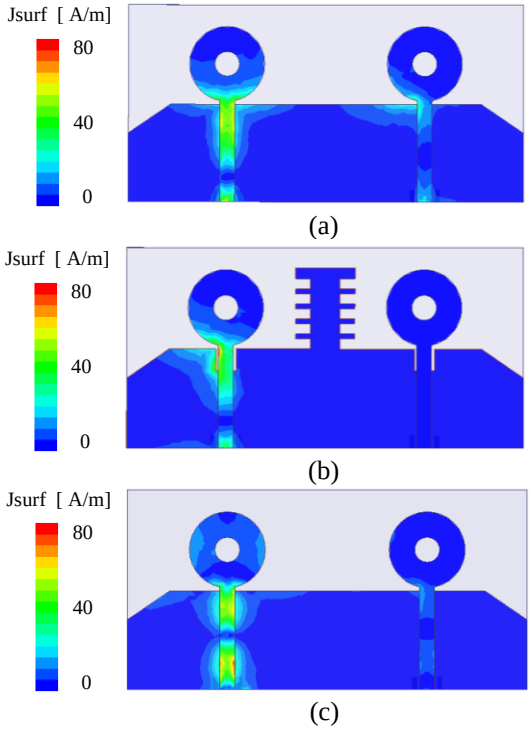

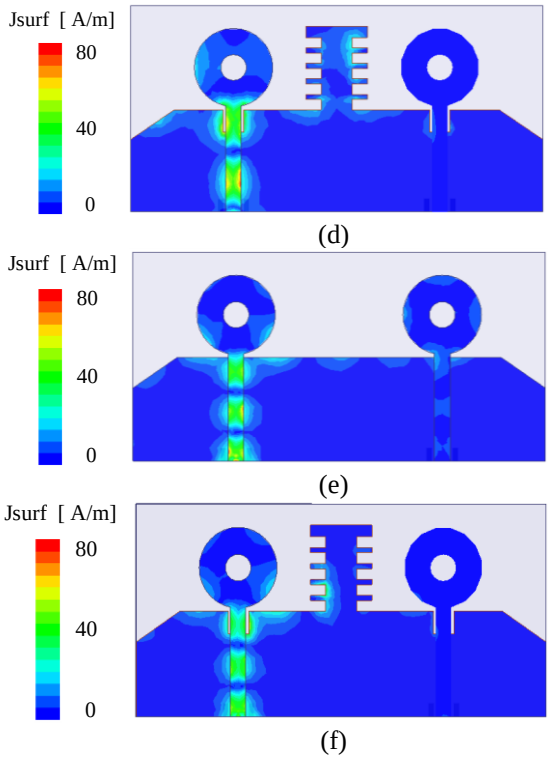

Fig. 5. Surface current distribution of antenna 1 and antenna 3: (a) antenna 1 at 3.5 GHz, (b) antenna 3 at 3.5 GHz, (c) antenna 1 at 7.0 GHz, (d) antenna 3 at 7.0 GHz, (e) antenna 1 at 10.0 GHz, and (f) antenna 3 at 10.0 GHz.

III. RESULTS AND DISCUSSION

Both the antenna 1 and the antenna 3 are fabricated using the FR4 substrate. Figure 6 shows the photograph of the fabricated prototype.

The fabricated antennas are measured by using Keysight E5063A and the measured *S*-parameters are shown in Fig. 7. From Fig. 4 and Fig. 7. The comparison between Fig. 4 and Fig. 7 presents that the measured results correlate well with the simulated ones. The slight difference between them may be caused by the errors in the manufacturing and measurement. As seen in Fig. 7, after the ground is expanded, the measured S_{12} of the antenna 3 falls below -20 dB over the entire UWB band. The result shows that the port isolation between the two antenna elements has been effectively increased. At the same time, the S_{11} of the antenna 3 remains below -10 dB, indicating that the antenna 3 still has a good impedance matching. In summary, the antenna 3, as the final design of the proposed antenna, can be better applied in the UWB MIMO communication systems.

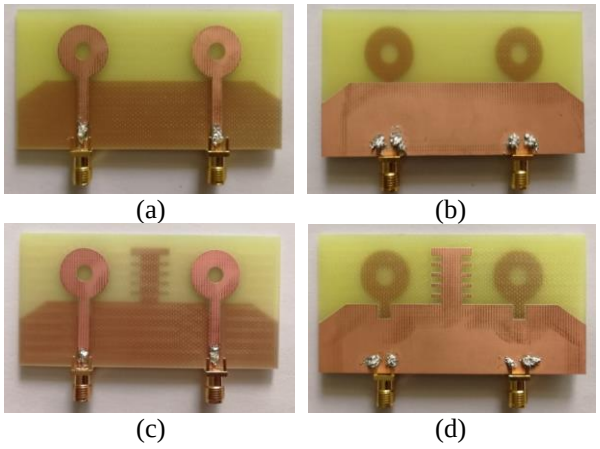

Fig. 6. Photograph of the fabricated antennas: (a) top view of antenna 1, (b) bottom view of antenna 1, (c) top view of antenna 3, and (d) bottom view of antenna 3.

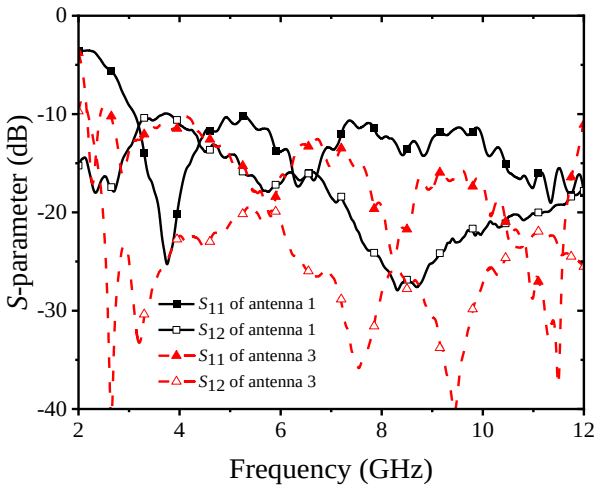

Fig. 7. Measured S-parameters of the proposed antenna.

Figure 8 shows the simulated radiation patterns of the proposed antenna at the different frequencies. From the figure, it can be observed that when the two ports of the proposed UWB MIMO antenna are fed separately. It indicates that the proposed antenna has good spatial diversity characteristics. In addition, in Table 2, the overall performance of the proposed MIMO array is compared with that of some typical designs in the literature. The overall performance of the proposed antenna is comparable to or superior to that of the previous designs.

Table 2: Performance comparison with previous designs in literature

Ref.	Antenna Size (mm^2)	Bandwidth (GHz)	Isolation (In Most of the Band) (dB)
[4]	73×73	3-18	>20
[5]	85×85	3.1-10.6	>15
[6]	110×120	3.0-10.0	>38
[8]	45×45	2-10.6	>17
[9]	42×25	3-12	>15
[11]	32×32	3.1-10.6	>15
[14]	24×40	4.6-10.1	>21
[16]	93×47	3.1-10.6	>31
[17]	24×40	3.1-10.9	>15
[19]	82×50	2.20-13.35	>15
This work	80×40	2.13-11.03	>20

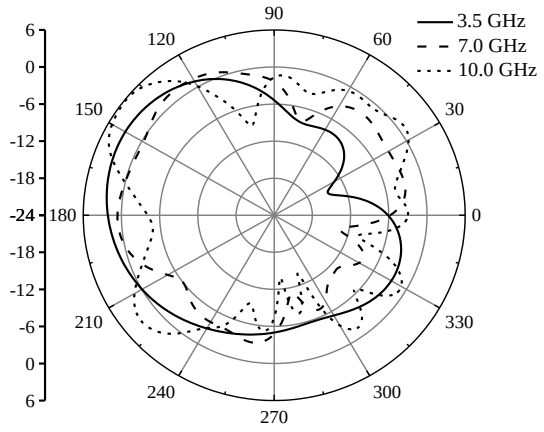

(a)

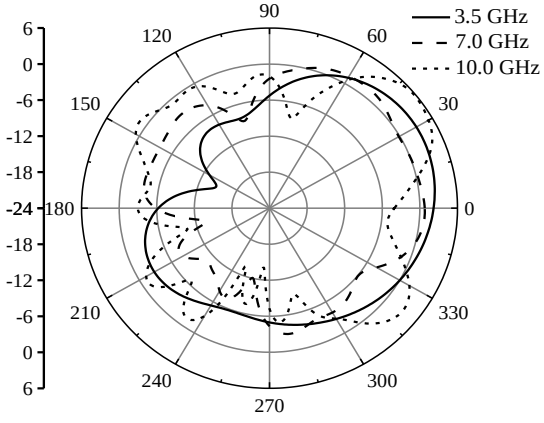

(b)

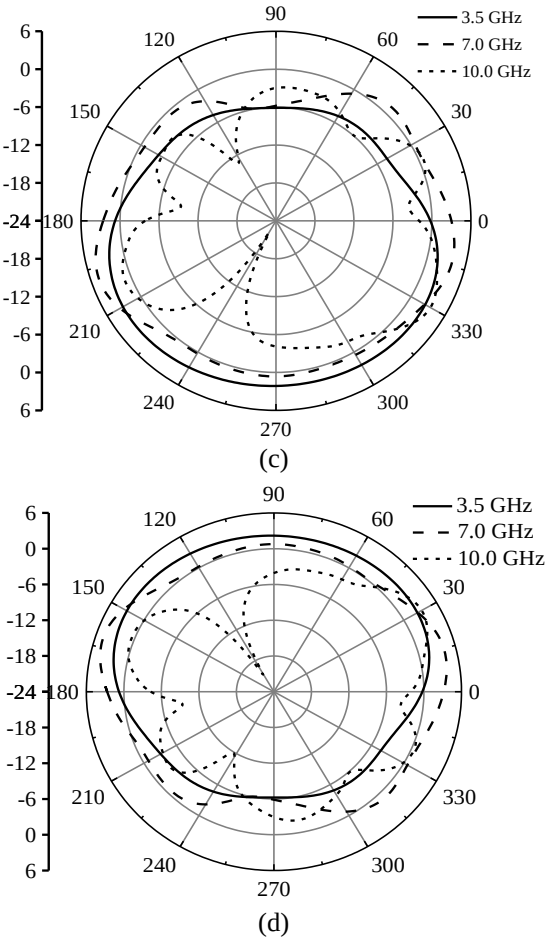

Fig. 8. Radiation patterns of the proposed antenna: (a) XOY plane with port1 excited, (b) XOY plane with port2 excited, (c) XOZ plane with port1 excited, and (d) XOZ plane with port2 excited.

IV. CONCLUSION

A compact UWB MIMO antenna has been proposed in this paper. The primary concern for the UWB MIMO design is isolation enhancement. And this paper utilize comprehensive methods to realize the good performance. Firstly, by expanding the ground with certain shapes, the port isolation between the antenna elements has been significantly increased. Furthermore, the antenna achieves a good impedance matching over the entire UWB band through etching slots on the ground plane, not only opposite the placement of feedlines but also within the rectangular shape expanded. Based on the above results, the proposed antenna is suitable for the UWB MIMO communication systems.

ACKNOWLEDGMENT

This work was supported by the 2019 State Grid Corporation Science and Technology Program under Grant SGJX0000KXJS1900161.

REFERENCES

[1] D. Ghosh, A. De, M. C. Taylor, T. K. Sarkar, M. C. Wicks, and E. L. Mokole, "Transmission and reception by ultra-wideband (UWB) antennas," *IEEE Antennas Propagat. Mag.*, vol. 48, no. 5, pp. 67-99, Oct. 2006.

[2] G. Srivastava and A. Mohan, "Compact MIMO slot antenna for UWB applications," *IEEE Antennas Wireless Propag. Lett.*, vol. 15, pp. 1057-1060, 2016.

[3] A. Toktas and A. Akdagli, "Compact multiple-input multiple-output antenna with low correlation for ultra-wide-band applications," *IET Microw. Antennas Propag.*, vol. 9, pp. 822-829, 2015.

[4] A. S. Eltrass and N. A. Elborae, "New design of UWB-MIMO antenna with enhanced isolation and dual-band rejection for WiMAX and WLAN systems," *IET Microw. Antennas Propag*., vol. 13, pp. 683-691, Apr. 17, 2019.

[5] R. Mathur and S. Dwari, "8-port multibeam planar UWB-MIMO antenna with pattern and polarisation diversity," *IET Microw. Antennas Propag*., vol. 13, pp. 2297-2302, Oct. 30, 2019.

[6] L. Y. Nie, X. Q. Lin, Z. Q. Yang, J. Zhang, and B. Wang, "Structure-shared planar UWB MIMO antenna with high isolation for mobile platform," *IEEE Trans. Antennas Propag*., vol. 67, pp. 2735-2738, 2019.

[7] T. K. Roshna, U. Deepak, V. R. Sajitha, K. Vasudevan, and P. Mohanan, "A compact UWB MIMO antenna with reflector to enhance isolation," *IEEE Trans. Antennas Propag*., vol. 63, pp. 1873-1877, 2015.

[8] S. Tripathi, A. Mohan, and S. Yadav, "A compact Koch fractal UWB MIMO antenna with WLAN band-rejection," *IEEE Antennas Wireless Propag. Lett.*, vol. 14, pp. 1565-1568, 2015.

[9] R. Mathur and S. Dwari, "Compact CPW-fed ultrawideband MIMO antenna using hexagonal ring monopole antenna elements," *AEU-Int. J. Electron. Commun*., vol. 93, pp. 1-6, 2018.

[10] A. Bhattacharya, B. Roy, R. F. S. Caldeirinha, and A. K. Bhattacharjee, "Low-profile, extremely wideband, dual-band-notched MIMO antenna for UWB applications," *Int. J. Microw. Wirel. Technol*., vol. 11, pp. 719-728, 2019.

[11] J. Ren, W. Hu, Y. Yin, and R. Fan, "Compact printed MIMO antenna for UWB applications," *IEEE Antennas Wireless Propag. Lett.*, vol. 13, pp. 1517-1520, 2014.

[12] C. R. Jetti and V. R. Nandanavanam, "Trident-shape strip loaded dual band-notched UWB MIMO antenna for portable device applications," *AEU-Int. J. Electron. Commun.*, vol. 83, pp. 11-21, 2018.

[13] E. Wang, W. Wang, X. Tan, Y. Wu, J. Gao, and Y.

Liu, "A UWB MIMO slot antenna using defected ground structures for high isolation," *Int. J. RF Microw. Comput-Aid. Eng*., vol. 30, 2020.

[14] L. Zhang, W. Liu, and T. Jiang, "A compact UWB MIMO antenna with high isolation," *Proc. IEEE Int. Symp. Antennas Propag.*, Fajardo, Puerto Rico, pp. 913-914, 2016.

[15] K. Chhabilwad, G. S. Reddy, A. Kamma, B. Majumder, and J. Mukherjee, "Compact dual band notched printed UWB MIMO antenna with pattern diversity," *Proc. IEEE Int.* Symp. *Antennas Propag*., Vancouver, Canada, pp. 2307-2308, 2015.

[16] A. H. Radhi, R. Nilavalan, Y. Wang, H. S. Al-Raweshidy, A. A. Eltokhy, and N. Ab Aziz, "Mutual coupling reduction with a wideband planar decoupling structure for UWB–MIMO antennas," *Int. J. Microw. Wirel. Technol*., vol. 10, pp. 1143-1154, 2018.

[17] M. G. N. Alsath and M. Kanagasabai, "Compact UWB monopole antenna for automotive communications," *IEEE Trans. Antennas Propag*., vol. 63, pp. 4204-4208, 2015.

[18] S. K. Dhar and M. S. Sharawi, "A UWB semi-ring MIMO antenna with isolation enhancement," *Microw. Opt. Technol. Lett*., vol. 57, no. 8, pp. 1941-1946, 2015.

[19] A. Toktas, "G-shaped band-notched ultra-wideband MIMO antenna system for mobile terminals," *IET Microw. Antennas Propag*., vol. 11, pp. 718-725, Apr. 15, 2017.

[20] Y. Li, B. Yu, H. Shen, L. Zhu, and G. Yang, "An 8-port planar UWB MIMO antenna for future 5G micro wireless access point applications," 2017 *Appl. Comput. Electromagn. Soc. Symp*., Suzhou, pp. 1-2, 2017.

[21] Y. Dong, Y. Li, K. Yu, and Y. Wang, "High isolation design of a two-element planar UWB-MIMO monopole antenna," 2017 *Appl. Comput. Electromagn. Soc. Symp*., Italy, Florence, pp. 1-2, 2017.

[22] H. Huang and Z. Zhang, "Mutual coupling reduction of a very compact UWB-MIMO linearly tapered slot antenna using a simple stepped slot," 2017 *Appl. Comput. Electromagn. Soc. Symp.*, Suzhou, pp. 1-2, 2017.

Yantao Yu received the B.Eng. degree (1st class honors) and the Ph.D. degree both from the National University of Singapore, in 2004 and 2009, respectively. From 2008 to 2009, he worked at Motorola Electronics Pte Ltd, Singapore, as an RF Engineer. From 2009 to 2010, he was a Research Fellow with the National University of Singapore. He is currently an associate professor in the School of Microelectronics and Communication Engineering, Chongqing University, China. His research interests include analysis and design of antennas/arrays, RF & microwave circuits and special topics in array signal processing, Internet of Things, collaborative communications.

Shenshen Mao received the B.S. degree from the Chongqing Normal University, China in 2016. She is now working toward the Master degree in the Chongqing University. Her research interests include antenna/array design.

Meng Li received the B.Eng. degree in 2017 and the Master degree in 2020 from the Chongqing University, China. His research interests include design of antenna/ array and microwave circuits.

Danting He received the B.Eng. degree from the Anhui University of Technology, China in 2018. She is now working toward the Master degree in the Chongqing University. Her research interests include antenna/array design using TCM analysis.

Reconfigurable Planar Monopole Antenna for Fifth-Generation Mobile Communication System

Peng Chen, Lihua Wang, and Zhonghua Ma

Information Engineering College
Jimei University, Xiamen, Fujian, 361021, China
chenpeng@jmu.edu.cn, liliya@jmu.edu.cn, mzhxm@jmu.edu.cn

Abstract ─ A frequency reconfigurable planar monopole antenna for fifth-generation (5G) mobile communication terminal equipment is presented. The proposed antenna uses a meandered monopole, branch resonance and other techniques to make the antenna resonant in multiple frequency bands. The antenna is compact in size (115 mm × 55 mm × 0.8 mm) and has a longitudinal length less than one-tenth of the resonant wavelength (working at 1.79 GHz). The pin diode is designed between the planar meandered monopole antenna and branch. The current path of the high-frequency current on the antenna can be easily controlled by controlling the DC bias voltage of the diode, and the operating frequency of the antenna is switched between three frequency bands. The antenna is fed directly through a 50 Ω matched transmission line. The measured data of the antenna in the anechoic chamber show good consistency with simulation data. The radiation pattern of the antenna shows good omnidirectional characteristics and good frequency characteristics, with a maximum radiation gain of 13.6 dBi. Experimental results demonstrate that the antenna can meet the design requirements of 5G communication.

Index Terms ─ 5G, branch-line coupler, frequency reconfigurability, planar monopole antenna.

I. INTRODUCTION

With the maturity of fifth-generation (5G) communication technology, several new wireless communication bands have been approved for use, but the division of 5G frequency points in different countries and regions also presents a decentralized situation. Even limited to the sub-6 band, users need the ability to switch freely between dozens of frequency combinations for cross-border, cross-carrier network use.

Faced with the increasing requirement of frequency matching and frequency selection in terminal equipment, the design idea of blindly expanding antenna bandwidth to cover more frequency ranges has become increasingly more limited.

A typical example is that many scholars are now realizing that UWB antennas used in UWB communications should be designed with frequency-specific notch points to be able to operate simultaneously with a wireless communication network and avoid interference by high-power wireless signals of the same frequency used in such a communication system [1–4].

Therefore, faced with the challenge of frequency switching, a frequency-reconfigurable antenna has become an alternative and solves the problem more effectively.

A large number of research results on frequency reconfigurable antennas exist [5–10]. Additionally, frequency-reconfigurable antennas have many advantages over traditional antennas, such as simplification and miniaturization, which can change the frequency [11−12].

A varactor diode and an external bias Tee structure were used in Ref. [13] to achieve flexible adjustment of the operating frequency band. A varactor diode combined with a bias circuit was also used in Ref. [14] to achieve dual-band frequency reconfiguration, and the monopole antenna has a lower profile. A sub-type patch structure and multiple PIN diodes were used in Ref. [15] to achieve coverage of three frequency bands from 1.45 to 4.52 GHz.

In this study, a frequency-reconfigurable planar monopole antenna that can be applied to 5G mobile communication terminal equipment is proposed.

Compared to the antenna described in Ref. [13], the frequency switching of the antenna described in this article through PIN diodes has low hardware cost, and its frequency-switching control method is simple. Compared with the antenna described in Ref. [14], the size of the low-profile monopole antenna proposed herein, applied to the low frequency at approximately 760 MHz, reaches 97 mm×97 mm×8 mm, its structure is more compact (28.3 mm×16.5 mm×0.8 mm), and its longitudinal length is less than one-tenth of the resonance wavelength. Compared with the antenna described in Ref. [15], the antenna described herein can support communication modes of more frequency bands, not only supporting 3G and 4G networks at the same

Submitted On: October 11, 2020
Accepted On: December 5, 2020

https://doi.org/10.47037/2020.ACES.J.360110

time, but also compatible with higher-frequency 5G communication networks, making the communication of mobile users more flexible and convenient.

II. BASIC PROPOSED ANTENNA STRUCTURE

The proposed antenna is a planar monopole antenna that has been miniaturized by using meandered monopole antenna technology. The monopole in the form of a copper microstrip is realized by printed-circuit-board technology, and the meandering structure is designed on the limited plane, which reduces the length of the antenna to less than one-tenth of the maximum wavelength. The equal-width microstrip line forms an S-bend and is connected to the microstrip feeder that connects the SMA connector to the antenna. The slot of the S-shaped monopole antenna near the feeder is equivalent to that of the capacitor, and the capacitance can be adjusted by adjusting the structure parameter *g* to realize the matching between the antenna and feeder.

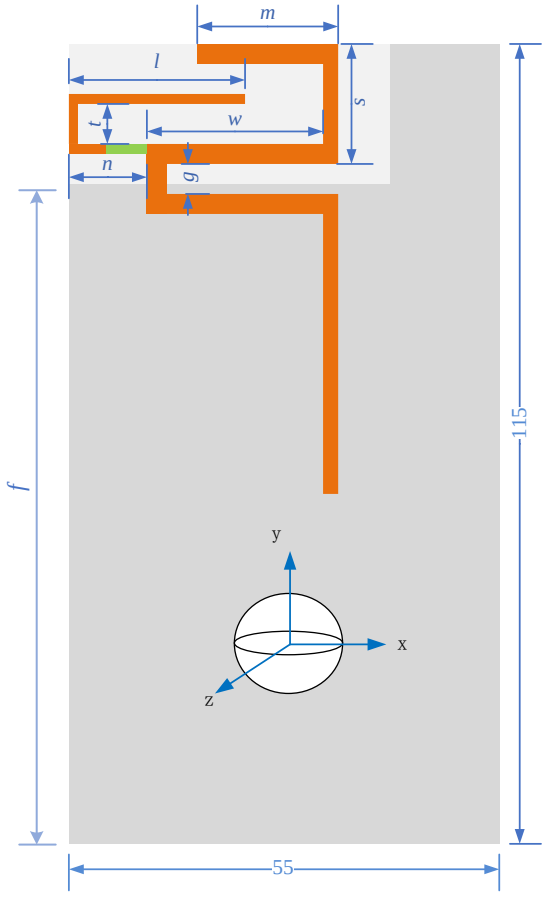

Fig. 1. Schematic of proposed antenna structure.

The structure of the proposed antenna is shown in Fig. 1, and a section of the U-shaped microstrip branch is connected with the S-shaped monopole antenna at the first bend. The connection is made by a PIN diode. The PIN diode used in the research are BAR50-02 of Infineon Company, which has low forward resistor, very low harmonics, and low capacitance at 0 V reverse bias at frequencies above 1 GHz (typ. 0.15 pF). It can work normally in 10 MHz—6 GHz. According to the PIN diode datasheet, the threshold voltage of 1.5V DC can control the ON-OFF state of the PIN diode. The diode represents a resistance of 3Ω for the ON state and a parallel circuit with a capacitance of 0.15 pF and a resistance of 5kΩ for the OFF state. When the diodes for the ON state has a low resistance which contribute to the insertion loss. According to the datasheet [16], the insertion loss is 0.27 dB.

By controlling the DC bias of the diode, it is easy to control the turning-on of the diode and realize the path reconstruction of the high-frequency current on the antenna surface, thus realizing the frequency control of the antenna.

To simulate the application environment, the antenna is designed on FR4 medium with an area of 115mm×55mm and thickness of 0.8 mm. The back of the antenna is covered with a large copper layer to simulate the integration of the antenna and circuit structure of the terminal equipment. The environmental parameters and structural parameters of the antenna are listed in Table 1.

Table 1: Parameters of antenna structure

Parameters	Value (mm)	Parameters	Value (mm)
t	5.8	*g*	1.7
l	19.4	*n*	7.7
s	11	*m*	25
w	17.5	*f*	100

The S-shaped monopole antenna with branches is equivalent to the circuit form shown in Fig. 2. The relationship between the branches and monopole antennas can be expressed as a parallel circuit. Branch and monopole antennas have different resonant frequencies because they have different current paths. The low-frequency radiation power is proportional to R_m and the high-frequency radiation power to R_b. The distributed capacitance introduced by the antenna is equivalent to that of C_a and the matching between the antenna and feeding circuit can be adjusted by controlling C_a. It is worth noting that the position relationship between the branch and the antenna is not reflected in the equivalent circuit; this part of the parameters also determines the antenna matching.

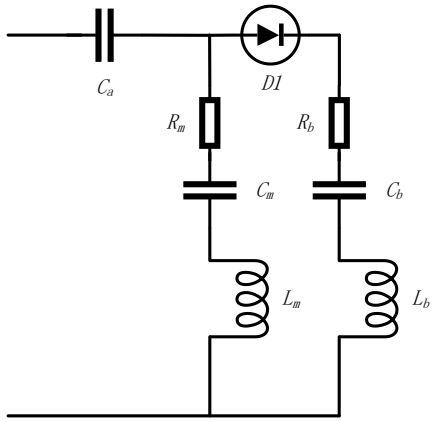

Fig. 2. Equivalent circuit of antenna.

The antenna has the advantages of simple structure, low process cost, and suitability for mobile terminal equipment. By controlling the DC bias of the diode, turning the diode on or off can be easily controlled and the antenna frequency can be reconfigured.

III. PARAMETRIC STUDY OF FREQUENCY RECONFIGURABLE ANTENNA

When the PIN diode is off, since the diode reactance in the frequency band is very large, it is equivalent to a short-circuit state and the branch is equivalent to the meandering monopole antenna coupled patch. By adjusting the length of the planar meandering monopole antenna, the resonant frequency of the antenna can be changed, as shown in Fig. 3.

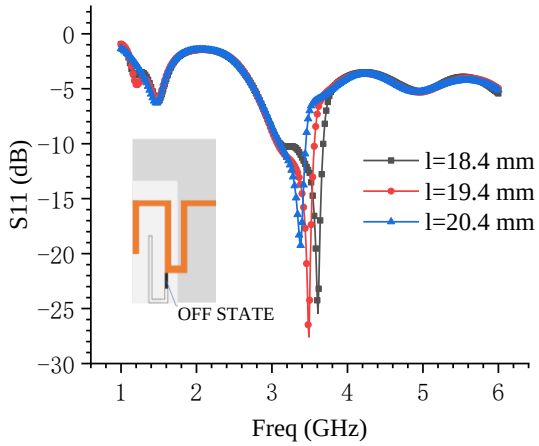

Fig. 3. Simulation results of antenna parameter S_{11}.

When the PIN diode is disconnected, here is an obvious resonance frequency point in the analysis frequency band, which corresponds to the arm length of the monopole antenna, When the arm length increases, the resonant frequency of the antenna moves to the low-frequency band, and when it decreases the resonant frequency of the antenna moves to the high-frequency band. As shown in Fig. 3, the length of the monopole antenna arm can be changed by adjusting the structural parameters *m* and *s*, thereby controlling the antenna resonance frequency. When the structural parameters *s*, *w*, and *g* are changed, the distributed capacitance of the antenna is also changed, and then the matching of the antenna changes.

According to a simulation analysis performed in Ansys HFSS software, when the PIN diode is disconnected and the antenna parameters are set as shown in Table 1, the impedance characteristics of the antenna are satisfactory. The impedance bandwidth (<−10dB) is 540MHz (3.07–3.61 GHz) and the relative bandwidth 16.2%, which can meet the requirement of 5G communication covering the (3.3–3.6)-GHz band.

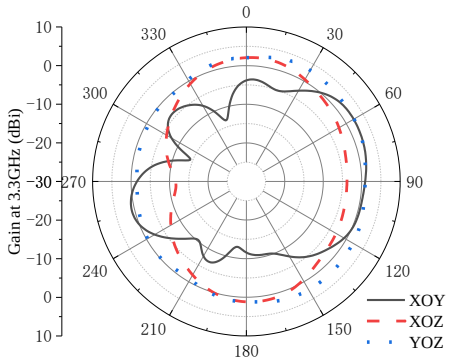

Fig. 4. Radiation pattern of proposed antenna when diode is off.

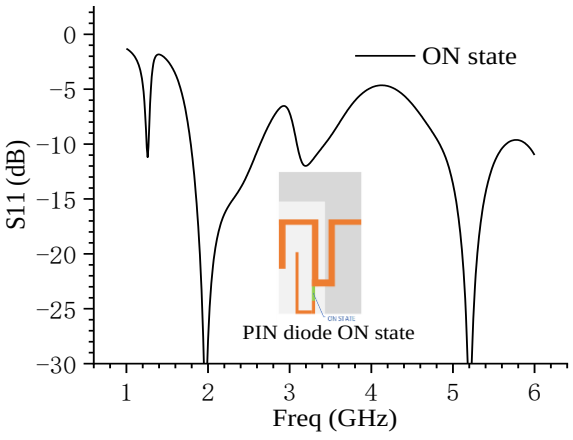

Fig. 5. Simulation results of antenna parameter S_{11}.

As shown in Fig. 4, the ZOX and ZOY plane patterns fully exhibit isotropy when the antenna operates at a central frequency of 3.3 GHz in this frequency band. In the XOY plane pattern, the directivity of the antenna is largely strong, maximum direction of radiation points

to φ= 60°, peak gain is 2.2 dBi, that of the corresponding back lobe level is−2.4 dBi, and front-to-back ratio is 4.6 dB.

At a DC bias of 1.6 V for the PIN diode, the diode will be turned on. At this time, the diode is equivalent to a resistance of 3 Ω for the current in the frequency band. Owing to the access of the single branch, the surface current on the single arm of the monopole is shunted. A new shorter surface current path is formed, so the antenna shows two resonant frequency points on the band characteristic curve.

Similar to the analysis of the state of the diode, the resonant frequency of the high frequency can be controlled by adjusting the structural parameters *t*, *l*, and *n*; the analysis process is not redundant. It should be noted that, due to the conduction of the diode, the function of the U-shaped microstrip line in the antenna is changed from the coupling patch when the diode is off to the current branch of the monopole antenna, driving the low-frequency resonant point to a significantly lower frequency.

According to the simulation results in Ansys HFSS, the antenna shows dual-band characteristics when the diode is on, the frequency band (s_{11}<−10 dB) of the antenna covers 1.79–2.63 and 4.827–5.66 GHz, and the relative bandwidth reaches 38% and 15.4%, respectively (Fig. 5). The coverage characteristics of the frequency band meet the requirements of DCS1800 (1710–1880MHz)/PCS1900 (18501990MHz)/UMTS2100 (1920–2170MHz)/LTE2300 (2350–2400MHz)/LTE2500 (2500–2690MHz) and the 5G communication frequency band of 4.8–5.0 GHz.

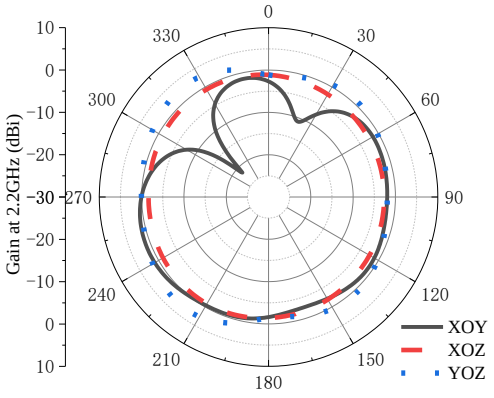

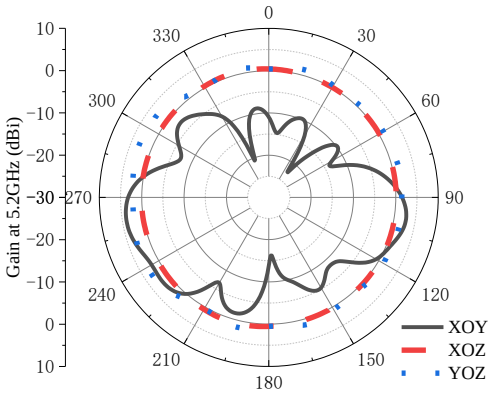

Fig. 6. Radiation pattern of proposed antenna when diode is on.

In terms of radiation characteristics, it can be seen from Fig. 6 that when the antenna operates at 2.2 GHz the antenna exhibits omnidirectional radiation characteristics in the YOZ and XOZ planes, and the XOY plane antenna shows good directivity with a maximum gain of 1.1 dBi. When the antenna operates at 5.2 GHz, the antenna shows omnidirectional radiation characteristics in the YOZ and XOZ planes, while the antenna shows good directivity with a maximum gain of 4.0dBi. The stability of the multi-frequency pattern ensures that the devices using the antenna can switch between several working frequency bands.

IV. RESULTS AND ANALYSIS

As shown in Fig. 7, the bias of the antenna can be supplied by abattery or DC voltage source. During design, the power switch can be manually switched to achieve the function of switching the working frequency of the antenna, in the form of the realization that the product form will use the switch control circuit. The antenna is installed in the anechoic chamber and the antenna parameters measured. As shown in Fig. 8, the measured PIN diode can cover the frequency range from 3.1 to 4.8 GHz with a bandwidth of 1.7 GHz. Compared with the simulation results, the 3.5 GHz resonant point has better consistency, measured data have a lower reflection coefficient, and resonance performance at high frequency is more obvious, so a new resonant point is formed near 3.9 GHz; the bandwidth is enlarged relative to the simulation result under double resonance.

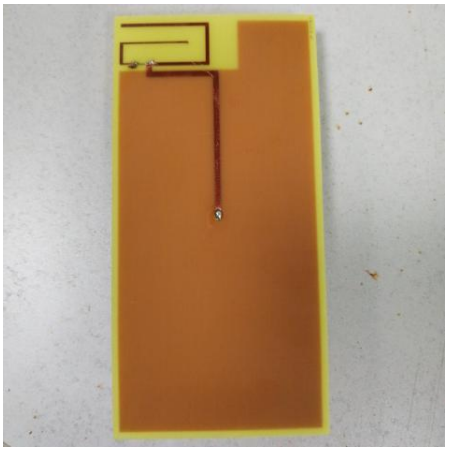

(a) Photograph of antenna front view

(b) Photograph of antenna rear view

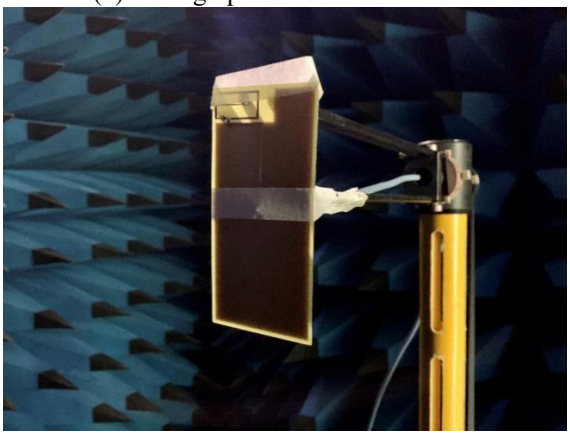

(c) Proposed antenna being measured in anechoic chamber

Fig. 7. Proposed reconfigurable planar monopole antenna test photos.

As can be seen from Fig. 9, with the decrease of n, the bandwidth of the antenna obviously becomes smaller, and the high frequency point and low frequency point produce frequency point offset. The size of f has a great influence on the performance of the antenna.

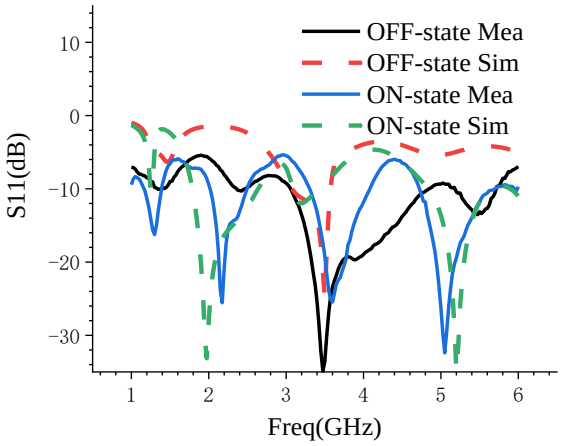

Fig. 8. Measured data of antenna parameter S_{11}.

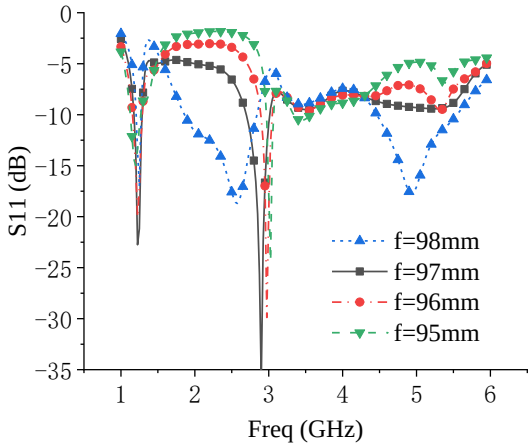

Fig. 9. Simulated reflection coefficients of the antenna for different n.

When the diode is on, the measured antenna can cover four frequency bands: 1.2–1.4, 2.0–2.5, 3.3–4.0, and 4.7–5.6 GHz. Compared with the simulation results, the coverage of the high-frequency band is closer, reflection coefficient of the low-frequency resonance relatively larger, and the low-frequency resonance point moves 200 MHz to the high-frequency part, which reduces the measured bandwidth by 200 MHz. However, the intermediate-frequency resonance points, which are not well matched in simulation, are also measured in experiment. The reason may be that the diode circuit is not more equivalent to the current distribution in the actual diode circuit.

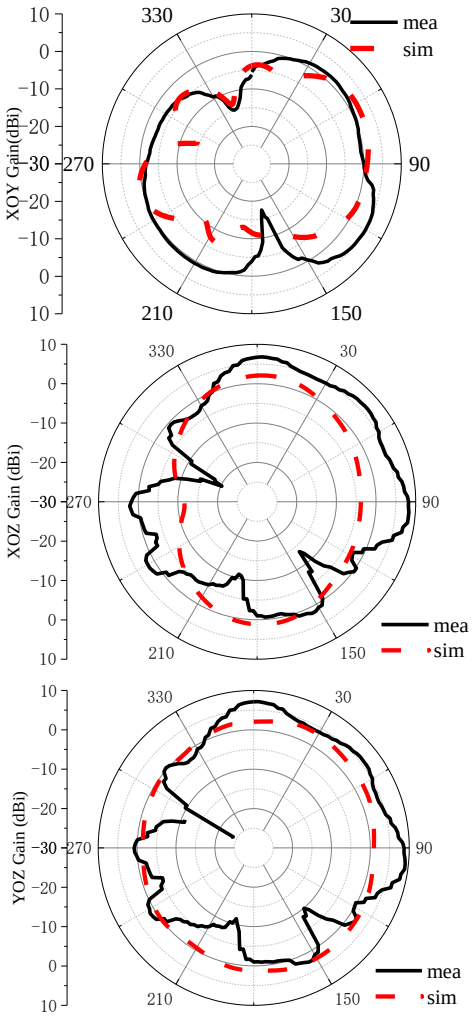

(a) Radiation Pattern at 3.3 GHz (diode OFF-state)

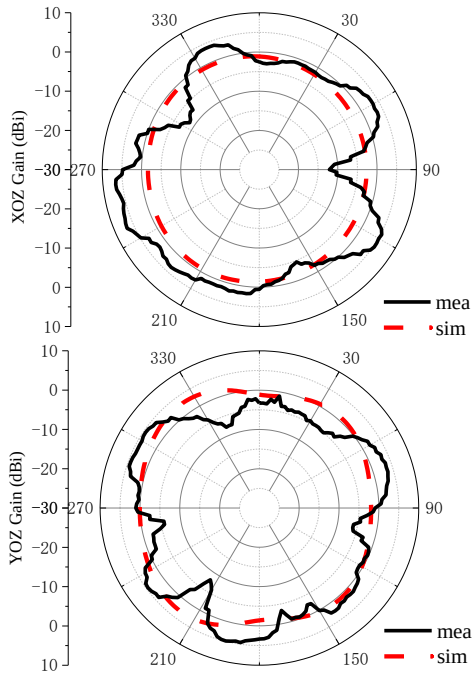

(b) Radiation Pattern at 2.2 GHz (diode ON-state)

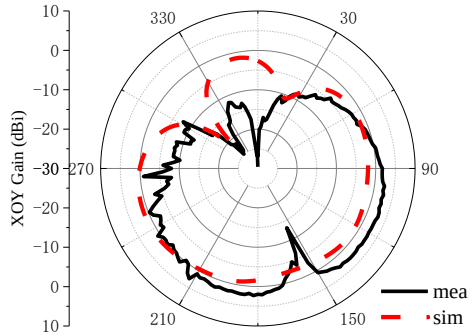

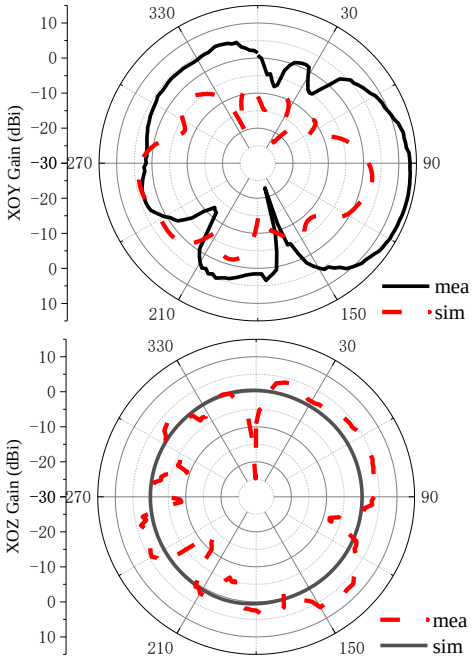

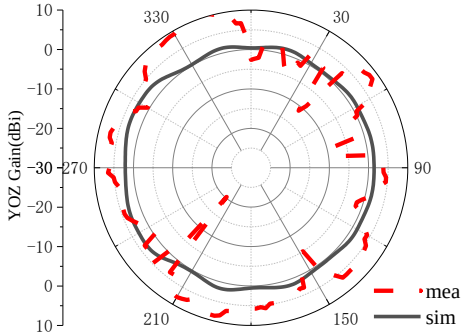

(c) Radiation Pattern at 5.2 GHz (diode ON-state)

Fig. 10. Antenna multi-frequency working pattern.

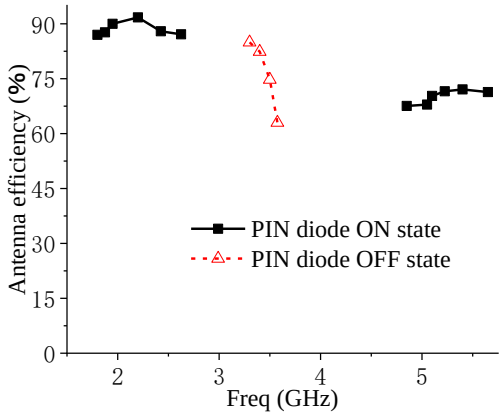

Fig. 11. Efficiency of the fabricated antenna at different frequency bands.

By switching the diode switch, the antenna can switch between three frequency bands easily. In three frequency bands, 2.2 GHz (diode ON), 3.3 GHz (diode OFF), and 5.2 GHz (diode ON) were selected to test the pattern.

According to the multi-frequency working pattern in Fig. 10, it can be seen that the radiation intensity in each direction of the three operating frequencies tested in the anechoic chamber exhibits little difference in the XOZ YOZ planes, and the omnidirectional characteristics are obvious; however, the directivity is stronger in the XOY plane. And the cross-polarization performance of the antenna is not ideal. The measured gains were 5.1 dBi (3.3 GHz), 2.7 dBi (2.2 GHz), and 13.6 dBi (5.2 GHz), respectively. The simulated antenna efficiency is shown in Fig. 11. As can be seen from the figure that the antenna efficiency is above 63% at different frequency bands. However, the efficiency of the antenna in the high frequency band is slightly reduced. Lower antenna efficiency is mostly due to the higher current flowing through the PIN diode.

Certainly, the error between the measured and simulated data needs further analysis, with the reasons for the error possibly caused by the following: First, welding and PCB processing and other process errors; second, consistency error of the antenna's dielectric material and transmission line; and, third, analysis of the diode equivalent circuit, reduction degree of the simulation software, and systematic error of the testing instrument.

ACKNOWLEDGMENT

This work was supported in the Fujian Natural Science Foundation Project (2020J02042 and 2019J01718) and the National Fund Training Project of Jimei University (ZP2021011).

REFERENCES

[1] C.-H. Lee, J.-H. Wu, C.-I. G. Hsu, H.-L. Chan, and H.-H. Chen, "Balanced band-notched UWB filtering circular patch antenna with common-mode suppression," *IEEE Antennas Wirel. Propag. Lett.*, vol.16, pp. 2812-2815, Sept. 2017.

[2] M. Elhabchi and M. N. Touahni, "CPW-fed miniaturized isosceles triangular slot UWB planar antenna with triple band-notched characteristics," *Prog.* Srifi, and R. *Electromagn. Res.*, vol. 87, pp. 59-66, 2019.

[3] M. Rahman, M. NagshvarianJahromi, S. S. Mirjavadi, and A. M. Hamouda, "Compact UWB band-notched antenna with integrated bluetooth for personal wireless communication and UWB applications," *Electronics*, vol. 8, no. 2, Feb. 2019.

[4] R. Sanyal, P. P. Sarkar, and S. Sarkar, "Octagonal nut shaped monopole UWB antenna with sextuple band notched characteristics," *AEU - Int. J. Electron. Commun.*, vol. 110, article ID 152833, Oct. 2019.

[5] Y. He, W. Tian, and L. Zhang, "A novel dual-broadband dual-polarized electrical downtilt base station antenna for 2G/3G applications," *IEEE Access*, vol. 5, pp. 15241-15249, June 2017.

[6] A. Chaugule, G. Mishra, and S. K. Sharma, "Investigations on frequency agile dual polarization dielectric lens high gain antenna," in *2016 IEEE International Symposium on Antennas and Propagation (APSURSI)*, article ID 16411953, pp. 837-838, June 2016.

[7] Z. Nie, H. Zhai, L. Liu, J. Li, D. Hu, and J. Shi, "A dual-polarized frequency-reconfigurable low-profile antenna with harmonic suppression for 5G application," *IEEE Antennas Wirel. Propag. Lett.*, vol. 18, no. 6, pp. 1228-1232, June 2019.

[8] Y. Li, W. Li, and Q. Ye, "A reconfigurable trip-notch-band antenna integrated with defected microstrip structure bandstop filter for ultra-wideband cognitive radio applications," *Int. J. Antennas Propag.*, vol. 2013, p. 13, article ID 472645, 2013.

[9] A. Singh and C. E. Saavedra, "Fluidically

reconfigurable MIMO antenna with pattern diversity for sub-6-GHz 5G relay node applications," *Canadian Journal of Electrical and Comuter Engineering-revue Canadienne Degenie Electrique Et Informatique*, vol. 43, no. 2, pp. 92-99, Spr. 2018.

[10] M. M. Fakharian, P. Rezaei, and A. A. Orouji, "A multi-reconfigurable CLL-Loaded planar monopole antenna," *Radioengineering*, vol. 29, no. 2, pp. 313-320, June 2018.

[11] S. F. Jilani, A. Rahimian, Y. Alfadhl, and A. Alomainy, "Low-profile flexible frequency-reconfigurable millimetre-wave antenna for 5G applications," *Flex. Print. Electron.*, vol. 3, no. 3, p. 035003, Aug. 2018.

[12] Y.-L. Tsai and J.-H. Chen, "Design of a dual-polarized beam-switching antenna for small base station application," in *2015 International Workshop on Electromagnetics: Applications and Student Innovation Competition (iWEM)*, article ID 15681179, Nov. 2015.

[13] I. Ben Trad, I. Rouissi, J.-M. Floc'h, and H. Trabelsi, "Frequency reconfigurable multiband planar antenna with wide tuning frequency range," in *2016 10th European Conference on Antennas and Propagation (EuCAP)*, article ID 16037660, Apr. 2016.

[14] N. Nguyen-Trong, A. Piotrowski, and C. Fumeaux, "A frequency-reconfigurable dual-band low-profile monopolar antenna," *IEEE Trans. Antennas Propag.*, vol. 65, no. 7, pp. 3336-3343, July 2017.

[15] Y. K. Choukiker and S. K. Behera, "Wideband frequency reconfigurable Koch snowflake fractal antenna," *IET Microw. Antennas Amp Propag.*, vol. 11, no. 2, pp. 203-208, Jan. 2017.

[16] Datasheet for Infineon BAR50-02V, Silicon PIN Diode, Infineon Technologies AG, 18 Sep. 2011. Available at http://www.farnell.com/datasheets/1500311.pdf.

Design of Dual Frequency Coupled Resonators Using DGS and Microstrip Resonators for Dual Band WPT Applications

Hany A. Atallah [1], Musallam Alzubi [2], Rasha Hussein [1], and Adel B. Abdlerhman [1,3]

[1] Electrical Engineering Department, Faculty of Engineering, South Valley University, Qena 83523, Egypt
h.atallah@eng.svu.edu.eg, rasha.h.ahmed@eng.svu.edu.eg

[2] Ministry of Communications, Po Box 318, Safat 11111, Kuwait

[3] School of Electronics, Communications and Computer Engineering, Egypt-Japan
University of Science and Technology, Alexandria 21934, Egypt

Abstract ─ This paper introduces a new design for a highly efficient and more compact size dual frequency wireless power transfer (WPT) system, which can operate at both 0.65 GHz and 1.56 GHz bands. The idea of the structure depends on designing a symmetrical system containing Tx and Rx. Each Tx and Rx has a feed line on the top layer with two stubs; each stub has different dimensions than the other one. The bottom layer contains two C-shaped defected ground structures (DGS). By changing the dimensions of one stub, the frequency resonance corresponds to this stub is changed without any change on the other resonance. The system has a size of 20 × 20 mm^2. Further, the system achieves efficiencies of 72 % and 89 % at 0.65 GHz and 1.56 GHz, respectively with a transmission distance of 8 mm. The proposed dual frequency WPT is implemented and verified. Good concurrences among electromagnetic (EM) simulations and the measurements have been attained. The system is suitable for recharging short-range applications.

Index Terms ─ Dual Band (DB), stub, Wireless Power Transfer (WPT).

I. INTRODUCTION

Wireless power transfer (WPT) technology comes with the promise of cutting the last cord by allowing recharge electronics devices as easily as data and the power will be transferred through the air without cables. WPT technology has been attracted many researchers in recent and previous periods for its impact in numerous prospective uses for instance sensor networks, controllable automated equipment (tablets, mobile phones, etc.), RFIDs, and so on [1-5]. The size of the system (particularly the receiver), the power transferring distance, and the efficiency are the furthermost key factors to be addressed in designing the building blocks of the WPT systems. Initially, the researchers have employed the coils for designing WPT systems and they have investigated the effects of the coil's parameters on the coupling efficiency and the working frequency. WPT is now applied as a viable method to power many types of devices including portable consumer electronics [6], electric vehicles [7], and biomedical implants [8]. Numerous of the short-range WPT methods are employing lumped components [9]. However, these components have sensible drawbacks in execution such as occupying an excessive space. In addition, they are lossy. Nonetheless, they are preferred in WPT applications at low frequencies.

Newly, defected ground structure (DGS) is the innovative technology that is presently used for designing WPT systems [10-13]. Some designs of the DGS are investigated and implemented for WPT like the C-shaped design [14]. Most of the published ideas investigate the usage of the modified DGS for obtaining single band operations [15].

Lately, they have improved the DGS to realize a dual band near-field WPT system [16-18]. However, the dual-band WPT has many benefits over the single band systems as implemented in [16]. The authors in [10] studied the WPT system by employing the DGS technique. Firstly, they suggested an H-shaped DGS with a size of 25 × 25 mm^2 and an efficiency of 68% at 0.3 GHz at a transmission distance of 5 mm. Secondly, the structure is enhanced and developed to be semi H-shaped. The system has a size of 20 × 20 mm^2 with an efficiency of 73%. In [11], a dual frequency system is proposed. Further, it depends on two circular DGS resonators whereas each circular is responsible for frequency resonance. The system has a size of 30 × 15 mm^2 and the efficiencies are 71% and 71% at 0.3 GHz and 0.7 GHz with a transmission distance of 16 mm. In [17], a dual band system is proposed with a size of 12.5 × 8.9 cm^2 and efficiencies of 78% and 70.6% at 6.78 MHz and 200 kHz, respectively. In [19], the author

Submitted On: July 6, 2020
Accepted On: November 29, 2020
https://doi.org/10.47037/2020.ACES.J.360111

introduced a dual-band rectifying circuit for wireless power transmission working at 2.45 GHz and 5.8 GHz. This system showed peak RF-to-DC efficiencies of 66.8% and 51.5% at 2.45 GHz and 5.8 GHz, respectively.

Recently, the DGS resonators are extensively explored for single and dual band operations of the WPT applications [10-12,15,18-22].

In this paper, a new dual frequency WPT system is proposed. The system introduces a new idea which designs two stubs with different sizes for obtaining dual band frequencies. The size of the system is 20 × 20 mm^2 with efficiencies of 72% and 89% at 0.65 and 1.56 GHz, respectively.

II. COUPLED RESONATOR DESIGN

Listed below the configuration of the suggested dual frequency system. Figure 1 (a) shows the top view which contains a feed line with a width of *W_f* and a length of 19.5 mm. The stubs are designed on the top with different sizes, that responsible for dual band frequency operation. Figure 1 (b) shows the bottom layer which contains a C-shaped DGS with the same shorted points connected with the top view. The design parameters are recorded in Table 1. Figure 2 (a) shows the setting of the suggested geometry of the coupled resonators which are parted by a space of *h* mm. Figure 2 (b) represents the equivalent circuit of the system. The equivalent circuit presents a dual band resonance circuit and each circuit is considered as a separate one. The equivalent circuit contains (L_{p1} and C_{p1}) which are the parallel elements of the tank circuit related to the first resonance frequency and (L_{p3} and C_{p3}) are related to the second resonance frequency.

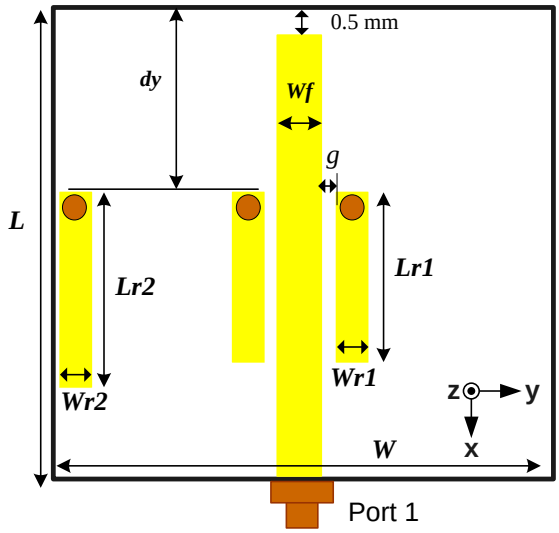

(a)

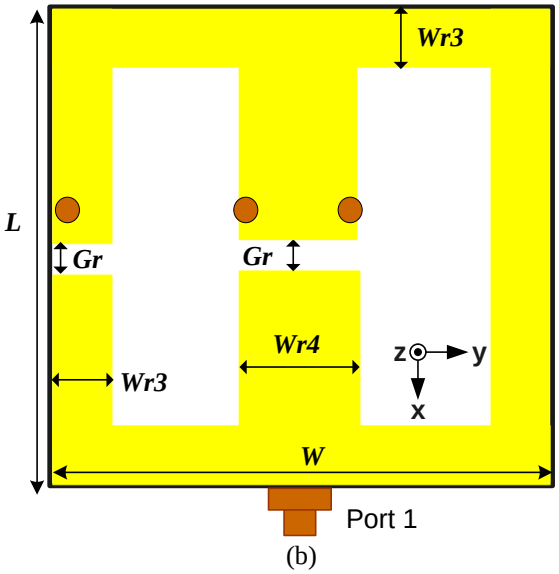

(b)

Fig. 1. Top and bottom layers of the proposed design: (a) top layer and (b) bottom layer.

Table 1: List of parameters

Parameter	Value / Type
Substrate	Rogers 4003C
ε_r	3.55
Thickness of substrate (*t*)	0.83 mm
L	20 mm
Lr1	8 mm
Lr2	11 mm
Wr1	1.5 mm
g	0.5 mm
W_f	2 mm
Wr2	1.75 mm
W	20 mm
Gr	0.5 mm
Wr3	2 mm
Wr4	5.5 mm

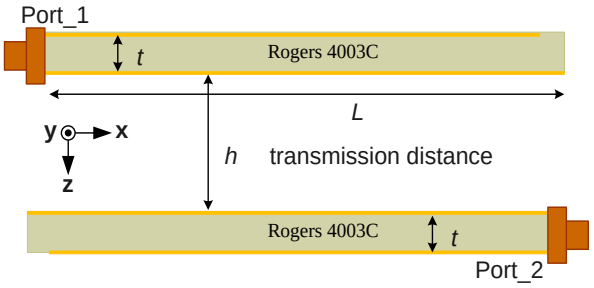

(a)

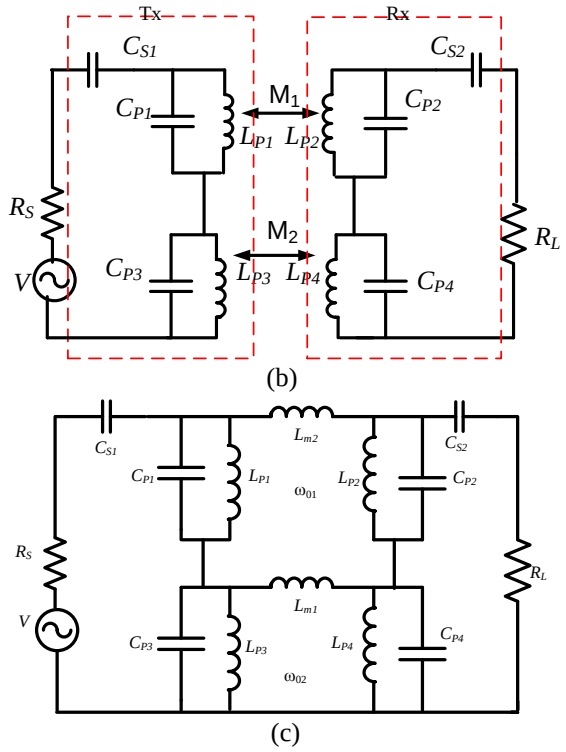

Fig. 2. Equivalent circuit and 3-D view. (a) 3-D view. (b) The equivalent circuit of the system. (c) The pi-equivalent circuit (π) of the system.

It is desired to compute and extract the values of the equivalent circuit parameters (C_p, L_p, L_{m1}, L_{m2}, and C_s) from the simulation consequences for validations. Where M_1 and M_2 are the mutual couplings between two resonators [22], L_{m1} and L_{m2} are the mutual inductances [22], and C_s is the series capacitance. Equations (1) and (2) are employed to calculate the equivalent circuit parameters [21]:

$$C_P = \frac{5f_c}{\pi[{f_0}^2 - {f_c}^2]} \quad pF, \tag{1}$$

$$L_P = \frac{250}{C_P[\pi f_0]^2} \quad nH, \tag{2}$$

where f_c is the cutoff frequency and f_o is the center resonance frequency at each band alone.

At the first resonance frequency, the frequencies are f_{c1} = 0.59372 GHz and f_{o1} = 0.64793 GHz. By substitution in equation (1) and (2), the extracted parameters are $C_{p1} = C_{p2}$ = 14 pF and $L_{p1} = L_{p2}$ = 4.29 nH. In the same way at the second resonance frequency, the frequencies are f_{c2} = 1.4516 GHz and f_{o2} = 1.5613 GHz. By substitution in equation (1) and (2), the extracted parameters are $C_{p3} = C_{p4}$ = 6.98 pF and $L_{p3} = L_{p4}$ = 1.48 nH.

Figure 3 compares the simulation results of the equivalent circuit of the proposed design employing the extracted parameters using the advanced design system (ADS) and the electromagnetic (EM) simulation by the computer simulation technology (CST). The used EM simulator is a 3D full wave solver based on a numerical analysis technique using finite difference time domain (FDTD) approach that computes the S-parameters. As a result, acceptable correspondence is observed between the two results.

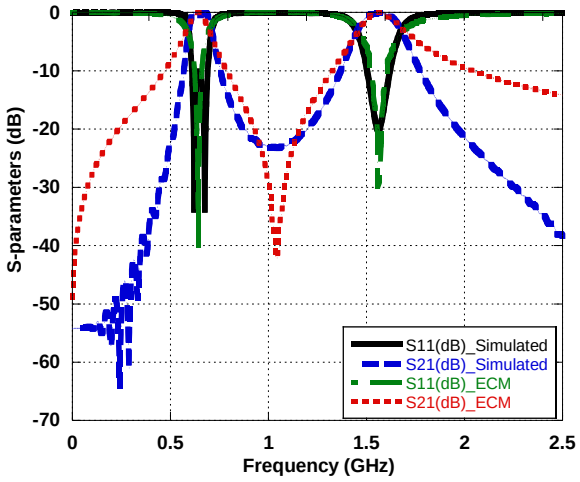

Fig. 3. Comparison between the equivalent circuit (ADS) and EM simulation (CST).

A. The study of transmission distance h

Figure (4) demonstrates the effect of the distance *h* on the S-parameters. To find out the optimum distance amid Tx (transmitter) and Rx (receiver), the transmission distances are examined within multiple ranges at 6 mm, 8 mm, and 10 mm. The splitting between Tx and Rx is noticeable at 6 mm, while the two resonances are acceptable at 10 mm as discussed in [10]. From this study, the 8 mm separation is a suitable transmission distance to be used for this design.

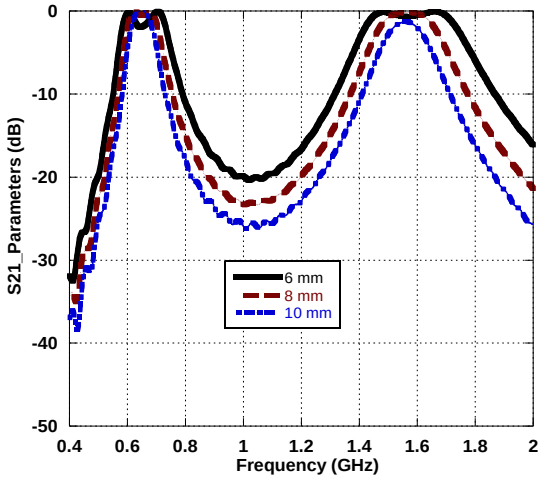

(a)

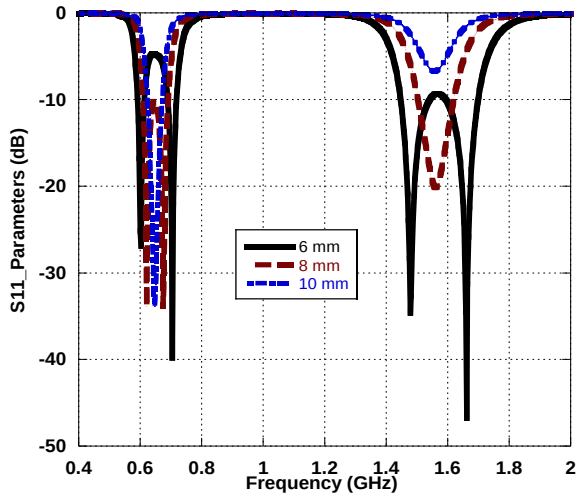

(b)

Fig. 4. The study of transmission distance *h*: (a) S21 parameters and (b) S11 parameters.

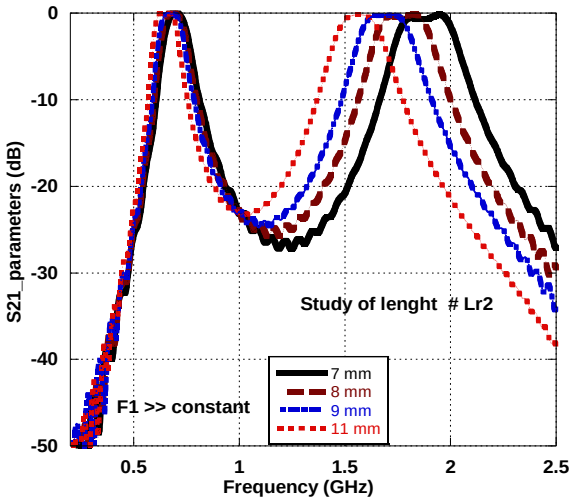

(b)

Fig. 5. Parametric study of the length *Lr2*: (a) S11 parameters and (b) S21 parameters.

B. Parametric study of Lr2

Figure 5 shows the effect of changing the length of *Lr2* from 7 mm to 11 mm. The study displays the changing of the second resonance without any effect on the first resonance frequency. This is suitable for controlling the second resonance while the first resonance is kept constant.

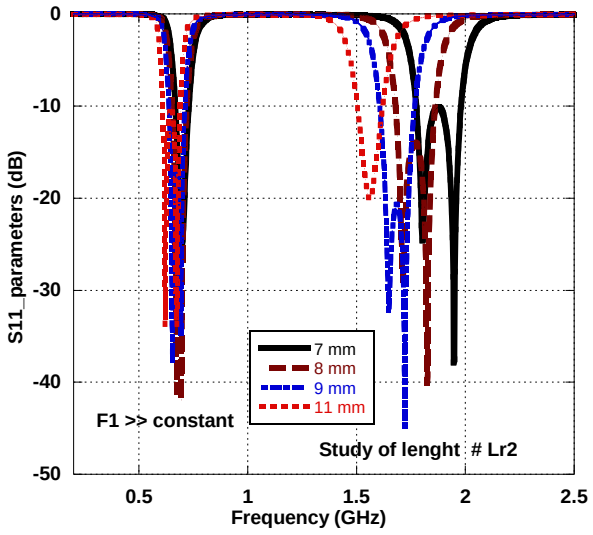

(a)

III. EXPERIMENTAL RESULTS

The proposed construction is fabricated and verified for validations with the specifications in Table 1. The fabrication of the proposed structure was done by a photolithographic method and the layers of the fabricated prototype are shown in Fig. 6 (a). Figure 6 (b) shows the configuration of the proposed structure at a separation distance of 8 mm. The measurements are done using the R&S ZVB20 vector network analyzer. The photograph of the fabricated sample is shown in Fig. 6 (a). Figure 6 (c) shows the comparison of the simulation and the measurements. The obtained measurements are in good correspondence with the simulation as displayed in Fig. 6 (c).

The coupling efficiency (η) of the system is calculated using equation (3) [10,20]. The figure of merits (FoM) demonstrates the performance of the system and calculated using equation (4) [10,20]. The measurement results are presented in Fig. 6 (c). The system achieved efficiencies of 72% and 89% at 0.65 GHz and 1.56 GHz at a transmission distance of 8 mm. The estimated FoMs using equation (4) are 0.288 and 0.356 at 0.65 GHz and 1.56 GHz, respectively:

$$\eta = \frac{|s_{21}|^2}{1-|s_{11}|^2}, \tag{3}$$

$$FoM = \eta \times \frac{h}{\sqrt{A}}, \tag{4}$$

where ɳ is the coupling efficiency and *A* is the total area of the resonator.

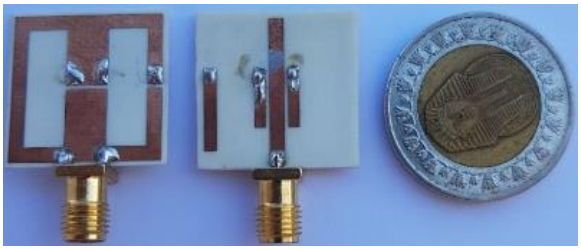

(a)

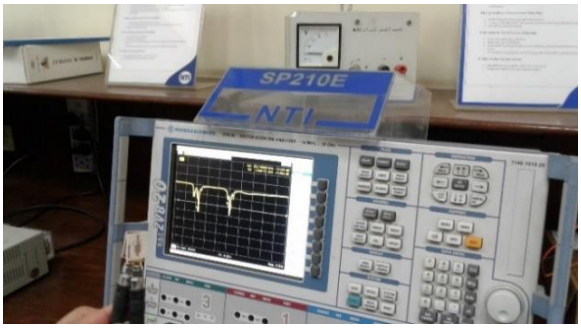

(b)

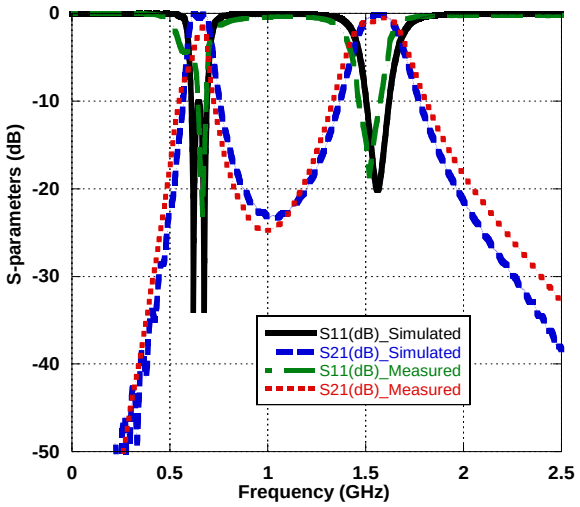

(c)

Fig. 6. The fabricated structure and experimental measurements. (a) Top and bottom views. (b) Measurement setting at a distance of 8 mm. (c) comparison between the measurement and simulation at a distance of 8 mm.

Table 2 offers a comparison between the proposed structure and other recent works in terms of size, FoM, efficiency, and separation distance. From Table 2, the proposed design has worthy FoM and size compared to the previous cited works.

Table 2: The differences between the suggested structure and previous works

System	**[21]**	**[17]**	**[22]**	**This work**
MHz	570 and 2440	0.2 and 6.78	280 and 490	650 and 1560
h (mm)	12	25	6	8
η_{WPT}%	69 and 81	70.6 and 78	91.2 and 79.43	72 and 89
FoM	0.331 and 0.388	0.17 and 0.19	0.27and 0.23	0.288 and 0.356
Size (mm^2)	25 × 25	125 × 89	20 × 20	20 × 20

IV. CONCLUSION

The dual frequency system is designed, analyzed, and fabricated. The system achieved efficiencies of 72% and 89% at 0.65 GHz and 1.56 GHz, correspondingly at 8 mm separation. The system has a compact size which is suitable for recharging electronics devices and biomedical devices. The experimental performance of the suggested design is in an appropriate concurrence with the simulated one.

REFERENCES

[1] M. Ghovanloo and K. Najafi, "A modular 32-site wireless neural stimulation microsystem," *IEEE J. Solid-State Circuits*, vol. 39, no. 12, pp. 2457-2466, Dec. 2004.

[2] S. D. Barman, A. W. Reza, N. Kumar, M. E. Karim, and A. B. Munir, "Wireless powering by magnetic resonant coupling: Recent trends in wireless power transfer system and its applications," *Renew. Sustain. Energy* Rev., vol. 51, pp. 1525-1552, Nov. 2015.

[3] M. Kiani and M. Ghovanloo, "An RFID-based closed-loop wireless power transmission system for biomedical applications," *IEEE Trans. Circuits Syst. II Express Briefs*, vol. 57, no. 4, pp. 260-264, Apr. 2010.

[4] M. Dionigi and M. Mongiardo, "A novel resonator for simultaneous wireless power transfer and near field magnetic communications," *IEEE/MTT-S International Microwave Symposium Digest*, Montreal, QC, Canada, pp. 1-3, June 17-22, 2012.

[5] S. Barmada and M. Tucci, "Theoretical study of different access points in coupled wireless power transfer – powerline communication systems," *Applied Computational Electromagnetics Society (ACES) Journal*, vol. 33, no. 10, pp. 1112-1116, Oct. 2018.

[6] M. Ghovanloo and S. Atluri, "A wide-band power-efficient inductive wireless link for implantable microelectronic devices using multiple carriers,"

IEEE Transactions on Circuits and Systems I: Regular Papers, vol. 54, no. 10, pp. 2211-2221, Oct. 2007.

[7] T. Imura, H. Okabe, and Y. Hori, "Basic experimental study on helical antennas of wireless power transfer for electric vehicles by using magnetic resonant couplings," *2009 IEEE Vehicle Power and Propulsion Conference*, Dearborn, MI, USA, pp. 936-940, Sept. 7-10, 2009.

[8] G. Wang, W. Liu, M. Sivaprakasam, and G. A. Kendir, "Design and analysis of an adaptive transcutaneous power telemetry for biomedical implants," *IEEE Transactions on Circuits and Systems I: Regular Papers*, vol. 52, no. 10, pp. 2109-2117, Oct. 2005.

[9] D. Kim, A. T. Sutinjo, and A. Abu-Siada, "Near-field analysis and design of inductively-coupled wireless power transfer system in FEKO," *Applied Computational Electromagnetics Society (ACES) Journal*, vol. 35, no. 1, pp. 82-93, Jan. 2020.

[10] S. Hekal, A. B. Abdel-Rahman, H. Jia, A. Allam, A. Barakat, and R. K. Pokharel, "A novel technique for compact size wireless power transfer applications using defected ground structures," *IEEE Transactions on Microwave Theory and Techniques*, vol. 65, no. 2, pp. 591-599, Feb. 2017.

[11] F. Tahar, A. Barakat, R. Saad, K. Yoshitomi, and R. K. Pokharel, "Dual-band defected ground structures wireless power transfer system with independent external and inter resonator coupling," *IEEE Transactions on Circuits and Systems II*: *Express Briefs*, vol. 64, no. 12, pp. 1372-1376, Dec. 2017.

[12] H. A. Atallah, "Compact and efficient WPT systems using half-ring resonators (HRRs) for powering electronic devices," *Wireless Power Transfer (WPT)*, vol. 5, no. 2, pp. 105-112, Sept. 2018.

[13] D.-G. Seo, S.-H. Ahn, J.-H. Kim, S.-T. Khang, S.-C. Chae, J.-W. Yu, and W.-S. Lee, "Power transfer efficiency for distance-adaptive wireless power transfer system," *Applied Computational Electromagnetics Society (ACES) Journal*, vol. 33, no. 10, pp. 1171-1174, Oct. 2018.

[14] R. Sharaf, S. Hekal, A. A. EL-Hameed, A. B. Abdel-Rahman, and R. K. Pokharel, "A new compact wireless power transfer system using C-shaped printed resonators," *2016 IEEE International Conference on Electronics, Circuits and Systems (ICECS)*, Monte Carlo, Monaco, France, pp. 321-323, Dec. 2016.

[15] R. Hussein, H. A. Atallah, S. Hekal, and A. B. Abdel-Rahman, "A new design for compact size wireless power transfer applications using spiral defected ground structures," *Radioengineering*, vol. 27, no. 4, pp. 1032-1037, Sept. 2018.

[16] A. Barakat, K. Yoshitomi, and R. K. Pokharel, "Design and implementation of dual-mode inductors for dual-band wireless power transfer systems," *IEEE Transactions on Circuits and Systems II: Express Briefs*, vol. 66, no. 8, pp. 1287-1291, Aug. 2019.

[17] D. Ahn and P. P. Mercier, "Wireless power transfer with concurrent 200-kHz and 6.78-MHz operation in a single-transmitter device," *IEEE Transactions on Power Electronics*, vol. 31, no. 7, pp. 5018-5029, July 2016.

[18] H. A. Atallah, R. Hussein, and A. B. Abdel-Rahman, "Novel and compact design of capacitively loaded c-shaped DGS resonators for dual band wireless power transfer (DB-WPT) Systems," *AEU-International Journal of Electronics and Communications*, vol. 100, pp. 95-105, Feb. 2019.

[19] D. Wang and R. Negra, "Design of a dual-band rectifier for wireless power transmission," 2013 *IEEE Wireless Power Transfer (WPT)*, Perugia, Italy, pp. 127-130, May 15-16, 2013.

[20] S. Verma, D. Rano, and M. Hashmi, "Enhancing the performance of defected ground structure type near-field radiofrequency WPT system by coupled-line impedance matching," *IET Microwaves, Antennas & Propagation*, vol. 14, no. 12, pp. 1431-1439, Oct. 2020.

[21] M. M. A. El-negm, H. A. Atallah, and A. B. Abdel-rahman, "Design of dual-band coupled resonators using complementary split ring resonators defected ground structure (CSRRS-DGS) for wireless power transfer applications," *2020 36th National Radio Science Conference*, Cairo, Egypt, pp. 22-27, June 2019.

[22] H. A. Atallah, R. Hussein, and A. B. Abdel-Rahman, "Compact coupled resonators for small size dual-frequency wireless power transfer (DF-WPT) systems," *IET Microwaves, Antennas & Propagation*, vol. 14, no. 7, pp. 617-628, May 2020.

Hany A. Atallah was born in Qena, Egypt in 1984. He received his B.Sc. and M.Sc. in Electrical Engineering, Electronics and Communications from South Valley University, Egypt, in 2007 and 2012, respectively. The Ph.D. degree in Antennas and Microwave Engineering at Egypt–Japan University for Science and Technology (E-JUST). He is currently working as an Assistant Professor at the Electrical Engineering Department, Qena Faculty of Engineering, South Valley University. He was a Visiting Researcher with the E-JUST Lab, School of Information

Science and Electrical Engineering, Kyushu University, Japan, from September 2015 to July 2016. His research interests include antenna design, dielectric resonators, metamaterials, tunable filters, reconfigurable antennas, antenna arrays, microwave filters, and FDTD. His recent research has been on cognitive radio (CR) antennas, wireless power transfer (WPT) for biomedical implants, electric vehicles, and electronic devices, breast cancer detection, smart meters, and the internet of things (IoT).

Musallam Alzubi was born in Kuwait. He received his B.Sc. in Electrical Engineering, Electronics and communication from Al-Ahliyya Amman University, Jordan, in 2016. He is currently working toward his M.Sc. at the Electrical Engineering Department, Qena Faculty of Engineering, South Valley University. He is currently working at Ministry of Communications at Kuwait. His research interests include filter design, and wireless power transfer (WPT) for biomedical implants and electronic devices.

Rasha Hussein was born in Qena, Egypt. She received her B.Sc. in Electrical Engineering, Electronics and communication from South Valley University, Egypt, in 2015. She is currently working as a Teaching Assistant at the Electrical Engineering Department, Qena Faculty of Engineering, South Valley University. Her research interests include antenna design, filter design, and wireless power transfer (WPT) for biomedical implants and electronic devices.

Adel B. AbdelRhman was born in Aswan, Egypt, in 1968. He received the B.Sc. and M.Sc. degrees in Electrical Engineering, Communication and Electronics, Assuit University, Egypt, in 1991 and 1998, respectively. The Ph.D. degree in Microwave Engineering at the University of Magdeburg, Magdeburg, Germany. He is currently working as Assoc. Prof. at the E-JUST, Alexandria, Egypt-on leave from the South Valley University, Qena 83523, Egypt. His research interests include the design and analysis of microstrip antennas, filters, and its application in WLAN and mobile communication. His recent research has been on cognitive radios, wireless power transfer, and on-chip antennas.

In Vitro Physical and Biological Evaluations of a 2.4 GHz Electromagnetic Exposure Setup

Mengxi Wang [1,2], Guohui Yang [2], Yu Li [3], and Qun Wu [2,*]

[1] The Fourth Affiliated Hospital of Harbin Medical University, Harbin 150001, China

[2] School of Electronic and Information Engineering, Harbin Institute of Technology, Harbin 150001, China

[3] Department of Life Science and Engineering, Harbin Institute of Technology, Harbin 150001, China
*qwu@hit.edu.cn

Abstract — In this paper, a 2.4 GHz electromagnetic radiation system for cells in vitro was designed from the perspective of optimal energy coupling of cell samples. The validity of the design was verified by FDTD simulation, physical test and biological experiment. The electromagnetic parameters of SAR (Specific Absorption Rate) and temperature rise were obtained by FDTD simulation. The validation of temperature simulation was confirmed by comparing the actual measurement data and the simulation data. The SAR relative uniformity between samples was tested by cell biological experiment, in which ROS (Reactive Oxygen Species), a typical and sensitive biological parameter reacting to electromagnetic radiation in cells, of different sample dishes induced by 2.4 GHz electromagnetic radiation with an incident power of 0.5 W was analyzed. We found that the size of cell dish affects the energy coupling intensity, the polarization characteristics of electromagnetic wave determines the distribution pattern of SAR, and the uniformity of sample energy absorption in this radiation system is good.

I. INTRODUCTION

In the electromagnetic radiation experiments of cells in vitro, the cell samples and their containers (such as test tubes [1], flasks [2] and dishes [3]) are generally placed in the radiation system to observe and test the biological effects of electromagnetic radiation. The cell radiation systems in vitro mainly include: TEM (Transverse Electromagnetic) cell [4], waveguide cavity [5], WPC (Wire Patch Cell) device [6], anechoic chamber [7], etc..

Some achievements have been made in the design and research of the radiation system so far, but there are still difficult points and deficiencies, which are mainly reflected in the following aspects: ① Most radiation devices could not guarantee the basic environment of the cell survival, such as constant temperature, humidity, carbon dioxide, oxygen, sterility, etc., which results in large systematic error of biology experiment results. ② Generally, most of the cells cultured in vitro have the characteristics of adherent growth and growth inhibition, which means that the cells will adhere to the bottom of the container and grow into a monolayer with a thickness of 5-10 μm. The sensitivity of the existing test instruments can hardly obtain the actual data of electric field intensity and SAR value in the cell layer. Even if the data is detected, the error is large. ③ Although the structure of the cell layer and cell samples is simple, it is difficult to obtain uniform radiation field in a cell layer, especially the uniformity of SAR between multiple samples in one radiation system. There is a lack of biological verification study on the influence of non-uniformity of SAR on biological results. ④ Lacking of standards for radiation environment, radiation mode, excitation source, spatial location relationship and size and sample coupling direction, results in poor repeatability and reliability of the biological conclusions. Hence, it is necessary to design a 2.4 GHz electromagnetic radiation system for cells in vitro, and comprehensively investigate the rationality and effectiveness of the design combined with biological and physical verification methods.

In daily life, the electromagnetic waves we exposed to are mostly 2.4 GHz uniform plane waves, and the polarization modes of the uniform plane waves are mainly linear polarization and circular polarization. The industrial microwave heating equipment and medical physiotherapy equipment in ISM (Industrial Scientific Medical) frequency band also produce Gaussian pulse waveform. Furthermore, it is found that the size of biological samples also affects the energy absorption of electromagnetic waves [8]. Considering that the characteristics of electromagnetic waves and sample size might influence the energy coupling in cell samples, the polarization and waveform characteristics of 2.4 GHz electromagnetic waves and the diameter of cell dishes were set as variable quantities in FDTD simulation of this study to get a comprehensive understanding of the essential factors that determine the interaction between

Submitted On: September 23, 2020
Accepted On: December 6, 2020

https://doi.org/10.47037/2020.ACES.J.360112

electromagnetic waves and biological samples.

II. CELL DISH MODEL

The basic requirements of the sample containers for cell radiation experiment are large bottom area with enough cells, low center of gravity and easy to set into the radiation system. Among the numerous containers for in vitro cell culture, the bottom of a test tube is hemispherical, and a special scaffold is needed to hold in place. The height of a culture flask is large and not easy to be placed into the radiation system. The cell dishes are low in height, large in bottom area and stable in placement. Hence, cell dishes are ideal containers for cell radiation experiment. The common cell dish types are 35-mm and 60-mm.

As shown in Fig. 1, the 60-mm cell dish with no lid was modeled as a hollow cylinder with an outer radius of 30 mm, an inner radius of 28.5 mm, a wall thickness of 1.5 mm and a height of 15 mm. The culture medium was modeled as a solid cylinder with a height of 1.6 mm. The radius of the culture medium cylinder was the same as the inner radius of the cell dish. The volume of the culture medium was 4 mL (a conventional amount in 60-mm cell dish). The electrical properties and thermal parameters are given in Table 1.

Table 1: Electrical properties and thermal parameters of materials at 37°C 2.4 GHz [7,9]

	ε_r	σ (Sm^{-1})	C (kJ $(kg°C)^{-1}$)	K (W $(km)^{-1}$)	ρ (kgm^{-3})
Medium	71	2.5	4.2	0.6	1000
Petri dish	2.5	0.001	0.12	L2	1100

The modeling of the 35-mm cell dish was similar to that of the 60-mm cell dish model. The outer diameter of the 35-mm cell dish was 35 mm, and the inner diameter was 32 mm. The wall thickness was 1.5 mm, and the height of the cell dish was 10 mm. The volume of the culture medium was 2 mL (a conventional amount in 35-mm cell dish).

There is an adherent cell monolayer between the cell dish and the culture medium. The thickness of the cell monolayer is the cell diameter, generally 5-10 μm. For such a thin cell layer, there are two methods of modeling. The first one is non-uniform grid modeling: set the grid height at 10 μm for the cell layer, then gradually increase the grid size from the cell layer to outwards. But the starting base of the grid size is too small, the design and calculation of the grid are very cumbersome. The second method is to design a uniform grid. If the grid is set according to the actual thickness of the cell layer of 10 μm, there will be too many calculations even for computers. Zhao [10] confirmed that for highly dissipative materials, the spatial step size around 0.1 mm would be small enough to reduce the finite differential error to an acceptable level. Considering the storage capacity and computing time of the computer, the space step size should be properly selected. Consequently, in this paper, uniform space step of 0.1 mm was used to model the cell dish, cell layer, culture medium and surrounding space, and a layer of grid above the inner bottom wall of the cell dish was set as the cell layer (Fig. 1 (b)).

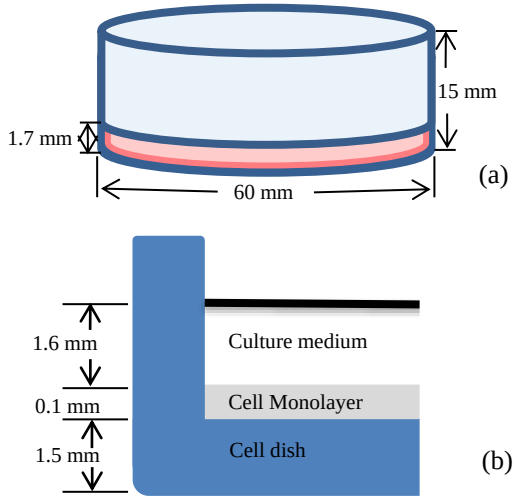

Fig. 1. 60-mm cell dish model: (a) cell dish size, and (b) local size of the cell dish.

MC3T3-E1 cells of mouse osteoblastic cell line were chosen as the cell samples for this electromagnetic radiation experiment. MC3T3-E1 cells in the induction culture have the characteristics of proliferation, differentiation and mineralization, consequently, the dielectric constant of the cell layer is changing in different periods of cell radiation experiments. The dielectric constant of osteoblasts could not be accurately calculated, nor could the dielectric constant of other cells or bone tissue be directly used for simulation. Considering that the energy transfer and heat production of the cell layer could be ignored [11], and the composition of the culture medium is very close to that of most cells in vitro, the dielectric constant of the cell layer was set the same to the dielectric constant of the culture medium.

III. EFFECT OF CELL DISH SIZE ON SAR DISTRIBUTION

The 35-mm and 60-mm cell dish models were respectively radiated by 2.4 GHz linearly polarized plane wave. The wave source was located right below the cell dish, and the PML boundary condition was used to simulate the distribution of SAR values in the cell layer of a single cell dish model in an infinite space.

The distribution of SAR values in one single cell dish were simulated by FDTD solutions. As shown in Fig. 2 and Fig. 3, the trend of SAR distribution in the cell layer of 35-mm cell dish and 60-mm cell dish is similar. However, the size of the cell dish can affect the aggregation intensity of electromagnetic waves in the

cell layer. The relatively high SAR values in the cell layer of the 60-mm cell dish account for more proportion than that of the 35-mm cell dish, which means the energy coupling effect of the cell layer in 60-mm cell dish is higher than that in 35-mm cell dish. Therefore, it is more likely to start the bioelectromagnetic effect of cells in 60-mm dish at 2.4 GHz.

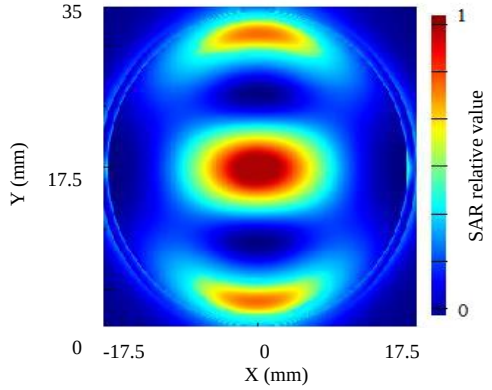

Fig. 2. SAR distribution in the cell layer of 35-mm dish at XOY plane with 2.4 GHz linear polarization plane wave.

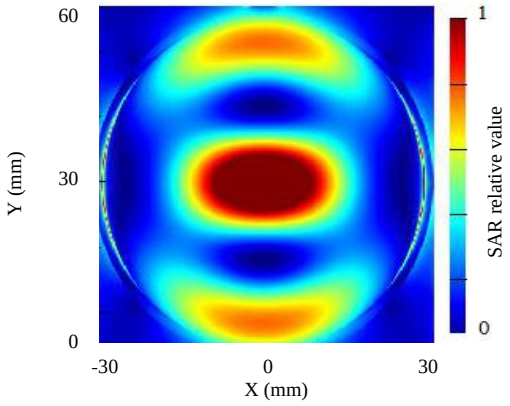

Fig. 3. SAR distribution in the cell layer of 60-mm dish at XOY plane with 2.4 GHz linear polarization plane wave.

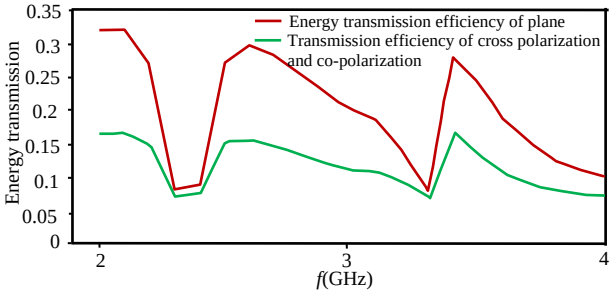

Fig. 4. The energy transmission efficiency of 2 GHz~4 GHz linear polarization plane wave through 60-mm dish sample model.

It can be seen from Fig. 4 that the overall energy transmission efficiency of 2 GHz~4 GHz linear polarization plane wave is basically below 30%, which means that the residual energy is less than 30% of the original incident energy after passing through the 60-mm cell dish, cell layer and culture medium. In the frequency range of 2 GHz~4 GHz, the transmission efficiency of co-polarization and cross polarization waves is the same. At 2.4 GHz, the overall energy transmission efficiency curve of linear polarization plane wave reaches the lowest point (less than 10%). Consequently, the 60-mm sample model has a significant energy absorption of linear polarization plane wave at 2.4 GHz, and more than 90% of the energy is absorbed by the sample dish model.

IV. EFFECT OF WAVEFORM ON SAR DISTRIBUTION

The SAR distribution in the cell layer of a single 60-mm dish model with 2.4 GHz linear polarization Gaussian wave is shown in Fig. 5. From the comparison of SAR distribution in Fig. 5 and Fig. 3, it can be concluded that wave forms have mild effect on the distribution pattern of SAR in the cell layer of the 60-mm cell dish model.

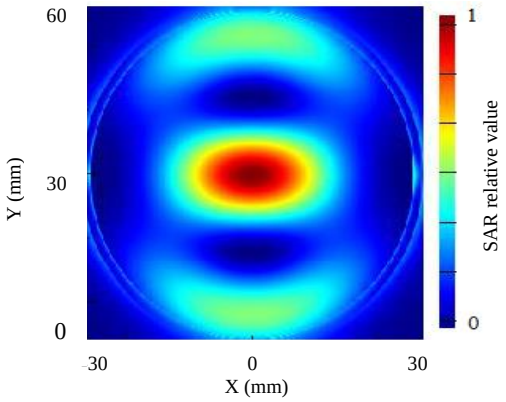

Fig. 5. SAR distribution in the cell of 60-mm dish at XOY plane with 2.4 GHz linear polarization Gaussian wave.

V. EFFECT OF POLARIZATION MODE ON SAR DISTRIBUTION

The cell layer SAR distribution of a single 60-mm dish model with 2.4 GHz circular polarization plane wave and circular polarization Gaussian wave is shown in Fig. 6 and Fig. 7.

As shown in Fig. 3, Fig. 5, Fig. 6 and Fig. 7, the polarization characteristics of 2.4 GHz electromagnetic waves are the main factors to the distribution pattern of SAR, while the waveforms have mild effect on the distribution pattern of SAR.

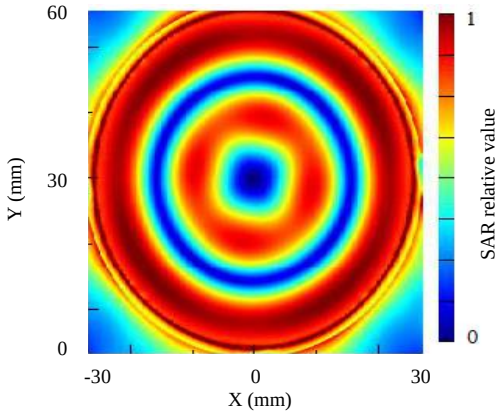

Fig. 6. SAR distribution in the cell layer of 60-mm dish model at XOY plane with 2.4 GHz circular polarization plane wave.

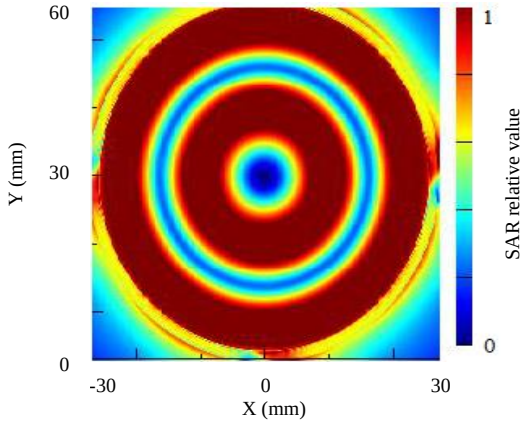

Fig. 7. SAR distribution in the cell layer of 60-mm dish model at XOY plane with 2.4 GHz circular polarization Gaussian wave.

VI. CELL RADIATION MODELING SYSTEM

The basic requirements of an ideal biological sample radiation system are: ① A stable air environment with constant temperature, humidity, carbon dioxide and oxygen and free from germs to ensure the basic living conditions for cells in vitro. ② A stable radiation environment with relatively uniform SAR values between samples and no interference of external radiation signal. ③ Multiple sample containers can be accommodated in the radiation system to provide an adequate amount of samples. ④ Maximize energy coupling of the samples can be achieved, so that the biological effects can be started easily.

It has been found that when the ratio between the sample size and wavelength is 0.4:1, the energy coupling effect is the best [8]. The wave length of 2.4 GHz electromagnetic wave is 12.24 cm, therefore the optimal size of sample is about 5 cm. The 60-mm cell dish with an inner diameter of 5.7 cm is the best cell container close to the optimal size. In part III of this study, it has been verified that the energy coupling effect of the cell layer in 60-mm cell dish is better than that in 35-mm cell dish. In order to increase the total amount of samples, six 60-mm cell dishes were set in the radiation system. The culture medium is right above the monolayer of adherent cells in the cell dish. The frequency of 2.4 GHz is 1/10 of the resonance frequency of water molecules. Water in the culture medium will strongly absorb the 2.4 GHz electromagnetic radiation. Therefore, the signal transmitting antenna was placed 3 cm below the cell dish to reduce the radiation loss and distance attenuation and to ensure a convective space. In order to achieve the maximum energy absorption and radiation uniformity, the signal transmitting antenna was placed perpendicular to the cell layer [13], as shown in Fig. 8.

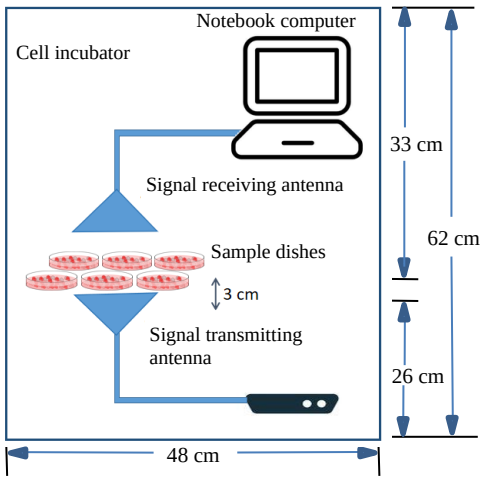

Fig. 8. Sketch map of sample placement in the cell incubator.

The environment of constant temperature, humidity, carbon dioxide and oxygen concentration and free from germs inside the cell incubator is the most ideal environment for cell culture. The double-layer metal shell of the cell incubator can also shield the interference of external electromagnetic waves, which meets the requirements of the radiation environment for the bioelectromagnetic experiments. The samples and the radiation equipment were placed in the cell incubator for cell radiation experiments, and the whole system could be considered as a TEM chamber. According to the requirements for the experimental space of the TEM chamber, the sample size should be less than 1/8 of the chamber size. Therefore, the length of the cell incubator used for cell radiation should not be less than 48 cm. According to the size of the incubator and the cell samples and the position of the radiation system components in the cell incubator, the 1:1 modeling was

built up (Fig. 8).

The temperature rise of cell layer was obtained by MATLAB software combined with the electric field strength simulated by FDTD solutions and biological heat conduction equation which has been deduced in our previous research [12]. 2.4 GHz plane wave was used in simulation, since all electromagnetic waves could be expanded by plane wave, which is similar to the sine component of Fourier expansion. The power intensity was set to 0.1 W and 0.5 W, and average SAR values of the cell layers are 0.17 W/Kg and 0.84 W/Kg respectively (Table 2).

Table 2: The SAR average and standard deviation of the cell layers in the six dishes

		1	2	3	4	5	6	Total
0.1W	Mean (W/Kg)	0.2519	0.2519	0.1387	0.1387	0.1107	0.1107	0.1671
	Deviation	0.1041	0.1041	0.0547	0.0847	0.0433	0.0433	0.0674
0.5W	Mean (W/Kg)	1.2594	1.2595	0.6936	0.6936	0.5537	0.5537	0.8356
	Deviation	0.5203	0.5203	0.2733	0.2733	0.2164	0.2194	0.3367

The general temperature trend of the cell monolayers of six cell dishes within 180 minutes is shown in Fig. 9. The temperature trend of the maximum temperature point of the cell monolayers within 180 minutes is shown in Fig. 10. The heat balance point is around 90 min. The maximum temperature rise point of cell layer is 0.2°C of 0.1 W 2.4 GHz plane wave, and 1.1°C of 0.5 W 2.4 GHz plane wave.

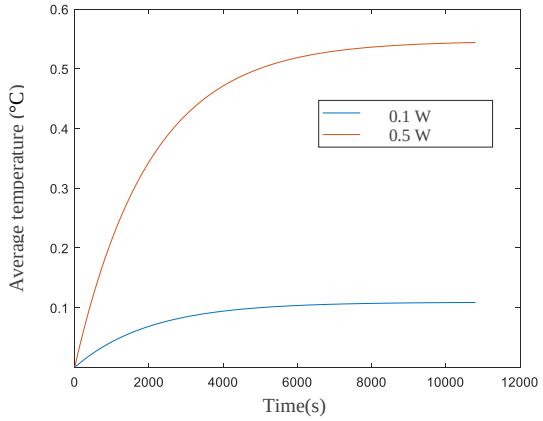

Fig. 9. General temperature trend of the cell monolayers of six cell dishes within 180 minutes.

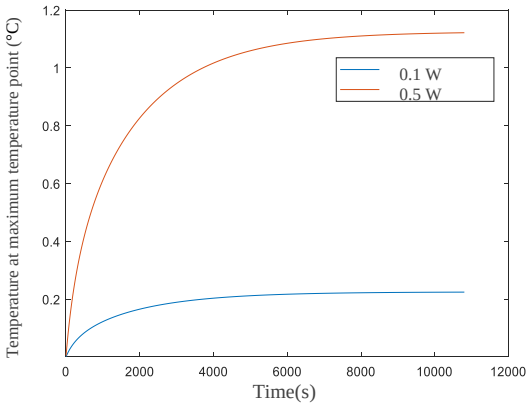

Fig. 10. Temperature trend of the maximum temperature point within 180 minutes.

VII. PHYSICAL VALIDATION

In an open space, 2.4 GHz plane wave was vertically radiated from the bottom of a single 60-mm sample dish. The power density values on the culture medium surface were measured at three random points, and the average value of the three random points was recorded. The energy transmission efficiency calculated from one average value of the power density was considered as one effective data. The energy transmission efficiency data were calculated and recorded for three times, then compared with the theoretical value of 2.4 GHz plane wave energy transmission efficiency obtained by FDTD simulation. It can be seen from Fig. 11 that the measured values of the energy transmission efficiency of 2.4 GHz plane wave are close to the theoretical value, and the simulated and measured energy absorption efficiency of samples are both more than 90%.

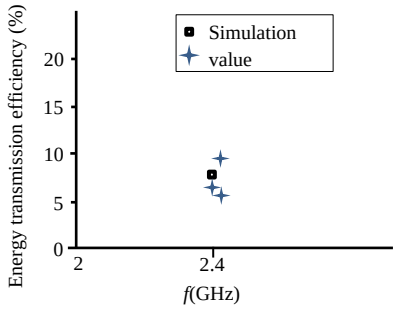

Fig. 11. Comparison between simulated theoretical value and measured value of the energy transmission efficiency.

In the cell radiation system, the temperature rise values of the cell layers in six dishes were measured, and the average values were recorded every 10 minutes, then compared with the simulated temperature rise. As shown in Fig. 12, the theoretical temperature rise trend is in good agreement with the measured temperature rise trend.

VIII. BIOLOGICAL VALIDATION

As shown in Table 2, the SAR values between cell

dishes are not identical. The thermal effect of 2.4 GHz electromagnetic radiation increases the temperature of the maximum temperature point of cell layer about 1°C with 0.5 W incident power (Fig. 10). The influence of the inhomogeneity of SAR between samples and the temperature rise in cell layers caused by the thermal effect of 2.4 GHz electromagnetic radiation on the biological experiment results need to be analyzed by cell biological experiments.

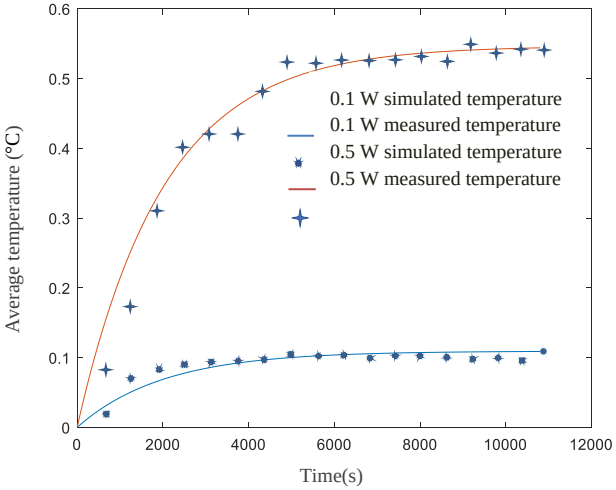

Fig. 12. Comparison between simulated theoretical temperature rise value and measured value.

ROS is a typical and sensitive biological parameter reacting to electromagnetic radiation [14]. Therefore, ROS was used to investigate the response of cells in six dishes to 2.4 GHz plane wave with an incident power of 0.5 W.

MC3T3-E1 cells induced by conditional culture were irradiated with 0.5 W 2.4 GHz plane wave for 90 minutes in a 37°C incubator. ROS was detected immediately after the 90-min irradiation. The amounts of ROS in the six cell dishes were recorded as 1#, 2#, 3#, 4#, 5# and 6#, respectively. Labeling sequence of the cell dishes was the same as Table 2. In the control group, the cell incubator temperature was 37°C, the radiation equipment was not turned on, and the ROS was measured. In the sham group, the cell incubator temperature was 37°C, the radiation equipment was turned on, but with no signal transmission, and the ROS was measured after the 90-min irradiation. In the T+1°C group, the radiation equipment was not turned on, but the temperature of the cell incubator increased to 38°C, and the ROS was measured after 90 minutes. The statistical results of experimental data are shown in Fig. 13.

As shown in Fig. 13, there is no significant difference between the T+1°C group and the control group, so the change of ROS is caused by the "non-thermal effect" of 2.4 GHz 0.5W plane wave irradiation, rather than the "thermal effect". There is no significant difference between the control group and the sham group, therefore the influence of heating from the radiation equipment and antenna on the biological experimental results can be excluded. Although the ROS levels of 1#, 2#, 3#, 4#, 5# and 6# cell dishes are statistically different from those of sham group, control group and T+1°C group, there is no significant difference among 1# to 6# cell dishes, which is equivalent to using a biological experiment method to verify the uniformity of sample energy absorption in the radiation system.

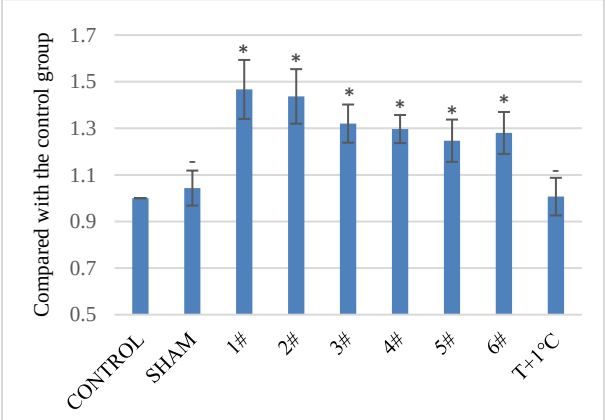

Fig. 13. ROS relative level in cells after 90-min 2.4 GHz 0.5W plane wave irradiation ($p \geq 0.05$ -, $p < 0.05$ *).

IX. CONCLUSION

A 2.4 GHz electromagnetic radiation system for cells in vitro was designed from the perspective of energy coupling of cell samples, and the parameters were optimized. This design could not only guarantee the basic environment of the cell survival but also the relatively consistent of radiation absorption between the samples on biological results. In the future, the different frequency bands and antennas and the signal processing method can be used for the experiments and data acquisition [15-21].

REFERENCES

[1] B. Çiğ and M. Nazıroğlu, "Investigation of the effects of distance from sources on apoptosis, oxidative stress and cytosolic calcium accumulation via TRPV1 channels induced by mobile phones and Wi-Fi in breast cancer cells," [J]. *Biochimica et Biophysica Acta (BBA)-Biomembranes*, vol. 1848, no. 10, pp. 2756-2765, Oct. 2015.

[2] J. Zhao and H. Lu, "Meniscus effect on the in vitro dosimetry of the T25 flask under 2.45 and 5.25 GHz exposures," [J]. *IEEE Microwave and Wireless Components Letters*, vol. 23, no. 2, pp. 105-107, Feb. 2013.

[3] J. Schuderer, T. Samaras, W. Oesch, D. Spat, and N. Kuster, "High peak SAR exposure unit with

tight exposure and environmental control for in vitro experiments at 1800 MHz," [J]. *IEEE Transactions on Microwave Theory and Techniques*, vol. 52, no. 8, pp. 2057-2066, Aug. 2004.

[4] N. Nikoloski, J. Fröhlich, T. Samaras, J. Schuderer, and N. Kuster, "Reevaluation and improved design of the TEM cell in vitro exposure unit for replication studies," [J]. *Bioelectromagnetics*, vol. 26, no. 3, pp. 215-24, Apr. 2005.

[5] P. Valbonesi, S. Franzellitti, F. Bersani, A. Contin, and E. Fabbri, "Activity and expression of Acetylcho-linesterase in PC12 cells exposed to intermittent 1.8 GHz 217-GSM mobile phone signal," [J]. *International Journal of Radiation of Radiation Biology*, vol. 92, no. 1, pp. 1-10, Jan. 2016.

[6] A. Paffi, M. Liberti, V. Lopresto, C. Merla, R. Lodato, G. A. Lovisolo, F. A. Apollonio, "Wire patch cell exposure system for in vitro experiments at Wi-Fi frequencies," [J]. *IEEE Transactions on Microwave Theory & Techniques*, vol. 58, no. 12, pp. 4086-4093, Dec. 2010.

[7] A. Collin, M. Cueille, A. Perrin, C. Pivain, and P. Lévêque, "Electromagnetic dosimetry and thermal analysis of a new exposure setup for in vitro studies on a large frequency band," [C]. *2007 IEEE/MTT-S International Microwave Symposium*, pp. 2221-2224, 2007.

[8] B. J. Klauenberg, M. Grandolfo, and D. N. Erwin, *Radiofrequency Radiation Standards: Biological Effects, Dosimetry, Epidemiology, and Public Health Policy*, [M]. Plenum Press, pp. 245-269, 1995.

[9] A. Paffi, M. Liberti, F. Apollonio, A. Sheppard, and Q. Balzano, "In vitro exposure: Linear and non-linear thermodynamic events in Petri dishes," [J]. *Bioelectromagnetics*, vol. 36, no. 7, pp. 527-37, Oct. 2015.

[10] J. Zhao, "In vitro dosimetry and temperature evaluations of a typical millimeter-wave aperture-field exposure setup," [J]. *IEEE Transactions on Microwave Theory and Techniques*, vol. 60, no. 11, pp. 3608-3622, Nov. 2012.

[11] M. Zhadobov, S. I. Alekseev, R. Sauleau, Y. Le Page, Y. Le Dréan, and E. E. Fesenko, "Microscale temperature and SAR measurements in cell monolayer models exposed to millimeter waves," [J]. *Bioelectromagnetics*, vol. 38, no. 1, pp. 11-21, Jan. 2017.

[12] W. Mengxi, Y. Guohui, L. Yu, W. Qun, and L. Yingsong, "Protective role of vitamin C in Wi-Fi-induced oxidative stress in MC3T3-E1 cells in vitro," [J]. *The Applied Computational Electromagnetics Society Journal*, vol. 35, no. 5, pp. 587-594, May 2020.

[13] M. Sangeetha, B. M. Purushothaman, and S. S. Babu, "Estimating cell phone signal intensity and identifying radiation hotspot area for tirunel veli taluk using RS and GIS," [J]. *International Journal of Research in Engineering and Technology*, vol. 3, no. 2, pp. 412-418, Feb. 2014.

[14] S. Shokri, A. Soltani, M. Kazemi, D. Sardari, and F. B. Mofrad, "Effects of Wi-Fi (2.45 GHz) exposure on apoptosis, sperm parameters and testicular histomorphometry in rats: A time course study," [J]. *Cell Journal (Yakhteh)*, vol. 17, no. 2, pp. 322-331, Summer 2015.

[15] Y. Li, W. Li, and Q. Ye, "A reconfigurable triple notch band antenna integrated with defected micro-strip structure band-stop filter for ultra-wideband cognitive radio applications," *International Journal of Antennas and Propagation*, vol. 2013, Article ID: 472645, pp. 1-13, 2013.

[16] Y. Li, W. Li, and W. Yu, "A multi-band/UWB MIMO/diversity antenna with an enhance isolation using radial stub loaded resonator," *Applied Computational Electromagnetics Society Journal*, vol. 28, no. 1, pp. 8-20, 2013.

[17] Y. Li, W. Li, and W. Yu, "A switchable UWB slot antenna using SIS-HSIR and SIS-SIR for multi-mode wireless communications applications," *Applied Computational Electromagnetics Society Journal*, vol. 27, no. 4, pp. 340-351, 2012.

[18] T. Jiang, T. Jiao, Y. Li, and W. Yu, "A low mutual coupling MIMO antenna using periodic multi-layered electromagnetic band gap structures," *Applied Computational Electromagnetics Society Journal*, vol. 33, no. 3, pp. 305-311, 2018.

[19] S. Luo, Y. Li, Y. Xia, and L. Zhang, "A low mutual coupling antenna array with gain enhancement using metamaterial loading and neutralization line structure," *Applied Computational Electromagnetics Society Journal*, vol. 33, no. 3, pp. 411-418, 2018.

[20] Y. Li, Z. Jiang, W. Shi, X. Han, and B. D. Chen, "Blocked maximum correntropy criterion algorithm for cluster-sparse system identification," *IEEE Transactions on Circuits and Systems II: Express Briefs*, vol. 66, no. 1, pp. 1915-1919, 2020.

[21] T. Liang, Y. Li, W. Xue, Y. Li, and T. Jiang, "Performance and analysis of recursive constrained least Lncosh algorithm under impulsive noises," *IEEE Transactions on Circuits and Systems II: Express Briefs*, 10.1109/TCSII.2020.3037877.

Dual-Band BSF with Enhanced Quality Factor

Asmaa E. Farahat and Khalid F. A. Hussein

Microwave Engineering Department
Electronics Research Institute, Cairo, 11843, Egypt
asmaa@eri.sci.eg, khalid_elgabaly@yahoo.com

Abstract ─ In the present work, a U-shaped CPW resonator (CPWR) with, generally, unequal arms is proposed to produce high Q-factor bandstop filter (BSF) based on broadside-coupling between the CPWR and a CPW through-line (CPWTL), which are printed on opposite faces of a thin substrate. The unequal arms of the U-shape and the finite width of the ground strips of the CPWR are shown to produce much higher Q-factor than that of equal arms and infinitely extending side ground planes. The dimensions of the CPWTL are optimized for impedance matching while the dimensions of the CPWR are optimized to obtain the highest Q-factor. The effect of the loss tangent of the dielectric substrate material on the Q-factor is investigated. It is shown that the difference between the lengths of the unequal arms of the U-shaped resonator can be used to control the Q-factor. Thanks to the computational efficiency of the employed electromagnetic simulator, enough number of trials has been successfully performed in reasonable time to arrive at the final design of the BSF. A prototype of the proposed BSF is fabricated for experimental investigation of its performance. The experimental measurements show good agreement when compared with the corresponding simulation results.

Index Terms ─ Bandstop filter, CPW resonator, dual-band filter, high Q-factor.

I. INTRODUCTION

High Q-factor bandpass and bandstop filters can be designed from microwave resonators such as such as printed transmission lines, two and three dimensional cavities such as printed slots and patches. Microwave high Q-factor bandstop filters (BSFs) have been widely used in communication systems for rejecting unwanted frequency signals to enhance the system performance [1-4]. For example, the BSF in the transceiver of the ground station of a satellite communication system. The BSFs are often needed in the frond-end to pass the downlink signals received by the ground station antenna and to block the uplink signals originated at the transmitting antenna of the same ground station. Multiple-band BSFs are required for many applications [5-10].

The principal advantage of CPW is that the signal line and the signal grounds are placed on the same substrate surface. This reduces the dielectric losses and eliminates the need for via holes which simplifies the circuit fabrication. Moreover, the absence of via holes allows simple connection of series as well as shunt components [11-13]. Also, the CPW exhibits lower conductor loss than microstrip lines which is a major advantage [14], [15].

CPW circuits design can be based on both the odd and the even CPW modes [16]. Moreover, CPWs are open structures, and do not require metallic enclosures [17]. Resonators composed of CPW have their distributed element construction avoiding uncontrolled stray inductances and capacitances, and, thereby, have better microwave properties than lumped element resonators.

Q-factor improvement of BSFs has been achieved in literature using printed transmission lines with defected ground structure (DGS) [18-21]. However, the achieved Q-factor is always limited to a few dozens or even lower with some complexity of the structure and needs for lumped elements. The end-coupled and edge-coupled CPW resonator structures are commonly used for microwave and millimeter-wave filter design [22]. The interchange of energy in the end-coupled resonators with the coupling gap may be insufficient, even when very narrow gaps are employed. Due to this reason parallel- or edge-coupled CPWRs are more commonly used than end-coupled CPWRs [22]. However, broadside coupling results in the strongest coupling among all these coupling methods [5]. In [23], a U-shaped CPWR of equal arms has been used to produce high Q-factor BSF. The present work employs U-shaped CPWR of unequal arms to get higher Q-factor. Moreover, the proposed resonator enables more control of the Q-factor by properly setting the difference between the arm lengths of the U-shaped resonator. In the BSF proposed in this work, the CPWR is printed on the bottom layer of the dielectric substrate and the CPW through-line (CPWTL) on the top layer, which enables enhanced broadside coupling. This structure has the advantage that the length over which the broadside coupling is achieved can be easily set to get

Submitted On: December 24, 2019
Accepted On: November 30, 2020

https://doi.org/10.47037/2020.ACES.J.360113

the required bandwidth of the BSF or, equivalently, the Q-factor. Another advantage is that the length of the CPWR is simply set to tune the center frequency of the stop band. Moreover, the input impedance of the CPWTL is not sensitive to the substrate thickness, which allows impedance matching independently of the substrate thickness. This provides the design freedom to use the substrate thickness as a major design parameter for controlling the strength of broadside coupling and, hence, the Q-factor of the BSF.

In the following section the proposed design of the BSF is presented. The rules of the design are given in Section III. A prototype of the proposed high Q-factor BSF is fabricated and experimentally studied for more understanding of the underlying physical principles of operation and for verifying some of the simulation results in Section IV.

II. THE PROPOSED BSF DESIGN

The geometry of the BSF proposed in this work is presented in Fig. 1 with the indicated symbolic dimensional parameters. This filter is constructed as a U-shaped CPWR with unequal arms broadside coupled to a CPWTL. Both the CPWR and the CPWTL have finite width ground strips as shown in the figure. The U-shaped CPWR is open-ended half-wavelength resonator. This design necessitates that the strips and slots of the CPWR have the same width as those of the CPWTL. The CPWTL is almost unloaded as long as the operating frequency is far from the resonant frequencies of the U-shaped CPWR, leading to complete microwave power transfer between the filter ports (1) and (2). The microwave power is absorbed and stored in the U-shaped CPWR only over a very narrow frequency band around the resonant frequency, this prevents any power transfer between the filter ports and, thereby, leading to high Q-factor BSF response.

The finite width of the side ground strips of the CPWR results in much higher Q-factor than that obtained when using a CPWR of infinitely extending side ground planes. This is because the lower profile of the CPW with finite-width ground results in lower radiation loss and narrower frequency band for coupling, which, in turn, enhances the Q-factor.

The input impedance (Z_{in}) matching at the filter ports, the center frequency (f_c) and the bandwidth (equivalently the Q-factor), are the most important design goals of the proposed BSF. One of the major advantages of the proposed design is that each of these design goals can be achieved (almost independently of the other two goals) by adjusting only one or two independent parameters. Table 1 gives a list of the dimensional parameters that can be used to achieve the required filter performance metrics.

Each of the design dimensional parameters, (s, w, L_R, L_B, h) can be set to affect significantly one of the design goal parameters (Z_{in}, f_c, Q) according to Table 1 without significant effects on the other design goal parameters. The theoretical design rules to achieve the BSF design goals are discussed in detail in Section III.

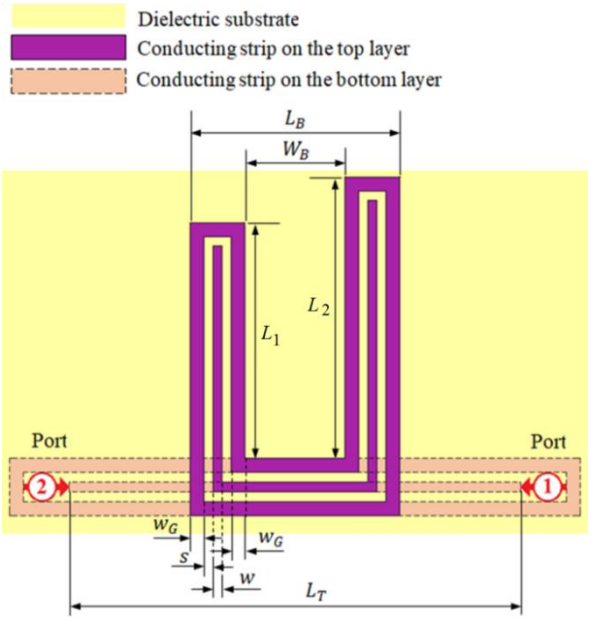

Fig. 1. Schematic of the proposed design for high Q-factor BSF constructed as CPWTL broadside-coupled to a U-Shaped CPWR.

Table 1: List of the independent design parameters that can be used to achieve the design goals of the BSF

Design Goal		Dimensional Parameter	
Symbol	**Description**	**Symbol**	**Description**
Z_{in}	Input Impedance	s	Central Strip Width
		w	Side Slots Width
f_c	Center Frequency	L_R	Resonator Length
Q	Q-Factor	L_B	Coupling Length
		h	Substrate Height

III. THEORETICAL ANALYSIS OF THE BSF DESIGN

The resonance frequency (f_n) of an open-ended CPWR is inversely proportional to the CPWR length (L_R), this can be expressed as follows [17]:

$$f_n = \frac{n\,c}{2L_R\sqrt{\varepsilon_{r_{eff}}}}, \qquad n = 1,2,\ldots \tag{1}$$

where $\varepsilon_{r_{eff}}$ is the effective dielectric constant of the

quasi-TEM mode of the CPW, c is the velocity of light in free space, and n is the resonance mode order.

The effective dielectric constant of the quasi-TEM mode of the CPW can be expressed as follows [17]:

$$\varepsilon_{r_{eff}} = 1 + \frac{\varepsilon_r - 1}{2} \frac{K(\acute{k}_0)}{K(k_0)} \frac{K(k_1)}{K(\acute{k}_1)}, \tag{2}$$

where ε_r is the dielectric constant of the substrate material and K denotes the complete elliptic integral of the first kind, which is defined as follows:

$$K(k) = \int_0^{\frac{\pi}{2}} \frac{d\theta}{\sqrt{1 - k \sin^2 \theta}}. \tag{3}$$

The arguments, k_0, $\acute{k}_0$, k_1, and $\acute{k}_1$, of K are defined as follows:

$$\begin{aligned} k_0 &= \frac{s}{s + 2w}, \\ \acute{k}_0 &= \sqrt{1 - k_0^2}, \\ k_1 &= \frac{\sinh\left(\frac{\pi s}{4h}\right)}{\sinh\left[\frac{\pi(s + 2w)}{4h}\right]}, \\ \acute{k}_1 &= \sqrt{1 - k_1^2}. \end{aligned} \tag{4}$$

The characteristic impedance of the quasi-TEM mode of the CPW is expressed as follows [17]:

$$Z_0 = \frac{30\pi}{\sqrt{\varepsilon_{r_{eff}}}} \frac{K(\acute{k}_0)}{K(k_0)}. \tag{5}$$

In spite of being formulated for a CPW of infinitely extending ground, the expressions (2) and (5) can be used as preliminary design rules for a CPW with side ground strips of finite width with good accuracy as long as the ground strip width w_G is kept greater than the central strip width and the side slot width. According to (5), by setting the proper values of the strip and slot widths, a 50Ω characteristic impedance of the CPWTL can be obtained.

A. Calculating the Q-factor of the BSF

The resonance frequency of the BSF can be shifted (from that of the unloaded resonator) due to the broadside coupling between the U-shaped CPWR and the CPWTL which causes external loading on the resonator. This is because of reactive coupling, as part of the energy is stored in the electric field of the coupling reactance. The broadside reactive coupling to the through-line can be considered as a loss channel, which decreases the resultant (loaded) Q-factor. Thus, the total (loaded) Q-factor can be evaluated through the following relation.

$$\frac{1}{Q} = \frac{1}{Q_u} + \frac{1}{Q_e}, \tag{6}$$

where, Q_u is the self or internal (unloaded) Q-factor of the CPWR without being coupled to the through-line and Q_e is the external Q-factor due to coupling. Theoretically, a lossless CPWR has infinite unloaded Q-factor, $Q_u = \infty$. However, practically, Q_u is limited by the conductor and dielectric losses. The external Q-factor Q_e dominates the total Q for low-loss CPWR.

The external Q-factor can be expressed as follows:

$$\frac{1}{Q_e} = \frac{1}{Q_R} + \frac{1}{Q_C}, \tag{7}$$

where Q_R is an equivalent Q-factor related to the radiation loss and Q_C is an equivalent Q-factor related to the reactive coupling between the resonator and the through-line, which can be considered as a loss channel.

B. Unloaded Q-factor of the CPWR

For the BSF design shown in Fig. 1, the CPW region forming the perimeter of the U-Shape can be considered an open-ended half-wavelength transmission line resonator. The unloaded Q-factor of both short-circuited and open-circuited half-wavelength CPWR can be expressed as follows [17],

$$Q_u = \frac{\pi}{2\alpha L_{R_{1/2}}} = \frac{\beta_0}{2\alpha} \sqrt{\varepsilon_{r_{eff}}} = \frac{\omega_0}{2c\alpha} \sqrt{\varepsilon_{r_{eff}}}, \tag{8}$$

where, $L_{R_{1/2}}$ is the length of the half-wavelength resonator, β_0 is the free space wave number, ω_0 is the resonant angular frequency, α is the attenuation constant of the CPW, and $\varepsilon_{r_{eff}}$ is given by (2).

The attenuation constant α of the CPW is related by the conductor and dielectric losses and, hence it can be expressed as follows:

$$\alpha = \alpha_c + \alpha_d, \tag{9}$$

where, α_c is the attenuation caused by the conductor loss whereas α_d is the attenuation caused by the dielectric substrate loss. For a transmission line made of high-conductivity metals like copper ($\sigma = 5.6 \times 10^7 \mathrm{S/m}$) the dielectric loss dominates, which means that $\alpha_d \gg \alpha_c$ and, hence, for a CPW carrying TEM mode, the attenuation constant can be approximated as follows:

$$\alpha \approx \alpha_d = \frac{\omega_0 \tan\delta}{2c} \sqrt{\varepsilon_{r_{eff}}}. \tag{10}$$

Making use of (10), the expression (8) of the unloaded Q-factor of the CPWR reduces to the following:

$$Q_u \approx \frac{1}{\tan\delta}. \tag{11}$$

Substituting from (11) into (6), the total Q-factor can be expressed as:

$$Q \approx \frac{Q_e}{1 + Q_e \tan\delta}. \tag{12}$$

If the loss tangent of the dielectric substrate is known, equation (12) can be used to calculate the external Q-factor, Q_e, given that Q has been obtained by simulation.

C. Calculating the coupling Q-factor using semi-analytical method

It may be useful to assess the effect of the reactive load caused by broadside-coupling to the CPWTL on the Q-factor of the U-shaped CPWR. This can be achieved by evaluating Q_C which is related to reactive coupling. As this Q-factor is difficult to be evaluated analytically, a semi-analytic method it is proposed in the present section. First, the total Q-factor, Q, of the BSF is obtained numerically by electromagnetic simulation, where the commercially available CST™ package is used in the present work for this purpose. A low profile of the CPW ensures low radiation loss and, hence, the term $1/Q_R$ in (7) can be neglected leading to the following expression for the external Q-factor:

$$Q_e \approx Q_C. \tag{13}$$

The last expression means that the external Q-factor is dominated by the coupling Q-factor for well-designed BSF. Making use of (12) and (13), the coupling Q-factor can be evaluated as follows:

$$Q_c \approx \frac{Q}{1 - Q\delta}. \tag{14}$$

IV. NUMERICAL RESULTS AND EXPERIMENTAL MEASUREMENTS

In the present section, both the numerical results obtained by simulation and the experimental results obtained by microwave measurements of the fabricated BSF prototype are presented, discussed and compared for the purpose of arriving at accurate performance assessment and understanding of the resonance mechanism underlying the proposed BSF operation.

In the electromagnetic simulations, for a substrate of size 40 mm × 40 mm and height 0.2 mm, the simulation (execution) time for each of the studied cases to reach the final design is about 20 minutes with accuracy of −40 dB using the frequency domain solver on a core I7-3.6 GHz processor, 16G RAM and 64-bit operating system. Hexahedral meshing is used with 15 cells/ wavelength for all simulations.

The results for the external Q-factor obtained by the semi-analytic method described in Section III-C are presented and discussed. It should be noted that the following presentations and discussions of numerical and experimental results are concerned with BSF with unequal arms as that shown in Fig. 1 designed with the following dimensional parameters, unless otherwise stated: $s = 0.1$ mm, $w = 0.1$ mm, $w_G = 0.2$ mm, $L_B = 10$ mm, $W_b = 8.6$ mm, $L_1 = 16.9$ mm, $L_2 = 13.1$ mm, and $L_T = 28$ mm, $L_R = L_1 + L_2 + L_B$. The substrate material is Rogers RO3003CTM with dielectric constant $\varepsilon_r = 3.38$, dielectric loss tangent $\tan\delta = 0.001$ and height $h = 0.25$ mm. The metal strips and ground are made of copper and have conductivity $\sigma = 5.6 \times 10^7 \mathrm{S/m}$. A model with the same dimensions as that of the experimental prototype of the BSF is constructed for electromagnetic simulation using the commercially available CST™ package. This model is presented in Fig. 2 showing the detailed dimensions. At the input and output ports of proposed filter, the transitional tapered CPW region is designed to satisfy impedance matching between the 50Ω impedance of the microwave source and the characteristic impedance of the CPWTL.

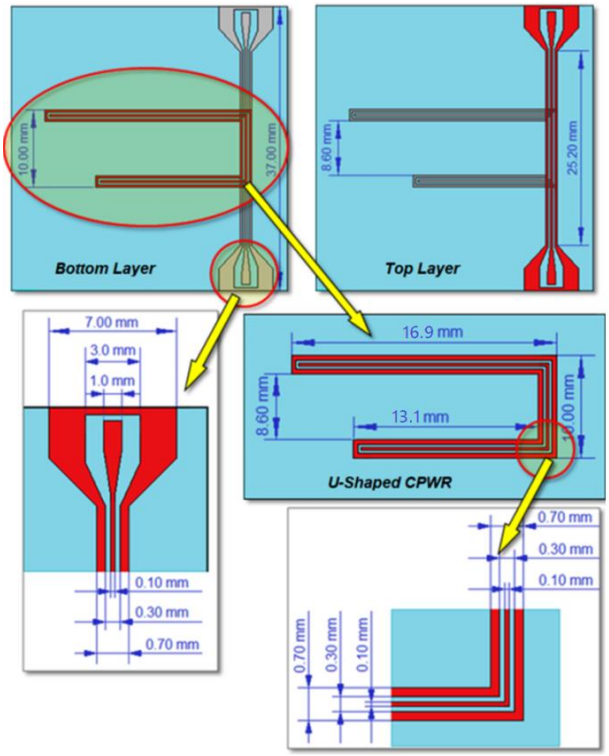

Fig. 2. Dimensions for the CST™ model of the proposed BSF (Note: the red color is for the strips printed on the viewed layer whereas the gray color is for the strips printed on the other layer).

In the following presentation, some comparisons are made between the simulation and experimental results concerned with the frequency response of the BSF at its 1st and 2nd resonances.

A. Frequency response of the proposed BSF

The frequency response of the transmission coefficients $|S_{21}|$ of the proposed dual BSF with the design parameters given in Fig. 2, is presented in Fig. 3. It is assumed that the CPWR is made of copper conductors on a dielectric substrate of $\varepsilon_r = 3$ and loss tangent $\delta = 0.001$. The frequency response exhibits two

sharp anti-peaks: the first one is at $f = 3.12$ GHz, with Q-factor of 155, whereas, the second anti-peak is at $f = 6.25$ GHz, with Q-factor of 46.

The mechanisms leading to these values of the resonant frequencies and the corresponding Q-factors can be explained in view of the surface current distributions at the 1st- and 2nd-order resonance frequencies of the open-ended CPWR formed by the perimeter of the U-shape, which is presented in Fig. 4. At the 1st-order resonance, the current distribution has one maximum value almost centered at the right corner of the U-shape, whereas the current distribution shows two maxima near the centers of the arms of the U-shape.

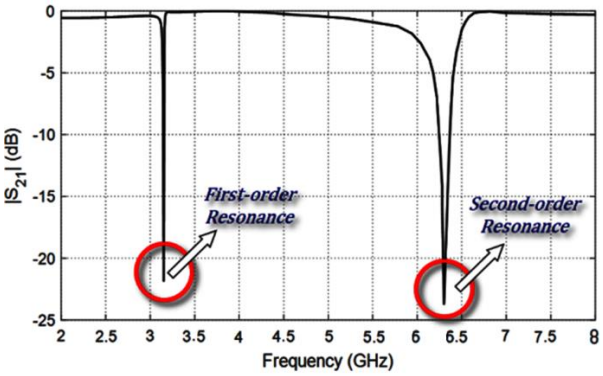

Fig. 3. Frequency response of the transmission coefficient $|S_{21}|$ of the BSF (with the design shown in Fig. 2) based on the U-shaped half-wave length CPWR.

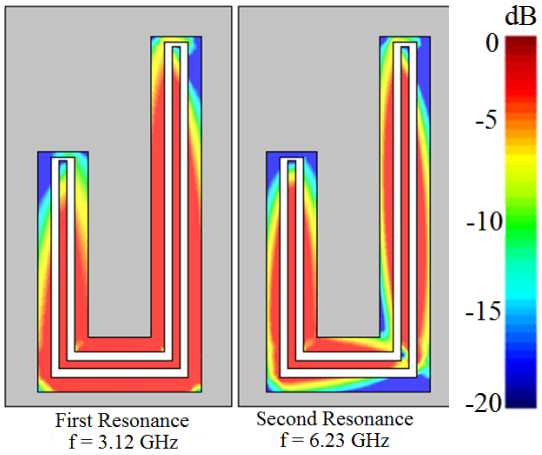

Fig. 4. Surface current on the conductors at the frequencies corresponding to the 1st-order and 2nd-order resonances of the U-shaped CPWR.

It is shown that, as this CPW region is a half-wavelength resonator whose total length is 38.4 mm, the resonance frequencies can be calculated using (1), which gives $f_1 = 3.3$ GHz and $f_2 = 6.4$ GHz. The slight deviation of the resonant frequencies obtained by simulation from the theoretical values obtained by (1) can be attributed to the reactive load resulting from coupling the CPWTL to the CPWR as part of the energy is stored in the electric field of the coupling capacitance and, thereby causing a shift of the resonant frequency. Moreover, a part of the frequency shift can be attributed to the error of the approximate analytic formula for $\varepsilon_{r_{eff}}$ given by (2).

A.1. Tuning the center frequency of the BSF

As given in Table 1, the main design parameter to tune the center frequency of the BSF according to (1) is the total length of the U-shaped CPWR, L_R. Figure 5 shows the change of the frequency response of the transmission coefficient $|S_{21}|$ of the BSF around the 1st resonance frequency with changing the resonator length, L_R while keeping the coupling length L_B constant. It clear that the resonance frequency decreases with increasing the resonator length L_R which agrees with the analytical formula given by (1). This is clear in Fig. 6 (a) which shows that the resonance frequency is inversely proportional to L_R. However, as shown in Fig. 6 (b), the Q-factor is almost independent of the resonator length L_R as long as the coupling length L_B is constant. The effect of the dielectric losses is also shown in Fig. 6 (b), where the increase in the dielectric losses degrades the Q-factor.

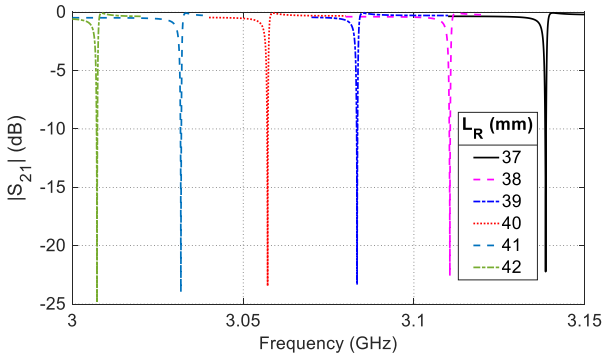

Fig. 5. Change of the frequency response of the transmission coefficient $|S_{21}|$ of the BSF around the 1st resonance frequency with changing the CPWR length, L_R.

A.2. Adjusting the Q-factor of the BSF

As previously discussed, the Q-factor of the BSF is dominated by the external Q-factor which is attributed mainly to the broadside coupling between the CPWR and the CPWTL. The coupling strength is strongly dependent on the length of the CPW regions over which the coupling is performed. Consequently, the length of the base of the U-shape, L_B, is an important design parameter that controls the Q-factor at each resonance frequency. Figure 7 shows the change of the frequency response of the transmission coefficient $|S_{21}|$ of the BSF

around the 1st resonance frequency with changing the coupling length, L_B, between the CPWR and CPWTL while keeping the total length of the CPWR constant. Figure 8 (a) plots the center frequency with changing L_B. It is clear from Fig. 7 and Fig. 8 (a) that the center frequency is almost constant as long as the resonator length L_R is kept constant. The slight change in the resonance frequency is due to the change of the reactive load impedance as a result of the broadside coupling. The Q-factor is considerably decreased with increasing the coupling length as shown in Fig. 8 (b). As the coupling length increases the reactive load caused by the broadside coupling increases leading to a decrease of the external Q-factor which, in turn, results in considerable decrease of the total Q-factor. The effect of the dielectric losses is investigated in the same figure, it is clear that the increase in tan δ decreases the Q-factor.

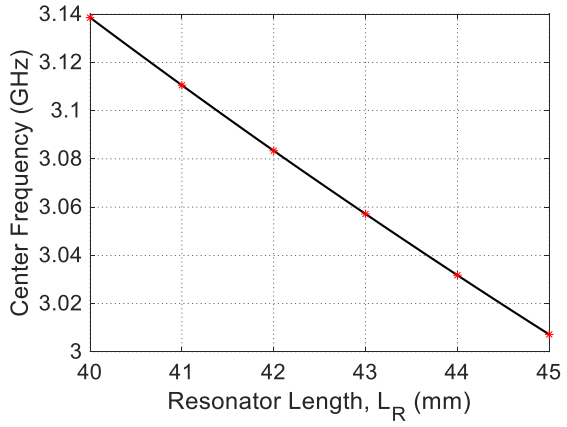

(a) Dependence of the center frequency on the CPWR length (tan $\delta = 0$)

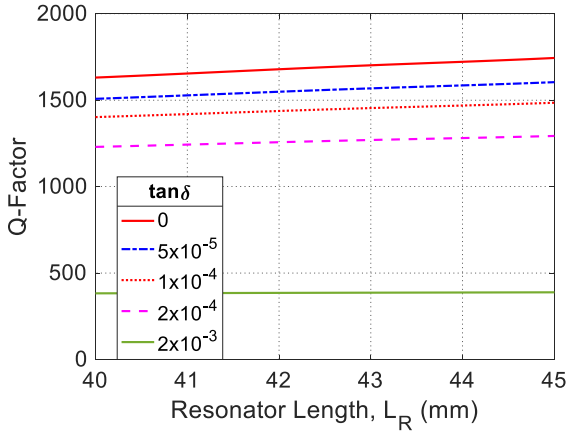

(b) Dependence of the Q-factor on the CPWR length for different values of tan δ

Fig. 6. Dependence of the center frequency and the Q-factor of the BSF on the resonator length at the 1st resonance frequency of the U-shaped CPWR.

The difference between the two arms of the resonator also affects the Q-factor. In Fig. 9 the frequency response of the transmission coefficient $|S_{21}|$ around the first resonance is studied with changing the difference in the length of the two arms, $d = |L_2 - L_1|$, while keeping the total length of the resonator, L_R constant. The change in the Q-factor with changing the difference d is shown in Fig. 10 at the first and second resonances. It is shown that the best Q-factor is achieved at the second resonance when the difference d is about 7.5 mm.

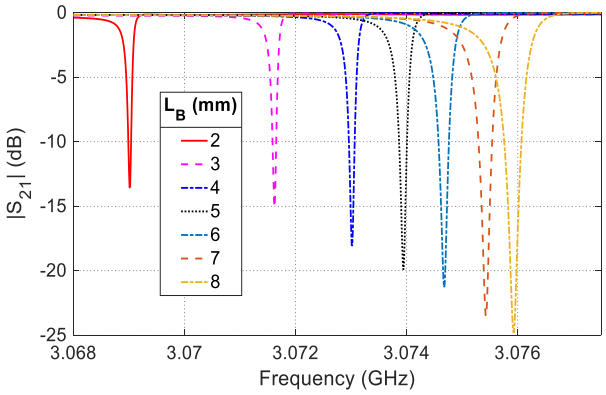

Fig. 7. Change of the frequency response of the transmission coefficient $|S_{21}|$ of the BSF around the 1st resonance frequency with changing the coupling length, L_B, while keeping the CPWR length, L_R constant.

A.3. Effect of substrate height on the Q-factor

The strength of broadside coupling is strongly dependent on the separation distance between the two coupled lines. Consequently, the height of the dielectric substrate, h, is an important design parameter that controls the Q-factor at each resonance frequency. Figure 11 shows the change of the frequency response of the transmission coefficient $|S_{21}|$ of the BSF around the 1st resonance frequency with changing the substrate height. It is clear that the resonance frequency slightly increases with increasing h due to the change of the reactive load impedance equivalent to the broadside coupling. Figure 12 (a) shows that the center frequency is slightly dependent on h. The Q-factor is considerably decreased with increasing the coupling length as shown in Fig. 12 (b). As the substrate height increases the reactive load caused by the broadside coupling increases leading to a decrease of the external Q-factor which, in turn, results in considerable decrease of the total Q-factor. By increasing the dielectric losses, tan δ, the Q-factor decreases as shown in Fig. 12 (b).

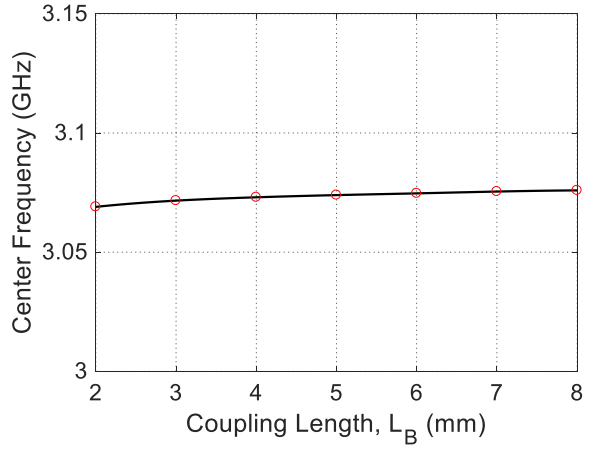

(a) Dependence of the center frequency on the coupling length ($\tan\delta = 0$)

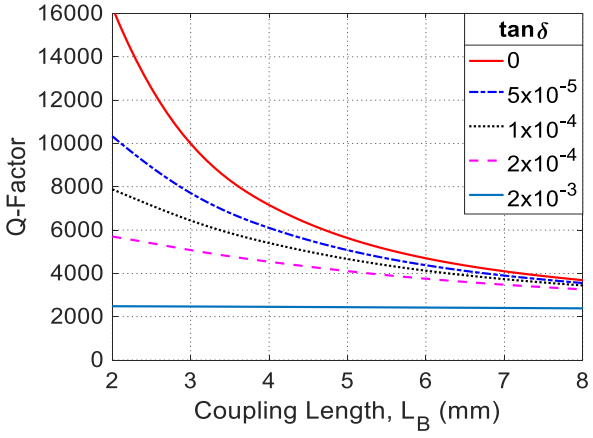

(b) Dependence of the Q-factor on the coupling length for different values of $\tan\delta$

Fig. 8. Dependence of the Q-factor and center frequency of the BSF on the coupling length at the 1st resonance frequency of the U-shaped CPWR.

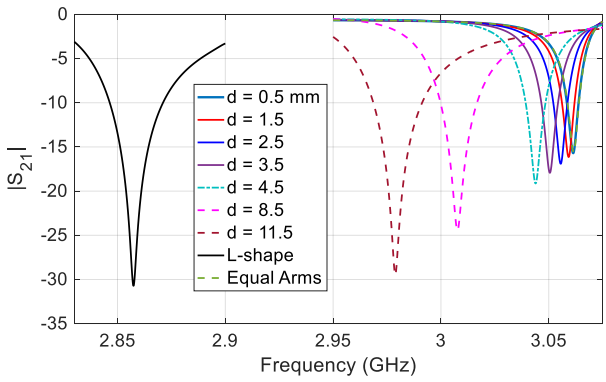

Fig. 9. Change of the frequency response of the transmission coefficient $|S_{21}|$ of the BSF around the 1st resonance frequency with changing the difference, d, between the U-resonator arm lengths.

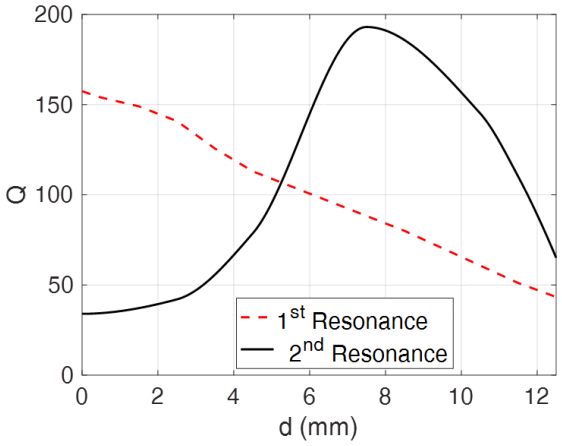

Fig. 10. Dependence of the Q-factor of the BSF at the 1st resonance frequency on the difference, d, between the lengths of the U-shaped CPWR arms.

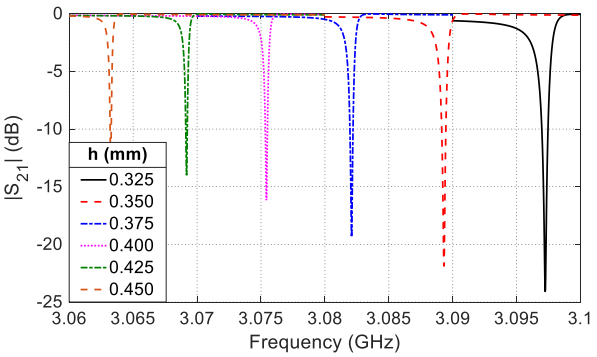

Fig. 11. Change of the frequency response of the transmission coefficient $|S_{21}|$ of the BSF around the 1st resonance frequency with changing the substrate height, h.

B. Experimental assessment of the BSF

The purpose of the experimental work is to study the underlying physical principles of operation and to investigate the performance of the proposed high Q-factor BSF based on broadside coupling between U-shaped CPWR and CPWTL.

B.1. Prototype fabrication

A prototype of the proposed BSF is fabricated for experimental studying of the underlying physical principles of operation and investigating the filter performance. The dimensional parameters of the fabricated filter are those presented in Fig. 2. The substrate used for fabrication is RO3003C™, with substrate height $h = 0.25$ mm, dielectric constant $\varepsilon_r = 3$ and dielectric loss tangent, $\tan\delta = 0.001$. The same design dimensions given at the beginning of Section IV are used for the fabrication process. A photograph of the fabricated prototypes is presented in Fig. 13, where its size is

compared to a metal coin of the standard one-inch diameter.

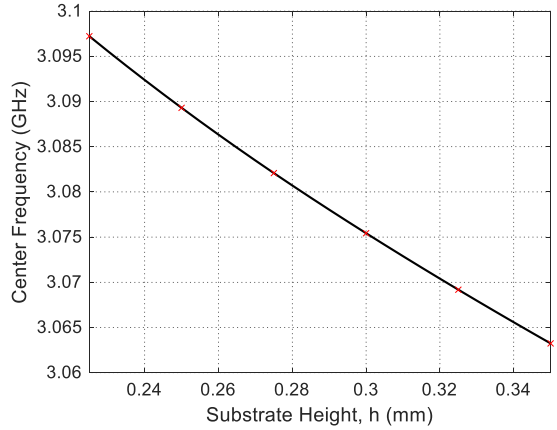

(a) Dependence of the center frequency on the substrate height ($\tan\delta = 0$)

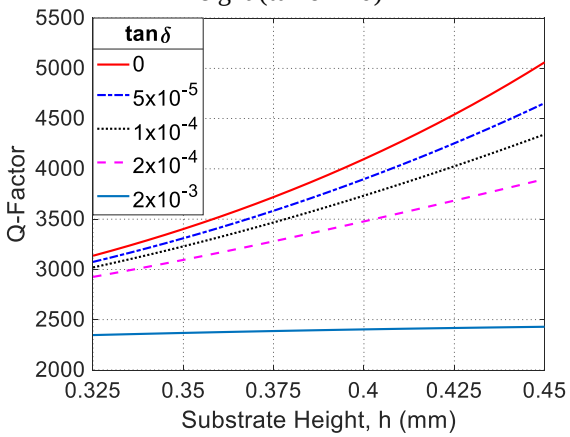

(b) Dependence of the Q-factor on the substrate height for different values of $\tan\delta$

Fig. 12. Dependence of the Q-factor and center frequency of the BSF on the substrate height at the 1st resonance frequency of the U-shaped CPWR.

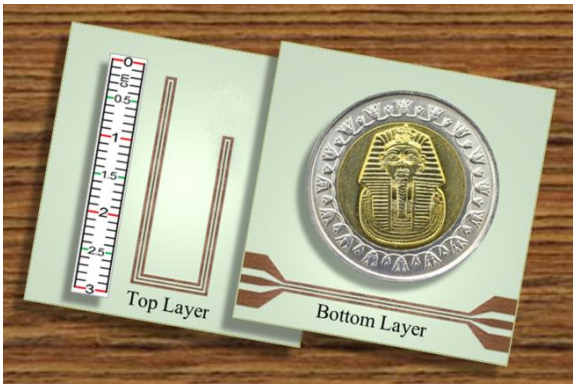

Fig. 13. The fabricated prototype of the proposed high Q-factor BSF.

B.2. Experimental setup

The vector network analyzer (VNA) of the Keysight (Agilent) FieldFox N9928A™ is used to measure the transmission and reflection coefficients $|S_{21}|$ and $|S_{11}|$, respectively, of the BSF prototype under test. For this purpose, the filter prototype is mounted on the substrate test fixture as shown in Fig. 14 (a). After performing the required settings and calibration procedure, the test fixture holding the prototype under test is connected to the VNA as shown in Fig. 14 (b).

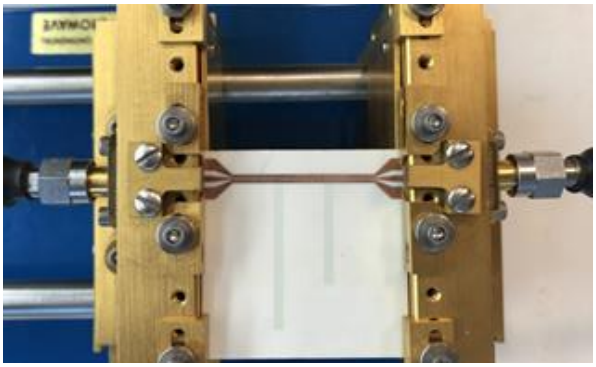

(a) The fabricated BSF mounted on the VNA test fixture

(b) Measurement of the transmission coefficient $|S_{21}|$ using the VNA

Fig. 14. Measurement of the frequency response of the fabricated prototype for experimental investigation of the proposed BSF.

B.3. Experimental results

The frequency responses of the transmission and reflection coefficients $|S_{21}|$ and $|S_{11}|$, of this filter over the frequency bands around the 1^{st} resonance is presented in Fig. 15. The measurements are achieved by the VNA and compared to that obtained by simulation using the commercially available CST™ software package. It is clear that the experimental measurements and simulation results show good agreement.

The experimental measurements of the frequency response at the lower band of the BSF show that the 1^{st} resonance occurs at $f_{1^{st}}^{(Exp)} = 3.18$ GHz, whereas and the simulation results show that this resonance occurs at $f_{1^{st}}^{(Sim)} = 3.176$ GHz. The corresponding Q-factors are $Q_{1^{st}}^{(Exp)} = 155$ and $Q_{1^{st}}^{(Sim)} = 168$. The external Q-factor, which is dominated by the coupling Q-factor as discussed before, can be obtained by a semi-analytic approach as described in Section IIIC. The unloaded Q-factor can be calculated in terms of the dielectric substrate loss tangent using (11) to get $Q_u = 457$. The external Q-factor, which is dominantly attributed to broadside coupling, can be obtained by (6) and (12) to get $Q_{e\,1^{st}}^{(Exp)} = 184$ using the measurement data, and $Q_{e\,1^{st}}^{(Sim)} = 203$ using the simulation data, where the subscript "1^{st}" indicates the 1^{st} resonance. Such a high value of the external Q-factor can be attributed to the strong broadside coupling between the CPWR and the CPWTL.

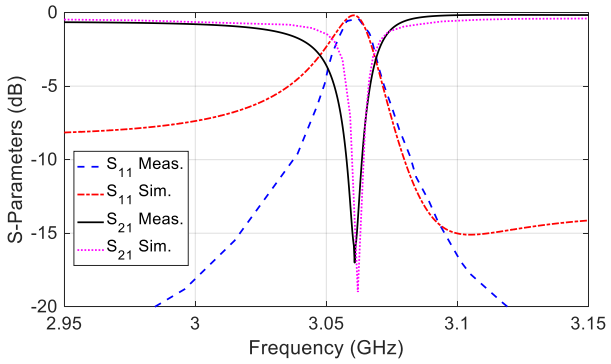

Fig. 15. Frequency responses of the transmission and reflection coefficients $|S_{21}|$ and $|S_{11}|$, respectively, of the BSF at the 1^{st} resonance of the half-wave U-shaped CPWR which is broadside-coupled to the CPWTL.

Comparisons among the Q-factors of some BSFs achieved experimentally in other published work compared with that achieved in the present work are listed in Table 2. The higher value of the Q-factor achieved in the present work is due to the strong broadside coupling and the optimized dimensions of the U-shaped CPWR mainly the coupling length L_c which is the length of the U-shape base.

It should be noted that, the proposed band stop filter design depends on broad side coupling as the feeder is printed on one side of the substrate whereas the resonator is printed on the facing side. This enables much stronger coupling between the feeding and resonator coplanar wave guide regions than that caused by the mechanism used in the other designs such as those presented in Table 2. Moreover, the coupling length (the base of the U-shape) can easily control the coupling strength and hence, the resulting value of the Q-factor.

Table 2: Comparison between Q-factors of BSFs achieved experimentally in other published work compared with that achieved in the present work.

Published Work	Huang et al. [21]	Woo et al. [20]	Liu et al. [2]	Lee et al. [18]	Kakhki et al. [19]	Fahmy et al. [23]	Present Work
Q-Factor	31.7	36.1	45	49.7	57	131	155

V. CONCLUSION

The design of high Q-factor BSF based on broadside-coupling between U-shaped CPWR of unequal arms and CPWTL is presented. The CPWTL is printed on one layer of relatively thin dielectric substrate whereas the CPWR is printed on the opposite layer. The proposed BSF is shown to have much higher Q-factor when compared with other published work. Such high Q-factor is attributed to the unequal arms of the U-shaped CPWR and the finite width of the side ground strips. Due to the lower profile of the CPW with finite-width, the radiation loss is reduced leading to enhanced Q-factor. The dimensions of the CPWTL are optimized for impedance matching whereas the dimensions of the U-shaped CPWR are optimized to obtain the highest possible Q-factor. The numerical results concerned with the effect of the loss tangent of the dielectric substrate material on the Q-factor are presented and discussed. A prototype of the proposed BSF is fabricated and experimentally studied where the measurements show good agreement when compared with the corresponding simulation results.

REFERENCES

[1] Q. Xiang, Q. Feng, and X. Huang, "Tunable BSF based on split ring resonators loaded coplanar waveguide," *Applied Computational Electromagnetics Society Journal*, vol. 28, pp. 591-596, 2013.

[2] G. Liu, Z.-Y. Wang, J.-J. Wu, and L. Li, "Capacitive loaded U-slot defected ground structure for BSF with improvement Q factor," *Progress in Electromagnetics Research*, vol. 65, pp. 31-36, 2017.

[3] H. G. Alrwuili and T. S. Kalkur, "A tunable microstrip BSF using compact spiral folded spurline for RF microwave systems," *International Applied Computational Electromagnetics Society*

Symposium (ACES), 2018.

[4] S. Lee, S. Oh, W.-S. Yoon, and J. Lee, "A CPW BSF using double hairpin-shaped defected ground structures with a high Q factor," *Microwave and Optical Technology Letters*, vol. 58, no. 6, pp. 1265-1268, 2016.

[5] P.-H. Deng, C.-H. Wang, and C. H. Chen, "Novel broadside-coupled bandpass filters using both microstrip and coplanar-waveguide resonators," *IEEE Transactions on Microwave Theory and Techniques*, vol. 54, no. 10, pp. 3746-3750, 2006.

[6] A. Kumar, A. K. Verma, and Q. Zhang, "Compact triple-band BSFs using embedded capacitors," *Progress in Electromagnetics Research*, vol. 63, pp. 15-21, 2016.

[7] S. Yang, Z. Xiao, and S. Budak, "Design of triband BSF using an asymmetrical cross-shaped microstrip resonator," *Progress in Electromagnetics Research*, vol. 86, pp. 35-42, 2019.

[8] J.-M. Yan, L. Cao, and H.-Y. Zhou, "A novel quad-band BSF based on coupled-line and shorted stub-loaded half-wavelength microstrip resonator," *Progress in Electromagnetics Research*, vol. 79, pp 65-70, 2018.

[9] O. A. Safia, A. A. Omar, and M. C. Scardelletti, "Design of dual-band bandstop coplanar waveguide filter using uniplanar series-connected resonators," *Progress in Electromagnetics Research*, vol. 27, pp. 93-99, 2011.

[10] Y. Li, S. Luo, and W. Yu, "A compact tunable triple stop-band filter based on different defected microstrip structures," *Applied Computational Electromagnetics Society*, vol. 33, no. 7, pp. 752-757, 2018.

[11] M. Naser-Moghadasi, "Harmonic suppression of parallel coupled-line bandpass filters using defected microstrip structure," *Applied Computational Electromagnetics Society*, vol. 33, no. 7, pp. 752-757, 2018.

[12] J. K. A. Everard and K. K. M. Cheng, "High performance direct coupled bandpass filters on coplanar waveguide," *IEEE Transactions on Microwave Theory and Techniques*, vol. 41, no. 9, pp. 1568-1573, 1993.

[13] A. Contreras, M. Ribó, L. Pradell, V. Raynal, I. Moreno, M. Combes, and M. Ten, "Compact fully uniplanar BSF based on slow-wave multimodal CPW resonators," *IEEE Microwave and Wireless Components Letters*, vol. 28, no. 9, pp. 780-782, 2018.

[14] K. C. Gupta, R. Garg, and I. Bahl, *Microstrip Lines and Slotlines*. Dedham, MA Artech, 1979.

[15] A. Gopinath, "Losses in coplanar waveguides," *IEEE Transactions on Microwave Theory and Techniques*, vol. 30, no. 7, pp. 1101-1104, 1982.

[16] F. D. Williams and S. E. Schwarz, "Design and performance of coplanar waveguide bandpass filters," *IEEE Transactions on Microwave Theory and Techniques*, vol. 31, no. 7, pp. 558-566, 1983.

[17] R. N. Simons, *Coplanar Waveguide Circuits, Components, and Systems*, vol. 165, John Wiley & Sons, 2004.

[18] S. Lee, S. Oh, W. S. Yoon, and J. Lee, "A CPW BSF using double hairpin-shaped defected ground structures with a high Q factor," *Microwave and Optical Technology Letters*, vol. 58, no. 6, pp. 1265-1268, 2016.

[19] M. A. Kakhki and M. H. Neshati, "Numerical investigation and experimental study of two novel band-reject DGS filters with a very high Q-factor," *19th Iranian Conference on Electrical Engineering, IEEE*, pp. 1-4, 2011.

[20] D. J. Woo, T. K. Lee, J. W. Lee, C. S. Pyo, and W. K. Choi, "Novel U-slot and V-slot DGSs for BSF with improved Q factor," *IEEE Transactions on Microwave Theory and Techniques*, vol. 54, no. 6, pp. 2840-2847, 2006.

[21] S. Y. Huang and Y. H. Lee, "A compact E-shaped patterned ground structure and its applications to tunable bandstop resonator," *IEEE Transactions on Microwave Theory and Techniques*, vol. 57, no. 3, pp. 657-666, 2009.

[22] M. Kumar and R. Gowri, "Review on various issues and design topologies of edge coupled coplanar waveguide filters," *Journal of Graphic Era University*, vol. 5, no. 2, pp. 91-96, 2017.

[23] W. M. Fahmy, A. E. Farahat, K. F. A. Hussein, and A. E. H A. Ammar, "High Q-factor BSF based on CPW resonator broadside-coupled to CPW through-line," *Progress in Electromagnetics Research*, vol. 86, pp. 121-138, 2020.

Quantitative Research on Cracks in Pipe Based on Magnetic Field Response Method of Eddy Current Testing

Feng Jiang [1,2], Shulin Liu [2], and Li Tao [3]

[1] School of Electrical and Information Engineering
Changzhou Institute of Technology, Changzhou, 213032, China
jiangf@jsit.edu.cn

[2] School of Mechatronics Engineering and Automation
Shanghai University, Shanghai, 200072, China
lsl346@shu.edu.cn

[3] Library and Information Center
Jiangsu Vocational College of Information Technology, Wuxi, 214153, China
tao_li_@126.com

Abstract ─ The quantitative evaluation of defects in eddy current testing is of great significance. Impedance analysis, as a traditional method, is adopted to determine defects in the conductor, however, it is not able to depict the shape, size and location of defects quantitatively. In order to obtain more obvious characteristic quantities and improve the ability of eddy current testing to detect defects, the study of cracks in metal pipes is carried out by utilizing the analysis method of three-dimensional magnetic field in present paper. The magnetic field components in the space near the crack are calculated numerically by using finite element analysis. The simulation results confirm that the monitoring of the crack change can be achieved by measuring the magnetic field at the arrangement positions. Besides, the quantitative relationships between the shape, length of the crack and the magnetic field components around the metal pipe are obtained. The results show that the axial and radial magnetic induction intensities are affected more significantly by the cross-section area of the crack. B_z demonstrates obvious advantages in analyzing quantitatively crack circumference length. Therefore, the response signal in the three-dimensional direction of the magnetic field gets to intuitively reflect the change of the defect parameter, which proves the effectiveness and practicability of this method.

Index Terms ─ Cracks evaluation, Eddy current testing, finite element method, magnetic field, pipe.

I. INTRODUCTION

Electromagnetic nondestructive testing is a kind of testing method to evaluate the structure and related properties of tested materials by utilizing the changes of electromagnetic characteristics under the action of the electromagnetic field [1-3]. It mainly includes eddy current testing (ECT), magnetic particle testing (MT) and magnetic flux leakage (MFL) testing. With the development of technology, a great many new electromagnetic nondestructive testing methods have appeared, such as alternating current field measurement (ACFM) and metal magnetic memory (MMM) testing. ECT, MFL and ACFM are commonly used to detect defects, although they differ in their principles of measurement.

Among the three methods mentioned above, what has been used in ECT as the physical quantity is coil impedance [4-6], while the physical quantity measured by MFL and ACFM is magnetic field which is a three-dimensional physical quantity that adequately characterizes geometric parameters such as length, as well as width of a defect. Therefore, the latter two methods gain significant advantages over ECT from the perspective of defect information contained in physical quantities. On the other hand, what also have been compared are excitation modes of three electromagnetic nondestructive testing. The excitation source is used in the local magnetization of the workpiece by MFL [7-9]. And DC magnetization has a high requirement for the current source. The excitation current is generally shown from several amperes to hundreds of amperes, and the electrical equipment is relatively complicated. Moreover, the direction of defects has exerted a great influence on the magnetic leakage field. Similarly, the excitation coil of ACFM needs to induce parallel and approximately uniform currents on the specimen surface, so as to generate approximately uniform alternating electromagnetic field [10-12]. Undoubtedly, the uniform

Submitted On: August 5, 2019
Accepted On: February 23, 2020

https://doi.org/10.47037/2020.ACES.J.360114

eddy current requires higher requirements on the structure of excitation devices. In addition, when the current direction is parallel to that of the crack, the sensitivity of the detection explores the lowest level and the missed detection may occur. However, the induced eddy current generated by the excitation coil of ECT is in the circumferential direction. Defects in any direction will cause a change in the eddy current, thereby generating a disturbing eddy current field. Moreover, the excitation method used in ECT is simple, convenient and easy under operation. Therefore, compared with the other two methods, the traditional ECT exhibits certain strengths according to the analysis of the excitation modes.

Considering the advantages and disadvantages of the above testing methods, the configurations of traditional ECT are retained, and the magnetic field analysis of MFL and ACFM is adopted in the present paper, so as to implement the quantitative study of the shape and circumference length of cracks in metal pipelines.

II. MATHEMATICAL MODEL OF THREE-DIMENSIONAL EDDY CURRENT FIELD

A typical solution domain V of the eddy current problem is assumed, where V_1 is the eddy current zone containing the conductive medium without the source current and V_2 is the non-eddy current zone including the given source current. S_{12} is the internal interface of V_1 and V_2. The outer boundary S of solution domain V is divided into S_B and S_H. The normal component of the magnetic induction intensity is given on S_B, and S_H provides the tangential component of the magnetic induction intensity.

Maxwell's equations describe the macroscopic properties of the electromagnetic field, which is not always convenient to be solved directly. $\boldsymbol{A}$, $\boldsymbol{\Phi}$-$\boldsymbol{A}$ method will be used to establish the mathematical model of eddy current analysis. In the eddy current area, magnetic vector potential $\boldsymbol{A}$ and scalar potential Φ are used as unknown functions, and in the non-eddy current area, only $\boldsymbol{A}$ is used as unknown functions. Substituting $\boldsymbol{B} = \nabla \times \boldsymbol{A}$ and $\boldsymbol{E} = -\frac{\partial \boldsymbol{A}}{\partial t} - \nabla\phi$ into Maxwell's equations, and specifying $\nabla \cdot \boldsymbol{A} = 0$, the governing equations and boundary conditions of eddy current field in region V are illustrated as follows:

$$\left.\begin{aligned} &\nabla \times \left(\nu \nabla \times \boldsymbol{A}\right) - \nabla\left(\nu \nabla \cdot \boldsymbol{A}\right) + \sigma \frac{\partial \boldsymbol{A}}{\partial t} + \sigma \nabla \phi = 0 \quad \text{(a)} \\ &\nabla \cdot \left(-\sigma \frac{\partial \boldsymbol{A}}{\partial t} - \sigma \nabla \phi\right) = 0 \quad \text{(b)} \end{aligned}\right\} \text{ in the } V_1, \tag{1}$$

$$\nabla \times \left(\nu \nabla \times \boldsymbol{A}\right) - \nabla\left(\nu \nabla \cdot \boldsymbol{A}\right) = \boldsymbol{J}_s \quad \text{in the } V_2, \tag{2}$$

$$\left.\begin{aligned} &\boldsymbol{n} \times \boldsymbol{A} = 0 \quad \text{(a)} \\ &\nu \nabla \cdot \boldsymbol{A} = 0 \quad \text{(b)} \end{aligned}\right\} \text{ on the } S_B, \tag{3}$$

$$\left.\begin{aligned} &\boldsymbol{n} \cdot \boldsymbol{A} = 0 \quad \text{(a)} \\ &\left(\nu \nabla \times \boldsymbol{A}\right) \times \boldsymbol{n} = 0 \quad \text{(b)} \end{aligned}\right\} \text{ on the } S_H, \tag{4}$$

$$\left.\begin{aligned} &\boldsymbol{A}_1 = \boldsymbol{A}_2 \quad \text{(a)} \\ &\nu_1 \nabla \cdot \boldsymbol{A}_1 = \nu_2 \nabla \cdot \boldsymbol{A}_2 \quad \text{(b)} \\ &\nu_1 \nabla \times \boldsymbol{A}_1 \times \boldsymbol{n}_{12} = \nu_2 \nabla \times \boldsymbol{A}_2 \times \boldsymbol{n}_{12} \quad \text{(c)} \\ &\boldsymbol{n} \cdot \left(-\sigma \frac{\partial \boldsymbol{A}}{\partial t} - \sigma \nabla \phi\right) = 0 \quad \text{(d)} \end{aligned}\right\} \text{ on the } S_{12}, \tag{5}$$

where σ is the electric conductivity, ν is the magnetoresistance, J_s is the source current density, n is the unit normal vector of S, n_{12} is the unit normal vector of S_{12}, and the direction is from V_1 to V_2.

However, the analytical method or the field-to-circuit method is unable to deal with a large number of engineering problems involving complex geometric and physical parameters [13-15]. Thanks to the rapid development of computer technology, it has promoted the progress of numerical analysis methods. Most importantly, the finite element method is the most widely used numerical method at present. Compared with other numerical methods, the finite element method shows prominent characteristics [16-18]. The finite element mesh can easily simulate the boundary and interface of different shapes. The discrete equations attained by the finite element method display sparse symmetric coefficient matrix, which simplifies the solution to the equations, and reduces the computer storage and computing time correspondingly.

Next, COMSOL Multiphysics, as the finite element analysis software is utilized to model the metal pipe and defects. Based on the three-dimensional magnetic field analysis, the solution in the specified field is obtained by the finite element method.

III. QUANTITATIVE STUDY OF CRACKS IN PIPES

A. Section shape of cracks

Figure 1 presents the three-dimensional model with a circumferential crack on the inner surface of the metal pipe. The cross-section shapes of the cracks are rectangle, semicircle and triangle, and their openings are kept at 4 mm and their depths are 2 mm. Only the influence of section shapes is considered here, so the three kinds of cracks are all-circle ones in the plane perpendicular to the axis. In addition, the excitation coil is a cylindrical coil coaxial with the metal pipe. The geometric parameters of the coil are listed as follows: inner radius r_{c1} = 8 mm, outer radius r_{c2} = 12 mm and height h = 6 mm. Based on such considerations, the three-dimensional model can be simplified into a two-dimensional axisymmetric one. In

this way, the finite element model gets to be simplified, and a more refined mesh is thus able to be used to improve the computational efficiency. The parameters of the finite element model are set as follows. It is assumed that the surrounding air medium is a cylinder with a radius of 20 mm and a height of 60 mm. Constraint conditions should be applied to the outer boundary and symmetry axis of the model. The central axis of the metal pipe should be set as the axisymmetric condition. The magnetic vector potential of the upper and lower ends of the metal pipe should be zero, and the magnetic insulation condition is applied to the outermost boundary of the air domain. The ultra-fine mesh processing is used, and the mesh is divided using triangular elements. The MUMPS direct solver is used and the relative tolerance is set to 0.001.

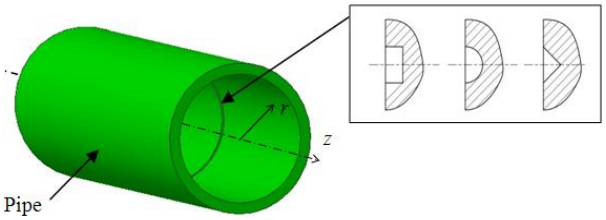

Fig. 1. The three-dimensional schematic diagram of the model.

The radial measurement points are 12.5 mm and 13.5 mm, respectively, and the measurement range in the z direction is from -20 mm to 20 mm. Figure 2 displays the distribution curves of radial and axial magnetic induction intensity under three kinds of cracks with different cross-section shapes. The curves indicated by the circle are the radial and axial magnetic induction intensity at the position of r = 13.5 mm without crack. The magnetic induction intensity varies with the axial distance as shown in Fig. 2, where the location of the excitation coil does not change. During the detection process, the magnetic sensor scans along the axial direction to obtain the magnitude of the magnetic induction intensity at each position.

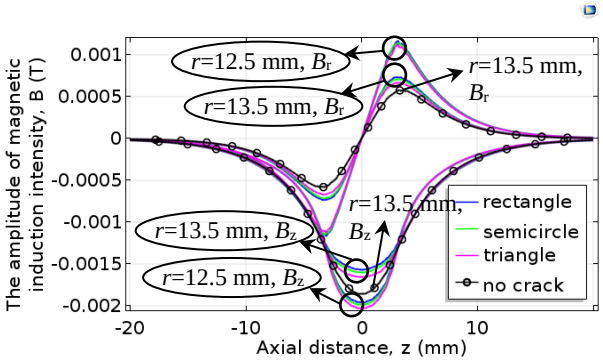

Fig. 2. The distribution curves of radial and axial magnetic induction intensity for cracks with different shapes.

The following four conclusions can be drawn from Fig. 2:

(1) The B_r curves show odd symmetrical distributions, reaching the maximum value at a certain distance in the axial direction. The B_z curves are distributed even symmetrically, with the maximum value at z = 0. As the axial distance increases, the value decreases gradually.

(2) Although the shapes of crack show no influence to the overall distribution of the magnetic induction intensity, it has a certain influence on the values of radial and axial magnetic induction intensity. As can be seen from Fig. 2, regardless of r = 12.5 mm and 13.5 mm, the changes of radial and axial magnetic induction intensities caused by rectangular crack are the most prominent, followed by the semi-circular section. What's more, the triangular section shows the least obvious influence. So, the following conclusion gets to be drawn: the larger the crack section area is, the more obvious the influence on the external magnetic field becomes. It is also helpful for us to judge and analyze the specific shape of crack by means of the change of the external magnetic field.

(3) The above conclusion is further confirmed by the distribution of electromagnetic fields. Figure 3 shows the induced current density inside the pipe and the distribution of contour lines of B_r and B_z near the crack. With the increase of the crack section area, the degree of the influence of the crack on the contour line B_r becomes more obvious. As shown in the black circled part of Fig. 3, it can be clearly seen that the curve near the crack is attracted to the side of the pipe. At this time, the value of the magnetic induction intensity in the vicinity increases. Similarly, as the section area of the crack increases, the degree of the influence of the crack on the contour line B_z becomes more obvious. As shown in the black rectangle marked in Fig. 3, it can be seen that the contour near the crack appears to be free from the restraint of the metal pipe and gradually moves toward the side of the excitation coil. At this time, the magnetic induction intensity near the crack decreases. Therefore, the radial and axial magnetic inductions show the changes shown in Fig. 2. Meanwhile, the electromagnetic field distribution further proves that the radial and axial magnetic induction intensities have opposite changes due to the crack shape.

(4) The following conclusion can be drawn from the results obtained from different radial measurements. On the one hand, the closer to the inner surface of the metal pipe is, the smaller the radial and axial magnetic induction intensities become, which is related to the fact that the external magnetic field is dominated by the source field generated by the coil. On the other hand, the closer to the inner surface

of the metal pipe is, the more obvious the change of magnetic field caused by crack shape can be detected. This characteristic is related to the eddy current field. Cracks with different cross-sections are supposed to cause different eddy currents to be induced on the surface of the metal pipe. And this eddy current will simultaneously induce different electromagnetic fields on the surface of the metal pipe.

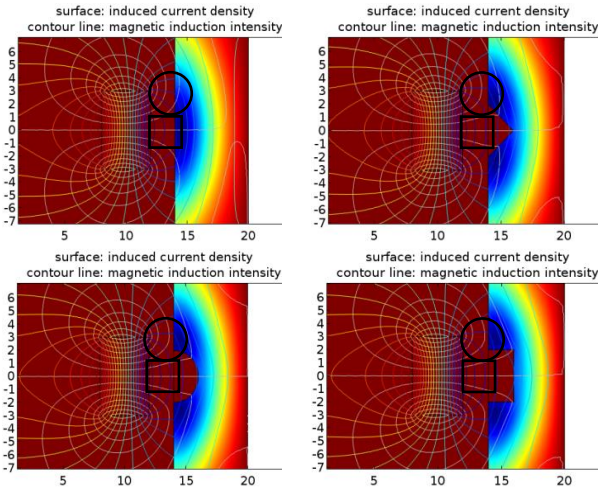

Fig. 3. Distribution of induced current density and magnetic induction intensity contours for cracks with different shapes.

Figure 4 shows the variations in the peak of radial and axial magnetic induction intensity with the cross-sectional area of the crack. As can be seen from Fig. 4, the peak of radial magnetic induction intensity increases with the crack-sectional area and shows a linear relationship. As the cross-sectional area increases from 5 mm^2 to 8 mm^2, the peak value of radial magnetic induction intensity increases by 6.764×10^{-5} T. Similarly, the peak of axial magnetic induction intensity decreases with the cross-sectional area of the crack, and shows a linear relationship. As the cross-sectional area increases from 5 mm^2 to 8 mm^2, the peak value of axial magnetic induction intensity decreases by 8.711×10^{-5} T. The results show that the relationship between the magnetic induction intensity and the cross-sectional area of the crack is linear, which is beneficial to the quantitative identification of the crack shape. In addition, both radial and axial magnetic induction intensity near the pipe can be used for the quantitative analysis of the crack shape, and axial magnetic induction intensity changes more significantly. Through the monitoring and comparison of the magnetic field in two directions, the measurement results can be further confirmed to avoid the influence of external interference. Moreover, effective signals in both directions provide more options for actual detection.

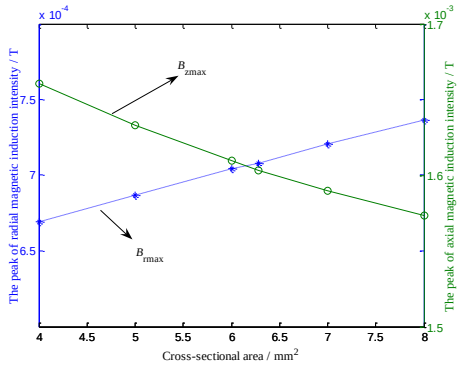

Fig. 4. The relationship between the peak of the magnetic induction intensity and cross-sectional area of the crack.

As the crack shape changes from a rectangle to semicircle and then to triangle, the peak values of axial magnetic induction increase by 2.979×10^{-5} T and 5.732×10^{-5} T, respectively. The change of response is measurable in practice as a result of advances in sensors and signal processing technology. Magnetic sensors based on TMR effects have the virtue of high accuracy, wide linear ranges and strong anti-interference capability, which have been widely used in electromagnetic nondestructive testing. The commercially available TMR2905 sensor, for example, has a sensitivity of 60 mV/V/Oe, noise <5nT/rtHz (@1Hz), and a resolution of 0.01μT. The magnetic sensor is able to completely meet the measurement requirements according to the changes of radial or axial magnetic induction intensities caused by crack shapes. Another noticeable external disturbance is the space geomagnetic field. The magnetic induction intensity of the earth's surface is about 0.5×10^{-4} T. Compared with the changes of the magnetic field caused by crack shapes, this value is still relatively obvious. Thus, some technical means must be adopted to suppress its effect. For instance, the frequency of excitation current is 1 kH_Z, so phase-locked amplifier can be used in the actual detection to remove the signal of non-selected frequency (i.e., noise) and retain the information of selected frequency.

B. Circumferential length of cracks

Six model components with different crack lengths are established in COMSOL Multiphysics. Different from the construction of rectangular or semicircle crack model, the research on the circumference length of crack requires the establishment of three-dimensional model. Compared with the two-dimensional model, the three-dimensional model takes a longer time to calculate. Therefore, the mesh type is adjusted to a free tetrahedral mesh during mesh generation, and its size is defined as refinement. However, it is found that the refined results are obviously not ideal, and the curve generated by post-processing is not smooth, which affects the quantitative

analysis of crack length to some extent. In order to save unnecessary calculation time, the method adopted in this paper is to further refine the key research areas, such as the area near the crack, and select the longest edge to split and the number of refinements to 2. By means of this technique, satisfactory calculation results can be obtained and the calculation time is acceptable. The basic parameters of the metal pipe and coil are exactly the same and the height and depth of the crack section are 2 mm, i.e., the crack section is square. The only difference exists in the circumferential length of the crack. The different lengths in the circumferential direction are represented by the central angles corresponding to the circular arcs, which are 0°, 60°, 120°, 180°, 270° and 360°, respectively, as shown in Fig. 5. Magnetic field measurement positions P1-P4 are selected at 0°, 90°, 180° and 270°, respectively, with radial distance r = 13.5mm. The measurement range of z direction is -20~20mm.

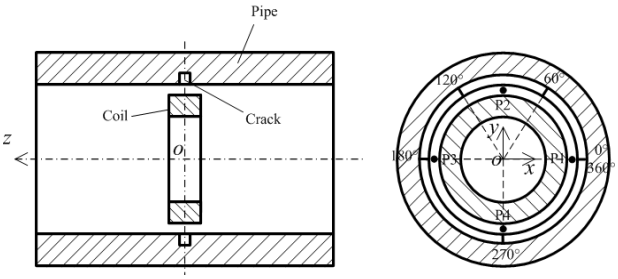

Fig. 5. Model schematic diagram and different length cracks in circumferential direction.

Figure 6 shows the distribution of magnetic induction intensities B_x, B_y and B_z measured at P1-P4 for the metal pipe without crack.

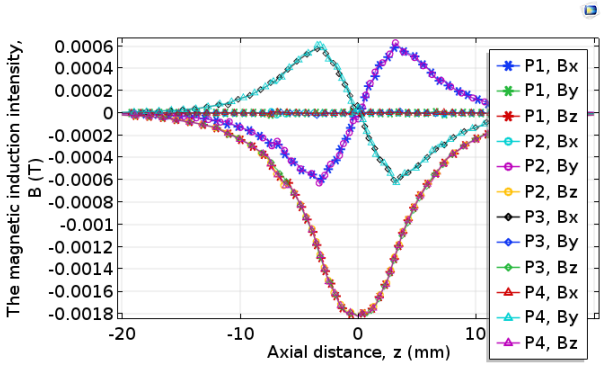

Fig. 6. The magnetic induction intensity at P1-P4 in the absence of cracks.

As shown in Fig. 6, B_x is oddly symmetric with respect to z = 0 at P1. When $z > 0$, B_x is a positive value, and when $z < 0$, B_x becomes negative, while B_y is always zero. Besides, B_z is always negative and even symmetric with respect to z = 0. In order to demonstrate the magnetic induction intensity in the area near P1 more clearly, the three-dimensional magnetic field distributions shown in Fig. 7 are established. As shown in Figs. 7 (a)-(c), the distribution of B_x, B_y and B_z at P1 is completely consistent with the previous two-dimensional figure.

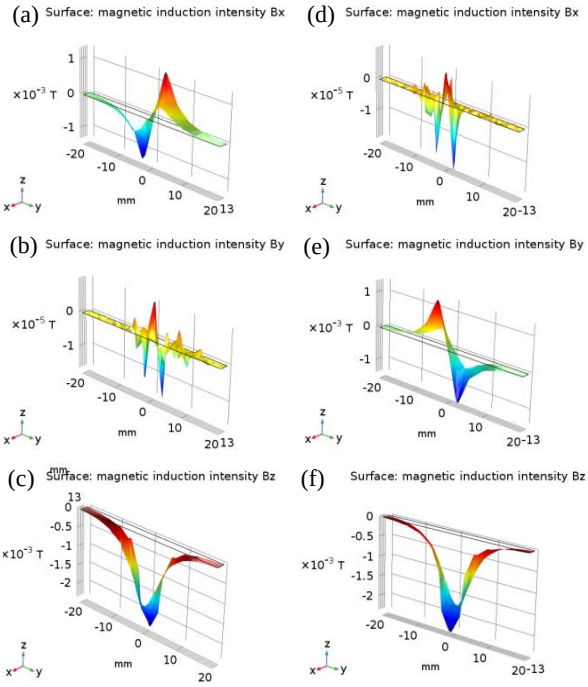

Fig. 7. Three-dimensional distribution of magnetic induction intensity near P1 and P4.

Similarly, the distribution of magnetic fields in three directions at the positions P2-P4 can be obtained from Fig. 6. In order to better understand the distribution of magnetic fields and the relationship, the schematic diagram shown in Table 1 is established.

Table 1: Distributions of magnetic induction intensity at P1-P4

	P1	P2	P3	P4
B_x	Odd symmetry (+)	0	Odd symmetry (-)	0
B_y	0	Odd symmetry (+)	0	Odd symmetry (-)
B_z	Even symmetry	Even symmetry	Even symmetry	Even symmetry

In the table, "+" indicates that the value of the magnetic induction intensity is the same as the symbol of the position value, while "-" suggests that the value

of the magnetic induction intensity is opposite to the symbol of the position value. In addition, the distribution of the magnetic induction intensity near P4 can be understood according to the three-dimensional figures shown in Figs. 7 (d)-(f).

Based on the above analysis, the influence of circumference length of crack on B_x is further analyzed. As shown in Fig. 8 (a), when there is no crack, that is, the corresponding angle of the crack is 0°, B_x at P1 and P3 would be symmetrically distributed. B_x at P2 and P4 are almost zero. As shown in Fig. 8 (b), when a crack with a central angle of 60° appears, the magnetic induction intensity at P1 is expected to increase to some extent, while the B_x of the other three positions are basically unchanged. Under such circumstance, the B_x at P1 and P3 is no longer symmetric. As can be seen from Fig. 8 (c), when the corresponding central angle of the crack increases from 60° to 120°, the magnetic induction intensity at P1 increases slightly, while the magnetic induction intensity at P3 changes a bit. Apart from those, as shown in Fig. 8 (d), when the corresponding central angle of the crack goes up from 120° to 180°, the magnetic induction intensity at P3 increases significantly. Meanwhile, the B_x at P1 and P3 are distributed symmetrically again. However, compared with the symmetry shown in Fig. 8 (a), both of them increase in amplitude. As depicted in Fig. 8 (e), when the corresponding central angle of the crack increases from 180° to 270°, double peaks appear at P4, in addition to a certain increase at P3. What's more, as shown in Fig. 8 (f), when the corresponding central angle of the crack increases from 270° to 360°, double peaks of the magnetic induction intensity observed in Fig. 8 (e) disappear because the model becomes an axisymmetric structure again. B_x at P1 also increases. At this time, the distributions of the magnetic induction intensity at four positions are similar to those without cracks. The difference is that the values of B_x at P1 and P3 increase significantly.

In the light of the previous analysis of changes of B_x, the schematic diagram shown in Table 2 is established, in which "↑" indicates a significant increase in the magnetic induction intensity, and "↗" refers to a certain increase in the magnetic induction intensity, and the symbol "—" suggests few changes appear in the magnetic induction intensity.

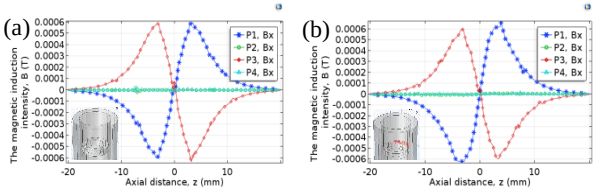

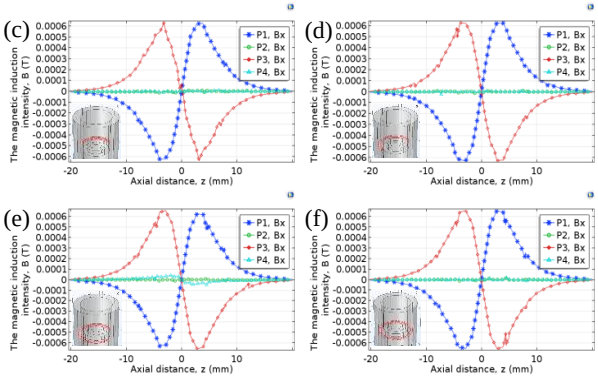

Fig. 8. B_x distribution for different circumferential lengths of cracks.

Table 2: The variation of B_x with the circumference length of crack at P1-P4

	P1	P2	P3	P4
0°	Symmetry with P3 (+)	0	Symmetry with P1 (+)	0
60°	↑	—	—	—
120°	↗	—	↗	—
180°	Symmetry with P3 (+)	—	↑, Symmetry with P1 (+)	—
270°	—	—	↑	Double peak appears
360°	↑, Symmetry with P3 (+)	—	Symmetry with P1 (+)	Double peak disappears

Therefore, the circumference length of crack mainly has a certain influence on B_x at P1 and P3, and exerts little effect on B_x at P2 and P4. By comparing the symmetry of B_x at P1 and P3, the length of the crack in the circumferential direction, thus, gets to be deduced.

Then, the effect of the circumference length on B_y is studied, as shown in Fig. 9. By monitoring the B_y at the P1, it can be found that only in the absence of crack and full-circumferential cracks, does no double peaks occur, and any other circumferential cracks would result in double peak in B_y. Moreover, the amplitude of the peak is not significantly affected by the circumference length of the crack. By monitoring B_y at P3, only when half-circumferential cracks are present and the phenomenon of double peaks appears, will no other circumferential cracks of any length lead to the double peaks in B_y. There is a slight change in B_y at P2 and P4, which, however, is not obvious. Therefore, several other special cracks, such as half-circumferential and whole-circumferential ones, get to be qualitatively assessed by the detection of B_y at P1 and P3.

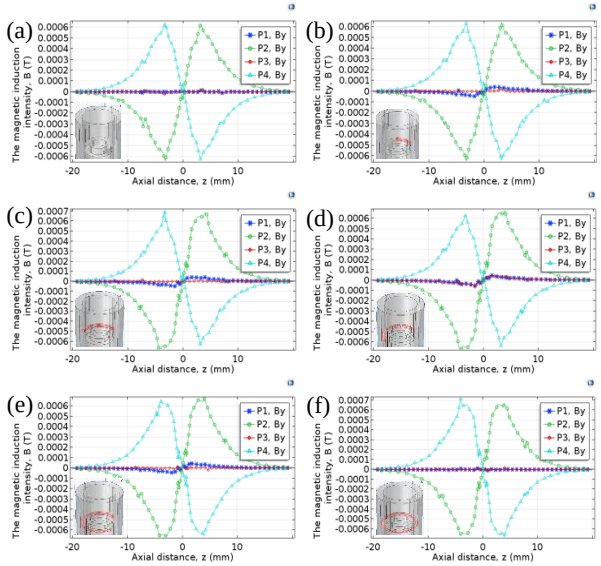

Fig. 9. B_y distribution for different circumferential lengths of cracks.

Finally, what is analyzed hereby is the influence of circumference length on B_z, as shown in Fig. 10. Based on the changes of B_z in Fig. 10, the schematic diagram presented in Table 3 is established. In the table, "↓" indicates a significant decrease in the peak of the magnetic induction intensity, and "↘" reveals a certain decrease in the peak of the magnetic induction intensity. Moreover, "—" shows that the peak of the magnetic induction intensity proves no change. As can be seen from the table, peaks of B_z at P1-P4 decrease sequentially with the ascendance of the circumference length of the crack. Therefore, circumference length of crack can also be quantitatively evaluated by analyzing the change of B_z.

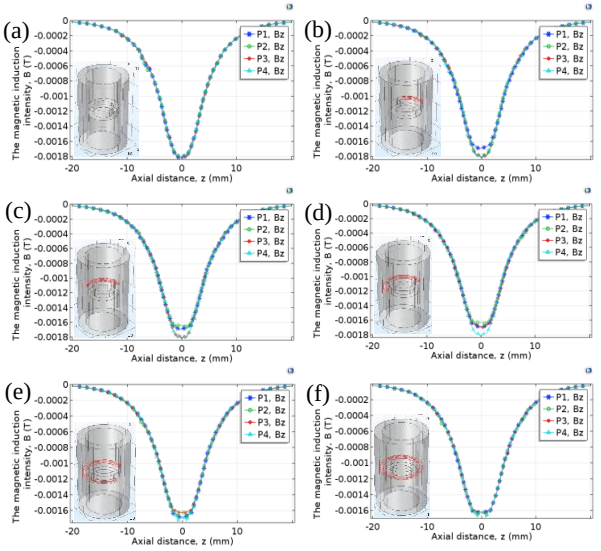

Fig. 10. B_z distribution for different circumferential lengths of cracks.

Table 3: The variation of B_z with the circumference length of crack at P1-P4

	P1	P2	P3	P4
0°	Even symmetry	Even symmetry	Even symmetry	Even symmetry
60°	↓	—	—	—
120°	—	↓	—	—
180°	—	—	↓	—
270°	—	—	—	↓
360°	↘	—	—	↘

Figure 11 shows the relationship between the abrupt positions of the *z*-direction component of the magnetic induction intensity and the different crack lengths. Crack length is represented by the corresponding central angle, and eight types of circumferential cracks with different central angles of 0°, 60°, 120°, 180°, 240°, 270°, 300° and 360° are used. The abrupt position of the *z*-direction component of the magnetic induction intensity is represented by the arc length corresponding to the measured radius of 13.5 mm. As shown in Fig. 11, there is an obvious linear relationship between the circumference length of the crack and the abrupt location of the magnetic induction intensity. In the test, the magnetic sensor is scanned along the circumference of r = 13.5 mm. By monitoring the change of the magnetic field, the information about crack location and crack length can be obtained in time. In addition, the magnetic field is approximately reduced from 1.8×10^{-3} T to 1.6×10^{-3} T for the circumferential cracks studied in this paper, and the abrupt change of about 0.2×10^{-3} T is relatively large, so the detection effect is quite obvious. Thus, it can not only quantitatively analyze the shape of the crack section, but also quantitatively understand the circumference length of the crack by using the characteristics of the magnetic field.

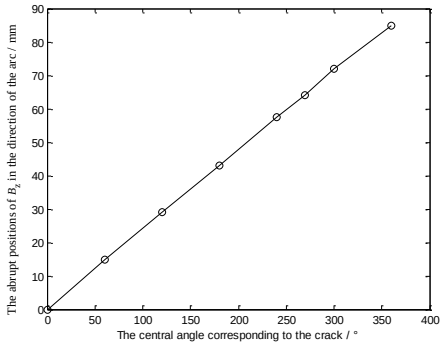

Fig. 11. The relationship between the abrupt position of B_z and the central angle of the crack.

In conclusion, the three directions of the magnetic induction intensity demonstrate their own characteristics in evaluating the circumference length of crack. The B_y is adopted to evaluate several special cracks, but it is not suitable for the quantitative study of crack lengths.

Furthermore, B_z suggests obvious advantages in the quantitative analysis of cracks. Meanwhile, B_x, to some extent, can also meet the demand of the quantitative analysis of circumference lengths in cracks and judge several special lengths.

IV. CONCLUSION

In present paper, the relationship between the crack in metal pipe and the magnetic field in the surrounding space is studied in detail by means of finite element simulation. It can be observed from these analyses that the eddy current field can reflect details such as crack shapes and circumference lengths. These results show that the eddy current testing based on the analysis of the three-dimensional magnetic field proposed in this paper is feasible, which is superior to MFL testing and other electromagnetic methods in many aspects. This method has expended the application range of eddy current non-destructive testing and provided guidance for the quantitative evaluation of pipeline cracks.

ACKNOWLEDGMENT

This work was supported by the National Natural Science Foundation of China (Grant numbers 51575331, 51175316 and 61603238) and Jiangsu Province University Outstanding Science and Technology Innovation Team Project (2019SJK07).

REFERENCES

[1] R. Grimberg, "Electromagnetic nondestructive evaluation: Present and future," *Strojniški vestnik – Journal of Mechanical Engineering*, vol. 2011, no. 3, pp. 204-217, Mar. 2011.

[2] K. Miya, "Recent advancement of electromagnetic nondestructive inspection technology in Japan," *IEEE Transactions on Magnetics*, vol. 38, no. 2, pp. 321-326, Apr. 2002.

[3] A. Sophian, G. Y. Tian, D. Taylor, and J. Rudlin, "Electromagnetic and eddy current NDT: A review," *Insight - Non-Destructive Testing and Condition Monitoring*, vol. 43, no. 5, pp. 302-306, May 2001.

[4] H. A. Sabbagh, R. K. Murphy, E. H. Sabbagh, J. C. Aldrin, J. Knopp, and M. Blodgett, "Computational electromagnetics and model-based inversion: A modern paradigm for eddy-current nondestructive evaluation," *Applied Computational Electromagnetics Society Journal*, vol. 24, no. 6, pp. 533-540, Dec. 2009.

[5] J. García-Martín, J. Gómez-Gil, and E. Vázquez-Sánchez, "Non-destructive techniques based on eddy current testing," *Sensors*, vol. 11, no. 3, pp. 2525-2565, Feb. 2011.

[6] D. Rifai, A. N. Abdalla, K. Ali, and R. Razali, "Giant magnetoresistance sensors: A review on structures and non-destructive eddy current testing applications," *Sensors*, vol. 16, no. 3, pp. 1-30, Mar. 2016.

[7] Y. Li, J. Wilson, and G. Y. Tian, "Experiment and simulation study of 3D magnetic field sensing for magnetic flux leakage defect characterisation," *NDT & E International*, vol. 40, no. 2, pp. 179-184, Mar. 2007.

[8] M. Ravan, R. K. Amineh, S. Koziel, N. K. Nikolova, and J. P. Reilly, "Sizing of 3-D arbitrary defects using magnetic flux leakage measurements," *IEEE Transactions on Magnetics*, vol. 46, no. 4, pp. 1024-1033, May 2010.

[9] J. J. Chen, "3-D defect profile reconstruction from magnetic flux leakage signals in pipeline inspection using a hybrid inversion method," *Applied Computational Electromagnetics Society Journal*, vol. 32, no. 9, pp. 826-832, Sep. 2017.

[10] C. K. Low and B. S. Wong, "Defect evaluation using the alternating current field measurement technique," *Insight - Non-Destructive Testing and Condition Monitoring*, vol. 46, no. 10, pp. 598-605, Oct. 2004.

[11] J. H. Ge, W. Li, G. M. Chen, and X. K. Yin, "Analysis of signals for inclined crack detection through alternating current field measurement with a U-shaped probe," *Insight - Non-Destructive Testing and Condition Monitoring*, vol. 59, no. 3, pp. 121-128, Mar. 2017.

[12] X. C. Hu, "Pulsed alternating current field measurement technique for defect identification and quantification," *Journal of Mechanical Engineering*, vol. 47, no. 4, pp. 121-128, Jan. 2011.

[13] F. Jiang, S. L. Liu, S. J. Xin, and H. L. Zhang, "Electromagnetic nondestructive testing model and surface magnetic field analysis for circumferential cracks on metal rod," *ASME - Journal of Non-destructive Evaluation, Diagnostics and Prognostics of Engineering Systems*, vol. 2, no. 4, pp. 044501, Nov. 2019.

[14] T. Theodoulidis and J. R. Bowler, "Eddy-current interaction of a long coil with a slot in a conductive plate," *IEEE Transactions on Magnetics*, vol. 41, no. 4, pp. 1238-1247, Apr. 2005.

[15] F. Jiang, S. L. Liu, S. J. Xin, et al., "Evaluation of circumferential cracks in metal tube based on magnetic field response model of eddy current testing," *Insight - Non-Destructive Testing and Condition Monitoring*, vol. 62, no. 2, pp. 91-97, Feb. 2020.

[16] Z. Zeng, L. Udpa, and S. S. Udpa, "Finite-element model for simulation of ferrite-core eddy-current probe," *IEEE Transactions on Magnetics*, vol. 46, no. 3, pp. 905-909, Apr. 2010.

[17] Y. Wei and S. L. Liu, "Numerical analysis of the dynamic behavior of a rotor-bearing-brush seal system with bristle interference," *Journal of*

Mechanical Science and Technology, vol. 33, no. 8, pp. 1-9, Aug. 2019.

[18] B. Helifa, M. Féliachi, I. K. Lefkaier, and B. Fouad, "Characterization of surface cracks using eddy current NDT simulation by 3D-FEM and inversion by neural network," *Applied Computational Electromagnetics Society Journal*, vol. 31, no. 2, pp. 187-194, Feb. 2016.

Feng Jiang was born in Yancheng, China, in 1981. He received the M.Sc. degree in the School of Mechanical Engineering from Jiangsu University, Zhenjiang, China, in 2006 and received Ph.D. degree from Shanghai University, Shanghai, China, in 2019. He is currently working as an Associate Professor in Electrical and Information Engineering at Changzhou Institute of Technology. His research interests include electromagnetic nondestructive evaluation, mathematical modeling and fault diagnosis.

Shulin Liu was born in 1963 and received the M.Sc. degree in the School of Mechanical Engineering from Yanshan University, Qinhuangdao, China, in 1989 and received his Ph.D. degree from Harbin Institute of Technology, Harbin, China, in 2003. Since 2008, he is a Professor and Doctoral Supervisor at School of Mechatronics Engineering and Automation, Shanghai University, China. His major research direction is complex equipment fault diagnosis.

The Reduction of Force Component Produced by Short Sides by Analyzing the Corner of Coil in Planar Motor with Halbach Magnet Array

Guangdou Liu, Shiqin Hou, and Wensheng Xiao*

College of Mechanical and Electronic Engineering
China University of Petroleum, Qingdao 266580, China
gdliu@upc.edu.cn, 1334273282@qq.com, xiaows@upc.edu.cn*

Abstract ─ The planar motor with moving-magnet is purely levitated by the stator coils. The forces produced by coils are calculated with the analytical model of magnet array and coil surface model for applying to the real time control. Take the coil and the Halbach magnet array which is at 45 degree with the long side of coil for analysis. The force component produced by short sides can be eliminated for conveniently controlling when the length of coil takes certain dimension. In practice, the force component produced by short sides is small but not zero. There are two reasons, one is the higher harmonics and the other is the corner segments of coil. The force integral expressions of coil corner segments are given by the Lorenz force law. Then the forces numerically calculated with harmonic model and coil full model are verified by comparing with the magnetic surface charge model and finite element model. In order to reduce the force component produced by short sides, the different corners of coil are analyzed. Comparing the forces of different corners of coil, the force component produced by short sides can be significantly reduced with slightly change of the other force components.

Index Terms ─ Corner segments, force reduction, Halbach array, planar motor.

I. INTRODUCTION

The magnetically levitated planar motor with moving magnets is attracting more and more attention with the advantages of high speed, high acceleration and high precision in the industry. The moving magnet array is purely levitated by the suspension force exerted by coils, and realizes the horizontal motion [1-13]. There are no transmission equipment, so the planar motor is without the mechanical friction, lubricating oil contamination, cable interference and so on. The structure of the planar motor is simplified, and of which the weight is reduced. The 2D Halbach permanent magnet array is applied in the planar motor, which can obtain high magnetic field on one side with fine sinusoidal waveform [6].

Compter [7] proposed the magnetically levitated planar motor with moving coils, and the magnet array is rotated -45° relative to the coils. The planar motor replaces the conventional structure with two linear motors to realize the horizontal motion. Jansen [8] applied the arrangement of coil and the magnet array to the planar motor of moving magnets, which is the inverse of planar motor of moving coils. The harmonic model of magnetic flux density for the Halbach magnet array is derived by Fourier series and scalar potential. The forces and torques generated by coils are calculated by using analytical model which is obtained by taking the first harmonic and coil surface model in order to be used in the real time control. Jansen [9] optimized the planar motor with moving magnets. The minimum power dissipation at the suspension status is selected to be the optimized objective function. The optimal dimensions of coil and magnet array are obtained. Peng [10] took the coil corner segments into account for calculating the force and torque of coil. The expressions of force and torque are derived by using the composite integration and the Newton-Leibniz formula with the analytical model of magnet array. But the higher harmonics is ignored.

As the Halbach magnet array is at 45 degree with the long side of one coil, the force component produced by short sides of coil can be eliminated when the length of coil takes certain dimension according to the force expression used in the real time control. In fact, the force is not zero due to the higher harmonics and corner segments of coil. In this paper, the integral force expression for the corner segments of coil is derived by the Lorenz force law. The forces calculated by using harmonic model and coil full model are verified to be accurate. The different winding moulds are proposed and the different coil structures are obtained. The forces of different coils are predicted by using the model verified before. Comparing the forces of different coils, the component produced by short sides can be

Submitted On: October 15, 2019
Accepted On: August 9, 2020

https://doi.org/10.47037/2020.ACES.J.360115

significantly reduced with slightly change of the other force components.

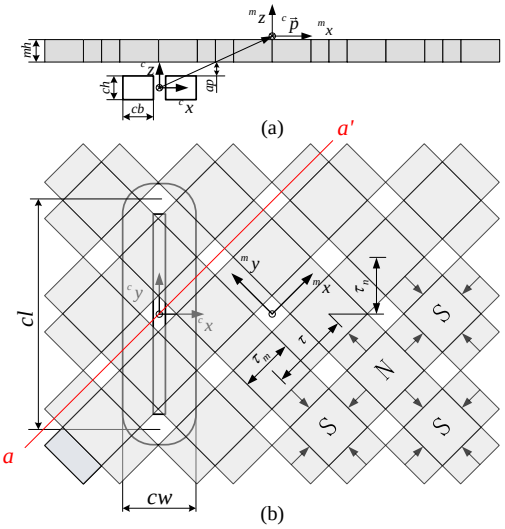

Fig. 1. The sketch of one coil and the Halbach magnet array in planar motor: (a) front view and (b) top view.

II. THE PLANAR MOTOR

The sketch of one coil and the Halbach magnet array in planar motor with moving magnets is shown in Fig. 1. In Fig. 1, the arrows mean the magnetization direction of magnets from *s*-pole to *n*-pole. *N* shows the magnetization direction outward the paper which is consistent with the positive direction of ${}^{m}z$ axis, and *S* is in the opposite direction. The global and local coordinates are located at the center of the coils and the Halbach magnet array, which are denoted with the superscript ^{c} and ^{m}, respectively.

The magnetic flux density of the Halbach magnet array shown in Fig. 1 is spatial distribution. The magnetic flux density is derived by using Fourier series and scalar potential and expressed in the local coordinate system. The derivation procedure is shown in reference [11]. The expression is:

$$ {}^{m}\vec{B}_3\left({}^{m}\vec{x}\right) = -\mu_0 \cdot \sum_{m=1}^{\infty}\sum_{n=1}^{\infty} K_3 e^{\lambda\,{}^{m}z} \begin{bmatrix} \frac{k\pi}{\tau}\cos\frac{k\pi\,{}^{m}x}{\tau}\sin\frac{l\pi\,{}^{m}y}{\tau} \\ \frac{l\pi}{\tau}\sin\frac{k\pi\,{}^{m}x}{\tau}\cos\frac{l\pi\,{}^{m}y}{\tau} \\ \lambda\sin\frac{k\pi\,{}^{m}x}{\tau}\sin\frac{l\pi\,{}^{m}y}{\tau} \end{bmatrix}, \quad (1) $$

where $\mu_r = 1$, and

$$ \lambda = \frac{\pi}{\tau}\sqrt{k^2+l^2}, \quad (2) $$

$$ a(k) = \frac{4}{k\pi}\cos\frac{k\tau_m\pi}{2\tau}\sin\frac{k\pi}{2}, \quad (3) $$

$$ b(k) = \frac{4}{k\pi}\sin\frac{k\tau_m\pi}{2\tau}\sin\frac{k\pi}{2}, \quad (4) $$

$$ K_3 = B_r\frac{\left(e^{-m_t\lambda}-e^{-m_b\lambda}\right)}{2\left(k^2+l^2\right)\pi\lambda\mu_0}\begin{pmatrix} b(k)b(l)\pi\left(k^2+l^2\right) \\ +a(k)b(l)k\lambda\tau \\ +a(l)b(k)l\lambda\tau \end{pmatrix}, \quad (5) $$

k and l are the harmonic numbers for the ${}^{c}x$- and ${}^{c}y$-direction, respectively, m_t and m_b are the height of magnet array, τ_m is the side length of the magnets magnetized in the ${}^{c}z$-direction, τ is the pole pitch, B_r is the residual magnetization of the permanent magnet, μ_r is the relative permeability of the permanent magnets, μ_0 is the permeability of vacuum.

Because the high quality sintered NdFeB permanent magnets ($\mu_r \approx 1.03$-1.05) is used in the planar motor. The relative permeability of the permanent magnets is considered equal to air, the error due to this assumption can be neglected.

The coil shown in Fig. 1 can be split into eight segments, including four straight segments and four corner segments. The Lorenz force law is applied to the calculation of force produced by coil [12]. The force expression is:

$$ \begin{aligned} {}^{c}\vec{F} &= -\int_{Vcoil}\vec{j}\times{}^{c}\vec{B}_3\,d\,{}^{c}V \\ &= -\left(\int_{Vstraight}\vec{j}\times{}^{c}\vec{B}_3\,d\,{}^{c}V + \int_{Vcorner}\vec{j}\times{}^{c}\vec{B}_3\,d\,{}^{c}V\right), \end{aligned} \quad (6) $$

The force F_y produced by short sides of coil shown in Fig. 1 is analyzed. In order to satisfied the real time control, the coil surface model and analytical model of Halbach magnet array are used [5]. The force F_y can be expressed as:

$$ \begin{aligned} {}^{c}F_y &= -jB_z e^{-\frac{\sqrt{2}\pi}{\tau}{}^{c}p_z}\left(cw-cb\right)\left(\frac{\tau}{\pi}\right)^2 \\ &\quad \sin\frac{cb\sqrt{2}\pi}{2\tau}\sin\frac{cl\sqrt{2}\pi}{2\tau}\sin\frac{\left({}^{c}y-{}^{c}p_y\right)\sqrt{2}\pi}{\tau}, \end{aligned} \quad (7) $$

where

$$ B_z = \sqrt{2}K_3\frac{\pi}{\tau}, \quad (8) $$

j is the surface current of coil, ${}^{c}p_z$ and ${}^{c}p_y$ are the coordinate of the point ${}^{c}\vec{p}$ shown in Fig. 1, cb is the conductor bundle width, cl is the length of coil.

The force F_y can be eliminated when $cl = \sqrt{2}n\tau$. Due to the higher harmonics and corner segments of coil, the actual force F_y is not zero.

The method of changing the structure of coil to reduce the force F_y is proposed. The different coils are obtained by changing the winding mould. The forces of these coils are predicted by using harmonic model and coil full model.

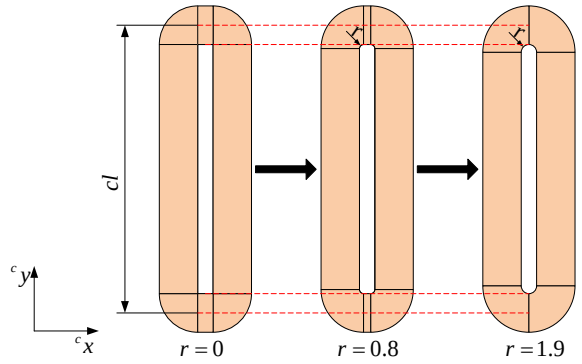

Fig. 2. The different corners of coil with different winding moulds.

III. COILS AND FORCE EXPRESSIONS

The different winding moulds are obtained by filleting the four edges. The different coils are shown in Fig. 2. The coil length *cl* keeps constant of these coils.

The dimensions of coil and magnets are decided according to the reference [6], and are listed in the Table 1 shown as follows.

Table 1: The dimensions of coil and magnets

Parameters	**Value**	**Unit**
Pole pitch (τ)	25	mm
Pole pitch of coordinate transformation (τ_n)	17.7	mm
Magnet pitch (τ_m)	17	mm
Clearance (*ap*)	1	mm
Coil length (*cl*)	70.8	mm
Coil width (c*w*)	22.8	mm
Conductor bundle width (*cb*)	9.5	mm
Coil height (*ch*)	7.4	mm
Remanence of the magnet (B_r)	1.24	T
current density (*j*)	10	A/mm^2
Magnet array height (*mh*)	7	mm

Take the coil with r=0.8mm for example to derive the force expressions of corner segments of coil. Figure 3 shows the coil, and there are eight segments marked with number from 1 to 8.

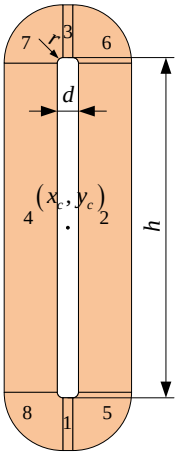

Fig. 3. The segments and dimensions of coil.

A. The straight segments of coil

The force expression of straight segments can be directly given by the Lorenz force law,

$$
\begin{aligned}
&{}^{c}\vec{F}_{straight} = \\
&-\int_{z_1}^{z_2}\int_{y_c-\frac{h}{2}-cb}^{y_c+\frac{h}{2}-r}\int_{x_c-\frac{d}{2}+r}^{x_c+\frac{d}{2}-r}\begin{bmatrix} j & 0 & 0\end{bmatrix}^{\mathrm{T}}\times {}^{c}\vec{B}_3 d\,{}^{c}x d\,{}^{c}y d\,{}^{c}z \\
&-\int_{z_1}^{z_2}\int_{y_c-\frac{h}{2}+r}^{y_c+\frac{h}{2}-r}\int_{x_c-\frac{d}{2}}^{x_c+\frac{d}{2}+cb}\begin{bmatrix} 0 & j & 0\end{bmatrix}^{\mathrm{T}}\times {}^{c}\vec{B}_3 d\,{}^{c}x d\,{}^{c}y d\,{}^{c}z \quad , (9)\\
&-\int_{z_1}^{z_2}\int_{y_c+\frac{h}{2}}^{y_c+\frac{h}{2}+cb}\int_{x_c-\frac{d}{2}+r}^{x_c+\frac{d}{2}-r}\begin{bmatrix} -j & 0 & 0\end{bmatrix}^{\mathrm{T}}\times {}^{c}\vec{B}_3 d\,{}^{c}x d\,{}^{c}y d\,{}^{c}z \\
&-\int_{z_1}^{z_2}\int_{y_c-\frac{h}{2}+r}^{y_c+\frac{h}{2}-r}\int_{x_c-\frac{d}{2}-cb}^{x_c-\frac{d}{2}}\begin{bmatrix} 0 & -j & 0\end{bmatrix}^{\mathrm{T}}\times {}^{c}\vec{B}_3 d\,{}^{c}x d\,{}^{c}y d\,{}^{c}z
\end{aligned}
$$

where

$$z_1 = -mh - ap - ch\,, \tag{10}$$

$$z_2 = -mh - ap\,, \tag{11}$$

${}^{c}\vec{B}_3$ is the transformation of the ${}^{m}\vec{B}_3$ into the global coordinate system, x_c, y_c are the coordinate value of the geometric center of coil in the global coordinate system, *d* and *h* are the length and width of the winding mould, respectively, *r* is the fillet radius.

B. The corner segments of coil

The corner segment 5 is picked for analyzing. There are two parts to be analyzed for calculating the force, the big circle and the small circle. The small circle segment will be subtracted in the force calculation. The current is in counter-clockwise direction.

The direction of current in the corner segment at any point is the tangential direction shown in Fig. 4, which can be decomposed into *x*- and *y*-component.

The two components are denoted with j_{5x} and j_{5y}, respectively. The expressions of j_{5x} and j_{5y} are described by:

$$j_{5x} = -j\frac{{}^{c}y - y_5}{\sqrt{\left({}^{c}x - x_5\right)^2 + \left({}^{c}y - y_5\right)^2}}, \tag{12}$$

$$j_{5y} = j\frac{{}^{c}x - x_5}{\sqrt{\left({}^{c}x - x_5\right)^2 + \left({}^{c}y - y_5\right)^2}}, \tag{13}$$

where

$$x_5 = x_c + \frac{d}{2} - r, \tag{14}$$

$$y_5 = y_c - \frac{h}{2} + r, \tag{15}$$

x_5 and y_5 are the coordinate value of the center point of the circle.

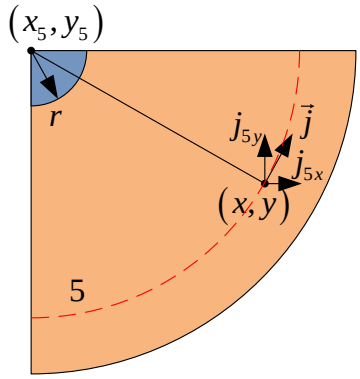

Fig. 4. The corner segment 5 of coil.

The force expression of the big circle segment is given by:

$$\begin{aligned} {}^{c}\vec{F}_{51} = -\int_{z_1}^{z_2}\int_{x_c+\frac{d}{2}-r}^{x_c+\frac{d}{2}+cb}\int_{f_{51}\left({}^{c}x\right)}^{y_c-\frac{h}{2}+r} \cdot \\ \begin{bmatrix} j_{5x} & j_{5y} & 0 \end{bmatrix}^{\mathrm{T}} \times {}^{c}\vec{B}_3 d\,{}^{c}x d\,{}^{c}y d\,{}^{c}z \end{aligned}, \tag{16}$$

where

$$f_{51}\left({}^{c}x\right) = -\sqrt{\left(cb + r\right)^2 - \left(x - x_{51}\right)^2} + y_{52}, \tag{17}$$

The current expressions in the small circle are the same as the big circle segment. The force expression can be expressed as:

$$\begin{aligned} {}^{c}\vec{F}_{52} = -\int_{z_1}^{z_2}\int_{x_c+\frac{d}{2}-r}^{{}^{c}x+\frac{d}{2}}\int_{f_{52}\left({}^{c}x\right)}^{y_c-\frac{h}{2}+r} \cdot \\ \begin{bmatrix} j_{5x} & j_{5y} & 0 \end{bmatrix}^{\mathrm{T}} \times {}^{c}\vec{B}_3 d\,{}^{c}x d\,{}^{c}y d\,{}^{c}z \end{aligned}, \tag{18}$$

where

$$f_{52}\left({}^{c}x\right) = -\sqrt{r^2 - \left(x - x_{51}\right)^2} + y_{52}, \tag{19}$$

Finally, the force expression of the corner segment 5 of coil is obtained and is expressed as:

$${}^{c}\vec{F}_5 = {}^{c}\vec{F}_{51} - {}^{c}\vec{F}_{52}, \tag{20}$$

The force expression of the other corner segments can be obtained by using the same method.

The force of the coil is calculated by using the harmonic model and coil full model, and the center point ${}^{c}\vec{p}$ of Halbach magnet array is along the line $a - a'$. In order to verify the accuracy, the forces calculated with harmonic model, magnetic surface charge model and finite element model are compared. The finite element model is obtained by the Ansoft Maxwell with percent error 0.1, which is a very professional electromagnetic field analysis software. The F_x and F_z of three models are shown in Fig. 5.

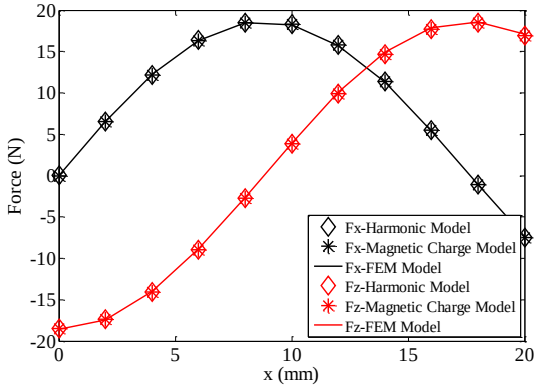

Fig. 5. The comparison of F_x and F_z of three models.

From the Fig. 5, it is found the error between the harmonic model and magnetic surface charge model is very small. Both the two models keep good consistency with the finite element model. For the F_z, the max error between the harmonic model and magnetic surface charge model is 0.032N and 0.203N between the harmonic model and finite element model, which are the 0.2% and 1.28% of the peak value of the harmonic, respectively.

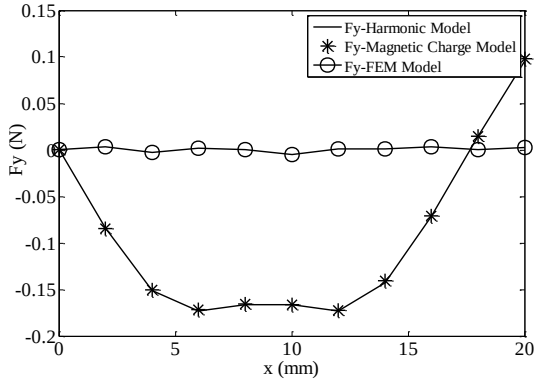

Fig. 6. The comparison of F_y of three models.

Figure 6 shows the F_y of three models. The force

F_y is small but not zero. The forces F_y of the harmonic model and magnetic surface charge model are in good agreement. The finite element model is not correct due to the small force F_y and the max error 0.203N obtained by F_z. The harmonic model is verified and selected to predict the force of different coils.

IV. FORCES OF DIFFERENT COILS

The different coils are obtained when fillet radius r takes 0, 0.5, 0.8, 1.2, 1.6 and 1.9. The forces are calculated and compared among these coils.

Figure 7 shows the comparison of F_x of different coils. The F_x decreases with the fillet radius r increase. The error of the peak value between the coil with r=0 and the coil with r=1.9 is 0.318N. It is the 1.70% of the peak value of the coil with r=0. The change of F_x is samll from the comparison.

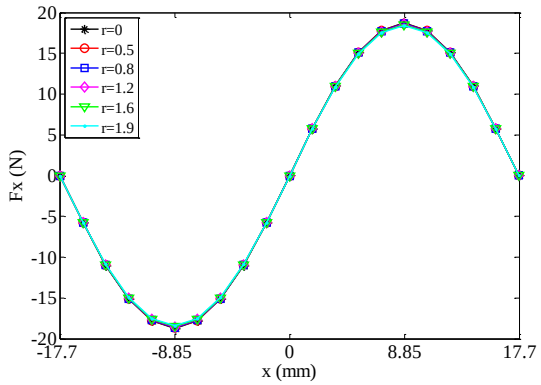

Fig. 7. The comparison of F_x of three models.

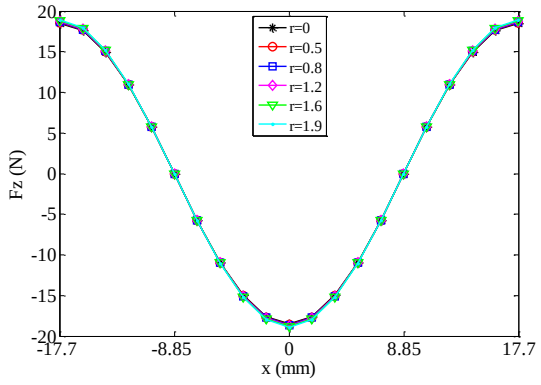

Fig. 8. The comparison of F_z of three models.

Figure 8 shows the comparison of F_z of different coils. The F_z increases with the increasing fillet radius r. The error of the peak value between the coil with r=0 and the coil with r=1.9 is 0.388N. It is the 2.10% of the peak value of the coil with r=0. The change of F_z is also samll from the comparison.

Figure 9 shows the comparison of F_y of different coils. It is found that the F_y decreases firstly to zero and then increases reversely with the fillet radius increase. In order to distinguish the forces generated by straight segments from the corner segments of coil, the F_y of two parts are compared.

The straight segments 1 and 3 of coil produce the force F_y. The range of straight segments 1 and 3 decreases with the fillet radius increase, so does the force F_y. Figure 10 shows the F_y generated by straight segments of these coils, which is in accordance with the inference. The magnitude of the F_y of the straight segment is very small.

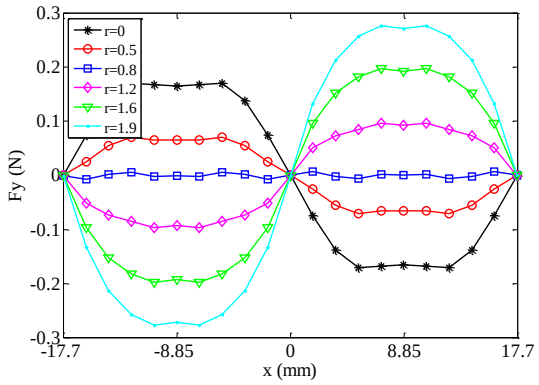

Fig. 9. The comparison of F_y of different coils.

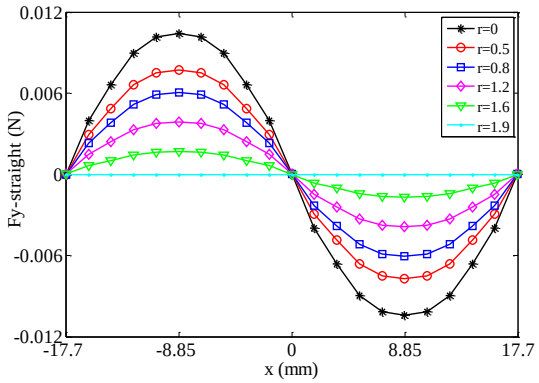

Fig. 10. The comparison of F_y generated by straight segments of different coils.

The major component of F_y is generated by corner segments of coil. To be more comprehensive, the F_y with different fillet radius are compared in one period, and is shown in the Fig. 11. The maximum value of F_y for each coil is listed in the Table. 2.

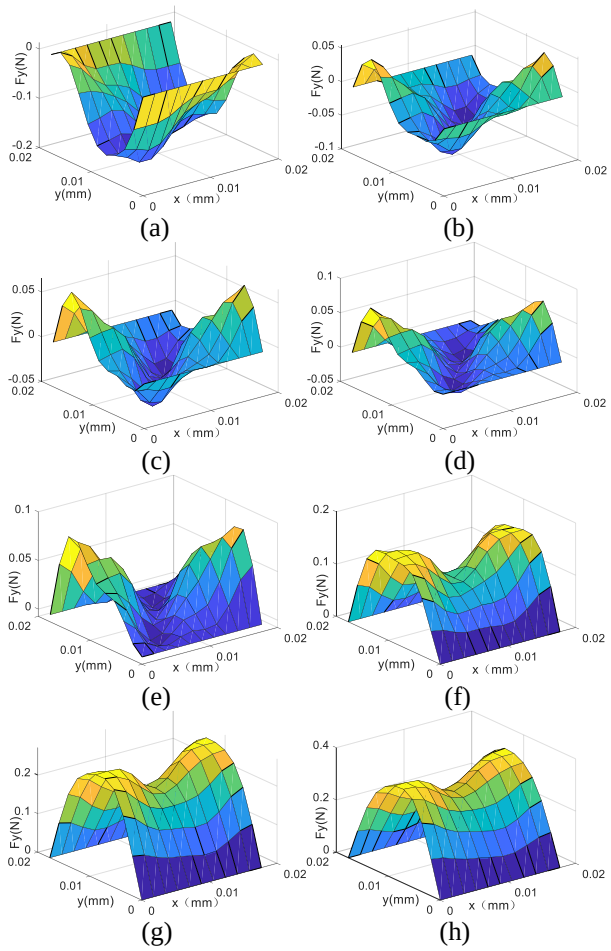

Fig. 11. The comparison of F_y with different fillet radius: (a) r=0, (b) r=0.5, (c) r=0.6, (d) r=0.7, (e) r=0.8, (f) r=1.2, (g) r=1.6, and (h) r=1.9.

Table 2: The max value of F_y with different fillet radius

r(mm)	Max value (N)	Ratio
0	0.1717	100%
0.5	0.0710	41.45%
0.6	0.0652	37.97%
0.7	0.0770	44.85%
0.8	0.0889	51.78%
1.2	0.1630	94.93%
1.6	0.2709	157.78%
1.9	0.3594	209.32%

Analyzing the value of Table 2 and the waveform of the Fig. 11, the F_y decreases firstly and then increases reversely with the fillet radius increase. The F_y can be reduced by optimizing the fillet radius of coil. For the planar motor of this paper, the F_y is significantly reduced when the fillet radius is equal to 0.6mm.

V. CONCLUSION

(1) The force integral expressions of corner segments of coil are given by Lorentz force law. The coil full model is used for calculating the force. The forces calculated by harmonic model, magnetic surface charge model and finite element model are compared, and the harmonic model is verified.

(2) The different coils can be obtained by changing the winding mould while keeping *cl* as constant. The forces of different coils are calculated by using the model verified before.

(3) The F_x decreases and the F_z increases with the fillet radius r increase. The F_y decreases firstly and then increases reversely as the fillet radius increase.

(4) The F_y caused by straight segments of coil is a small proportion. The F_y can be reduced by optimizing the fillet radius of coil. The F_y of short sides of coil is significantly reduced when the fillet radius takes 0.6. It has good theoretical and practical significance.

ACKNOWLEDGMENT

Research was supported by the Shandong Provincial Natural Science Foundation (ZR2020ME204) and the Ministry of Industry and Information Technology “Seventh Generation Ultra Deep Water Drilling Platform (ship) innovation project ([2016] No. 24)”.

REFERENCES

[1] D. L. Trumper, M. E. Williams, and T. H. Nguyen, “Magnet arrays for synchronous machines,” *Industry Applications Society Annual Meeting, 1993, Conference Record of the 1993 IEEE*, pp. 9-18, 1993.

[2] M. Lahdo, T. Ströhla, and S. Kovalev, “Magnetic propulsion force calculation of a 2-DoF large stroke actuator for high-precision magnetic levitation system,” *Applied Computational Electromagnetics Society Journal*, vol. 32, no. 8, pp. 663-669, 2017.

[3] A. Nejadpak, M. R. Barzegaran, and O. A. Mohammed, “Evaluation of high frequency electro-magnetic behavior of planar inductor designs for resonant circuits in switching power converters,” *Applied Computational Electromagnetics Society Journal*, vol. 26, no. 9, pp. 737-748, 2011.

[4] W.-J. Kim and D. L. Trumper, “High-precision magnetic levitation stage for photolithography,” *Precision Engineering*, vol. 22, pp. 66-77, 1998.

[5] A. Shiri and A. Shoulaie, “Investigation of frequency effects on the performance of single-sided linear induction motor,” *Applied Computational Electromagnetics Society Journal*, vol.

27, no. 6, pp. 497-504, 2012.

[6] K. Halbach, "Design of permanent multipole magnets with oriented rare earth cobalt materials," *Nuclear Instruments and Methods*, vol. 169, no. 6, pp. 1-10, 1980.

[7] J. C. Compter, "Electro-dynamic planar motor," *Precision Engineering*, vol. 28, pp. 171-180, 2004.

[8] J. W. Jansen, C. M. M. van Lierop, E. A. Lomonova, and A. J. A. Vandenput, "Modeling of magnetically levitated planar actuators with moving magnets," *IEEE Transactions on Magnetics*, vol. 43, no. 1, pp. 15-25, 2007.

[9] J. W. Jansen, C. M. M. van Lierop, E. A. Lomonova, and A. J. A. Vandenput, "Magnetically levitated planar actuator with moving magnets," *IEEE Transactions on Industry Applications*, vol. 44, no. 4, pp. 1108-1115, 2008.

[10] J. Peng, Y. Zhou, and G. Liu, "Calculation of a new real-time control model for the magnetically levitated ironless planar motor," *IEEE Transactions on Magnetics*, vol. 49, no. 4, pp. 1416-1422, 2013.

[11] Y. Zhou, G. Liu, R. Zhou, L. Huo, and W. Ming, "Modeling and comparison of the Halbach array with different segments per pole," *International Journal of Applied Electromagnetics and Mechanics*, vol.47, no. 3, pp. 629-641, 2015.

[12] G. Liu, Y. Zhou, R. Zhou, W. Ming, and L. Huo, "Analysis and optimization of a 2-D magnet array with hexagon magnet," *Applied Computational Electromagnetics Society Journal*, vol. 28, no. 10, pp. 976-983, 2013.

[13] G. Liu, Y. Wang, X. Xu, W. Ming, and X. Zhang, "The optimal design of real time control precision of planar motor," *Applied Computational Electromagnetics Society Journal*, vol. 32, no. 10, pp. 948-954, 2017.